Structured light induced control of ultracold atomic dynamics

Grant W. Henderson

SUPA & Department of Physics

University of Strathclyde, Glasgow

This thesis is the result of the author's original research. It has been composed by the author and has not been previously submitted for examination which has led to the award of a degree.

The copyright of this thesis belongs to the author under the terms of the United Kingdom Copyright Acts as qualified by University of Strathclyde Regulation 3.50. Due acknowledgement must always be made of the use of any material contained in, or derived from, this thesis.

Signed:

Date:

Abstract

The ability to reliably transport ultracold atoms is a highly sought feature in a range of fields including quantum and ultracold atomic sciences. Here, we merge the typically separate fields of ultracold atomic physics and nonlinear optical systems, proposing to use light that carries orbital angular momentum (OAM) as a reliable atomic guide. By theoretically and numerically considering atom-light interactions where the two involved fields co-propagate, we open several novel approaches to structure formation, atomic localisation, trapping, and atomic guiding. By additionally considering a physical setup in which the interactions occur within a driven optical cavity, we extend this work to outline the capacity for further atomic transport, rich pattern formation, alternative mechanisms for atomic vortex lattice formation, and persistent current generation. These results are of significant prospective interest across a range of settings in which ultracold atomic systems are studied and applied, including in atomic transport, atomtronics, quantum and superfluid simulation, and vortex simulation.

Contents

Contents

Contents

List of Figures

Acknowledgements

There are many individuals to whom I am greatly indebted for their help in getting me to this point of submission.

Firstly, my grateful thanks go to my supervisory team of Dr. Alison M. Yao, Prof. Gian-Luca Oppo, and Dr. Gordon R. M. Robb, with whom I have had the privilege to work closely over the past few years. Their engagement with the project, guidance, and continuing support of my development as a researcher have been greatly appreciated, and have significantly helped shape large sections of the work that I now present. I wish to pay particular thanks and tribute to Alison: I cannot express my gratitude for your approachability, dedication, and responsiveness. Thank you for your extraordinary support throughout. I look forward to our continued research together!

A big part of my (non-Physics) life is in my love of music making, and I want to acknowledge the friendship, support, and musical joy I have experienced throughout my studies in both the Strathclyde University Concert Band and, latterly, the Dunbartonshire Concert Band. Thank you to the many wonderful members of these groups for their close friendship. There are too many to name individually, but please know that you have supported and sustained me throughout these years. My time in Glasgow would have been very different, and immeasurably worse, without you all.

Finally, I want to thank my family, both for their very direct assistance in the preparation of this thesis, but more fundamentally for their support throughout my life. You have always encouraged me to follow my interests, and have lovingly supported me in that endeavour. To those still here, and those no longer with us: thank you for your constant guidance, support, and love.

Part I

Introduction

Chapter 1

Thesis Introduction

The ability to control and direct the dynamics of ultracold atoms is highly sought after, with applications across a range of scientific fields including quantum technologies, simulation, condensed matter physics, and measurement sciences. This thesis proposes a new approach to atomic control: by directing them with light that has *structured* phase, we outline the capacity for customised, dynamic atomic localisation, trapping, and transport. We start by providing a broad introduction to the relevant scientific fields of ultracold atoms and light with structured phase.

1.1 Ultracold Atoms

In common parlance the word 'atom' connotes the fundamental building block of the world around us. Indeed, it derives from classical Greek 'atomos' meaning 'uncut', a reflection of the contemporary belief in the fundamental nature of atoms [1]. Since then, a sub-atomic realm has, of course, been identified [2], but studies at the atomic scale remain broad, active physical fields [3]. One such field of study is in the collective behaviour of ensembles of atoms at very low temperatures. The development of evaporative cooling techniques in the late 1980s, a process by which atomic ensembles, much

like a cup of tea, are progressively cooled (though with magnetic fields) enabled the realisation of collections of 'cold', localised atoms [4–7]. This approach, acting upon pre-cooled atoms from a magneto-optical trap [8–11], enabled, in the mid 1990s, the famous initial realisations of atomic ensembles occupying solely the thermal ground state: a Bose-Einstein condensate (BEC) of 'ultracold' atoms [12–16]. Two of these studies were fundamental to the award of the Nobel Prize for Physics in 2001 [14, 16, 17].

At ultracold temperatures individual atoms within an ensemble become indistinguishable and the ensemble acts as a single coherent, wave-like structure: an effective atomic superfluid [18]. Following the initial realisation of BECs, the field of ultracold atomic sciences grew rapidly [19], and their (relative) accessibility for probing quantum mechanical properties has since found many applications in quantum simulation [20], atom lasers [21], atomic clocks [22], and, due to their high sensitivity to forces, weak field sensing [23].

An electromagnetic field may produce a range of impactful forces upon coupled atomic ensembles [24, 25], including the optomechanical force, arising from interactions between atomic and coherent optical fields [26–29]. In such a scheme, the difference in oscillation frequencies between the two fields is known as their detuning. If the detuning is significantly larger than the natural linewidth of the atoms - a condition referred to as far detuned - then the optomechanical force may be used to alter the collective behaviour of atoms within a BEC [30–33]. The nature of such a force depends on the nature of the detuning: red-detuned fields will transport atoms to bright optical regions, whilst blue-detuned fields transport them to regions of optical darkness [29, 33–35]. This capability to reliably manipulate atoms by virtue of the nature of the atom-field detuning has been of great utility in laser cooling and optomechanical schemes.

1.2   Light with Structured Phase

In this thesis we consider atom-light interactions, focusing on cases where the optical field carries orbital angular momentum (OAM) [36]. Light, as well as having an amplitude that has homogeneous [37] or structured [38] form, may have a helical phase

front, and therefore carry OAM of index m [36]. Such fields with helical phase are often referred to as 'structured light', having both structured amplitude and phase [39–42]. Optical fields carrying OAM have extensive applications in trapping and rotating macroscopic objects [43], microscopy [44], optical and radio communications [45], low-loss optical fibre creation [46], quantum entanglement and communication [47], chiral light-matter interactions [48], and in electron dynamics [49, 50].

OAM has also been used extensively in interactions between light and various forms of matter [51]. Demonstrations of the capacity of OAM-carrying beams to manipulate physical media have included rotating particles held at the centre of an optical beam [52–57], acoustically swirling water-microparticle mixes [58], and rotating the entire propagation medium of the beam [59]. More recently, the impact of beams with OAM in atomic media has been explored, with studies proposing controlled nonlinear propagation in hot rubidium vapours [60], the optomechanical transport of cold atoms [61], the formation of optical 'compasses' [62] or 'Ferris wheels' [63], and the generation of persistent atomic flow in toroidal traps [64].

Here, we extend the last of these applications of OAM-carrying light, considering beams carrying OAM within ultracold atomic ensembles. We build on the ability of atom-light detuning to transport ultracold atoms to bright or dark optical regions [32, 33], introducing OAM to the system, and explore its potential to induce additional azimuthal motion upon such dynamics [36].

1.3   Layout of the Thesis

The main subject matter of this thesis is split into five Parts I - V, which are further divided into shorter Chapters 1 - 12 for ease of reading.

Throughout, we consider the interactions of ultracold matter and optical fields, generally (but not exclusively) with structured intensity and phase. These are typically separate fields, each with a wealth of existing research but limited overlap, and so in **Part I** we introduce the theoretical background of each field, used as the basis of the

research presented here. It consists of

- **Chapter 2**, which outlines the field of Bose-Einstein condensation, and how such collective ultracold atomic ensembles may be numerically modelled;

- **Chapter 3**, which considers the approaches behind structuring the intensity and phase of optical beams, and how such fields may be numerically modelled; and

- **Chapter 4**, which discusses a range of existing nonlinear dynamics observed in a variety of ultracold atomic and optical fields.

In **Part II**, we consider a physical setup where the coupled, interacting ultracold atomic and optical fields co-propagate alongside one another, building directly on Refs. [32, 33]. Part II contains

- **Chapter 5**, which outlines a theoretical description of such a physical setup through coupled nonlinear equations for the two fields;

- **Chapter 6**, which discusses the ability of these light-matter interactions to form coupled filamentation patterns on initially homogeneous fields;

- **Chapter 7**, which considers similar pattern formation on intensity structured fields, before developing the nonlinear model used to describe this process; and

- **Chapter 8**, which employs the revised model to investigate the ability of optical fields carrying OAM to guide ultracold atoms for controllable atomic transport.

In **Part III**, we consider an alternative physical configuration of light-matter interactions, envisaging a stationary BEC interacting with an optical field within a driven optical cavity. Part III contains

- **Chapter 9**, which discusses the theoretical alterations required to describe such atom-light interactions within a driven optical cavity;

- **Chapter 10**, which considers the capability of such a system to realise a wealth of spontaneous patterns on initially homogeneous atomic and optical fields;

- **Chapter 11**, which extends such patterns to intensity and phase structured

fields, generating high-index atomic vortex arrays; and

- **Chapter 12**, which outlines the creation of dynamic atomic persistent currents from optical vortex beams carrying OAM.

In **Part IV**, we conclude by comparing the OAM-induced atomic transport across the two physical configurations studied. We consider potential applications of the results outlined, and provide a brief discussion on the next steps that future research should take in this direction.

Part V, which provides further details of the two model derivations outlined in Chapters 5 and 9 in addition to a lookup table, is followed by a bibliography.

1.4 Field Visualisation

In this thesis, we regularly show two-dimensional (2D) field amplitude distributions, with a colour assigned to each point on the grid representing the amplitude of that point in the field. Our approach is summarised by Fig. 1.1, where the 'top-down' view typically considered here is shown under a three-dimensional (3D) profile, with the third dimension corresponding to the field's amplitude. Given that we consider coupled atomic and optical fields simultaneously, we assign each a different colour scheme, and so in Fig. 1.1 we show the same Gaussian as an (a) atomic and (b) optical field.
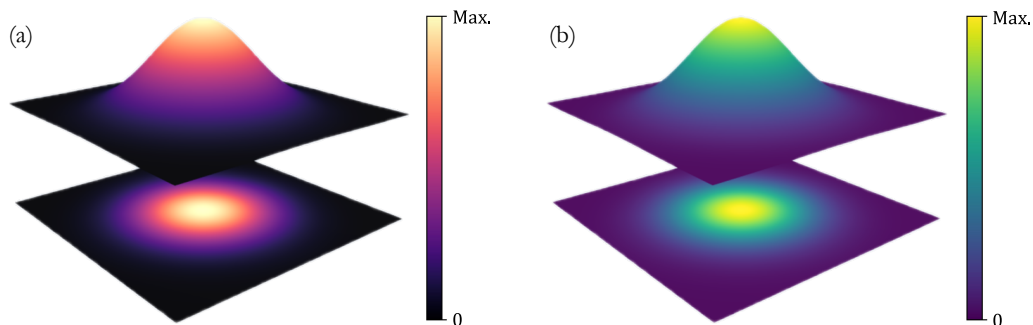
Figure 1.1: Transverse field plotted as an (a) atomic or (b) optical field. Bottom: 'top-down' transverse amplitude profiles used in this thesis. Top: equivalent 3D field, with the third dimension the field amplitude. Fields indicative of Gaussians, of beam waist thirty-five percent of the total transverse domain, where the beam waist represents the position at which the field amplitude falls to $1/e$ of its maximal value.

We also consider the phase structure of fields, a measure of the orientation difference between the electric and magnetic components, assigning it a separate cyclic colour scheme to differentiate it from amplitude distributions. Again, this is presented in a 'top-down' view, as summarised by Fig. 1.2 which demonstrates (a) the amplitude distribution of a Laguerre-Gaussian optical beam, and (b) its corresponding phase structure, both in 3D (upper) and 2D (lower), equivalently to Fig. 1.2.
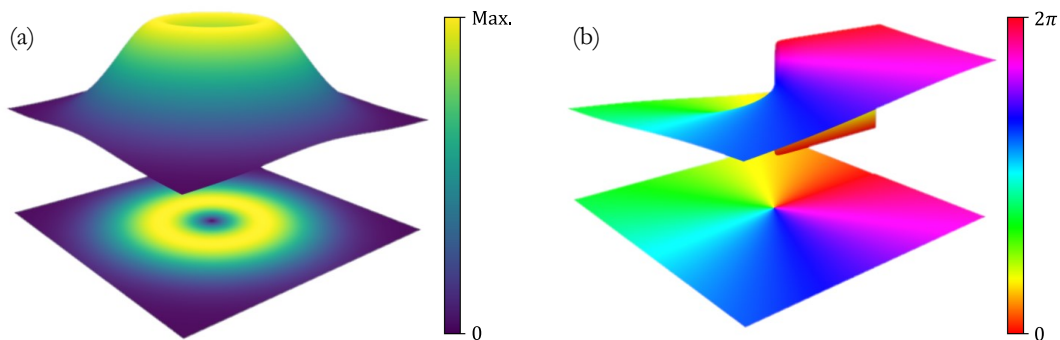
Figure 1.2: Transverse field phase visualisation procedure used throughout this thesis, showing (a) an optical field's amplitude, and (b) the same field's phase distribution. The bottom row shows the 'top-down' profiles used throughout, with the top row showing a three-dimensional equivalent visualisation, with the third dimension given by the field amplitudes or phase values, respectively. The field is an indicative Laguerre-Gaussian, of OAM index $m = 1$ and beam waist half the total transverse domain, and contains a helical phase of $0 \rightarrow 2\pi$ in the azimuthal direction around its amplitude ring.

1.5 Previously Published and in Preparation Works

Several works relating to results presented here exist, which we now outline in chronological order, along with an indication of the sections of the thesis they relate to.

G. Henderson, G. R. M. Robb, G.L. Oppo, and A. M. Yao, *"Mutual self structuring and novel Kerr-like fragmentation in coupled light/matter-wave interactions"*, Nonlinear Optics, NM1B.6 (2021): Chapters 5-8.

G. Henderson, G. R. M. Robb, G.L. Oppo, and A. M. Yao, *"Propagation of coupled atom-light solitons carrying angular momentum in a Bose-Einstein Condensate"*, Nonlinear Photonics, NpM2E.3 (2022): Chapters 5-8.

G. W. Henderson, G. R. M. Robb, G.L. Oppo, and A. M. Yao, *"Control of light-atom solitons and atomic transport by optical vortex beams propagating through a Bose-Einstein condensate"*, Phys. Rev. Lett. **129**, 073902 (2022): Chapters 5-8.

G. W. Henderson, G. R. M. Robb, G.L. Oppo, and A. M. Yao, *"Re-shaping Bose-Einstein condensates with complex light for atomic persistent currents and trapping"*, Complex Light and Optical Forces XVII; 1243608 (2023): Chapters 5-8.

G. W. Henderson, G. R. M. Robb, G.L. Oppo, and A. M. Yao, *"Structuring ultracold atoms with light in an optical cavity"*, Complex Light and Optical Forces XVII, 1243607 (2023): Chapters 9, 12.

G. W. Henderson, G. R. M. Robb, G.L. Oppo, and A. M. Yao, *"Generating Ultracold Atomic Persistent Currents with Structured Light"*, European Quantum Electronics Conference 2023, EA-2-5 (2023): Chapters 9, 12.

Additionally, there are several works currently in preparation for submission also relating to work presented here.

G. W. Henderson, G. R. M. Robb, G.L. Oppo, and A. M. Yao, *"Ultracold atomic persistent currents from structured light in a driven optical cavity"*: Chapters 9, 12.

G. W. Henderson, T. Ackemann, G. R. M. Robb, G.L. Oppo, and A. M. Yao, *"Spontaneous pattern formation between ultracold atoms and light in a driven optical cavity"*: Chapters 9, 10.

G. W. Henderson, G. R. M. Robb, G.L. Oppo, and A. M. Yao, *"Rotating ultracold atomic clusters and vortex lattices in optical darkness"*: Chapters 9, 11.

Finally, a further work was published during the time of the research described here, but does not directly relate to the results presented within this document.

A. Di Carli, G. Henderson, S. Flannigan, C. D. Colquhoun, M. Mitchell, G.L. Oppo, A. J. Daley, S. Kuhr, E. Haller, *"Collisionally inhomogeneous Bose-Einstein condensates with a linear interaction gradient"*, Phys. Rev. Lett. **125**, 183602 (2020).

Chapter 2

Bose-Einstein Condensation

In this chapter, we outline the essential background theory of the behaviour of atomic ensembles at ultracold temperatures. In *Section 2.1*, we outline the origins of such Bose-Einstein Condensates (BECs), considering the broad experimental cooling procedures required to create such a state of matter. In *Section 2.2* we introduce the Gross-Pitaevskii equation as a means of modelling such structures, deriving this model from the mean-field Hamiltonian describing atomic interactions within the BEC subject to an external trapping potential. Finally, in *Section 2.3*, we discuss how this description of the condensate's dynamics also gives an expression for the BEC's ground state; a Thomas-Fermi distribution, providing a description of the system's zero-energy state.

2.1   Origins

The fundamental requirement for BEC formation is that the collection of atoms involved exclusively occupies the system's ground energy state, and thus displays a single, coherent velocity [14, 18]. The advanced atomic cooling techniques required to reach such a state pre-date the initial realisations of condensates significantly, therefore in this section we briefly review the origins of ultracold atomic sciences.

The theoretical origins of BECs trace to the mid 1920s, when Einstein developed Bose's theory that a phase transition would occur in a non-interacting bosonic medium at the appropriate thermal conditions, leading to a collection of atoms *solely* in the ground state of the system [12, 13]. A qualitative description of the dynamics of an atomic ensemble undergoing this procedure is given in Fig. 2.1 [65, 66]. Panel (a) represents a generic system at a 'high' temperature $T \gg 10^{-4}$K [67]. Under such conditions, the behaviour of individual atoms within a collective medium may simply be thought of as 'billiard ball'-like, and they have a significant thermal velocity, v, and low ensemble density, proportional to the mean distance separating atoms, d.
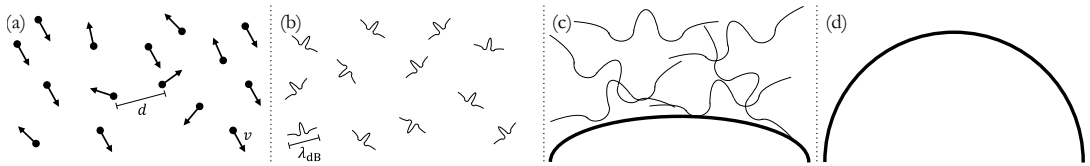
Figure 2.1: General concept of the behaviour of an ensemble of bosonic atoms as temperature decreases (a)-(d). After Refs. [65, 66].

To obtain quantum mechanical dynamics, the atomic temperature and hence the thermal velocity must be reduced substantially. Under these conditions, the atomic de Broglie wavelength, λ_{dB}, a measure of an atom's ability to display wave-like features, becomes significant. This is defined [68] as

$$\lambda_{\mathrm{dB}} = \sqrt{\frac{h^2}{2\pi m_{\mathrm{a}} k_{\mathrm{B}} T}}, \tag{2.1}$$

with h the Planck constant, k_{B} the Boltzmann constant, and m_{a} the atomic mass. With decreased thermal velocity, the wave-like nature of atoms becomes significant, and they act as individual wave-packets, Fig. 2.1(b).

At a critical temperature T_{C}, where the distance separating the atoms is comparable to their de Broglie wavelength (Fig. 2.1(c)) the matter waves overlap and act as a single coherent wavefunction rather than as many constituent atoms. Finally, at an idealised zero temperature, represented by Fig. 2.1(d), one no longer discerns individual atoms, either as particles or individual matter waves, but instead observes a single, collective

matter wave. In these conditions, the entire atomic medium has condensed to the thermal ground state of the system.

The approach to condensation has a number of requirements. Fundamentally, the atomic medium must be bosonic, enabling an integer spin and avoiding the Pauli exclusion principle of fermions [14]. We note that although fermions may also condense to realise a molecular BEC, more complex schemes are required (see, e.g., Refs. [69–72]).

In addition to this bosonic condition, Eqn. (2.1) requires the atomic ensemble to be at low temperatures. If we consider T_C as the temperature at which condensation begins to occur, then we may write the condition that

$$\lambda_{\mathrm{dB}} \approx \frac{1}{\sqrt[3]{n}}, \tag{2.2}$$

with n the condensate atom number density, related to the mean atomic separation by

$$\frac{1}{\sqrt[3]{n}} = d. \tag{2.3}$$

Using Eqn. (2.1), we may equate Eqn. (2.2) to the required critical temperature

$$T_C(n) \quad = \quad \frac{h^2}{2\pi m_a k_B} n^{2/3}. \tag{2.4}$$

Taking $n \approx 10^{14}$ cm^{-3}, typical for a dilute atomic gas [19], and selecting an appropriate m_a for caesium (see Appendix C), one finds a critical temperature on the order of 10^{-7}K: a free-space *ultracold* threshold. We note that this threshold may be significantly altered through the application of external potentials upon the atomic medium [73].

As such, before the first experimental realisation of a BEC became possible, there was a requirement to cool atoms beneath such a threshold. To this end, the authors of Ref. [14], the first reported BEC realisation, followed a combination of methods, beginning by directing room temperature Rubidium atoms into a magneto-optical trap (MOT). This device uses a succession of counter-propagating circularly polarized optical beams which act as a molasses on interference, cooling and slowing atoms to the $\sim$mK

scale [8, 74], a procedure that led to the award of the Nobel Prize for Physics in 1997 [75].

Following this initial period of cooling within the MOT, the optical field gradients were increased, with this compressed trap further cooling the atomic cloud to $\sim 20\mu$K [76]. From this stage, the optical portion of the MOT was removed, and the magnetic trap set to rotate [10], an approach enabling evaporative cooling controlled by progressively weakening the strength of the trap and rotational frequency [4–7, 10]. Though a lossy approach, with the most thermally excited atoms escaping with each trap alteration, the remaining atoms will have a lower mean temperature. The authors of Ref. [14] utilised such a procedure, and, as shown in Fig. 2.2, observed an increasing central condensate fraction in the velocity distribution of their atomic ensemble for trapping frequencies below 4.25MHz.
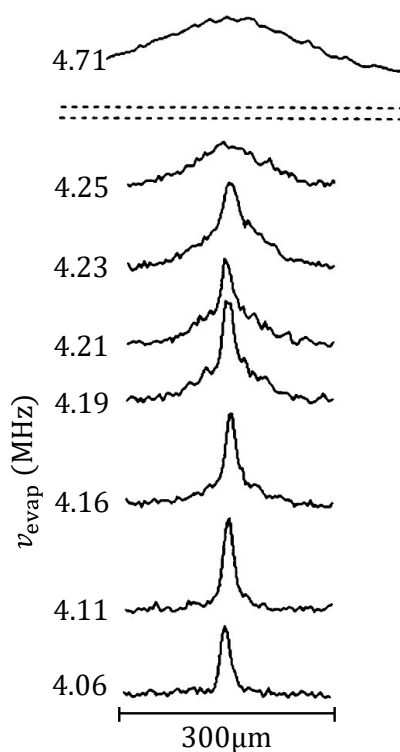
Figure 2.2: Evaporative cooling of Rb^{87} atoms for magnetic trap frequencies v_{evap} high (top) to low (bottom). Onset of condensate when $v_{\text{evap}} < 4.25$MHz signified by the narrow central uniform velocity fraction. From Ref. [14]. Reprinted with permission from AAAS.

This first BEC realisation in Rubidium-87 vapours [14] was quickly followed by additional independent realisations in both Lithium-7 [15] and Sodium-23 [16]. Each was also significant: the Li^7 BEC was the first with attractive interatomic interactions, and the Na^{23} BEC significantly increased the total condensate atom number, facilitating a later demonstration of the coherent nature of BECs by interfering two condensates that had been split [77]. Two of these works, Refs. [14, 16], were subsequently awarded the Nobel Prize for Physics in 2001 [17].

The field of ultracold atomic sciences has grown significantly and developed since the first BECs were generated [78, 79]. Further atomic media have been condensed, including potassium [80], sodium [81], rubidium [82], and caesium [83], with the Feshbach resonance, a phenomenon occurring when a two-atom collision leads to mixing between typically open and closed molecular channels, of the latter three atomic species also enabling the nature and strength of BEC interatomic collisions to be altered through an applied magnetic field [84]. Hydrogen [85] and helium [86] BECs have also been created, in addition to more complex spinor BECs, multi component structures each with a different spin, in rubidium [87, 88] and sodium [89]. These structures paved the way for mixed BEC states for a variety of isotopic and atomic combinations [90–94], dipolar Chromium [95], Dysprosium [96], and Erbium [97] BECs, or BEC-Fermi gas mixes [98]. Condensates have wide applications given their exhibition of quantum mechanical properties [77]. They have been employed for quantum simulation [20], the creation of atom lasers [21], atomic clocks for accurate timekeeping [22], and in the high sensitivity sensing of gravitational, rotational and magnetic fields [23]. Ultracold atomic science continues to be an evolving field, with the first condensate having recently been created in space [99].

2.2 Nonlinear Modelling

The dynamics of the matter-wave that describes the evolution of a BEC may be modelled by a nonlinear partial differential equation. The derivation of such a model is integral to the work of this thesis, and although a commonly accepted procedure, we

provide here a brief summary of the derivation. We follow the methods of Ref. [100], and so begin by considering N interacting bosons, confined by an external trapping potential, V_{ext}. In such a scheme, a many-body Hamiltonian to describe the interactions of the atomic ensemble is given by

$$\hat{H} = \int d\mathbf{r}\hat{\Psi}^\dagger(\mathbf{r})\left[-\frac{\hbar^2}{2m_{\text{a}}}\nabla^2 + V_{\text{ext}}(\mathbf{r})\right]\hat{\Psi}(\mathbf{r}) + \frac{1}{2}\int d\mathbf{r}d\mathbf{r}'\hat{\Psi}^\dagger(\mathbf{r})\hat{\Psi}^\dagger(\mathbf{r}')V(\mathbf{r}-\mathbf{r}')\hat{\Psi}(\mathbf{r}')\hat{\Psi}(\mathbf{r}),$$
$$(2.5)$$

where $\hat{\Psi}^\dagger$ and $\hat{\Psi}$ are particle creation and annihilation operators respectively, $\mathbf{r}$ represents the position where the operation takes place, and $V(\mathbf{r}-\mathbf{r}')$ provides a potential arising from two-body collisions between atoms.

The time evolution of the matter-wave may be written in terms of the system's Hamiltonian using the Heisenberg equation [101]:

$$i\hbar\frac{\partial}{\partial t}\hat{\Psi}(\mathbf{r},t) = \left[\hat{\Psi}, \hat{H}\right],$$
$$(2.6)$$

which, applying Eqn. (2.5), becomes

$$\begin{aligned}
i\hbar\frac{\partial}{\partial t}\hat{\Psi}(\mathbf{r},t) &= \left[\int d\mathbf{r}\hat{\Psi}^\dagger(\mathbf{r},t)\left[-\frac{\hbar^2}{2m_{\text{a}}}\nabla^2 + V_{\text{ext}}(\mathbf{r})\right]\hat{\Psi}(\mathbf{r},t)\right.\\
&\left.+ \frac{1}{2}\int d\mathbf{r}d\mathbf{r}'\hat{\Psi}^\dagger(\mathbf{r},t)\hat{\Psi}^\dagger(\mathbf{r}',t)V(\mathbf{r}-\mathbf{r}')\hat{\Psi}(\mathbf{r}',t)\hat{\Psi}(\mathbf{r},t)\right]\hat{\Psi}(\mathbf{r},t). \quad (2.7)
\end{aligned}$$

It follows that

$$i\hbar\frac{\partial}{\partial t}\hat{\Psi}(\mathbf{r},t) = \left[-\frac{\hbar^2}{2m_{\text{a}}}\nabla^2 + V_{\text{ext}}(\mathbf{r}) + \int d\mathbf{r}'\hat{\Psi}^\dagger(\mathbf{r}',t)V(\mathbf{r}'-\mathbf{r})\hat{\Psi}(\mathbf{r}',t)\right]\hat{\Psi}(\mathbf{r},t). \quad (2.8)$$

We introduce a complex wave function to describe the matter wave $\psi(\mathbf{r},t)$, which may be related to the field operator $\hat{\Psi}(\mathbf{r},t)$ through its expectation value

$$\psi(\mathbf{r},t) \equiv \langle\hat{\Psi}(\mathbf{r},t)\rangle. \quad (2.9)$$

We note also the condition that the BEC density $n(\mathbf{r},t) = |\psi(\mathbf{r},t)|^2$.

Considering the new complex wave function $\psi(\mathbf{r}, t)$, Eqn. (2.8) may be recast into

$$i\hbar \frac{\partial}{\partial t}\psi(\mathbf{r}, t) = \left[-\frac{\hbar^2}{2m_\mathrm{a}}\nabla^2 + V_\mathrm{ext}(\mathbf{r}) + \int d\mathbf{r}' V(\mathbf{r}' - \mathbf{r})|\psi(\mathbf{r}', t)|^2 \right]\psi(\mathbf{r}, t). \qquad (2.10)$$

Finally, we identify that, in the case of a dilute, cold gas of atoms, two-body atomic collisions represented by the term $V(\mathbf{r}' - \mathbf{r})$ are directly given by the s-wave scattering length. As such, we re-write this term as

$$V(\mathbf{r}' - \mathbf{r}) = g\delta(\mathbf{r}' - \mathbf{r}), \qquad (2.11)$$

where

$$g = \frac{4\pi\hbar^2 a_\mathrm{s}}{m_\mathrm{a}}, \qquad (2.12)$$

acting as a scattering parameter, controlled by a_s, the scattering length of the atomic medium. This term may be positive, negative, or zero, correspond to repulsive, attractive, or non-interacting atomic scattering, respectively [100, 102]. Inserting Eqn. (2.11) into Eqn. (2.10), we reach

$$i\hbar \frac{\partial}{\partial t}\psi(\mathbf{r}, t) = \left[-\frac{\hbar^2}{2m_\mathrm{a}}\nabla^2 + V_\mathrm{ext}(\mathbf{r}) + g|\psi(\mathbf{r}, t)|^2 \right]\psi(\mathbf{r}, t). \qquad (2.13)$$

Eqn. (2.13) is the Gross-Pitaevskii equation [103–105], and describes the temporal dynamics of a BEC matter-wave subject to an external trapping potential $V_\mathrm{ext}(\mathbf{r})$. It takes a similar form to the nonlinear Schrödinger equation in optics [106, 107], in recognition of the parity between light and ultracold matter. The dynamics of the condensate are strongly determined by the sign and strength of the scattering parameter g, which determines whether its nonlinearity is focusing (attractive interatomic interactions) or defocusing (repulsive interatomic interactions).

2.3 Ground State

It is possible to proceed from the Gross-Pitaevskii equation and obtain a ground state of the system, which the atoms will ideally occupy before evolution. Again, we follow the approach of Ref. [100], partitioning the temporal and spatial components of the wave function according to

$$\psi(\mathbf{r}, t) = \psi(\mathbf{r}) \exp\left(-i\mu_\mathrm{C} t/\hbar\right), \tag{2.14}$$

with μ_C the chemical potential of the system. Eqn. (2.13) then becomes

$$\mu_\mathrm{C}\psi(\mathbf{r}) = \left[-\frac{\hbar^2}{2m_\mathrm{a}}\nabla^2 + V_\mathrm{ext}(\mathbf{r}) + g|\psi(\mathbf{r})|^2\right]\psi(\mathbf{r}). \tag{2.15}$$

If we neglect the term in ∇^2 corresponding to the atomic kinetic energy from Eqn. (2.15) to obtain a stationary ground state, in the limit of large total atom numbers $N \gtrsim 10^4$ we find [108–110]

$$\mu_\mathrm{C}\psi(\mathbf{r}) = \left[V_\mathrm{ext}(\mathbf{r}) + g|\psi(\mathbf{r})|^2\right]\psi(\mathbf{r}),$$
$$\Rightarrow \qquad |\psi(\mathbf{r})|^2 = g^{-1}\left[\mu_\mathrm{C} - V_\mathrm{ext}(\mathbf{r})\right]. \tag{2.16}$$

Eqn. (2.16) is referred to as the Thomas-Fermi approximation, and gives the transverse ground state density of a BEC described by the Gross-Pitaevskii equation. It will have a non-zero density when $\mu_\mathrm{C} > V_\mathrm{ext}(\mathbf{r})$, and otherwise an atomic density $|\psi(\mathbf{r})|^2 = 0$ when $\mu_\mathrm{C} < V_\mathrm{ext}(\mathbf{r})$.

We may write a generalised expression for a Thomas-Fermi distribution, of a similar form to Eqn. (2.16), that depends on a maximum initial amplitude A_ψ and a customisable transverse field width w_ψ with $r^2 = x^2 + y^2$, as:

$$\psi(r) = A_\psi\left[1 - r^2/\left(2w_\psi^2\right)\right]. \tag{2.17}$$

Note that from Eqn. (2.17) we consider $\psi(r) < 0 \to 0$, as standard.

Fig. 2.3 shows a Thomas-Fermi distribution of maximum amplitude A_ψ and $w_\psi = 50\mu$m, on a total 2D grid of size $400 \times 400\mu$m, as well as a 1D cross section of this field. We also plot, on the right hand side of Fig. 2.3, its phase, homogeneous as expected from Eqn. (2.17).
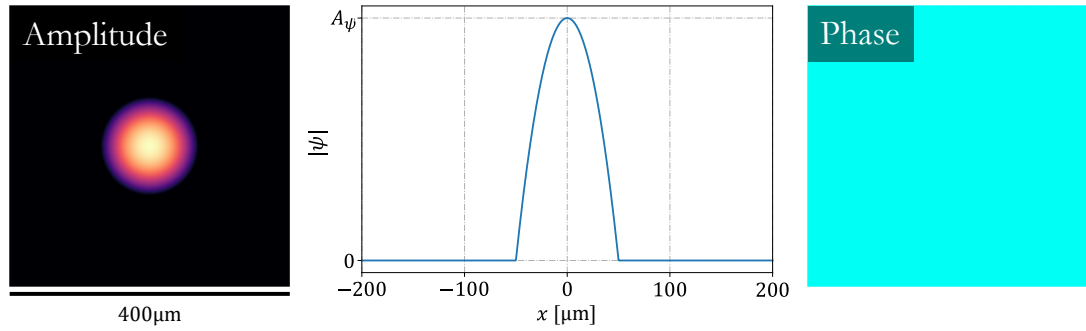
Figure 2.3: Typical Thomas-Fermi distribution of Eqn. (2.17), for a maximum BEC amplitude of A_ψ and transverse width $w_\psi = 50\mu$m, on a total 2D grid of size 400μm $\times$ 400μm. Left shows field amplitude, centre shows 1D cross section of field, and right shows 2D field phase.

Chapter 3

Propagating Structured Light

In this chapter, we outline the behaviour of an optical field propagating within a nonlinear medium. In *Section 3.1*, we show how such a system may be modelled numerically, beginning from the familiar Maxwell equations to derive a nonlinear Schrödinger (NLS) equation that describes the behaviour of the field within such a medium. In the rest of the chapter, we consider solutions of the linear paraxial wave equation, used to derive the NLS, and initially outline in *Section 3.2* the simplest case, a homogeneous field, with no structure in amplitude or phase. In *Section 3.3* we consider a Gaussian field, which has a structured amplitude, before finally employing both Laguerre-Gaussian and Bessel-Gaussian modes, with their simultaneously structured amplitude and phase, in *Section 3.4*.

3.1   Light in a Nonlinear Medium

Before outlining the various forms of structure that light may hold, we must first consider the typical approach used to theoretically describe a propagating optical field. Therefore, we first study optical fields evolving within a generic nonlinear medium, which will be extended to propagation through a BEC in later chapters. We begin by

outlining the procedure to derive the paraxial nonlinear wave equation, also referred to as the nonlinear Schrödinger equation, and explore its similarities with, and differences from, the Gross-Pitaevskii equation (Eqn. (2.13)).

3.1.1 Nonlinear Wave Equation

For an optical beam propagating through a medium, Maxwell's equations take the general form

$$\nabla \cdot \tilde{\mathbf{D}} = \tilde{\rho}, \tag{3.1}$$

$$\nabla \cdot \tilde{\mathbf{B}} = 0, \tag{3.2}$$

$$\nabla \times \tilde{\mathbf{E}} = -\frac{\partial \tilde{\mathbf{B}}}{\partial t}, \tag{3.3}$$

$$\nabla \times \tilde{\mathbf{H}} = \frac{\partial \tilde{\mathbf{D}}}{\partial t} + \tilde{\mathbf{J}}, \tag{3.4}$$

where $\mathbf{E}$ and $\mathbf{H}$ represent the electric and magnetic fields, respectively, $\mathbf{D}$ and $\mathbf{B}$ represent the electric displacement and magnetic induction fields, ρ and $\mathbf{J}$ represent the free charge and current densities, and we indicate quantities fluctuating rapidly in time with a tilde.

Assuming that there are no free charges, such that $\tilde{\rho} = 0$, that there are no free currents, such that $\tilde{\mathbf{J}} = 0$, and that any material is non-magnetic, we can write $\tilde{\mathbf{B}} = \mu_0 \tilde{\mathbf{H}}$. We relate the fields $\tilde{\mathbf{D}}$ and $\tilde{\mathbf{E}}$ with the relationship

$$\tilde{\mathbf{D}} = \epsilon_0 \tilde{\mathbf{E}} + \tilde{\mathbf{P}}, \tag{3.5}$$

where $\tilde{\mathbf{P}}$ describes the polarisation of the medium. Typically, this can be written as

$$\tilde{\mathbf{P}} = \epsilon_0 \left[\chi^{(1)} \tilde{\mathbf{E}} + \chi^{(2)} \tilde{\mathbf{E}}^2 + \chi^{(3)} \tilde{\mathbf{E}}^3 + ... \right], \tag{3.6}$$

$$= \tilde{\mathbf{P}}^{(1)} + \tilde{\mathbf{P}}^{(2)} + \tilde{\mathbf{P}}^{(3)} + ..., \tag{3.7}$$

where the first term represents the linear response, the second the second-order nonlinear response, and the third the third-order nonlinear response, of the medium.

19

Making use of Eqn. (3.5), we transform Eqn. (3.3) through

$$
\begin{aligned}
\nabla \times \left(\nabla \times \tilde{\mathbf{E}} \right) &= -\frac{\partial}{\partial t} \left(\nabla \times \tilde{\mathbf{B}} \right), \\
&= -\mu_0 \frac{\partial}{\partial t} \left(\nabla \times \tilde{\mathbf{H}} \right), \\
&= -\mu_0 \frac{\partial^2}{\partial t^2} \tilde{\mathbf{D}}, \\
&= -\mu_0 \frac{\partial^2}{\partial t^2} \left(\epsilon_0 \tilde{\mathbf{E}} + \tilde{\mathbf{P}} \right), \\
&= -\frac{1}{c^2} \frac{\partial^2 \tilde{\mathbf{E}}}{\partial t^2} - \frac{1}{\epsilon_0 c^2} \frac{\partial^2 \tilde{\mathbf{P}}}{\partial t^2}, \qquad \left(\text{as } \epsilon_0 \mu_0 = \frac{1}{c^2} \right)
\end{aligned}
$$

$$
\Rightarrow \qquad \nabla \times \left(\nabla \times \tilde{\mathbf{E}} \right) + \frac{1}{c^2} \frac{\partial^2 \tilde{\mathbf{E}}}{\partial t^2} = -\frac{1}{\epsilon_0 c^2} \frac{\partial^2 \tilde{\mathbf{P}}}{\partial t^2}. \tag{3.8}
$$

Eqn. (3.8) is a general form of the wave equation, which describes the behaviour of an optical field within a medium. It may be further simplified by writing the first term on the left hand side as

$$
\nabla \times \left(\nabla \times \tilde{\mathbf{E}} \right) = \nabla \left(\nabla \cdot \tilde{\mathbf{E}} \right) - \nabla^2 \tilde{\mathbf{E}}, \tag{3.9}
$$

and recognising that, as we consider no free charges, $\nabla \left(\nabla \cdot \tilde{\mathbf{E}} \right) = 0$. This transforms the wave equation into the more familiar form

$$
\nabla^2 \tilde{\mathbf{E}} - \frac{1}{c^2} \frac{\partial^2 \tilde{\mathbf{E}}}{\partial t^2} = \frac{1}{\epsilon_0 c^2} \frac{\partial^2 \tilde{\mathbf{P}}}{\partial t^2}. \tag{3.10}
$$

Recalling from Eqn. (3.6) that the medium may have both a linear and nonlinear response, we consider these two contributions separately, assigning

$$
\tilde{\mathbf{P}} = \epsilon_0 \chi^{(1)} \tilde{\mathbf{E}} + \tilde{\mathbf{P}}^{\mathrm{NL}}, \tag{3.11}
$$

where (to third order nonlinearity)

$$
\tilde{\mathbf{P}}^{\mathrm{NL}} = \epsilon_0 \left[\chi^{(2)} \tilde{\mathbf{E}}^2 + \chi^{(3)} \tilde{\mathbf{E}}^3 \right]. \tag{3.12}
$$

The second-order nonlinear response, $\epsilon_0 \chi^{(2)} \tilde{\mathbf{E}}^2$, is typically zero if the propagation

medium does not show inversion symmetry. We then consider that

$$\tilde{\mathbf{P}}^{\mathrm{NL}} = \epsilon_0 \chi^{(3)} \tilde{\mathbf{E}}^3. \tag{3.13}$$

Combining Eqns. (3.10), (3.11) and (3.13), a nonlinear wave equation is obtained for propagation within a nonlinear, isotropic medium of

$$\nabla^2 \tilde{\mathbf{E}} - \frac{1}{c^2} \frac{\partial^2 \tilde{\mathbf{E}}}{\partial t^2} = \frac{\chi^{(1)}}{c^2} \frac{\partial^2 \tilde{\mathbf{E}}}{\partial t^2} + \frac{1}{\epsilon_0 c^2} \frac{\partial^2 \tilde{\mathbf{P}}^{\mathrm{NL}}}{\partial t^2},$$

$$\Rightarrow \qquad \nabla^2 \tilde{\mathbf{E}} - \frac{1 + \chi^{(1)}}{c^2} \frac{\partial^2 \tilde{\mathbf{E}}}{\partial t^2} = \frac{1}{\epsilon_0 c^2} \frac{\partial^2 \tilde{\mathbf{P}}^{\mathrm{NL}}}{\partial t^2},$$

$$\Rightarrow \qquad \nabla^2 \tilde{\mathbf{E}} - \frac{\epsilon^{(1)}}{c^2} \frac{\partial^2 \tilde{\mathbf{E}}}{\partial t^2} = \frac{1}{\epsilon_0 c^2} \frac{\partial^2 \tilde{\mathbf{P}}^{\mathrm{NL}}}{\partial t^2}. \tag{3.14}$$

In Eqn. (3.14), we define the relative permittivity of the medium $\epsilon^{(1)} = 1 + \chi^{(1)}$ to reach a description of the propagation of an optical field in a nonlinear medium.

3.1.2 Paraxial Wave Equation

If we consider the case of $\epsilon^{(1)} = n^2$, where n is the medium's refractive index, then we find that each frequency component of the optical field propagating through the nonlinear medium will satisfy the wave equation

$$\nabla^2 \tilde{\mathbf{E}} - \frac{n^2}{c^2} \frac{\partial^2 \tilde{\mathbf{E}}}{\partial t^2} = \frac{1}{\epsilon_0 c^2} \frac{\partial^2 \tilde{\mathbf{P}}^{\mathrm{NL}}}{\partial t^2}. \tag{3.15}$$

We make the ansatz that the field has rapidly fluctuating spatial (z) and temporal (t) components. These components may be separated as

$$\tilde{\mathbf{E}}_n(\mathbf{r}, t) = \mathbf{A}_n(\mathbf{r}) \exp\left(i(k_n z - \omega_n t)\right) + c.c., \tag{3.16}$$

$$\tilde{\mathbf{P}}_n(\mathbf{r}, t) = \mathbf{p}_n(\mathbf{r}) \exp\left(i(k_n z - \omega_n t)\right) + c.c., \tag{3.17}$$

where the fields are assigned complex amplitudes $\mathbf{A}_n$ and $\mathbf{p}_n$, wavevectors k_n, and angular frequencies ω_n, with $k_n = (\omega_n n)/c$. Applying this to Eqn. (3.15), and splitting

the Laplacian into its transverse ($\perp = (x, y)$) and longitudinal (z) components, we obtain

$$\nabla_\perp^2 \tilde{\mathbf{E}} + \nabla_z^2 \tilde{\mathbf{E}} - \frac{n^2}{c^2}\frac{\partial^2 \tilde{\mathbf{E}}}{\partial t^2} = \frac{1}{\epsilon_0 c^2}\frac{\partial^2 \tilde{\mathbf{P}}^{\mathrm{NL}}}{\partial t^2},$$

$$\left[\nabla_\perp^2 + \partial_z^2 + 2ik_n\partial_z - k_n^2 + \frac{n^2}{c^2}\omega_n^2\right]\mathbf{A}_n \exp\left(i(k_n z - \omega_n t)\right) = -\frac{\omega_n^2}{\epsilon_0 c^2}\mathbf{p}_n \exp\left(i(k_n z - \omega_n t)\right),$$

$$\nabla_\perp^2 \mathbf{A}_n + 2ik_n\partial_z\mathbf{A}_n = -\frac{\omega_n^2}{\epsilon_0 c^2}\mathbf{p}_n, \tag{3.18}$$

where Δk accounts for any difference between k_n' and k_n. This ignores second order temporal derivatives, since for slowly varying amplitudes $\partial_z^2 << k_n\partial_z$. Considering the linear case, such that $\mathbf{p}_n = 0$,

$$\partial_z\mathbf{A}_n = \frac{i}{2k_n}\nabla_\perp^2\mathbf{A}_n. \tag{3.19}$$

This is a form of the paraxial wave equation to describe an electromagnetic wave propagating along the z-axis.

3.1.3 Nonlinear Schrödinger Equation

Eqn. (3.18) may be further simplified to obtain a relationship depending solely on the field amplitude $\mathbf{A}_n$. To do this, we again consider the nonlinear components of the polarisation response, defined in Eqn. (3.13) as

$$\tilde{\mathbf{P}}^{\mathrm{NL}} = \epsilon_0\chi^{(3)}\tilde{\mathbf{E}}^3$$

Applying Eqn. (3.16), the nonlinear polarisation component takes the form

$$\tilde{\mathbf{P}}^{\mathrm{NL}} = \epsilon_0\chi^{(3)}\left[\mathbf{A}_n^3 \exp\left(3i(k_n z - \omega_n t)\right) + 3|\mathbf{A}_n|^2\mathbf{A}_n \exp\left(i(k_n z - \omega_n t)\right) + c.c.\right]. \tag{3.20}$$

Considering only the term at frequency ω in Eqn. (3.20), the nonlinear polarisation component becomes

$$\tilde{\mathbf{P}}^{\mathrm{NL}} = \epsilon_0\chi^{(3)}\left[3|\mathbf{A}_n|^2\mathbf{A}_n \exp\left(i(k_n z - \omega_n t)\right)\right],$$

$$= 3\epsilon_0 \chi^{(3)} |\mathbf{A}_n|^2 \tilde{\mathbf{E}}_n. \tag{3.21}$$

Using Eqns. (3.11) and (3.21), the total polarisation may be written as

$$
\begin{aligned}
\tilde{\mathbf{P}} &= \epsilon_0 \chi^{(1)} \tilde{\mathbf{E}} + \tilde{\mathbf{P}}^{\mathrm{NL}}, \\
&= \epsilon_0 \chi^{(1)} \tilde{\mathbf{E}} + 3\epsilon_0 \chi^{(3)} |\mathbf{A}_n|^2 \tilde{\mathbf{E}}, \\
&= \epsilon_0 \left[\chi^{(1)} + 3\chi^{(3)} |\mathbf{A}_n|^2 \right] \tilde{\mathbf{E}}, \\
&= \epsilon_0 \chi^{(\mathrm{eff})} \tilde{\mathbf{E}},
\end{aligned}
\tag{3.22}
$$

with $\chi^{(\mathrm{eff})} = \chi^{(1)} + 3\chi^{(3)} |\mathbf{A}_n|^2$. This gives a total medium refractive index of

$$
\begin{aligned}
n^2 &= 1 + \chi^{(\mathrm{eff})}, \\
&= 1 + \chi^{(1)} \tilde{\mathbf{E}} + 3\chi^{(3)} |\mathbf{A}_n|^2, \\
&= n_0^2 \left(1 + \frac{3\chi^{(3)}}{n_0^2} |\mathbf{A}_n|^2 \right),
\end{aligned}
$$

and, as such,

$$n \approx n_0 + \frac{3\chi^{(3)}}{2n_0} |\mathbf{A}_n|^2, \tag{3.23}$$

where $n_0^2 = 1 + \chi^{(1)}$.

In Eqn. (3.23) the refractive index consists of linear and nonlinear components, n_0 and $n_2 = \frac{3\chi^{(3)}}{2n_0}$, respectively. It has previously been shown that for waves of the form in Eqn. (3.16), $\chi^{(3)}$ may be related to n_2 through the relationship [107]

$$\chi^{(3)} = \frac{n_0^2 \epsilon_0 c}{3} n_2. \tag{3.24}$$

From this,

$$\mathbf{p}_n = n_0^2 \epsilon_0^2 c n_2, \tag{3.25}$$

leading to the alternative form of the paraxial wave equation

$$\nabla_\perp^2 \mathbf{A}_n + 2ik_n \partial_z \mathbf{A}_n = -\frac{n_0^2 \epsilon_0 n_2}{c} \omega_n^2 |\mathbf{A}_n|^2 \mathbf{A}_n, \tag{3.26}$$

which can be written as

$$\partial_z \mathbf{A}_n = \frac{i}{2k_n}\nabla_\perp^2 \mathbf{A}_n + \frac{i}{2}k_n c\epsilon_0 n_2 |\mathbf{A}_n|^2 \mathbf{A}_n, \qquad (3.27)$$

where $k_n^2 = \frac{n_0^2 w_n^2}{c^2}$.

Eqn. (3.27) is the nonlinear Schrödinger equation [106, 107], and describes the propagation of an optical beam through a third order nonlinear medium. When $n_2 < 0$, the field is subject to a defocusing nonlinearity, whilst for $n_2 > 0$, the field is subject to a focusing nonlinearity. This is similar to Eqn. (2.13), which describes the dynamics of a BEC subject to an external potential. Here, there is no external potential, but the other terms may be mapped directly, with the atomic parameter g having a similar role to the optical parameter n_2.

3.2   Homogeneous Fields

The linear paraxial wave equation, Eqn. (3.19), admits several field solutions through the ansatz of Eqn. (3.16). The simplest of these solutions is a homogeneous optical field, given simply by

$$\mathbf{A}_n(r, z) = \mathcal{A}, \qquad (3.28)$$

where $\mathcal{A}$ is the mode amplitude and $r^2 = x^2 + y^2$. Such a field will have uniform amplitude and phase, as represented by Fig. 3.1 on a two-dimensional (x, y) grid.
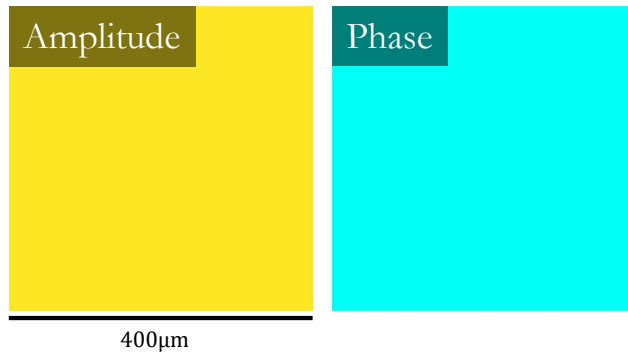
Figure 3.1: Typical homogeneous field, as in Eqn. (3.28), for a field amplitude of $\mathcal{A}$, on an arbitrary 2D 400μm $\times$ 400μm grid. Left shows field amplitude, right shows phase.

3.3 Structured Amplitude

An alternative form of optical field that satisfies the ansatz of Eqn. (3.16) is a Gaussian field. This introduces structure to the amplitude of the optical field. We define a mode with a transverse beam waist w_0 and a radius r as [111]

$$\mathbf{A}_n(r,z) = \mathcal{A}\frac{w_0}{w(z)}\exp\left(\frac{-r^2}{w(z)^2}\right)\exp\left(\frac{ikr^2}{2R(z)}\right)\exp\left(i\Phi(z)\right), \qquad (3.29)$$

with

$$w(z) = w_0\sqrt{\left[1+\left(\frac{z}{z_R}\right)^2\right]}, \qquad (3.30)$$

$$R(z) = z\left[1+\left(\frac{z_R}{z}\right)^2\right], \qquad (3.31)$$

$$\Phi(z) = -\arctan\left(\frac{z}{z_R}\right). \qquad (3.32)$$

Here, $w(z)$ represents the $1/e$ radius of the field distribution, $R(z)$ is the radius of curvature of the wavefront, and $\Phi(z)$, the Gouy phase, represents the spatial variation of the phase of the wave as it propagates. z_R is the Rayleigh range of the beam,

$$z_R = \frac{\pi w_0^2}{\lambda}, \qquad (3.33)$$

with λ the wavelength of the optical field. This is the z-distance at which the beam waist increases to $\sqrt{2}w_0$ as a result of diffraction, see Fig. 3.2.
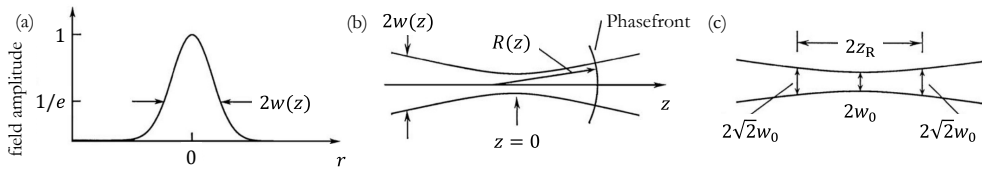
Figure 3.2: Typical Gaussian distribution characteristics from Eqns. (3.29)-(3.33) for $\mathcal{A} = 1$. (a) 1D cross section of field amplitude distribution at $z = 0$. (b) Beam radius $w(z)$ and radius of curvature $R(z)$ variation with position z. (c) Comparison between the beam waist w_0 and Rayleigh range z_R. Used with permission of Elsevier Science & Technology Journals, from Ref. [107]; permission conveyed through Copyright Clearance Center, Inc.

Throughout this thesis, initial optical distributions are considered to be at the beam waist at $z = 0$, i.e. $w(0) = w_0$. The Gaussian distribution is then given by

$$G(r) = A \exp\left(-\frac{r^2}{w_0^2}\right), \tag{3.34}$$

where a field amplitude A has been introduced. This form of field is shown in Fig. 3.3.
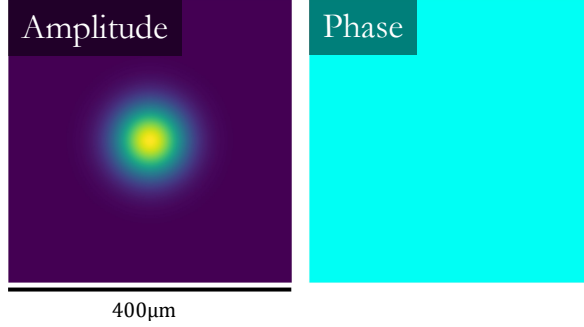
Figure 3.3: Typical Gaussian field distribution of Eqn. (3.34), for a maximum field amplitude of A and beam waist $w_0 = 50\mu$m, on a total 2D grid of size 400μm $\times$ 400μm. Left shows field amplitude, right shows field phase.

3.4 Structured Phase

In this section we consider beams which may also have a structured helical phase and therefore possess an orbital angular momentum (OAM) of index m [36, 39].

3.4.1 Laguerre-Gaussian Modes

A Laguerre-Gaussian (LG) mode is given by [39, 112–114]

$$\mathbf{A}_n(r, z) = \mathrm{LG}_p^m(r, z), \tag{3.35}$$

where

$$\mathrm{LG}_p^m(r, z) = \sqrt{\frac{2p!}{\pi(p + |m|)!}} \frac{1}{w(z)} \left(\frac{r\sqrt{2}}{w(z)}\right)^{|m|} \exp\left(\frac{-r^2}{w(z)^2}\right) \mathrm{L}_p^{|m|}\left(\frac{2r^2}{w(z)^2}\right) \exp(im\varphi)$$
$$\exp\left(\frac{ik_0 r^2 z}{2(z^2 + z_\mathrm{R}^2)}\right) \exp\left(-i(2p + |m| + 1) \arctan\left(\frac{z}{z_\mathrm{R}}\right)\right), \tag{3.36}$$

and $w(z)$ is as defined in Eqn. (3.30). Introducing p and m indices that represent the number of radial nodes and the azimuthal index respectively of the beam, the Gouy phase is now given by $(2p + |m| + 1) \arctan (z/z_R)$, whilst $L_p^{|m|}$ represents an associated Laguerre polynomial controlled by the two mode indices. This may be related to the standard Laguerre polynomials L_n [115, 116] by

$$L_p^{|m|}(x) = (-1)^{|m|} \frac{d^{|m|}}{dx^{|m|}} L_{p+|m|}(x). \tag{3.37}$$

At the beam waist, Eqn. (3.36) has the form

$$LG_p^m (r, \varphi) = A \left(\frac{r\sqrt{2}}{w_0} \right)^{|m|} \exp \left(-\frac{r^2}{w_0^2} \right) L_p^{|m|} \left(\frac{2r^2}{w_0^2} \right) \exp \left(im\varphi \right). \tag{3.38}$$

Depending on the selection of p and m indices, Eqn. (3.38) permits a wide range of structured beams that (when $m \neq 0$) also have helically structured phase. Fig. 3.4 gives examples of several LG modes for a variety of p and m selections.
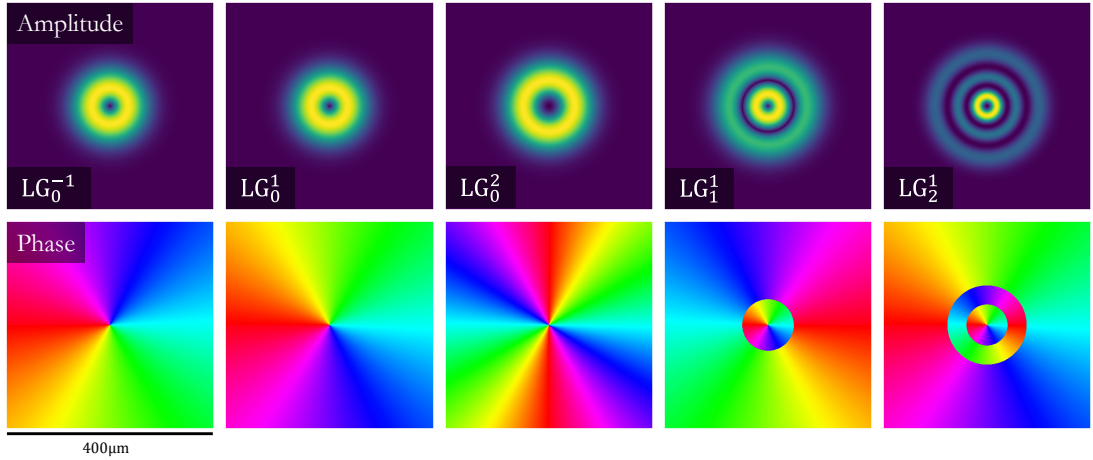
Figure 3.4: Typical Laguerre-Gaussian modes from Eqn. (3.38), for a field amplitude of A and beam waist $w_0 = 50\mu$m, on a 2D grid of 400μm $\times$ 400μm. Top (bottom) row shows field amplitude (phase), for p and m combinations indicated.

The LG modes of Fig. 3.4 display a number of characteristic features, determined by the p and m-indices. The p, radial index controls the number of off-axis rings present, given by $p+1$. The m, azimuthal index introduces a topological charge to the mode, seeding a

helical phase gradient through the final term of Eqn. (3.38), $\exp(im\varphi)$, which provides an OAM of $m\hbar$ per photon [36]. In Fig. 3.4, the first two panels show a switch in the gradient direction, reflecting the difference between $m = \mp 1$, whilst as m increases for $\mathrm{LG}_0^1 \to \mathrm{LG}_0^2$ an additional 2π phase jump occurs and the phase gradient doubles. The phase gradient of each mode also introduces a central phase singularity: an on-axis optical vortex, with an undefined phase at the mode centre, providing the ring-like profiles observed.

Importantly, the phase gradient of an LG mode causes the Poynting vector of the beam to spiral along the direction of propagation, as illustrated in Fig. 3.5. This induces an azimuthal flow around each ring and, as the phase gradient's magnitude is controlled by m, the azimuthal flow rate therefore depends on the m-index of the beam.
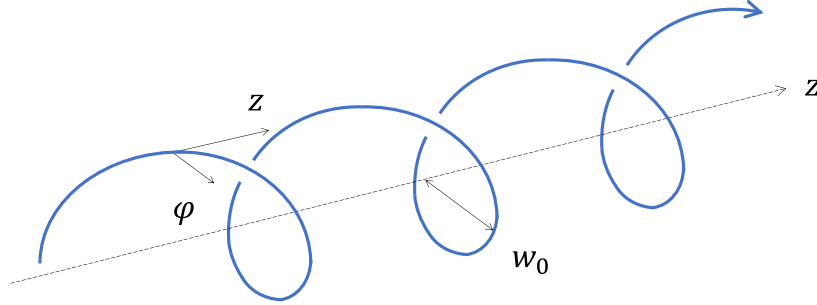
Figure 3.5: Poynting vector of a Laguerre-Gaussian mode propagating along z. After Ref. [36].

We note that, as the m-index of an LG mode increases, the radius of its maximum intensity ring also increases - see $\mathrm{LG}_0^1 \to \mathrm{LG}_0^2$ in Fig. 3.4. From Eqn. (3.38),

$$\partial_r \left(\mathrm{LG}_0^m (r, \varphi) \right) = A \left(\frac{r\sqrt{2}}{w_0} \right)^{|m|} \left[|m| (r)^{-1} - \frac{2r}{w_0^2} \right] \exp \left(-\frac{r^2}{w_0^2} \right) \exp (im\varphi). \qquad (3.39)$$

The position of maximum radial intensity, $r_{\max}$, occurs when $\partial_r \left(\mathrm{LG}_0^m \right) = 0$. From Eqn. (3.39) this leads to the condition that

$$\frac{|m|}{r_{\max}} = \frac{2r_{\max}}{w_0^2},$$

$$\Rightarrow \qquad r_{\max} = \sqrt{\frac{|m|}{2}} \, w_0. \qquad (3.40)$$

A change in topological charge Δm therefore requires a beam waist alteration proportional to $\sqrt{2/|\Delta m|}$ to preserve the ring's maximum intensity radius.

Experimentally, there are numerous approaches to creating beams with helical phase gradients, such as an LG mode. The most common of these are using spiral phase plates to transform Gaussian modes into LG modes [117], using q-plates based on spin and orbital angular momentum coupling [118], and using either a spatial light modulator (SLM) with a diffraction grating or a digital mirror device to convert a Gaussian beam to a helically phased beam [119–121].

3.4.2 Bessel-Gaussian Modes

All of the beams considered so far diffract as they propagate. In order to minimise diffraction we also consider Bessel-Gaussian (BG) modes, which encompass as limiting cases the diffraction-free Bessel beam and the Gaussian beam, leading to diffractionless propagation dynamics. Their spatial distribution may be described by [122–125]

$$\mathrm{BG}^m(r, \varphi, 0) = A J_m\left(\kappa_{\mathrm{BG}} r\right) e^{-\frac{r^2}{w_{\mathrm{G}}}} e^{im\varphi}, \qquad (3.41)$$

with J_m the mth order Bessel function, w_{G} representing a transverse width control of the spatial coverage of the Bessel rings, and κ_{BG} an optional parameter used to ensure maximal overlap between the central ring of the BG and equivalent LG optical mode. Again a term related to OAM, $e^{im\varphi}$, has been included such that the BG modes may possess an azimuthal phase, with topological charge depending on the selection of m.

Fig. 3.6 provides a comparison between matched LG_0^1 and BG^1 modes. The presence of the additional radial rings, which act to confine the field and suppress diffraction, is clear in both the amplitude and phase distribution of the BG mode.

BG modes have been realised experimentally, typically by directing a Gaussian beam upon an axicon to obtain a beam resembling the zeroth order Bessel function. This is shown in Fig. 3.7 where, in the shaded area, the resultant beam has a profile similar to, and acts in the expected non-diffractive manner of, a Bessel beam [126].
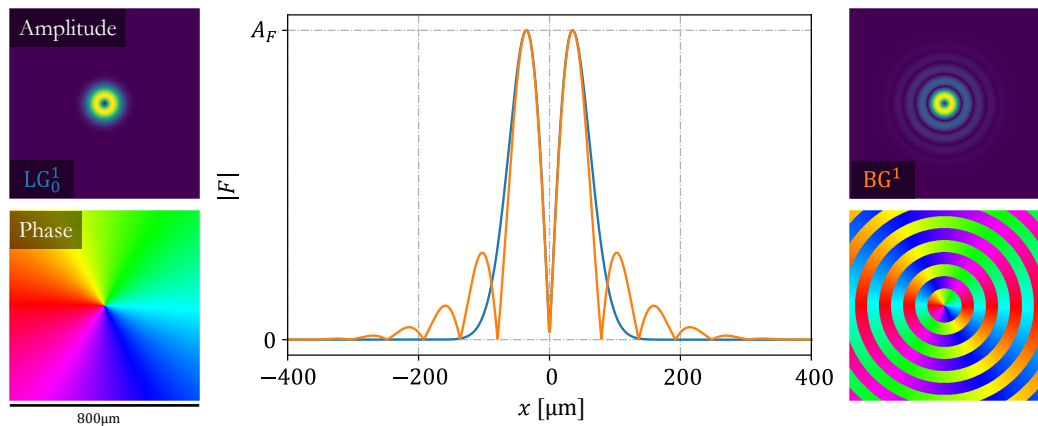
Figure 3.6: LG (left) and BG (right) modes of $m = 1$ and $w_0 = 50\mu$m, on a 800μm $\times$ 800μm grid, with $\kappa_{\mathrm{BG}} = 0.084$ and $w_{\mathrm{G}} \approx 267\mu$m. Top (bottom) row shows 2D field amplitude (phase), with central panel a 1D cross section of both modes.

Higher order Bessel beams, such as those of Fig. 3.6, may be generated through a similar scheme based on holograms mimicking the effect of an axicon [127]. Such beams have found extensive uses due to their diffractionless properties, including in optical tweezing [128, 129] and in particle rotation [130]. Furthermore, their tendency for self-healing after perturbation has additional applications for propagation in turbulent and scattering media [131].
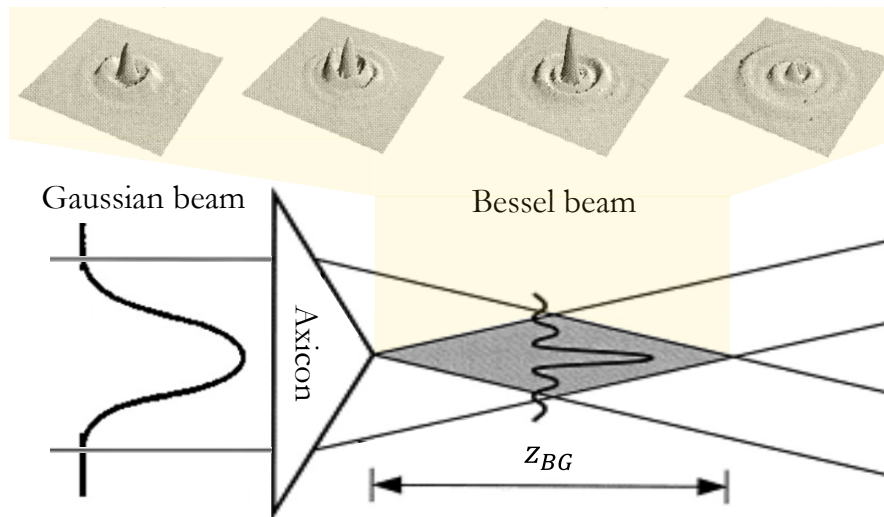
Figure 3.7: A Gaussian beam meets an axicon, creating a Bessel beam within the region z_{BG}. Insets above give field distributions in same region. Adapted from Ref. [126], with permission from Elsevier.

Chapter 4

Dynamics in Kerr Media

This thesis studies ultracold atomic dynamics led by prior research of optical fields subject to a third order 'Kerr' nonlinearity. In this chapter, we consider this setting, inherently similar to Eqns. (2.13) and (3.27), outlining two potential dynamical features. In *Section 4.1*, we consider the formation of spatial solitary structures, self-trapped features that arise with a balancing of competing focusing and defocusing effects, before in *Section 4.2* introducing the ability of the systems to form spontaneous Turing patterns, arising from the interplay between diffraction and nonlinearity. We then consider a further two features that arise both in Kerr media and in other settings. In *Section 4.3* we outline the dynamics of vortices, a defined minimum with an associated phase singularity, and in *Section 4.4* review persistent currents as a fixed, constant azimuthal rotation of a material around a central point.

4.1 Spatial Solitons

Spatial solitons are localised fields that maintain their spatial profile as they propagate [132]. They exist thanks to a precise balance of focusing and defocusing effects such as a self-focusing Kerr nonlinearity and diffraction. As conceptually summarised

in the bottom row of Fig. 4.1, a solitary structure is self-trapped with an idealised balancing between competing phenomena [133]. Initially observed by John Scott Russell in the fluid dynamics of the Union Canal [134, 135], solitons have since been investigated and observed in fields as diverse as optical fibres [136], hydrodynamics [137], (anti-)ferromagnetic systems [138], superconductors [139] and cosmology [132].
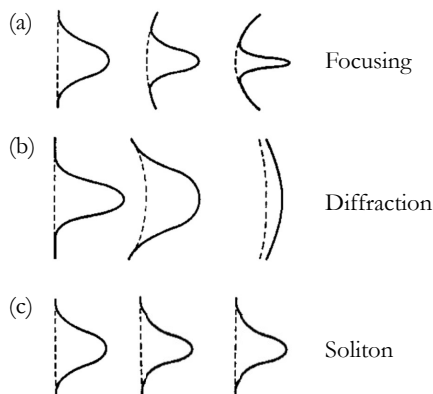
Figure 4.1: Typical behaviour for self-focusing (top), diffraction (centre) and soliton propagation (bottom). Increased evolution left to right. From Ref. [133]. Reprinted with permission from AAAS.

Spatial solitons also arise within ultracold atomic fields, as described by Eqn. (2.13), when the defocusing effects of atomic kinetic energy (incorporated within the term in ∇^2) are balanced by an attractive interatomic scattering (the term in g, which may be focusing or defocusing depending on the sign of the scattering). Various atomic solitary structures have been observed, including bright (an intensity maximum) [140] and dark (an intensity minimum) [141, 142] structures, in addition to lattices of multiple solitons [143]. In non-ideal conditions breathers, bright solitons with fluctuating total intensity, have recently been observed, coupled with signatures of higher-order soliton formation [136, 144–146].

For optical fields within a nonlinear medium, as described by Eqn. (3.27), similar bright spatial optical solitons arise when the diffraction of a Gaussian beam (the term in ∇^2) is balanced by self-focusing due to a Kerr nonlinear medium (the term in n_2) [132, 147]. If the optical field carries an OAM of index m [36], its ring-like intensity distribution will fragment into spatial optical solitons. These solitons are subsequently tangentially

ejected from the ring, thereby conserving angular momentum within the field [148, 149].
These dynamics are summarised in Fig. 4.2, adapted from Ref. [148], which predicted
tangential ejection for a Laguerre-Gaussian optical mode (Eqn. (3.38)) of indices $p = 0$,
$m = 1$, in a self-focusing, saturating Kerr medium.
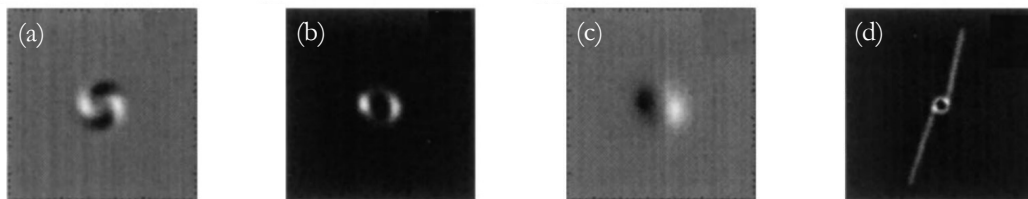
Figure 4.2: Optical soliton formation with a Laguerre-Gaussian mode with $m = 1$.
Panels: transverse (a) real, (b) intensity, and (c) phase field distributions during radial
fragmentation and soliton formation; (d) superposition of field intensities during propa-
gation, showing soliton formation and ejection. Note that the transverse domain in (d)
is ~ 2.5 times greater than (a)-(c). Reprinted figure with permission from Ref. [148].
Copyright (1997) by the American Physical Society.

In this system, the number of solitons formed depends, in general, on the OAM index,
m, of the beam. This 'rule' arises as a result of the real part of the field (panel (a))
having $2|m|$ peaks. Under modulational instability these peaks grow, leading to an or-
dered azimuthal fragmentation into $2|m|$ peaks, which is reflected by the relative phases
of each soliton in panel (c) [148, 149]. This process has been observed experimentally,
using hot rubidium [60] and sodium vapours [150] as the Kerr medium, as well as in
nonlinear colloidal suspensions [151, 152].

In this thesis, we study the dynamics of numerous spatial solitons, including coupled
atom-light solitons in Chapter 8. We also consider solitons within an optical cavity, in
Chapter 10, where their presence is restricted to either an atomic or optical field, and
again in Chapter 12, where their presence is mutual across both fields.

4.2   Turing Patterns

The spontaneous formation and growth of Turing-like patterns has been shown in
a range of settings [153]. Arising from the interplay of activating and inhibiting

forces [154, 155], such patterns are most familiar in biological systems [156]. Their presence is clearest as a growth on initially homogeneous fields, such as those of Fig. 4.3(a), which demonstrates patterns in both activator and inhibitor fields.
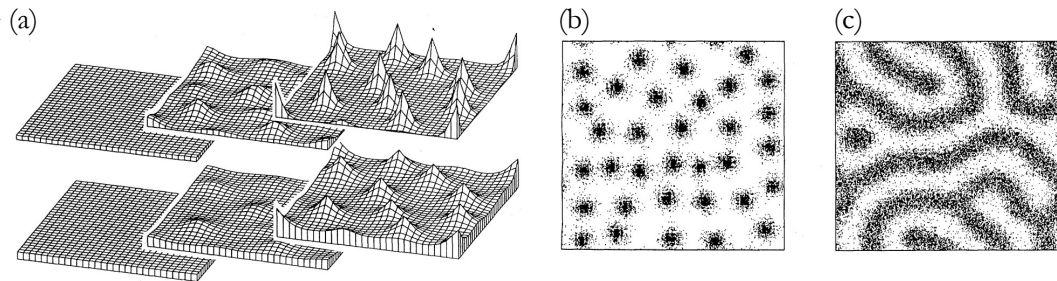
Figure 4.3: Pattern formation in an activator-inhibitor model. (a) Small spatial domain pattern growth (time increasing left to right) for activator (top) and inhibitor (bottom). (b,c) Pattern varieties on larger spatial grid sizes. Reprinted figure with permission from Ref. [156]. Copyright (1994) by the American Physical Society.

A variety of pattern types, including peak and labyrinth patterns, may form as shown in Fig. 4.3(b-c). This mechanism is evidently integral to many natural phenomena, including animal skin markings [157], in cell development [158], vegetation patterns and desertification [159], and the development of ecosystems [160]. Similar growth behaviour also arises in areas as diverse as thin solid [161] and liquid [162] films, in chemical systems [163, 164], cardiovascular settings [155], snowflake crystals [165], and in hydrodynamics [166, 167].

There have been several optically-based observations of spontaneous pattern formation, typically occurring when the optical field evolves within a driven optical cavity, placing the dynamics within a feedback loop that meets the activator and inhibitor requirement for formation [168–170]. A vast range of patterns is possible, including rolls, hexagons, labyrinths, honeycombs, and domain wall growths [171–173].

If the optical field has structure, such as a LG mode, pattern formation in an optical cavity will still occur around its ring of maximum intensity. With its helical phase front, these patterns will azimuthally rotate [174]. One such structure is shown in Fig. 4.4, a rotating lattice of optical peaks on a ring of radius R.

Atomic fields, when coupled to optical fields, have also exhibited pattern formation,
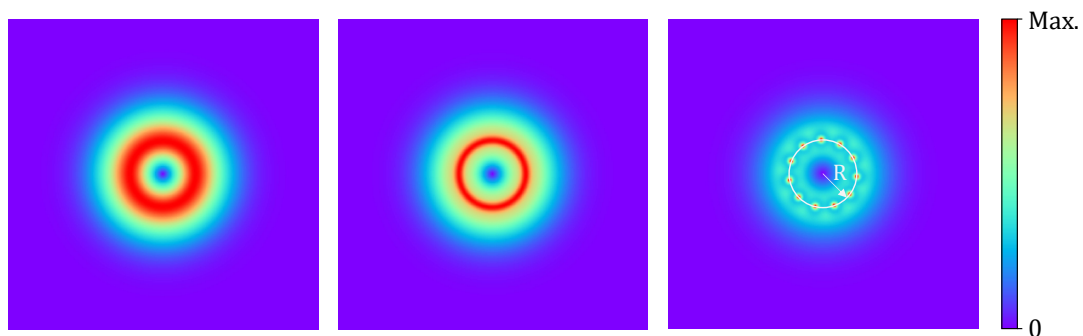
Figure 4.4: Rotating Turing pattern formation in the presence of OAM on an LG mode, of radius R, for increasing time left to right. After Ref. [174].

including in hot atomic vapours [175–177] or cold atoms [67, 178–182]. In these cases, the atom-light coupling provides the required activator-inhibitor role, and the patterns formed are coupled across the two media. Within ultracold atoms, complex BEC setups have been required to return only partial subsets of the rich range of patterns attained in other media. To date observations have been restricted to domain growth in ferromagnetic condensates [183] and pattern formation in polariton [184], driven [185], mixed [186], and dipolar [187–190] condensates.

Typically, a system exhibiting pattern formation is likely to display hysteresis [191]. Hysteresis, which arises is many systems, may be illustrated by the case shown in Fig. 4.5(a). Within a singly resonant optical parametric oscillator (SPORO), when the value of the seed intensity $|E_{IN}|^2$ is altered, the intensity of the output SPORO field, I_S, changes in turn. When $20 \lesssim |E_{IN}|^2 \lesssim 28$ the strength of the field follows different paths depending on whether $|E_{IN}|^2$ increases or decreases, with the pattern varieties obtained (Fig. 4.5(b-d)) varying in turn. The bistability of the system creates a 'closed loop' trajectory as it transitions between various pattern varieties within these limits: a hysteresis cycle occurring between the two accessible branches [192].

Hysteresis is a widespread phenomenon in a range of settings, including in ferromagnetic materials, mechanical gears, smart materials, and in regulatory systems [193, 194]. In nonlinear systems, cycles arise in vehicles in motion, magneto-rheological systems, and fault diagnosis in mechanical systems [195]. The presence of hysteresis in ultracold
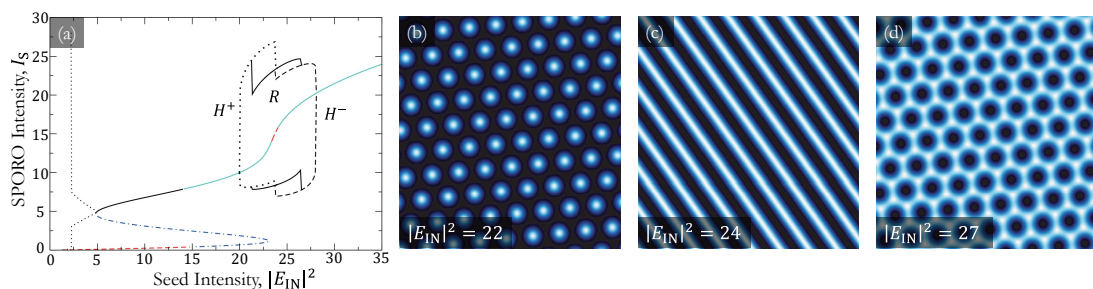
Figure 4.5: Hysteresis cycle arising from pattern formation within a SROPO when $20 \lesssim |E_{\mathrm{IN}}|^2 \lesssim 28$, between a seed intensity parameter $|E_{\mathrm{IN}}|^2$ and SROPO intensity I_{S}. (a) System stability analysis. (b)-(d) patterns in SPORO intensity distributions when; (b) $|E_{\mathrm{IN}}|^2 = 22$, hexagons: H^+, (c) $|E_{\mathrm{IN}}|^2 = 24$, rolls: R, (d) $|E_{\mathrm{IN}}|^2 = 27$, honeycombs: H^-. Reprinted figure with permission from Ref. [192]. Copyright (2013) by the American Physical Society.

atomic settings promises potential atomtronic-based control systems [196–198].

In this thesis, we consider the formation of patterns within ultracold atoms where, much like in the case of cold atoms, patterns may arise through a coupled optical beam within a driven cavity. We consider such structures in Chapter 10, where we outline the wealth of pattern varieties accessible, in addition to the hysteresis displayed. We also consider pattern formation in Chapter 11, in this case on spatially structured fields, and in Chapter 12, where we consider coupled atom-light pattern formation in the additional presence of structured optical phase.

4.3 Vortices

Typically, when modelling the collective effects of an ensemble as a single field, any transverse motion will lead to the generation of vortices, a defined point of singularity representing an absence of the ensemble constituent [199]. Such structures are ubiquitous in nature, appearing in settings including ensembles of animals (e.g. Fig. 4.6) [199], fluid dynamics [200], turbulent optical dynamics [201], and have been theorised in black holes [202]. Vortices are also intrinsically linked to optical beams carrying OAM that possess a central phase singularity, in other words a vortex, of similar structure to those seen elsewhere.

Figure 4.6: Vortex-like structures in animal populations: (a) a mill in army ants, (b) a flying doughnut in bats, (c) a mill in jack fish. Used with permission of University of Chicago Press - Journals from Ref. [199]; permission conveyed through Copyright Clearance Center, Inc.

The generation of vortices in ultracold atomic ensembles is typically spontaneous with motion [198], and obtaining a vortex with a central charge of $m = 1$ is possible by condensate stirring [203, 204] or interconversion between two component condensates [205]. Additionally, higher numbers of vortices may be obtained using alternative motion directions, which may show random spatial organisation [206–208], or may follow more organised, lattice-style arrangements in stirred, [204, 209, 210], pumped [211, 212], and box-trapped condensates [213].

As we go on to consider the effects of optical beams with OAM-induced transverse motion interacting with a ultracold atoms, many of the fields considered contain vortices. Those that include helically structured phase contain optical vortices (covered in Chapters 3, 8, 11, and 12). Within the atomic field, we also consider the formation of vortices as a by-product of atom-light soliton formation in Chapter 8, and report on the formation of uniform atomic vortex arrays in Chapter 11.

4.4 Persistent Currents

Persistent currents arise in several areas of physics as a constant azimuthal rotation of a substance around a central fixed point. They take the general form shown in Fig. 4.7; a schematic of their realisation in a mesoscopic metal ring induced by a magnetic quantum flux, Φ [214, 215]. They have been demonstrated in several settings, including

in metallic objects [215, 216] and superconducting solenoids [217], but their presence in most materials is improbable as a result of their high susceptibility to destruction due to natural material resistance [218].
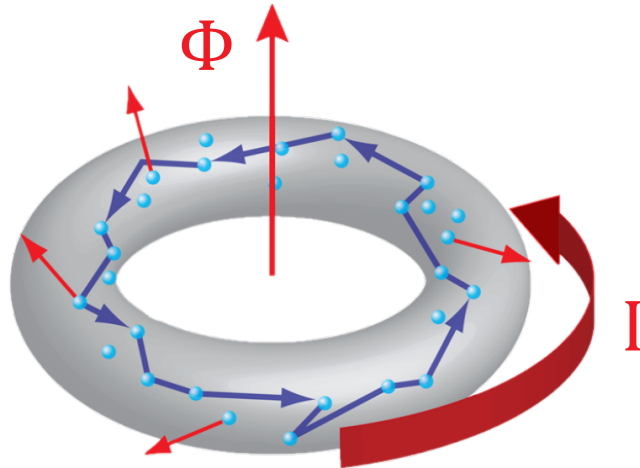
Figure 4.7: Schematic of a metallic persistent current, I, realised using a magnetic flux Φ. Reproduced from Ref. [214] with permission of APS/Alan Stonebraker.

BECs provide a promising potential medium to realise a persistent current of ultracold atoms, thanks to the resistance free matter-wave description of such neutral atoms. The promised quantised circulation and topological protection of such a current [219] would have significant applications toward matter-wave interferometry [220], and in the growing field of atomtronic device generation [197, 198]. Several attempts have been made to realise such circulation, including in arrays of ring-shaped BECs [221], in spinor BECs subject to a trapping potential [219, 222, 223], and in toroidal BECs [64, 196, 224, 225]. As with spontaneous pattern formation, such current realisations require either complex BEC forms, or utilise sensitive static trapping potentials, leaving currents susceptible to circulation decay from excitations, thermal fluctuations, vortices and vortex rings [197], or dynamic phase imperfections [198].

In this thesis, we consider short-term current formation in Chapter 8, induced by the optical field upon the atoms. We then study atomic persistent currents in Chapter 12, obtaining dynamic currents by exploiting characteristic features of a driven optical cavity.

Part II

Co-Propagating Ultracold Atomic and Optical Fields

Chapter 5

Theory

In this chapter, we derive a theoretical model describing coupled, co-propagating optical and ultracold atomic fields. In *Section 5.1*, we provide a general schematic, discussing its viability for current state-of-the-art experimental techniques. In *Section 5.2*, we present a complete derivation of a model of the dynamics of the co-propagating fields. Following existing work, we reach coupled evolution equations for both fields, and outline their analogy with a Kerr-like description of an optical field.

5.1   System of Interest

A proposed schematic of co-propagating ultracold atomic and optical fields is given in Fig. 5.1. We consider a coherent optical beam, either initially homogeneous (Chapter 6) or with structured intensity and phase (Chapters 7-8). If helical phase structure is required, then it may be incident upon a spatial light modulator (SLM), which contains an 'm'-forked diffraction grating [120], converting the beam into an optical vortex beam: a Laguerre-Gaussian (LG) mode carrying an orbital angular momentum (OAM) of $m\hbar$ per photon [36].

The optical beam is focused onto a Bose-Einstein condensate (BEC). We envisage a
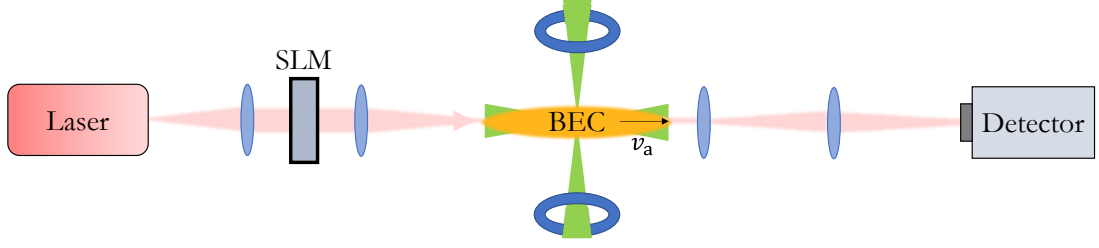
Figure 5.1: Proposed schematic for co-propagating ultracold atomic, of velocity v_a, and optical fields.

cigar-shaped, elongated matter wave, and include additional horizontal and vertical magnetic trapping fields, one of several ways to seed a matter-wave velocity v_a, with which the ultracold atomic beam moves [21, 226]. The two fields co-propagate along the longitudinal axis for a distance controlled by the dimensions of the BEC and the relative wavelengths, and therefore k-vectors, of the two fields. Following this, the optical field exits the BEC and is focused onto an arbitrary detector to image its spatial profile, which, as a result of the coupling between the fields, will be inherently related to the distribution of the ultracold atomic field.

5.2 Theoretical Model

In this section, we provide a derivation of the numerical models used throughout Part II. Supplementary details are provided in Appendix A.

5.2.1 Co-Propagating BEC and Optical Fields

To describe the coupled evolution of the co-propagating fields outlined in Section 5.1, we follow Ref. [33], a development of Ref. [32]. We consider the atomic ensemble to be a Bose gas comprising two-level atoms, described by the collective wavefunction

$$\Phi' = \Phi'_\mathrm{g} \exp\left(-i\frac{E_\mathrm{g}t}{\hbar}\right) + \Phi'_\mathrm{e} \exp\left(-i\frac{E_\mathrm{e}t}{\hbar}\right), \tag{5.1}$$

where g signifies the ground state and e the excited state, with energies E_g and E_e and wavefunctions Φ'_g and Φ'_e, respectively. We assume throughout that the excited atomic state population is small, with the large majority of the atoms contained in the ground

state, enabling adiabatic elimination of the excited state in due course.

The atomic ensemble, of frequency ω_a, evolves in an optical field at frequency ω_L that has the form

$$A_\mathrm{TOT} = \frac{1}{2}\left(A' e^{-i\omega_\mathrm{L}t} + A'^* e^{i\omega_\mathrm{L}t}\right). \tag{5.2}$$

The atomic dynamics, when at ultracold temperatures, will follow coupled Schrödinger equations for ground and excited states of the form [31, 227, 228]

$$i\hbar\partial_t\Phi'_\mathrm{g} = -\frac{\hbar^2}{2m_\mathrm{a}}\nabla^2\Phi'_\mathrm{g} - \frac{1}{2}\mu A'^*\Phi'_\mathrm{e}e^{i\Delta t} + \frac{4\pi\hbar^2 a_\mathrm{gg}}{m_\mathrm{a}}|\Phi'_\mathrm{g}|^2\Phi'_\mathrm{g}, \tag{5.3}$$

$$i\hbar\partial_t\Phi'_\mathrm{e} = -\frac{\hbar^2}{2m_\mathrm{a}}\nabla^2\Phi'_\mathrm{e} - \frac{1}{2}\mu A'\Phi'_\mathrm{g}e^{-i\Delta t} - i\hbar\frac{\gamma}{2}\Phi'_\mathrm{e}, \tag{5.4}$$

where μ is the matrix element of the atomic dipole moment, m_a is the mass of the atom, Δ represents the field detuning ($\Delta = \omega_\mathrm{L} - \omega_\mathrm{a}$), γ is the spontaneous decay rate of the excited atoms, a_gg is the scattering length of the ground state atoms, and the ∇^2 term represents the atomic kinetic energy ($\nabla^2 = \nabla^2_\perp + \partial^2_z = \partial^2_x + \partial^2_y + \partial^2_z$). Use of Eqns. (5.3)-(5.4) leads to a field normalisation condition $\int d^3x\,(|\Phi'_\mathrm{g}|^2 + |\Phi'_\mathrm{e}|^2) = N$, the total number of atoms in the BEC. We note that, assuming far detuned fields and a small excited state population, a term reflecting spontaneous excited state decay has been neglected in Eqn. (5.3).

Eqn. (5.3) resembles Eqn. (2.13), where the external potential acting on the atomic ensemble arises from both the excited atomic state and the coupled optical field. Turning to this optical field, its slowly varying amplitude will be given by

$$\frac{2i\omega_\mathrm{L}n^2}{c^2}\partial_t A' = -\nabla^2 A' - \frac{\omega^2_\mathrm{L}n^2}{c^2}A' - \frac{\omega^2_\mathrm{L}}{c^2\epsilon_0}P', \tag{5.5}$$

with c the speed of light in a vacuum, ϵ_0 the vacuum permittivity, and n the refractive index of the medium. Dipole forces between the atomic and optical fields will influence the final polarization term,

$$P' = \mu\Phi'^*_\mathrm{g}\Phi'_\mathrm{e}e^{i\Delta t}, \tag{5.6}$$

and so Eqn. (5.5) takes the form

$$\frac{2i\omega_{\mathrm{L}}n^2}{c^2}\partial_t A' = -\nabla^2 A' - \frac{\omega_{\mathrm{L}}^2 n^2}{c^2}A' - \frac{\omega_{\mathrm{L}}^2}{c^2\epsilon_0}\mu\Phi_{\mathrm{g}}'^*\Phi_{\mathrm{e}}'e^{i\Delta t}. \tag{5.7}$$

Returning to Eqns. (5.3)-(5.4), including corrections due to induced polarization in dense atomic media through the substitution [30, 31, 229]

$$A' \rightarrow A' + \frac{P'}{3\epsilon_0} \tag{5.8}$$

causes the atomic equations to take the form (see Appendix A.1)

$$i\hbar\partial_t\Phi_{\mathrm{g}}' = -\frac{\hbar^2}{2m_{\mathrm{a}}}\nabla^2\Phi_{\mathrm{g}}' - \frac{1}{2}\mu A'^*\Phi_{\mathrm{e}}'e^{i\Delta t} - \frac{1}{2}\frac{\mu^2\Phi_{\mathrm{g}}'}{3\epsilon_0}|\Phi_{\mathrm{e}}'|^2 + \frac{4\pi\hbar^2 a_{\mathrm{gg}}}{m_{\mathrm{a}}}|\Phi_{\mathrm{g}}'|^2\Phi_{\mathrm{g}}', \tag{5.9}$$

$$i\hbar\partial_t\Phi_{\mathrm{e}}' = -\frac{\hbar^2}{2m_{\mathrm{a}}}\nabla^2\Phi_{\mathrm{e}}' - \frac{1}{2}\mu A'\Phi_{\mathrm{g}}'e^{-i\Delta t} - \frac{1}{2}\frac{\mu^2\Phi_{\mathrm{e}}'}{3\epsilon_0}|\Phi_{\mathrm{g}}'|^2 - i\hbar\frac{\gamma}{2}\Phi_{\mathrm{e}}'. \tag{5.10}$$

We assume that both optical and atomic fields are monochromatic, paraxial beams. We therefore introduce an atomic wavenumber, $k_{\mathrm{a}} = m_{\mathrm{a}}v_{\mathrm{a}}/\hbar$ where v_{a} is the atomic beam velocity and $\hbar\omega = m_{\mathrm{a}}v_{\mathrm{a}}^2/2$, and an optical wavenumber, $k_{\mathrm{L}} = \omega_{\mathrm{L}}n/c$. At this stage we make no inherent assumptions about the magnitudes of k_a and k_{L}, but note that later in this chapter we specify limits upon these terms, whilst in Chapter 9 they remain unrestricted. We therefore substitute

$$A'(x,y,z,t) \rightarrow A(x,y,z)e^{ik_{\mathrm{L}}z}, \tag{5.11}$$

$$\Phi_g'(x,y,z,t) \rightarrow \Phi_g(x,y,z)e^{i(k_{\mathrm{a}}z-\omega t)}, \tag{5.12}$$

$$\Phi_e'(x,y,z,t) \rightarrow \Phi_e(x,y,z)e^{i((k_{\mathrm{L}}+k_{\mathrm{a}})z-(\omega+\Delta')t)}, \tag{5.13}$$

with $\Delta' = \Delta - k_{\mathrm{L}}v_{\mathrm{a}}$ from the Doppler shift resulting around the mean atomic motion.

From Eqns. (5.11)-(5.13), the spatial and temporal derivatives of the fields may be obtained.

$$\frac{\partial^2 A'}{\partial z^2} = \partial_z^2 Ae^{ik_{\mathrm{L}}z} + 2ik_{\mathrm{L}}\partial_z Ae^{ik_{\mathrm{L}}z} - k_{\mathrm{L}}^2 Ae^{ik_{\mathrm{L}}z}, \tag{5.14}$$

$$\frac{\partial^2 \Phi_{\mathrm{g}}'}{\partial z^2} = \partial_z^2 \Phi_{\mathrm{g}} e^{i(k_{\mathrm{a}}z - \omega t)} + 2ik_{\mathrm{a}} \partial_z \Phi_{\mathrm{g}} e^{i(k_{\mathrm{a}}z - \omega t)} - k_{\mathrm{a}}^2 \Phi_{\mathrm{g}} e^{i(k_{\mathrm{a}}z - \omega t)}, \tag{5.15}$$

$$\frac{\partial^2 \Phi_{\mathrm{e}}'}{\partial z^2} = \left(\partial_z^2 \Phi_{\mathrm{e}} + 2i(k_{\mathrm{L}} + k_{\mathrm{a}}) \partial_z \Phi_{\mathrm{e}} - (k_{\mathrm{L}} + k_{\mathrm{a}})^2 \Phi_{\mathrm{e}} \right) e^{i((k_{\mathrm{L}} + k_{\mathrm{a}})z - (\omega + \Delta')t)}, \tag{5.16}$$

$$\frac{\partial \Phi_{\mathrm{g}}'}{\partial t} = -i\omega \Phi_{\mathrm{g}} e^{i(k_{\mathrm{a}}z - \omega t)}, \tag{5.17}$$

$$\frac{\partial \Phi_{\mathrm{e}}'}{\partial t} = -i(\omega + \Delta') \Phi_{\mathrm{e}} e^{i((k_{\mathrm{L}} + k_{\mathrm{a}})z - (\omega + \Delta')t)}. \tag{5.18}$$

As we consider slowly varying amplitudes, $\partial_z^2 \alpha << k \partial_z \alpha$, Eqns. (5.14)-(5.16) become

$$\frac{\partial^2 A'}{\partial z^2} \approx 2ik_{\mathrm{L}} \partial_z A e^{ik_{\mathrm{L}}z} - k_{\mathrm{L}}^2 A e^{ik_{\mathrm{L}}z}, \tag{5.19}$$

$$\frac{\partial^2 \Phi_{\mathrm{g}}'}{\partial z^2} \approx 2ik_{\mathrm{a}} \partial_z \Phi_{\mathrm{g}} e^{i(k_{\mathrm{a}}z - \omega t)} - k_{\mathrm{a}}^2 \Phi_{\mathrm{g}} e^{i(k_{\mathrm{a}}z - \omega t)}, \tag{5.20}$$

$$\frac{\partial^2 \Phi_{\mathrm{e}}'}{\partial z^2} \approx \left(2i(k_{\mathrm{L}} + k_{\mathrm{a}}) \partial_z \Phi_{\mathrm{e}} - (k_{\mathrm{L}} + k_{\mathrm{a}})^2 \Phi_{\mathrm{e}} \right) e^{i((k_{\mathrm{L}} + k_{\mathrm{a}})z - (\omega + \Delta')t)}. \tag{5.21}$$

With these substitutions we can write

Eqn. (5.9) as
$$i\hbar \left(-i\omega \Phi_{\mathrm{g}} e^{i(k_{\mathrm{a}}z - \omega t)} \right) = -\frac{\hbar^2}{2m_{\mathrm{a}}} \left[\nabla_\perp^2 \Phi_{\mathrm{g}} + 2ik_{\mathrm{a}} \partial_z \Phi_{\mathrm{g}} - k_{\mathrm{a}}^2 \Phi_{\mathrm{g}} \right] e^{i(k_{\mathrm{a}}z - \omega t)}$$
$$- \frac{1}{2} \mu A^* e^{-ik_{\mathrm{L}}z} \Phi_{\mathrm{e}} e^{i((k_{\mathrm{L}} + k_{\mathrm{a}})z - (\omega + \Delta')t)} e^{i\Delta t} - \frac{1}{2} \frac{\mu^2 \Phi_{\mathrm{g}} e^{i(k_{\mathrm{a}}z - \omega t)}}{3\epsilon_0} |\Phi_{\mathrm{e}}|^2$$
$$+ \frac{4\pi\hbar^2 a_{\mathrm{gg}}}{m_{\mathrm{a}}} |\Phi_{\mathrm{g}}|^2 \Phi_{\mathrm{g}} e^{i(k_{\mathrm{a}}z - \omega t)}, \tag{5.22}$$

Eqn. (5.10) as
$$i\hbar \left(-i(\omega + \Delta') \Phi_{\mathrm{e}} e^{i((k_{\mathrm{L}} + k_{\mathrm{a}})z - (\omega + \Delta')t)} \right) = -\frac{\hbar^2}{2m_{\mathrm{a}}} \Big[\nabla_\perp^2 \Phi_{\mathrm{e}}$$
$$+ 2i(k_{\mathrm{L}} + k_{\mathrm{a}}) \partial_z \Phi_{\mathrm{e}} - (k_{\mathrm{L}} + k_{\mathrm{a}})^2 \Phi_{\mathrm{e}} \Big] e^{i((k_{\mathrm{L}} + k_{\mathrm{a}})z - (\omega + \Delta')t)}$$
$$- \frac{1}{2} \mu A e^{ik_{\mathrm{L}}z} \Phi_{\mathrm{g}} e^{i(k_{\mathrm{a}}z - \omega t)} e^{-i\Delta t} - \frac{1}{2} \frac{\mu^2 \Phi_{\mathrm{e}} e^{i((k_{\mathrm{L}} + k_{\mathrm{a}})z - (\omega + \Delta')t)}}{3\epsilon_0} |\Phi_{\mathrm{g}}|^2$$
$$- i\hbar \frac{\gamma}{2} \Phi_{\mathrm{e}} e^{i((k_{\mathrm{L}} + k_{\mathrm{a}})z - (\omega + \Delta')t)}, \tag{5.23}$$

and Eqn. (5.7) as
$$\frac{2i\omega_{\mathrm{L}} n^2}{c^2} \partial_t A e^{ik_{\mathrm{L}}z} = - \left[\nabla_\perp^2 A + 2ik_{\mathrm{L}} \partial_z A - k_{\mathrm{L}}^2 A \right] e^{ik_{\mathrm{L}}z} - \frac{\omega_{\mathrm{L}}^2 n^2}{c^2} A e^{ik_{\mathrm{L}}z}$$
$$- \frac{\omega_{\mathrm{L}}^2}{c^2 \epsilon_0} \mu \Phi_{\mathrm{g}}^* e^{i(-k_{\mathrm{a}}z + \omega t)} \Phi_{\mathrm{e}} e^{i((k_{\mathrm{L}} + k_{\mathrm{a}})z - (\omega + \Delta')t)} e^{i\Delta t}. \tag{5.24}$$

Since $\Delta >> k_{\mathrm{L}} v_{\mathrm{a}}$, and thus $e^{\Delta'} \approx e^{\Delta}$, we simplify Eqns. (5.22)-(5.24) to reach

$$i\frac{\hbar^2 k_{\mathrm{a}}}{m_{\mathrm{a}}}\partial_z \Phi_{\mathrm{g}} = -\frac{\hbar^2}{2m_{\mathrm{a}}}\left(\nabla_\perp^2 \Phi_{\mathrm{g}} - k_{\mathrm{a}}^2 \Phi_{\mathrm{g}}\right) - \hbar\omega\Phi_{\mathrm{g}} - \frac{1}{2}\mu A^* \Phi_{\mathrm{e}}$$
$$-\frac{1}{2}\frac{\mu^2}{3\epsilon_0}|\Phi_{\mathrm{e}}|^2\Phi_{\mathrm{g}} + \frac{4\pi\hbar^2 a_{\mathrm{gg}}}{m_{\mathrm{a}}}|\Phi_{\mathrm{g}}|^2\Phi_{\mathrm{g}}, \tag{5.25}$$

$$i\frac{\hbar^2 (k_{\mathrm{L}} + k_{\mathrm{a}})}{m_{\mathrm{a}}}\partial_z \Phi_{\mathrm{e}} = -\frac{\hbar^2}{2m_{\mathrm{a}}}\left(\nabla_\perp^2 \Phi_{\mathrm{e}} - (k_{\mathrm{L}} + k_{\mathrm{a}})^2 \Phi_{\mathrm{e}}\right) - \hbar(\omega + \Delta')\Phi_{\mathrm{e}}$$
$$-\frac{1}{2}\mu A \Phi_{\mathrm{g}} - \frac{1}{2}\frac{\mu^2}{3\epsilon_0}|\Phi_{\mathrm{g}}|^2\Phi_{\mathrm{e}} - i\hbar\frac{\gamma}{2}\Phi_{\mathrm{e}}, \tag{5.26}$$

$$\frac{2i\omega_{\mathrm{L}} n}{c}\left(\frac{n}{c}\partial_t A + \partial_z A\right) = -\nabla_\perp^2 A - \frac{\omega_{\mathrm{L}}^2}{c^2 \epsilon_0}\mu\Phi_{\mathrm{g}}^*\Phi_{\mathrm{e}}, \tag{5.27}$$

with full details provided in Appendix A.2.

Introducing

$$\zeta = z + \frac{c}{n}t, \tag{5.28}$$

it follows that

$$\frac{\partial}{\partial\zeta} = \frac{\partial}{dz} + \frac{n}{c}\frac{\partial}{\partial t}, \tag{5.29}$$

and on applying Eqn. (5.29) to Eqn. (5.27) we obtain

$$\frac{2i\omega_{\mathrm{L}} n}{c}\left(\partial_\zeta A\right) = -\nabla_\perp^2 A - \frac{\omega_{\mathrm{L}}^2}{c^2 \epsilon_0}\mu\Phi_{\mathrm{g}}^*\Phi_{\mathrm{e}}. \tag{5.30}$$

We now consider, as discussed around Eqns. (5.11)-(5.13), that the atomic and optical fields have similar effective wavelengths, and therefore similar k-vectors, such that $k_{\mathrm{a}}/k_{\mathrm{L}} \approx 1$. Under these conditions, the atomic velocity, v_{a}, is given by (with $k_{\mathrm{a}} = m_{\mathrm{a}} v_{\mathrm{a}}/\hbar$ and $k_{\mathrm{L}} = \omega_{\mathrm{L}} n/c$)

$$\frac{m_{\mathrm{a}} v_{\mathrm{a}} c}{\hbar\omega_{\mathrm{L}} n} \approx 1,$$

$$\Rightarrow \qquad v_{\mathrm{a}} \approx \frac{\hbar\omega_{\mathrm{L}} n}{m_{\mathrm{a}} c}. \tag{5.31}$$

Taking $\lambda = 720$nm, $n = 1$, and using atomic parameters for Caesium from Ref. [230], we find that $v_{\mathrm{a}} \approx 10^{-3}$m s^{-1}. Under such conditions, $\zeta \approx z$ unites the two propagation dimensions [33], and Eqns. (5.25)-(5.27) become

$$i\frac{\hbar^2 k_{\mathrm{a}}}{m_{\mathrm{a}}}\partial_z\Phi_{\mathrm{g}} = -\frac{\hbar^2}{2m_{\mathrm{a}}}\left(\nabla_\perp^2\Phi_{\mathrm{g}} - k_{\mathrm{a}}^2\Phi_{\mathrm{g}}\right) - \hbar\omega\Phi_{\mathrm{g}} - \frac{1}{2}\mu A^*\Phi_{\mathrm{e}} - \frac{1}{2}\frac{\mu^2}{3\epsilon_0}|\Phi_{\mathrm{e}}|^2\Phi_{\mathrm{g}}$$
$$+ \frac{4\pi\hbar^2 a_{\mathrm{gg}}}{m_{\mathrm{a}}}|\Phi_{\mathrm{g}}|^2\Phi_{\mathrm{g}}, \tag{5.32}$$

$$i\frac{\hbar^2(k_{\mathrm{L}} + k_{\mathrm{a}})}{m_{\mathrm{a}}}\partial_z\Phi_{\mathrm{e}} = -\frac{\hbar^2}{2m_{\mathrm{a}}}\left(\nabla_\perp^2\Phi_{\mathrm{e}} - (k_{\mathrm{L}} + k_{\mathrm{a}})^2\Phi_{\mathrm{e}}\right) - \hbar(\omega + \Delta^{'})\Phi_{\mathrm{e}} - \frac{1}{2}\mu A\Phi_{\mathrm{g}}$$
$$- \frac{1}{2}\frac{\mu^2}{3\epsilon_0}|\Phi_{\mathrm{g}}|^2\Phi_{\mathrm{e}} - i\hbar\frac{\gamma}{2}\Phi_{\mathrm{e}}, \tag{5.33}$$

$$\frac{2i\omega_{\mathrm{L}}n}{c}\partial_z A = -\nabla_\perp^2 A - \frac{\omega_{\mathrm{L}}^2}{c^2\epsilon_0}\mu\Phi_{\mathrm{g}}^*\Phi_{\mathrm{e}}. \tag{5.34}$$

We now re-scale the propagation and transverse domains using w_{L}, a characteristic beam waist. Generally, we consider $w_{\mathrm{L}} \equiv w_0$, the initial beam waist of the optical field. The longitudinal and transverse scalings are given by

$$\zeta = \frac{z}{k_{\mathrm{L}}w_{\mathrm{L}}^2}, \tag{5.35}$$

$$(\xi, \eta) = \frac{\sqrt{2}(x, y)}{w_{\mathrm{L}}}, \tag{5.36}$$

respectively [33]. From Eqn. (5.35), propagation to $\zeta = 1$ is equivalent to $2z_{\mathrm{R}}$, with $z_{\mathrm{R}} = (k_{\mathrm{L}}w_{\mathrm{L}}^2)/2$, the Rayleigh range.

Applying Eqns. (5.35)-(5.36) to Eqns. (5.32)-(5.34) gives (see Appendix A.3)

$$i\partial_\zeta\Phi_{\mathrm{g}} = -\nabla_\perp^2\Phi_{\mathrm{g}} + \frac{k_{\mathrm{a}}^2 w_{\mathrm{L}}^2}{2}\Phi_{\mathrm{g}} - \frac{m_{\mathrm{a}}w_{\mathrm{L}}^2\omega}{\hbar}\Phi_{\mathrm{g}} - \frac{m_{\mathrm{a}}w_{\mathrm{L}}^2\mu}{2\hbar^2}A^*\Phi_{\mathrm{e}} - \frac{m_{\mathrm{a}}w_{\mathrm{L}}^2\mu^2}{6\hbar^2\epsilon_0}|\Phi_{\mathrm{e}}|^2\Phi_{\mathrm{g}}$$
$$+ 4\pi w_{\mathrm{L}}^2 a_{\mathrm{gg}}|\Phi_{\mathrm{g}}|^2\Phi_{\mathrm{g}}, \tag{5.37}$$

$$i\partial_\zeta\Phi_{\mathrm{e}} = -\nabla_\perp^2\Phi_{\mathrm{e}} + \frac{w_{\mathrm{L}}^2(k_{\mathrm{L}} + k_{\mathrm{a}})^2}{2}\Phi_{\mathrm{e}} - \frac{m_{\mathrm{a}}w_{\mathrm{L}}^2}{\hbar}(\omega + \Delta)\Phi_{\mathrm{e}} - \frac{m_{\mathrm{a}}w_{\mathrm{L}}^2\mu}{2\hbar^2}A\Phi_{\mathrm{g}}$$
$$- \frac{m_{\mathrm{a}}w_{\mathrm{L}}^2\mu^2}{6\hbar^2\epsilon_0}|\Phi_{\mathrm{g}}|^2\Phi_{\mathrm{e}} - i\frac{m_{\mathrm{a}}w_{\mathrm{L}}^2\gamma}{\hbar}\Phi_{\mathrm{e}}, \tag{5.38}$$

$$i\partial_\zeta A = -\nabla_\perp^2 A - \frac{\omega_{\mathrm{L}}^2 w_{\mathrm{L}}^2\mu}{2c^2\epsilon_0}\Phi_{\mathrm{g}}^*\Phi_{\mathrm{e}}. \tag{5.39}$$

We now renormalise the optical field F:

$$F = \frac{\mu A}{2\hbar} \frac{k_{\mathrm{L}} w_{\mathrm{L}}^2}{v_{\mathrm{a}}} \frac{1}{\sqrt{|\delta|}},$$

$$\Rightarrow \qquad A = \frac{2\hbar v_{\mathrm{a}} \sqrt{|\delta|}}{\mu k_{\mathrm{L}} w_{\mathrm{L}}^2} F, \tag{5.40}$$

where we have introduced

$$\delta = \frac{w_{\mathrm{L}}^2 m_{\mathrm{a}} \Delta}{\hbar}. \tag{5.41}$$

Applying Eqn. (5.40) to Eqns. (5.37)-(5.39) gives (see Appendix A.4)

$$(i\partial_\zeta + \nabla_\perp^2)\Phi_{\mathrm{g}} = -\sqrt{|\delta|} F^* \Phi_{\mathrm{e}} + \frac{m_{\mathrm{a}} w_{\mathrm{L}}^2}{\hbar^2} \left(-\frac{\mu^2}{6\epsilon_0} |\Phi_{\mathrm{e}}|^2 + \frac{4\pi \hbar^2 a_{\mathrm{gg}}}{m_{\mathrm{a}}} |\Phi_{\mathrm{g}}|^2 \right) \Phi_{\mathrm{g}}, \tag{5.42}$$

$$(i\partial_\zeta + \nabla_\perp^2)\Phi_{\mathrm{e}} = -\sqrt{|\delta|} F \Phi_{\mathrm{g}} - \frac{m_{\mathrm{a}} w_{\mathrm{L}}^2}{\hbar^2} \frac{\mu^2}{6\epsilon_0} |\Phi_{\mathrm{g}}|^2 \Phi_{\mathrm{e}} - \delta \left(1 + i \frac{m_{\mathrm{a}} w_{\mathrm{L}}^2}{\hbar} \frac{\gamma}{2\delta} \right) \Phi_{\mathrm{e}}, \tag{5.43}$$

$$(i\partial_\zeta + \nabla_\perp^2)F = -\frac{k_{\mathrm{L}}^2 w_{\mathrm{L}}^4 m_{\mathrm{a}} \mu^2}{4\epsilon_0 \hbar^2 \sqrt{|\delta|}} \Phi_{\mathrm{g}}^* \Phi_{\mathrm{e}}. \tag{5.44}$$

We now eliminate the excited atomic state from the model, in recognition of its small population in comparison to the ground state. As we are in the regime of large field detuning, we can neglect the imaginary part of the final term of Eqn. (5.43) corresponding to spontaneous emission and, by taking Φ_{e} to be fast with respect to Φ_{g}, an adiabatic elimination of Eqn. (5.43) gives (see Appendix A.5)

$$\Phi_{\mathrm{e}} = -\frac{sF\Phi_{\mathrm{g}}}{\sqrt{|\delta|}} \left[1 - \frac{1}{|\delta|} \left(\frac{s m_{\mathrm{a}} w_{\mathrm{L}}^2}{\hbar^2} \frac{\mu^2}{6\epsilon_0} |\Phi_{\mathrm{g}}|^2 + |F|^2 \right) + \mathcal{O}\left(\frac{1}{|\delta|^2} \right) \right], \tag{5.45}$$

where s represents the sign of δ, and therefore that

$$|\Phi_{\mathrm{e}}|^2 \approx \frac{|F|^2 |\Phi_{\mathrm{g}}|^2}{|\delta|}, \tag{5.46}$$

when neglecting higher order terms in $1/|\delta|$.

47

We apply Eqns. (5.45)-(5.46) to Eqn. (5.42) to obtain atomic dynamics described by

$$(i\partial_\zeta + \nabla_\perp^2)\Phi_g = s|F|^2\Phi_g - \frac{s|F|^2}{|\delta|}\left(\frac{sm_a w_L^2}{\hbar^2}\frac{\mu^2}{6\epsilon_0}|\Phi_g|^2 + |F|^2\right)\Phi_g$$
$$+ \frac{m_a w_L^2}{\hbar^2}\left(-\frac{\mu^2}{6\epsilon_0}\frac{|F|^2|\Phi_g|^2}{\delta} + \frac{4\pi\hbar^2 a_{gg}}{m_a}|\Phi_g|^2\right)\Phi_g. \qquad (5.47)$$

Rescaling Φ_g through

$$\psi = \Phi_g \frac{k_L w_L^2 \mu}{2\hbar}\sqrt{\frac{m_a}{\epsilon_0|\delta|}},$$

$$\Rightarrow \qquad\qquad \Phi_g = \frac{2\hbar}{k_L w_L^2 \mu}\sqrt{\frac{\epsilon_0|\delta|}{m_a}}\psi, \qquad\qquad (5.48)$$

with

$$|\Phi_g|^2 = \frac{4\hbar^2}{k_L^2 w_L^4 \mu^2}\frac{\epsilon_0|\delta|}{m_a}|\psi|^2, \qquad\qquad (5.49)$$

and applying these two relationships to Eqn. (5.47), we obtain (see Appendix A.6.1)

$$(i\partial_\zeta + \nabla_\perp^2)\psi = s|F|^2\psi - \frac{2s^2|F|^2}{3k_L^2 w_L^2}|\psi|^2\psi - s\frac{|F|^4}{|\delta|}\psi - \frac{2|F|^2}{3k_L^2 w_L^2}|\psi|^2\psi + \frac{16\pi\hbar^2\epsilon_0|\delta|a_{gg}}{k_L^2 w_L^2 m_a\mu^2}|\psi|^2\psi.$$
$$(5.50)$$

We introduce the parameters

$$\beta_{dd} = \frac{2}{3k_L^2 w_L^2}, \qquad\qquad (5.51)$$

$$\beta_{col} = \frac{16\pi\epsilon_0\hbar^2 a_{gg}|\delta|}{k_L^2 w_L^2 m_a\mu^2}, \qquad\qquad (5.52)$$

and transform Eqn. (5.50) into

$$(i\partial_\zeta + \nabla_\perp^2)\psi = s\left(1 - \frac{|F|^2}{|\delta|}\right)|F|^2\psi - 2\beta_{dd}|F|^2|\psi|^2\psi + \beta_{col}|\psi|^2\psi. \qquad (5.53)$$

Turning to the optical field, Eqn. (5.44), we again eliminate the excited atomic state, before introducing the new atomic state ψ given by Eqn. (5.49). This gives an optical field whose dynamics are described by (see Appendix A.6.2)

$$(i\partial_\zeta + \nabla_\perp^2)F = s\left(1 - \frac{|F|^2}{|\delta|}\right)|\psi|^2 F - \beta_{\text{dd}}|\psi|^4 F. \tag{5.54}$$

As $|\delta|$ is large, we can neglect the Kerr parameter ($|\Omega|^2/|\delta|$) in both Eqns. (5.53)-(5.54). This leaves the coupled equations

$$\partial_\zeta \psi = i\nabla_\perp^2 \psi - i\left(s|F|^2 - 2\beta_{\text{dd}}|F|^2|\psi|^2 + \beta_{\text{col}}|\psi|^2\right)\psi, \tag{5.55}$$

$$\partial_\zeta F = i\nabla_\perp^2 F + i\left(-s|\psi|^2 + \beta_{\text{dd}}|\psi|^4\right)F, \tag{5.56}$$

which describe the co-propagation of an optical field F coupled to an ultracold atomic beam ψ that moves with a velocity v_a, where we have assumed $k_\text{a} \approx k_\text{L}$. The model has a '2D+1' dimensionality, where the two transverse dimensions (ξ, η) evolve in the space-time domain ζ, defined in Eqn. (5.28). We summarise the various terms and parameters within Eqns. (5.55)-(5.56) in Appendix C.

The terms in Eqns. (5.55)-(5.56) represent physical processes whose interplay determines the field dynamics. In Eqn. (5.55), an effective Gross-Pitaevskii description of the atomic dynamics, $\nabla_\perp^2 \psi$ represents the kinetic energy atomic contributions, $s|F|^2$ represents a focusing or defocusing nonlinearity (dependent on the sign of the detuning s) that arises from the dipole field forces, $2\beta_{\text{dd}}|F|^2|\psi|^2$ represents a higher order dipole-dipole correction, and finally $\beta_{\text{col}}|\psi|^2$ represents interatomic scattering, focusing or defocusing depending on β_{col}, which is related to the BEC's scattering length, a_{gg}.

In Eqn. (5.56), an effective nonlinear Schrödinger description of the optical dynamics, $\nabla_\perp^2 F$ represents diffraction, whilst $s|\psi|^2$ represents a focusing or defocusing nonlinearity dependent on the sign of the detuning s, again arising from dipole forces between the fields. Finally, $\beta_{\text{dd}}|\psi|^4$ represents a dipole-dipole correction that gives a higher order focusing nonlinearity.

5.2.2 Optical-Only Reduction

The model of Eqns. (5.55)-(5.56) may be reduced through a further adiabatic procedure that assumes an instantaneous atomic medium, akin to a Kerr-based approach. This gives a single equation that describes the propagation of the optical field through a non-responsive BEC, which acts as a potential upon the atomic field rather than a fully dynamic, coupled field.

From Eqn. (5.55), setting $\partial_\zeta \psi \to 0$ and $\nabla_\perp^2 \psi \to 0$ in an adiabatic elimination gives

$$\left(s|F|^2 - 2\beta_{\mathrm{dd}}|F|^2|\psi|^2 + \beta_{\mathrm{col}}|\psi|^2\right)\psi = 0,$$

$$\Rightarrow \qquad 2\beta_{\mathrm{dd}}|F|^2|\psi|^2 - \beta_{\mathrm{col}}|\psi|^2 = s|F|^2. \qquad (5.57)$$

Eliminating the term in β_{dd}, as it is significantly smaller than the term in β_{col}, gives

$$|\psi|^2 = -\frac{s}{\beta_{\mathrm{col}}}|F|^2, \qquad (5.58)$$

which links a propagating optical field F and an instantaneous atomic medium ψ. We note that, when using this reduction, it should be ensured that selections of s and β_{col} satisfy the requirements of Eqn. (5.58).

Substituting Eqn. (5.58) into Eqn. (5.56) for $\beta_{\mathrm{dd}} \to 0$ and $s^2 \equiv 1$ gives

$$\partial_\zeta F = i\nabla_\perp^2 F + \frac{i}{\beta_{\mathrm{col}}}|F|^2 F. \qquad (5.59)$$

Eqn. (5.59) has the form of a nonlinear Schrödinger equation, Eqn. (3.27). When $\beta_{\mathrm{col}} > 0$, the optical field propagates in a self-focusing medium, and in a self-defocusing medium when $\beta_{\mathrm{col}} < 0$. It follows that the BEC is acting like a Kerr medium with nonlinear strength proportional to $1/\beta_{\mathrm{col}}$.

5.3   Conclusions and Outlook

In this chapter, we have derived coupled nonlinear equations that model the dynamics of the co-propagation of ultracold atomic and optical fields, and outlined a reduction of this model to a single differential equation for the assumption of a 'static' BEC field, showing that it was equivalent to the nonlinear Schrödinger equation.

This model will be used throughout Chapters 6 - 8, considering both a range of forms of initial optical fields and parameter regimes, before discussing some prospective applications of the obtained dynamics.

Chapter 6

Homogeneous Fields

In this chapter, we consider the case of initially homogeneous atomic and optical fields. In *Section 6.1*, we outline the form of these initial fields. In *Sections 6.2 - 6.3*, we consider their evolution, and discuss the realisation of coupled atom-light patterns for blue *(6.2)* and red *(6.3)* atom-field detuning. Finally, in *Section 6.4*, we analyse the stability of these patterns for various potential operating regimes.

6.1   Initial Field Form

We now consider homogeneous atomic and optical fields of initial form

$$\psi(\xi, \eta, \zeta(0)) = A_\psi, \tag{6.1}$$

$$F(\xi, \eta, \zeta(0)) = A_F, \tag{6.2}$$

where A_ψ and A_F are the initial amplitudes of the atomic and optical fields, respectively.

We begin by considering the parameters used in Ref. [33], and so select $A_\psi = 4$ and $A_F = 6$, along with $\beta_{\mathrm{dd}} = 1.6 \times 10^{-4}$ and $\beta_{\mathrm{col}} = 3.5$. For Caesium atoms, this reflects a weakly repulsive condensate with a scattering length $a_s \approx 15a_0$, with a_0 the

Bohr radius [33, 230]. Random noise is applied to both fields to seed a modulational instability, and we select a 1% level of the initial maximal amplitude for this to match Ref. [33], but emphasise that the selected level is largely arbitrary. We consider the effect of the atom-light detuning, as in Figs. 2 and 3 of Ref. [33].

6.2 Blue Atom-Field Detuning

Considering first blue atom-field detuning, i.e. $s = +1$ as in Fig. 2 of Ref. [33], the atoms can be described as 'dark-seeking', with the dipole forces leading them to positions of optical darkness. This is shown in Fig. 6.1, the transverse amplitude distributions of the atomic and optical fields at propagation distances $\zeta = 0.0, 0.5, 1.0$, and 2.0, with the far-fields shown as insets for each panel.
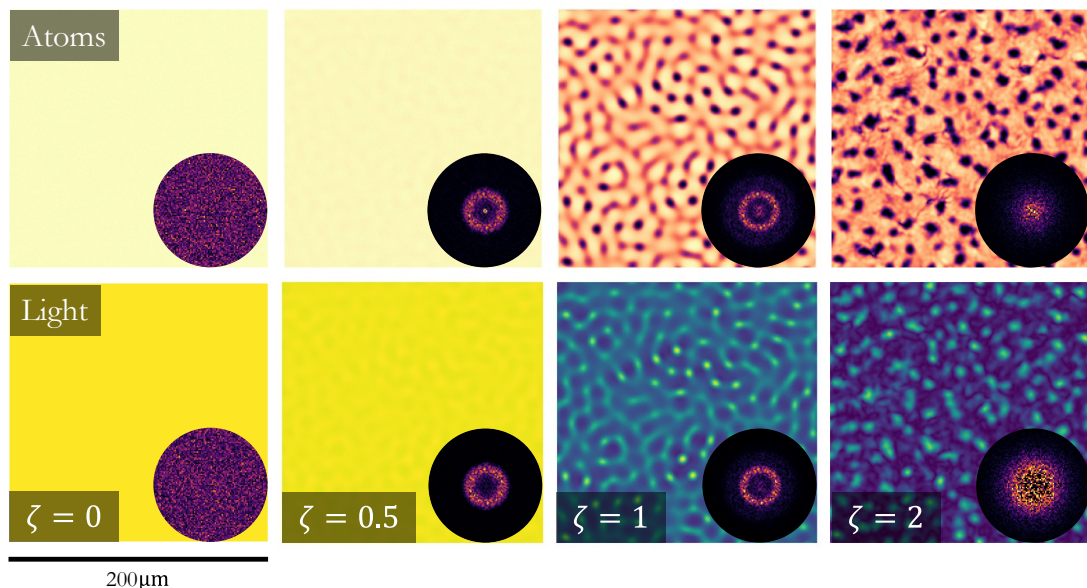
Figure 6.1: Main panels: Blue-detuned initially homogeneous BEC (upper) and optical (lower) amplitude distributions at $\zeta = 0, 0.5, 1$ and 2 (left to right). Insets: Far-field of each panel. Parameters: $A_\psi = 4, A_F = 6, s = 1, \beta_{dd} = 1.6 \times 10^{-4}, \beta_{col} = 3.5$.

The noise fluctuations on the initially homogeneous fields are amplified by the dipole forces, leading to the development of mutual structures in both fields. As a result of the blue detuned fields, a pattern maximum in one field corresponds to a minimum in the other, and the patterns may be described as 'interleaved'. These structures grow

progressively as the propagation distance increases: at $\zeta = 0.5$ in Fig. 6.1, the patterns are barely discernible in each field, but at $\zeta = 1$ they are clearly visible. Soon after their formation however, the patterns begin to filament, and their clarity is lost. At $\zeta = 2$ structures remain in both fields, but without their prior order.

The formation of far-field ring-like structures corresponds to the emergence of structure in the near-field. Ring onset occurs in advance of the near-field formation, being clear at $\zeta = 0.5$ whilst the near-field patterns only become evident closer to $\zeta = 1$. With further propagation, the far-field structures break down as the near-field spatial patterns begin to filament, in good agreement with prior studies of pattern formation in a range of systems, see, for example, Refs. [32, 173, 231].

The near- and far-field dynamics of Fig. 6.1 are particularly like those of Ref. [32], which also numerically modelled co-propagating ultracold atomic and optical fields through

$$\partial_\zeta \psi \;=\; i\alpha_1 \nabla_\perp^2 \psi - i s_1 |F|^2 \psi, \tag{6.3}$$

$$\partial_\zeta F \;=\; i\nabla_\perp^2 F - i s_1 (1 - |F|^2)|\psi|^2 F. \tag{6.4}$$

Comparing Eqns. (6.3)-(6.4) to Eqns. (5.55)-(5.56), s_1 is equivalent to s, the sign of the atom-light detuning, whilst the optical dipole-dipole force (the final term in Eqn. (6.4)) is dependent on both the sign of the detuning and the intensity of both fields. Notably, terms relating to dipole-dipole coupling and interatomic scattering in Eqn. (6.3) are neglected in Ref. [32], meaning that any dynamics obtained are driven by the dipole force between the fields. Selecting $A_\psi = A_F = 0.1$ and setting $s_1 = 1$ and $\alpha_1 = 0.1$, Ref. [32] obtains similar near- and far-field pattern formation as in Fig. 6.1. This suggests that the dipole term is the dominant nonlinearity, and our parameter selection provides a self-focusing BEC medium that, through the dipole force, enables coupled pattern formation. The significant additional benefit of the model provided by Eqns. (5.55)-(5.56) is that, by varying the additional atomic and optical parameters largely neglected by Ref. [32], we may explore other operating regimes to obtain alternative dynamics.

6.3   Red Atom-Field Detuning

For red atom-field detuning, i.e. $s = -1$ as in Fig. 3 of Ref. [33], the atoms may be considered as 'light-seeking', with the dipole forces transporting them to positions of optical intensity. In an otherwise identical procedure to the blue atom-field detuning case, we obtain the formation of coupled patterns across both fields shown in Fig. 6.2.
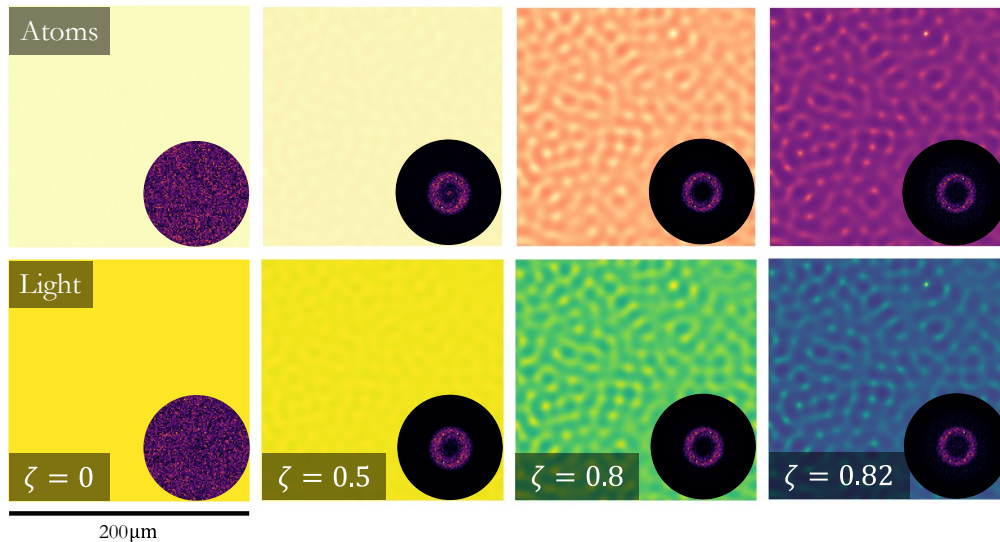
Figure 6.2: Main panels: Red-detuned initially homogeneous BEC (upper) and optical (lower) amplitude distributions at $\zeta = 0 \rightarrow 0.82$ (left to right). Insets: Far-field of each panel. Parameters: $A_\psi = 4, A_F = 6, s = -1, \beta_{dd} = 1.6 \times 10^{-4}, \beta_{col} = 3.5$.

The patterns again grow from the noise fluctuations in both fields, becoming visible in both amplitude distributions at $\zeta = 0.5$, a slightly smaller ζ-value than the equivalent blue-detuned case. Again, structure is clear in both far field distributions, further verifying the ongoing pattern formation. At $\zeta = 0.8$, the patterns dominate both fields where, due to the red atom-field detuning, both fields have coincident structure. The ring structure again exists in the far fields, remaining notably well defined. However, for red-detuned fields the reinforcing effect of coincident atomic and optical maxima further enhances the self-focusing BEC effect on the optical field, and filamentation occurs very rapidly, as shown for $\zeta = 0.82$ in Fig. 6.2, with structures rapidly localising before undergoing mutual collapse. We find that with red atom-field detuning there is little possibility of achieving pattern formation with stable subsequent dynamics.

6.4 Parameter Stability Regimes

In this section we explore potential regimes conducive to pattern formation.

Initial Field Amplitudes

Altering the amplitudes of the initial homogeneous BEC and optical fields, A_ψ and A_F, respectively, we vary each parameter between $0 \leq A_x \leq 12$, and co-propagate both fields to a distance of $\zeta = 1$ before analysing the strength of any patterns through the size of modulation in the atomic field's amplitude.

For blue atom-field detuning, i.e. interleaved patterns, the result is shown in the left panel of Fig. 6.3.
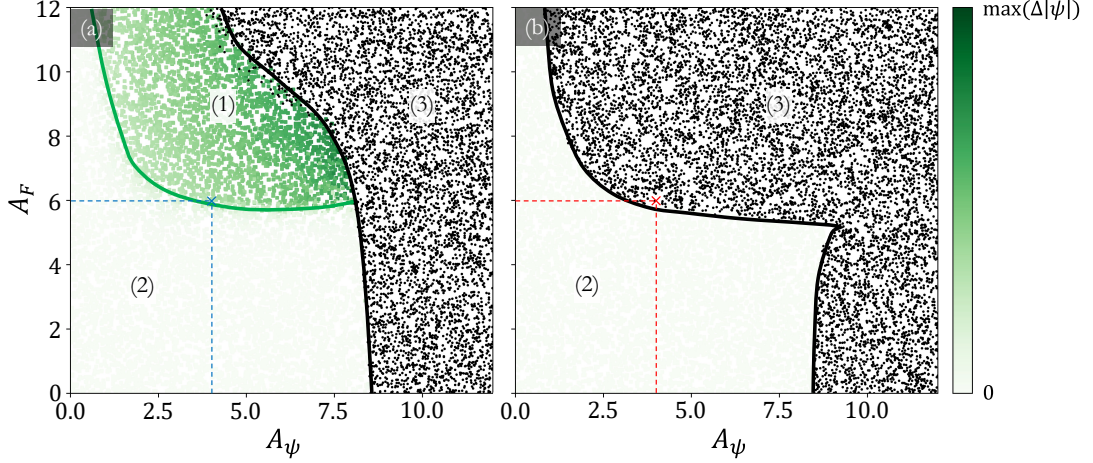
Figure 6.3: Pattern stability in atomic field for $0 \leq A_\psi, A_F \leq 12$ at $\zeta = 1$ with (a) blue and (b) red atom-field detuning. Regions show: (1) pattern formation; (2) homogeneous field return; (3) field collapse. Other parameters as in Figs. 6.1 - 6.2 respectively.

The upper left central section of Fig. 6.3(a) indicates a reasonably large parameter space available for pattern formation (1), where the green coloured squares indicate the presence of well-defined patterns. The depth of colour reflects the strength of pattern, with a darker green signifying a larger modulation in field amplitude. Considering the selection of $A_\psi = 4$, $A_F = 6$ as used in Section 6.2, indicated by the blue cross, the reported patterns are in the lower limits of the parameter space, with more distinct patterns accessible through moderate increases to one, or both, of the initial field

amplitudes. The lightly shaded region marked (2) corresponds to conditions where the amplitudes of the two initial fields are not sufficient to cause pattern formation through the dipole force by $\zeta = 1$, and so the fields remain homogeneous, with only small additional fluctuations. Finally, the area indicated by black dots (3) reflects filamentation and collapse of the field. In this region, the initial strength of the fields has contributed to localisation which overwhelms the system, leading to collapse.

Fig. 6.3(b) is the equivalent plot for the $s = -1$, red-detuned configuration. The region of patterns at $\zeta = 1$ is far smaller, reflecting the coincident nature of BEC and optical structures in this case, which are far more susceptible to localisation and instability. Indeed, considering the case where $A_\psi = 4$, $A_F = 6$ as used in Section 6.3, indicated by the red cross, this lies in a region of fragmentation by $\zeta = 1$, unlike the pattern region of the blue-detuned case. Fig. 6.3(b) suggests that almost any region of red-detuned pattern formation will lead to a mutual collapse (3), with all non-collapsed regions restricted to homogeneous fields with small fluctuations (2).

We emphasise that in Fig. 6.3, regions not marked as exhibiting a particular feature may do so at increased ζ values. The maps shown here simply are to provide an indication of the nature of the fields at $\zeta = 1$.

BEC Scattering Length

By tuning the Feshbach resonance, the atomic scattering length, a_{gg}, of Caesium atoms may be controlled to transition between repulsive and attractive interactions [232]. Here, we consider changes of around $-23 < a_{gg} < 45$ which, considering atomic transition parameters for Caesium atoms [230], corresponds to alterations of $-5 \leq \beta_{col} \leq 10$. These changes cause the collisional nonlinearity to transition from focusing to defocusing across this range, and we examine how this affects the formation of patterns for both blue and red atom-field detuning.

Initially, we consider the relative sizes of the nonlinear terms contributing to Eqn. (5.55), the description of the atomic field evolution. The absolute magnitude of these terms is plotted against β_{col} in Fig. 6.4, where $|\psi| = 4$ and $|F| = 6$. We find that the

interatomic scattering term becomes the dominant nonlinearity for either $\beta_{\text{col}} \lesssim -2.5$, when it provides a focusing effect, or $\beta_{\text{col}} \gtrsim 2.5$, when it provides a defocusing effect.
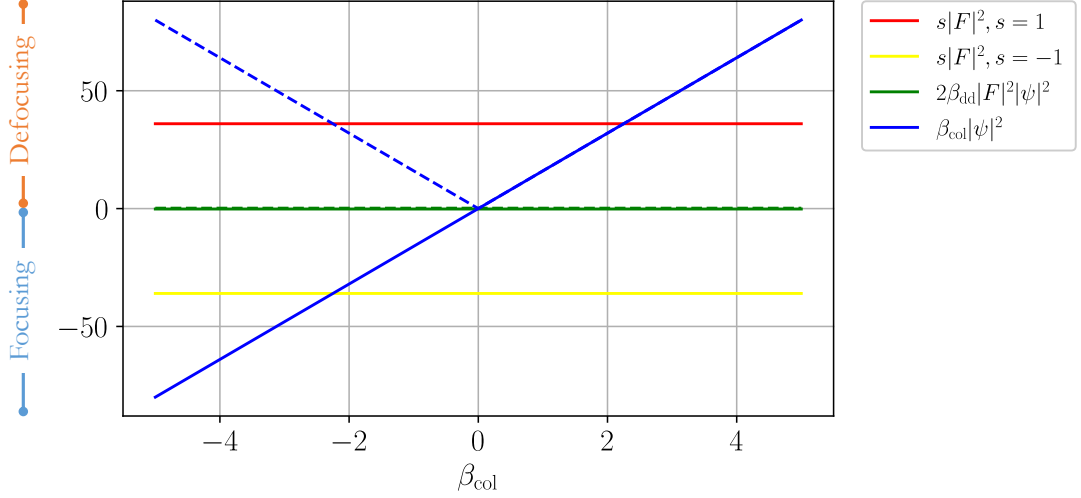
Figure 6.4: Relative nonlinear term sizes (dotted: absolute magnitude) of Eqn. (5.55) for $-5 \leq \beta_{\text{col}} \leq 10$, with $\beta_{\text{dd}} = 1.6 \times 10^{-4}$.

Propagating homogeneous fields within the same scattering length range, we find similar pattern stability thresholds to those predicted by Fig. 6.4. For blue atom-field detuning, we obtain patterns in the regions indicated in the top row of Fig. 6.5, for $A_\psi = 4$ and $A_F = 6$ between $0.5 \leq \zeta \leq 2$.

We again observe several regions (1)-(3), dependent on both β_{col} and ζ. For $\beta_{\text{col}} < 0$, both fields almost exclusively have collapsed by $\zeta = 0.5$, region (3). Such a phenomenon occurs significantly earlier than previously discussed as a result of the transition to attractive interatomic interactions where, with $\beta_{\text{col}} < 0$, the respective term in Eqn. (5.55) becomes focusing, further enhancing the other focusing forces in localising structures and causing collapse to occur at smaller ζ values. We note that this occurs for values of $\beta_{\text{col}} < -2.5$, the threshold predicted by Fig. 6.4, demonstrating the rapid cascading impact of the focusing nonlinearity provided by attractive atomic interactions.

Upon reaching $\beta_{\text{col}} \geq 0$, where the sign of the scattering changes, we enter a regime of pattern formation, region (1), enabled by the scattering nonlinearity in Eqn. (5.55) being first negligible for $\beta_{\text{col}} \approx 0$, and then increasingly defocusing for $\beta_{\text{col}} > 0$. This
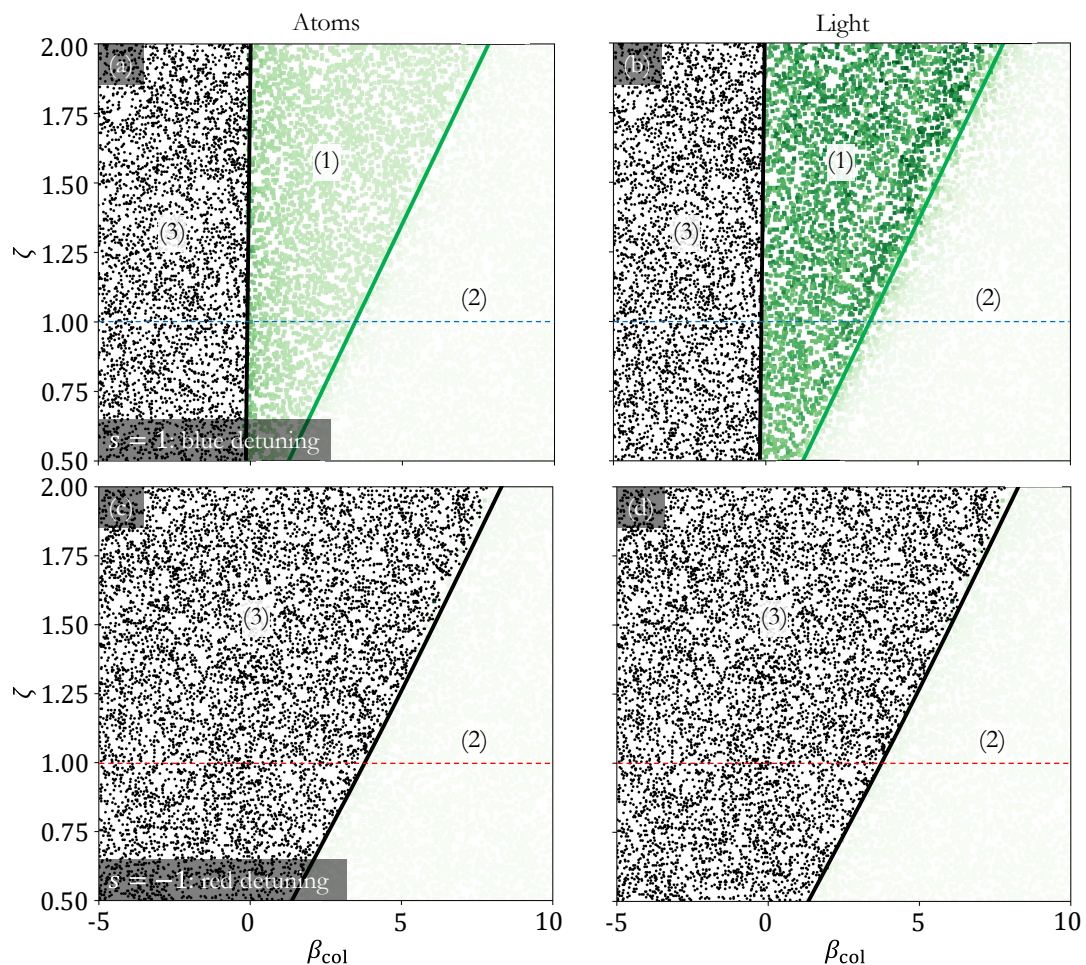
Figure 6.5: Pattern stability for $-5 \leq \beta_{\text{col}} \leq 10$ between $0.5 \leq \zeta \leq 2$ for atomic (a,c) and optical (b,d) fields with blue (a-b) and red (c-d) atom-field detuning. Regions show: (1) pattern formation; (2) homogeneous field return; (3) field collapse. Other parameters as in Figs. 6.1 - 6.2 respectively. Colour scales as in Fig. 6.3.

additional repulsive force stabilizes the dynamics, with patterns present for a variety of β_{col} selections when $\zeta > 0.5$. If β_{col} is too large, the pattern formation is entirely suppressed by a dominant defocusing scattering nonlinearity which overwhelms the dipole forces, region (3). As reflected by the colour depths, we also note the relative strengths of the pattern formation regimes in each field: for increasing β_{col} values, the optical map pattern is stronger than the atomic pattern. This represents the increasingly repulsive nature of the BEC suppressing first its own patterns, but not yet having such a strong suppressive effect on the optical field through the dipole force. It

is only when $\beta_{\text{col}} \approx 0$ that the atomic patterns dominate over the optical field's.

For red atom-field detuning, shown in the bottom row of Fig. 6.5, no stable pattern formation is observed. The large region (1) of pattern formation present for blue-detuned fields is now destroyed by the additional self-focusing of coincident patterns leading to filamentation, region (3) here. Again, the region of homogeneous fields (suppressed pattern formation due to large β_{col}, region (2)) remains largely unaffected by the detuning selection, suggesting that here the dominant force is the interatomic scattering.

Dipole-Dipole Forces

Finally, we briefly consider changes to β_{dd}, representing higher-order corrections due to dipole-dipole coupling between the fields. Given the modest nature of this term, we consider its contributions on a logarithmic scale between $10^{-4} < \beta_{\text{dd}} < 10^{-1}$, and plot the relative strength of the competing nonlinear terms in Eqns. (5.55)-(5.56) in Fig. 6.6.
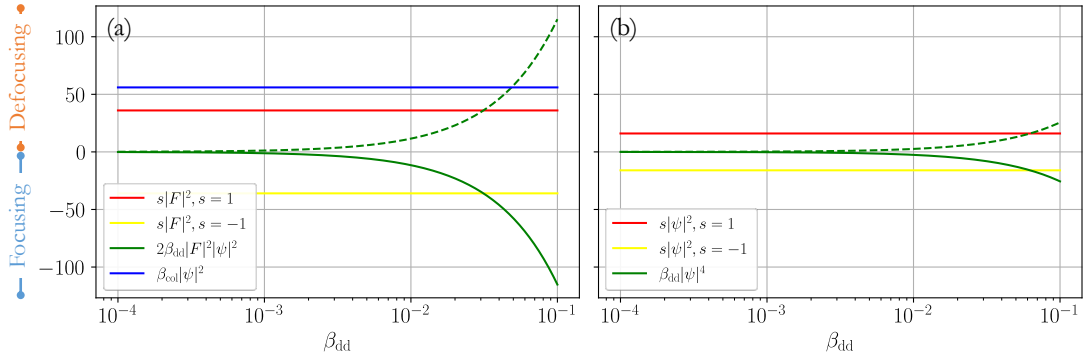
Figure 6.6: Relative nonlinear term sizes (dotted: absolute magnitude) of (a) Eqn. (5.55) and (b) Eqn. (5.56), for $10^{-4} < \beta_{\text{dd}} < 10^{-1}$, with $\beta_{\text{col}} = 3.5$.

In both cases, we observe exponential growth of the dominance of the term corresponding to dipole-dipole interactions. For this parameter selection, we find that in Eqn. (5.55) the dipole-dipole forces exceed the dipole nonlinearity when $\beta_{\text{dd}} \gtrsim 0.03$, and become the dominant nonlinear force when $\beta_{\text{dd}} \gtrsim 0.05$, whilst in Eqn. (5.56) they dominate over the dipole force when $\beta_{\text{dd}} \gtrsim 0.06$. As it is always a focusing term, this

will further contribute to the localisation dynamics previously described. We again consider varying $10^{-4} < \beta_{\mathrm{dd}} < 10^{-1}$ for homogeneous fields. The results are shown for blue atom-field detuning, across $\zeta = 0.5 \to 2$, in Fig. 6.7.
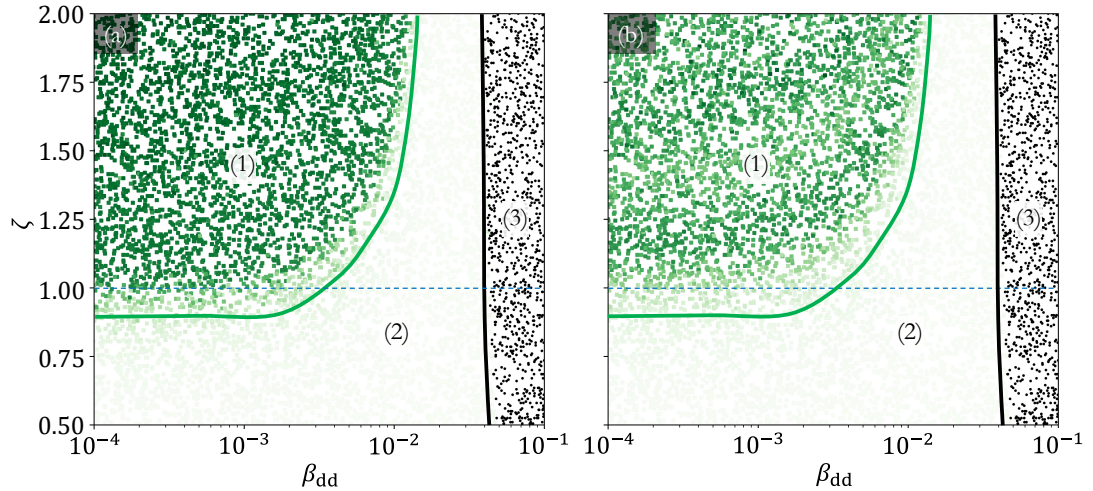
Figure 6.7: Pattern stability for $10^{-4} < \beta_{\mathrm{dd}} < 10^{-1}$ with blue-detuned atomic (a) and optical (b) fields between $0.5 \leq \zeta \leq 2$. Regions show: (1) pattern formation; (2) homogeneous field return; (3) field collapse. Other parameters as in Fig. 6.1. Colour scales as in Fig. 6.3.

Within region (1) of Fig. 6.7, contributions from the dipole-dipole corrections are negligible, the fixed colour representing an unchanged pattern modulation strength. Above $\beta_{\mathrm{dd}} \approx 10^{-2}$, region (2), the increasingly dominant dipole-dipole term suppresses pattern formation, before its focusing nature causing numerical instability and breakdown, region (3), in agreement with Fig. 6.6. We see similar behaviour when $s = -1$, and therefore may conclude that when $\beta_{\mathrm{dd}} < 10^{-2}$, its contributions remain negligible within the system.

6.5 Conclusions and Outlook

In Chapter 6, we studied the dynamics of initially homogeneous co-propagating optical and ultracold atomic fields. In agreement with Refs. [32, 33], we obtained coupled interleaved or coincident filamentation patterns depending on the sign of the atom-light detuning. The appearance of ring structures in the far field, again in good agreement

with Ref. [32], gave an indication as to the presence and clarity of spatial structures in the near field. The patterns were shown to be short-lived to $\zeta \lesssim 2$ and, for several interleaved and most coincident patterns, were shown to be prone to instability and collapse from self-focusing, despite exploring large potential operating regimes.

If nonlinear self-focusing effects can be suppressed, there is the potential for significant impacts through such structures. If such phenomena occur on physically defined fields, representative of experimental BEC [100] and optical [39, 112] transverse distributions, then the guidance of atoms into bright and dark regions of the optical field according to the sign of the detuning may be employed for atomic trapping [25], manipulation into alternative transverse structures [198], or soliton generation [32, 33].

Chapter 7

Structured Fields I: Patterns

In this chapter, we build on the results of Chapter 6, introducing intensity structure to the initial atomic and optical fields. In *Section 7.1*, we consider replicating these patterns on structured fields for both forms of field detuning, again discussing the relative stability regimes of patterns obtained, and the analogies between the systems. In *Section 7.2*, we develop the model outlined in Chapter 5, providing a case by case justification of the alterations made, to extend the parameter regime for stable propagation whilst continuing to obtain mutual structure formation.

7.1   Pattern Formation on Spatial Structures

Our intensity structured initial atomic and optical fields are as outlined in Chapters 2-3. The initial optical field is a Gaussian at the beam waist, defined in Eqn. (3.34) as

$$F\left(r, \zeta(0)\right) = A_F \exp\left(-\frac{r^2}{2w_F'^2}\right),$$

where the optical field's beam waist w_F is set by $w_F' = w_F/w_{\mathrm{L}}$, w_{L} is the characteristic beam waist introduced through Eqns. (5.35)-(5.36), and $r^2 = \xi^2 + \eta^2$. The initial atomic

field is a Thomas-Fermi distribution, given in Eqn. (2.17) as

$$\psi(r, \zeta(0)) = A_\psi \left(1 - \frac{r^2}{2w'_\psi{}^2} \right),$$

with w'_ψ controlling the transverse size of the BEC through $w'_\psi = w_\psi/w_\mathrm{L}$. Such structure is typical of transverse ultracold atomic distributions [100].

To allow comparison with Chapter 6 and Ref. [33], we again set $A_\psi = 4$ and $A_F = 6$, with noise applied at the 1% level. We select transverse domains of $w_F = w_\psi = 100\mu$m, ensuring that the fields have cross-sectional areas large enough, with sufficient amplitudes, for the dipole force to dominate the dynamics. This gives initial fields of the form shown in Fig. 7.1.
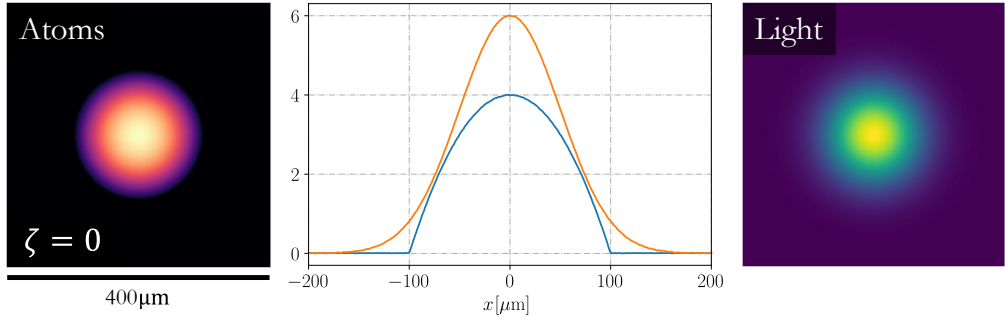
Figure 7.1: Initial transverse BEC (left) and optical (right) amplitude distributions. Centre: 1D cross-section of distributions. Parameters: $A_\psi = 4, A_F = 6$, and $w_F = w_\psi = 100\mu$m according to Eqns. (3.34) and (2.17). Colour scales from zero to maximum field amplitude of each panel.

As before, we investigate the co-propagation of these fields using Eqns. (5.55)-(5.56) for both signs of the atom-field detuning.

7.1.1 Blue Atom-Field Detuning

For the case of blue atom-field detuning ($s = 1$), above a required amplitude threshold and on a sufficiently large transverse area, one obtains the formation of mutual structures in both fields, similar to those on homogeneous fields as outlined in Chapter 6. Such structures are shown in Fig. 7.2, which, like Fig. 6.1, shows the two transverse domains at $\zeta = 0.5, 1$, and 2.
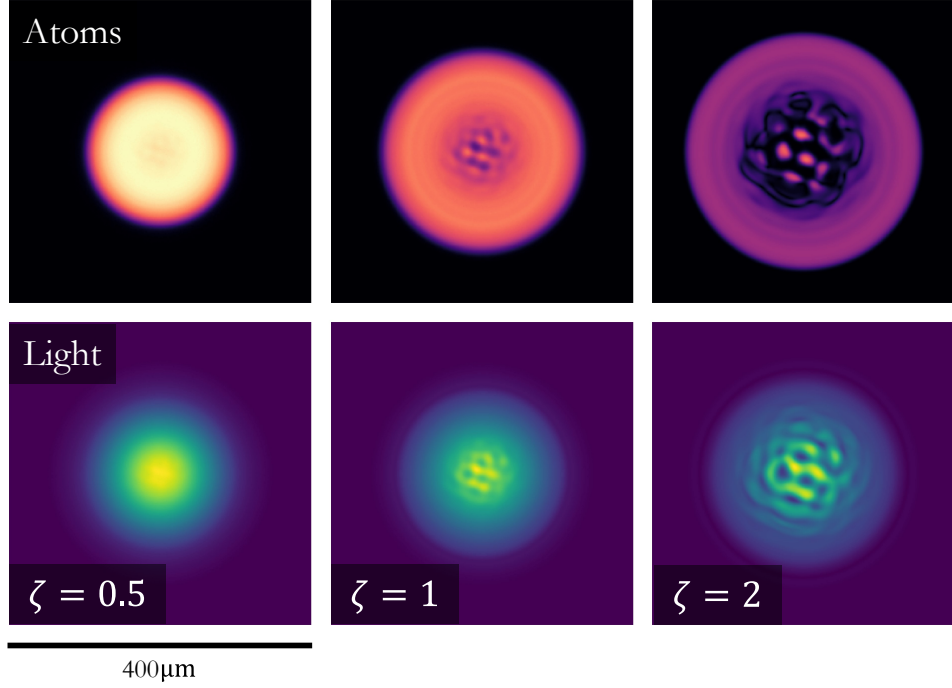
Figure 7.2: Transverse BEC (upper) and optical (lower) amplitude distributions at $\zeta = 0.5, 1$ and 2 (left to right) for initially Thomas-Fermi and Gaussian beams, respectively, and blue atom-field detuning. Parameters: $s = 1, A_\psi = 4, A_F = 6, \beta_{\text{col}} = 3.5, \beta_{\text{dd}} = 1.6 \times 10^{-4}$, and $w_F = w_\psi = 100\mu$m. Colour scales from zero to max. field amplitude.

We again observe interleaved structures across the atomic and optical fields, arising through the dipole nonlinearity that links the fields. At $\zeta = 0.5$ in Fig. 7.2, the patterns are early in their formation, manifest as slight modulations upon the distributions, forming despite a developing minimum in the central atomic field as atoms are transported away from bright optical regions. At $\zeta = 1$, the formation of mutual interleaved structures is evident in both fields. These structures are limited to regions of the fields with sufficient overlap above a threshold amplitude for pattern formation, and as such they only form in the central regions of the field, with additional uniform surrounding structures. The transport of atoms outward from the optically intense region has continued, with a ring of relative intensity surrounding the patterns as this process combines with the kinetic energy contributions. The optical field also shows diffraction, with its transverse extent having increased notably.

At $\zeta = 2$, both fields show clear evidence of their respective kinetic energy and diffrac-

tion contributions, and though mutual structures remain, they are broader in spatial scale and weaker in amplitude. From this point, the defocusing contributions from a combination of atomic kinetic energy, interatomic scattering and optical diffraction continue to dominate, and the mutual interleaved structures persist but continue to spatially broaden. These dynamics replicate the results of Ref. [33], which first reported such patterns. Although not discussed here, we have also replicated other results of Ref. [33], where an atomic region of zero intensity guides optical solitons in a blue detuned regime.

For the dynamics of Fig. 7.2 stability maps may again be produced, displaying the nature of interleaved patterns formed for a range of initial field amplitudes at $\zeta = 1$, Fig. 7.3(a).
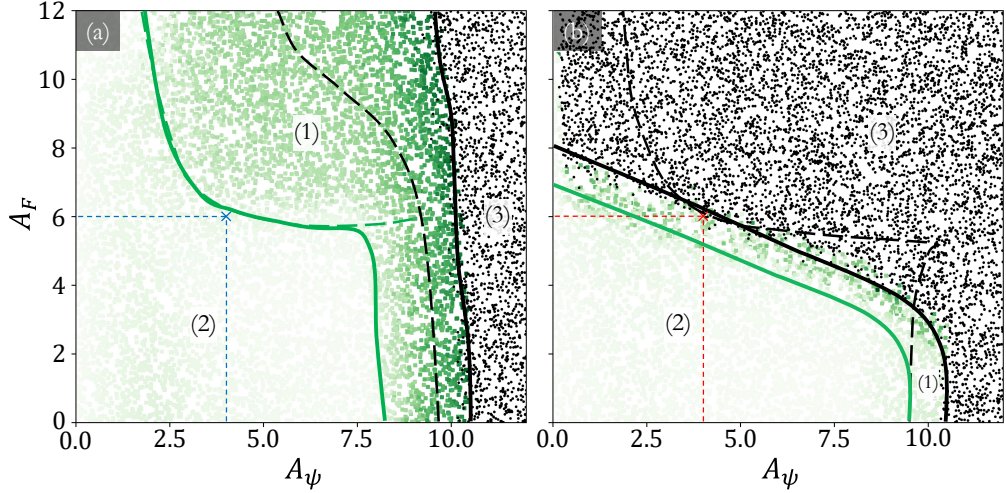
Figure 7.3: Pattern stability in atomic field for $0 \leq A_\psi, A_F \leq 12$ with blue (a) and red (b) atom-field detuning for initially intensity structured fields at $\zeta = 1$. Regions show: (1) pattern formation; (2) homogeneous field return; (3) field collapse. Dotted dividing lines indicate equivalent regions for homogeneous fields (Fig. 6.3)). Other parameters as in Fig. 7.2.

The addition of spatial structure to both fields opens new parameter spaces for pattern formation compared to the homogeneous equivalent, Fig. 6.3, where the uniformity of the fields across the spatial domain prevents kinetic and diffractive contributions. Here, such terms provide a loss of atomic and optical intensity from the pattern forming regime, with patterns from previously unstable high-amplitude initial field combinations

now realisable thanks to the lesser amplitudes involved after mutual field ejection.

7.1.2 Red Atom-Field Detuning

For red atom-field detuning, with 'light-seeking' atoms and coincident patterns, collapse, manifest as numerical instability and breakdown from overwhelmingly focusing nonlinearities, was observed for homogeneous fields across a widespread operating regime. Similar pattern formation on intensity structured fields is shown in Fig. 7.4. Again coupled coincident structure formation occurs in both fields, evident as minor perturbations on top of both fields at $\zeta = 0.5$, and then as distinct structures by $\zeta = 0.7$. The formation process is similar to the blue detuned case in the previous section, and agrees well with the patterns of homogeneous fields, with an atomic peak corresponding to an optical peak. We also find a rapid filamentation process occurring, with filaments present after $\zeta = 0.8$, and the fields having mutually collapsed by $\zeta = 0.85$.
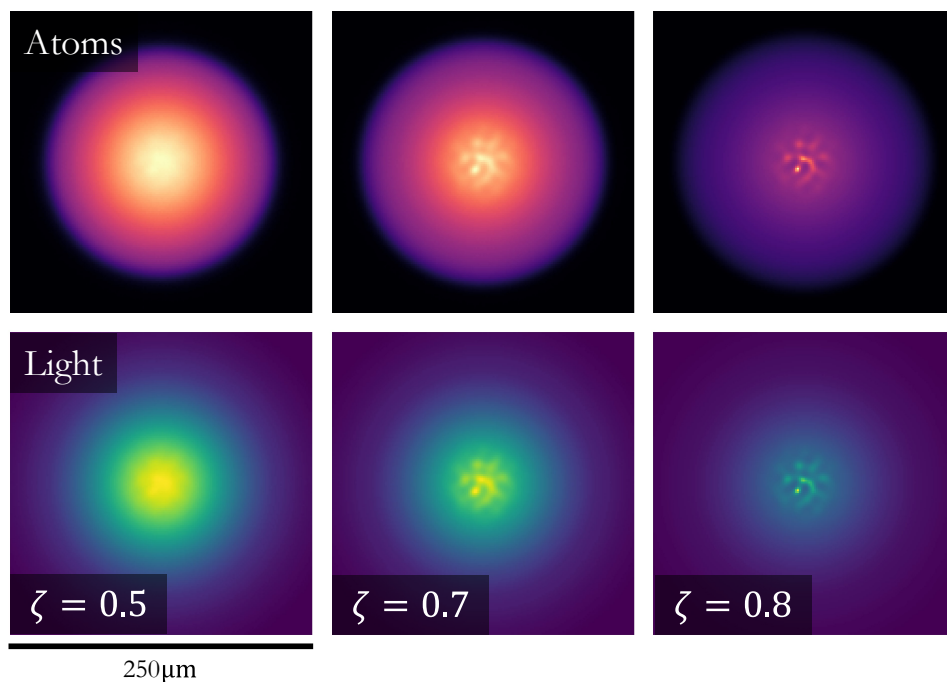
Figure 7.4: Transverse BEC (upper) and optical (lower) amplitude distributions at $\zeta = 0.5, 0.7$, and 0.8 (left to right) for initially Thomas-Fermi and Gaussian beams, respectively, and red atom-field detuning. Parameters: $s = -1, A_\psi = 4, A_F = 6, \beta_{\mathrm{col}} = 3.5, \beta_{\mathrm{dd}} = 1.6 \times 10^{-4}$, and $w_F = w_\psi = 100\mu\mathrm{m}$.

To explore further the stability of these patterns, an equivalent atomic parameter map at $\zeta = 1$ for various initial field amplitudes is shown in Fig. 7.3(b). These again show a significant narrowing of pattern forming regions arising from the change of detuning and associated breakdown from increased focusing nonlinearities. Comparing this to the homogeneous field equivalent, Fig. 6.3(b), we see a similar growth in parameter spaces not displaying a collapse as for blue-detuning, which is again due to the additional contributions of the kinetic energy and diffraction terms for spatially defined fields. However, we note that for the majority of the parameter space studied, collapse from filamentation is observed for red-detuned fields.

7.2   Model Developments

For both interleaved and coincident patterns, we have reported several instances of collapse from filamentation after pattern formation. In this section, we alter the model used to describe each field in an effort to increase the propagation of these patterns further than previously possible. We firstly outline each change individually, verifying that pattern formation occurs unchanged as a benchmark of the model against existing literature studies, before combing the changes and verifying that the alterations acting in parallel both permit pattern formation and enable further stable co-propagation.

7.2.1   Importance of Dipole-Dipole Contributions

We first consider the importance of the dipole-dipole corrections in Eqns. (5.55) and (5.56), ie. the terms $-2\beta_{\mathrm{dd}}|F|^2|\psi|^2$ and $\beta_{\mathrm{dd}}|\psi|^4$, respectively. In Chapter 6.4, these contributions were found to be negligible for $\beta_{\mathrm{dd}} \lesssim 10^{-2}$. Recalling that from Eqn. (5.51),

$$\beta_{\mathrm{dd}} = \frac{2}{3k_{\mathrm{L}}^2 w_{\mathrm{L}}^2},$$

with w_{L} equating to the optical beam waist. Taking $\lambda \approx 10^{-7}$m, for this term to become the dominant term a beam waist on the order of μm or smaller would be required. Such a waist size is an order of magnitude smaller than the smallest value that we consider, and so we exclude this term from the dynamics.

7.2.2 Inclusion of Optical Saturation

We now consider the inclusion of optical saturation in the model. This accurately captures regions of high optical intensity, and has been shown to be important for avoiding the collapse of optical beams within a Kerr medium [60, 233]. We introduce a new parameter σ_{sat}, representing the strength of the saturating nonlinearity experienced by the optical field. Eqn. (5.56) becomes

$$\partial_\zeta F = i\nabla_\perp^2 F + i\left(\frac{-s|\psi|^2 + \beta_{\mathrm{dd}}|\psi|^4}{1 + \sigma_{\mathrm{sat}}|F|^2}\right)F. \qquad (7.1)$$

In the Kerr case $\sigma_{\mathrm{sat}} = (4P_{\mathrm{L}})/(3I_{\mathrm{sat}}w_F^2) \approx I_{\mathrm{L}}/I_{\mathrm{sat}}$, where P_{L} is the power of the incident laser beam, I_{L} is the beam's intensity, and I_{sat} is the saturation intensity [60]. From this, we set $\sigma_{\mathrm{sat}} \approx 10^{-3}$ [148], and under these conditions obtain near-identical pattern formation with Eqns. (5.55)-(7.1), shown in the upper row of Fig. 7.5.
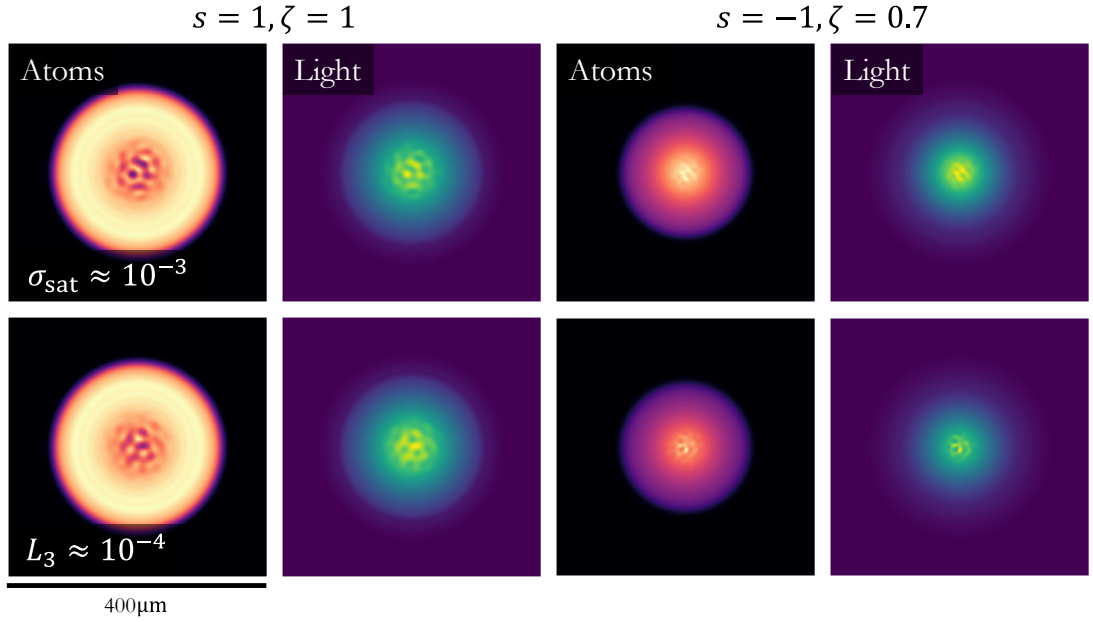
Figure 7.5: Transverse BEC and optical patterns for blue (left) and red (right) atom-field detuning with $\sigma_{\mathrm{sat}} \approx 10^{-3}$ (top) and $L_3 \approx 10^{-4}$ (bottom). ζ-values as indicated above panels. Parameters: $A_\psi = 4$, $A_F = 6$, $\beta_{\mathrm{col}} = 3.5$, and $w_F = w_\psi = 100\mu$m.

7.2.3   Inclusion of Three-Body Atomic Loss

Finally, we account for three-body atomic losses in the model. These arise due to three-body collisions within the BEC and are significant for dense atomic regions [234, 235]. These collisions can lead to the thermal ejection of one (or more) atoms which escape the ground state, leading to a reduction in the total atom number [236]. Following the procedure of Refs. [232, 237], Eqn. (5.55) becomes

$$\partial_\zeta \psi = i\nabla_\perp^2 \psi - i\left(s|F|^2 - 2\beta_{dd}|F|^2|\psi|^2 + \beta_{col}|\psi|^2 - iL_3|\psi|^4\right)\psi, \qquad (7.2)$$

where L_3 represents a three-body loss parameter. We find that $L_3 \approx 10^{-4}$, in agreement with previous estimates for Caesium [232, 237, 238]. The result is shown in the bottom row of Fig. 7.5, which demonstrates near-identical coupled patterns to Figs. 7.2 and 7.4 respectively.

7.2.4   Enhanced Model Stability

We now consider all the outlined model alterations simultaneously, namely neglecting dipole-dipole contributions whilst including optical saturation and atomic three-body losses. These contributions transform Eqns. (5.55)-(5.56) into [239–242]

$$\partial_\zeta \psi = i\nabla_\perp^2 \psi - i\left(s|F|^2 + \beta_{col}|\psi|^2 - iL_3|\psi|^4\right)\psi, \qquad (7.3)$$

$$\partial_\zeta F = i\nabla_\perp^2 F + i\left(\frac{-s|\psi|^2}{1 + \sigma_{sat}|F|^2}\right)F. \qquad (7.4)$$

When evolving coupled BEC and optical fields according to Eqns. (7.3)-(7.4), we again obtain coupled patterns, as shown in Fig. 7.6 [239–241]. The formation of these patterns at the same ζ-values as previously reported verifies the parallel alterations to the model.

The full benefit of these alterations becomes apparent after pattern formation, as significantly enhanced propagation stability is obtained. To demonstrate this, we again produce stability maps for various initial field amplitude combinations, with the map for blue atom-field detuning, comparable to that obtained prior to the alterations in
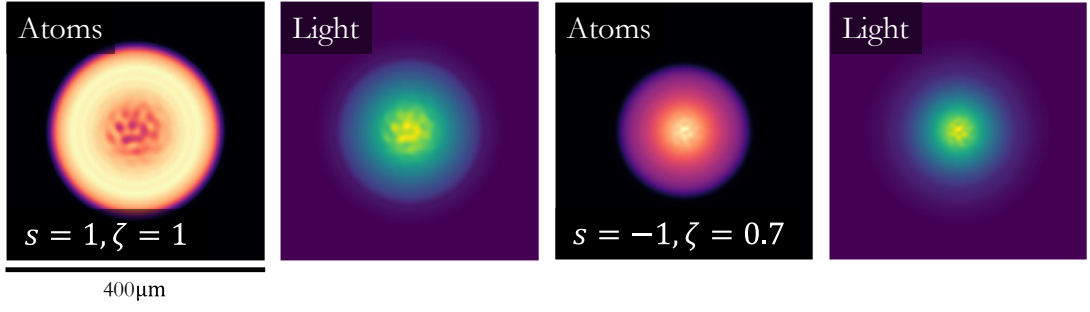
Figure 7.6: Transverse atomic and optical pattern formation for blue (left) and red (right) atom-field detuning, with the model of Eqns. (7.3)-(7.4). Parameters: $A_\psi = 4$, $A_F = 6$, $\beta_{\text{col}} = 3.5$, $w_F = w_\psi = 100\mu\text{m}$, $\sigma_{\text{sat}} = 0.0011$, and $L_3 = 0.00022$.

Fig. 7.3, see Fig. 7.7(a). The regions of stable pattern formation at $\zeta = 1$ have grown substantially from those previously obtained. Remarkably, for $0 \leq A_\psi, A_P \leq 12$, we find *no* numerical breakdown occurring, with the additional terms of Eqns. (7.3)-(7.4) enabling the system to remain entirely stable under propagation whilst still displaying the familiar pattern formation effects.
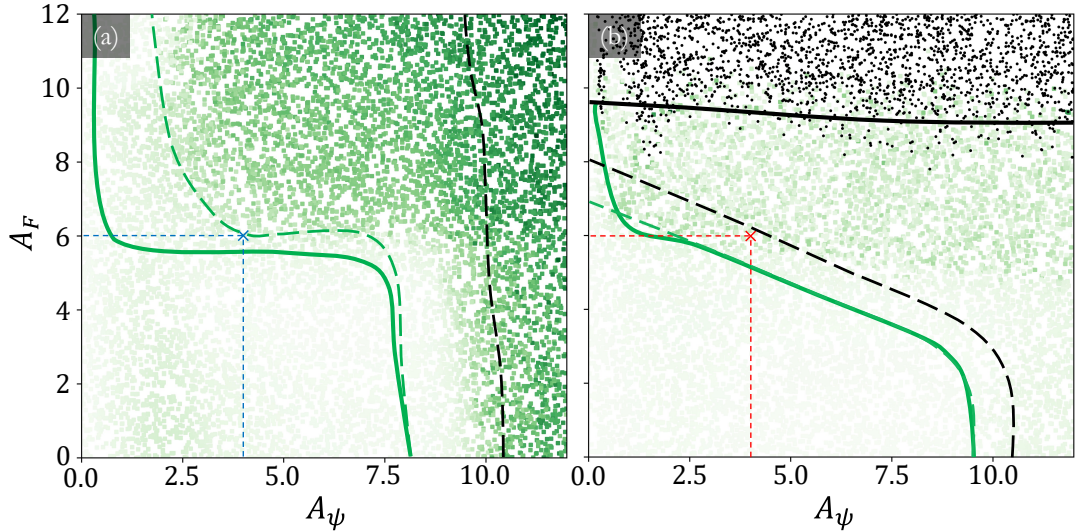
Figure 7.7: Pattern stability in atomic field for $0 \leq A_\psi, A_F \leq 12$ with blue (a) and red (b) field detuning at $\zeta = 1$ according to Eqns. (7.3)-(7.4). Regions show: (1) pattern formation; (2) homogeneous field return; (3) field collapse. Dotted dividing lines indicate equivalent regions for model of Eqns. (5.55)-(5.56) (Fig. 7.3)). Other parameters as in Fig. 7.6.

For red atom-field detuning, $s = -1$, an equivalent map is given in Fig. 7.7(b). Again,

we find that Eqns. (7.3)-(7.4) have a profound effect on the stability of both fields, with a large parameter space returning stable pattern formation at $\zeta = 1$. Unlike in the blue-detuned case, here some regions still demonstrate collapse, but are significantly smaller than previously reported. In particular, the model alterations successfully restrict atomic driven instabilities, and it is only when $A_F > 10$ that instability occurs consistently.

Fig. 7.7 demonstrates that the alternative model provides significant stability enhancement for both forms of field detuning, whilst maintaining the known pattern formation dynamics. We therefore use the model of Eqns. (7.3)-(7.4) in the rest of Part II.

7.3 Conclusions and Outlook

We have demonstrated that the patterns reported in Chapter 6 are realisable on physical, spatially structured initial atomic and optical fields. Although some additional stability was obtained with this alteration, under many conditions instability and collapse was still obtained, particularly for red detuned fields. By including several additional terms, we reached an updated set of coupled nonlinear equations which we demonstrated are capable of obtaining patterns as reported in Ref. [33], but with the significant advantage of avoiding subsequent numerical instability and breakdown, instead achieving stable propagation.

With stable propagation of both atomic and optical fields now achievable, the model provided by Eqns. (7.3)-(7.4) may be used with a wide variety of initially structured optical and atomic fields, which we shall consider in subsequent chapters. Particular emphasis will be placed upon the effects of field detuning to lead to the movement of ultracold atoms to regions of bright or dark optical intensity. With these dipole forces now accessible on longer propagation scales, a particular focus of this model for controllable atomic transport shall be explored [51, 243]. As discussed previously, there are also potential applications of these dynamics on more complex structured fields for atomic manipulation into counter intuitive transverse structures [198], or for soliton generation [32, 33].

Chapter 8

Structured Fields II: Atomic Guiding

In this chapter, we introduce more complex structure to the initial optical fields than was considered in Chapter 7. In *Section 8.1*, we consider alternative forms of intensity structure using optical ring modes, and again report on a strong influence of the field detuning on the co-propagation dynamics. In *Section 8.2*, we introduce structured phase to the optical field, considering Laguerre-Gaussian modes, Bessel-Gaussian modes, and scalar mode superpositions. We report on profound alterations to the dynamics arising from structured phase, and consider the optically-induced re-shaping and sculpting of atomic transverse intensity distributions, the formation of controllable atom-light clusters, atomic vortex ring creation, and dark atomic cluster trapping.

8.1 Intensity Structured Optical Beams

We now apply the model of Eqns. (7.3)-(7.4) to a range of initial optical intensity profiles. We use Eqn. (3.38), the definition of a Laguerre-Gaussian mode at the beam waist, to create intensity-only optical ring modes, disregarding the OAM of the beam.

Such modes may be created several ways experimentally. Routes include following a similar scheme to creating beams with fractional OAM [244], and through beam shaping [245]. Eqn. (3.38) is modified to obtain initial optical modes of the form

$$|\mathrm{LG}_p^m\,(r)\,| = A\,r^{|m|}e^{-\frac{r^2}{2}}\mathrm{L}_p^{|m|}\left(r^2\right).\tag{8.1}$$

8.1.1 Patterns on Intensity Rings

Initially, we consider pattern formation on optical ring-modes. We retain the parameters used in Chapter 7, with $A_F = 4$, $A_\psi = 6$, and $w_F = w_\psi = 100\mu$m, but consider the initial optical field to be a $|\mathrm{LG}_0^1|$ ring mode from Eqn. (8.1). Again we observe pattern formation in regions of sufficient field intensity for both $s = \pm 1$, Fig. 8.1. For red detuned fields such behaviour is expected, given the dipole attraction of atoms to bright optical regions, but the pattern formation is also present in blue-detuned fields, along with an expected central region of uniformly trapped atoms, with the light acting as an effective lens upon the atoms in this region.
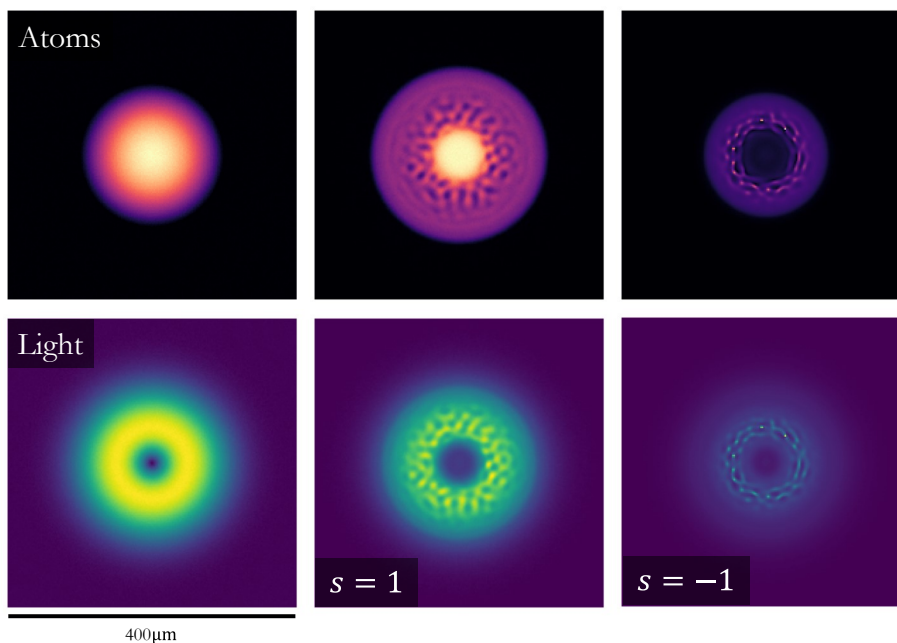
Figure 8.1: Patterns on atomic (upper) and optical (lower) fields with an $|\mathrm{LG}_0^1|$ optical mode at $\zeta = 0$ (left) and 0.7 for $s = 1$ (centre) and -1 (right). Parameters: $A_\psi = 4$, $A_F = 6$, $w_F = w_\psi = 100\mu$m, $\beta_{\mathrm{col}} = 3.5, \sigma_{\mathrm{sat}} = 0.0011$, and $L_3 = 0.00022$.

We observe pattern formation like that shown in Fig. 8.1 across a wide range of parameters and initial field sizes, suggesting that any desired configuration of patterns is possible, assuming sufficient transverse size and amplitude overlap between the two initial fields.

8.1.2 Optically Induced Atomic Reshaping

Building on the central region of trapped atoms in Fig. 8.1 with blue detuning, we now explore the ability of more complex optical structures to re-shape ultracold atoms. Setting $w_\psi = 50\mu$m for a more straightforward experimental setup [246, 247] and $w_F = 25\mu$m to ensure that the initial optical field remains captured within the transverse domain of the BEC, other parameters are maintained at their previous values.

Blue Atom-Field Detuning

When the atoms are dark seeking, we find that optical intensity rings act as effective atomic traps. In Fig. 8.2, therefore, we consider optical modes with amplitude configurations that derive from Eqn. (8.1). For the simplest case of a single initial optical ring, a large atomic population is trapped in the central dark regime by $\zeta = 1$. Though diffraction causes the spatial domain of this trap to grow, atomic trapping and localisation is realised, despite repulsive interatomic interactions. With $p \neq 0$, the number of optical rings increases, and superpositions of atomic rings formed in surrounding regions of darkness are observed. In both cases a highly effective multi-ringed atomic trap is realised, again overcoming repulsive interactions. This suggests a novel and straightforward means of sculpting complex atomic distributions is possible by shaping the initial optical distribution. This offers an alternative to current approaches with fixed trapping fields that enables more complex distributions to be realised.
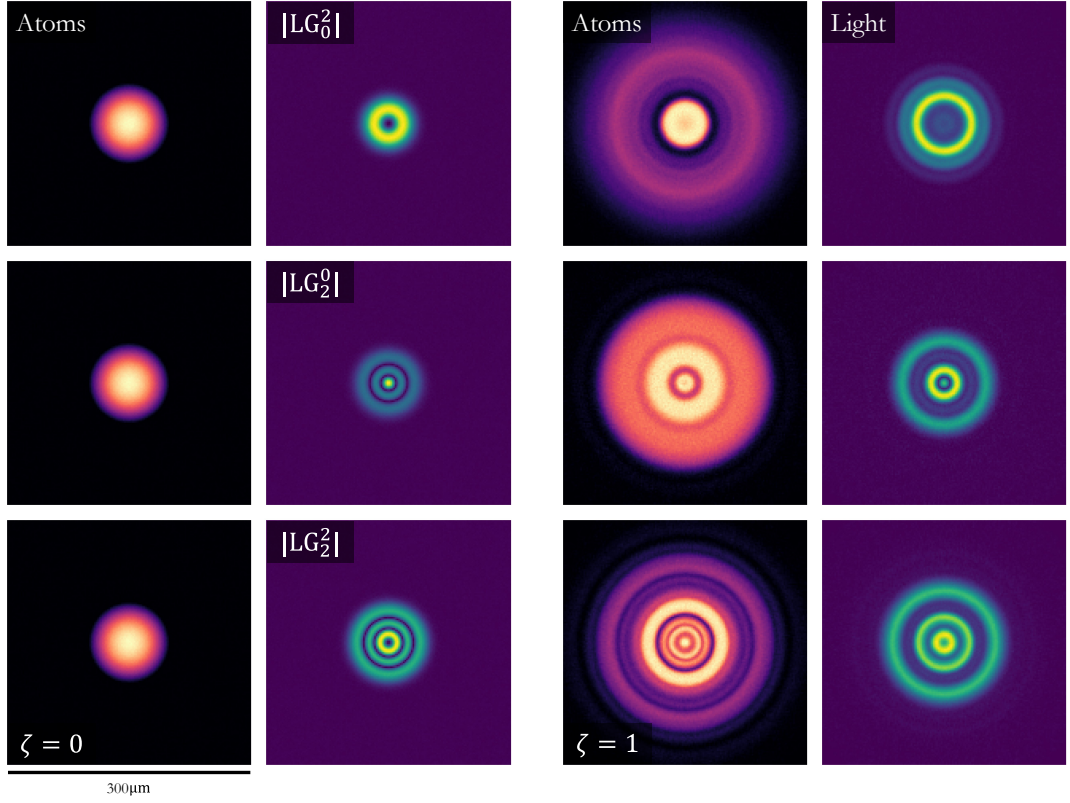
Figure 8.2: Blue-detuned propagation of various intensity-only LG optical modes, as defined in Eqn. (8.1), within a BEC, at $\zeta = 0$ (left hand side) and $\zeta = 1$ (right hand side). Parameters: $A_\psi = 4$, $A_F = 6$, $w_\psi = 50\mu$m, $w_F = 25\mu$m, $\beta_{\rm col} = 3.5$, $\sigma_{\rm sat} = 0.0011$, and $L_3 = 0.00022$.

Red Atom-Field Detuning

For bright-seeking atoms, we initially observe a rapid optically-induced re-shaping of the atomic field to optically intense areas. Following this, unlike in the blue-detuned case where diffraction dominated the dynamics, the now coincident fields self-localise, forming mutual intense central peaks, see the right hand side of Fig. 8.3. When $m = 0$, due to the central peak of the optical field, localisation occurs rapidly. When $m \neq 0$, coincident structures first form around the off-axis ring(s). If the ring lies close to the field centre, as is the case with $|{\rm LG}_2^2|$, then it collapses into a central peak, but if the ring lies further from the field centre, for example with $|{\rm LG}_0^2|$, it entirely fragments, with subsequent filaments collapsing into the field centre. In all cases, the fields will collapse by $\zeta = 1$.
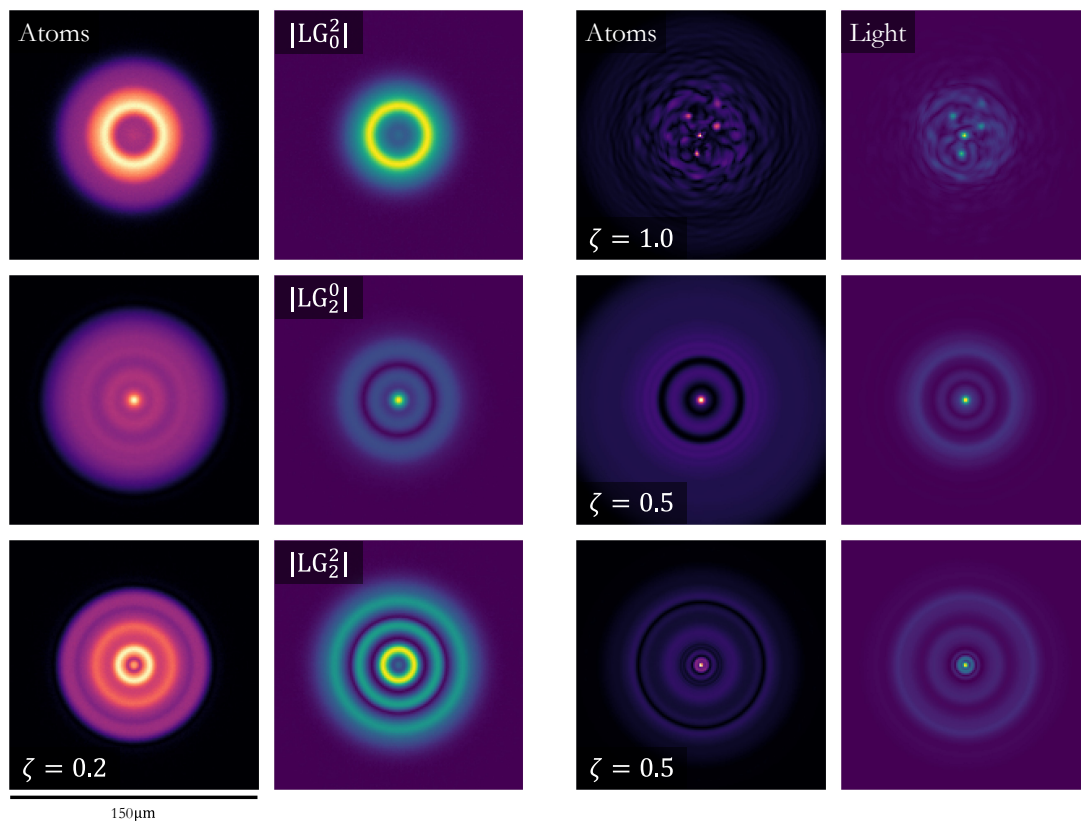
Figure 8.3: Red-detuned propagation of various intensity-only LG optical modes, as defined in Eqn. (8.1), within a BEC, at $\zeta = 0.2$ (left) and indicated distances (right). Initial fields as given in Fig. 8.2 (note domain change). Parameters otherwise as in Fig. 8.2.

8.2 Intensity and Phase Structured Optical Beams

We now consider the introduction of phase structure to the optical field.

8.2.1 Laguerre-Gaussian Modes

Re-introducing the phase of the Laguerre-Gaussian optical modes, $\exp(im\varphi)$ in Eqn. (3.38), we maintain the same ring-like amplitude distributions as in the previous section, but find that the introduction of helical phase, so that the optical beam now carries OAM, has a profound impact on the dynamics depending on the sign of the atom-light detuning.

77

Blue Atom-Field Detuning

Fig. 8.4 is the counterpart to Fig. 8.2 with OAM included. Introducing OAM does not significantly alter the dynamics when considering dark-seeking atoms, with the atoms again directed to such regions. When $p \neq 0$, we find the relative amplitudes of the optical rings differs with OAM under co-propagation and the second optical ring acts as the strongest atomic trap, but diffraction again dominates, with OAM causing no significant alteration here.
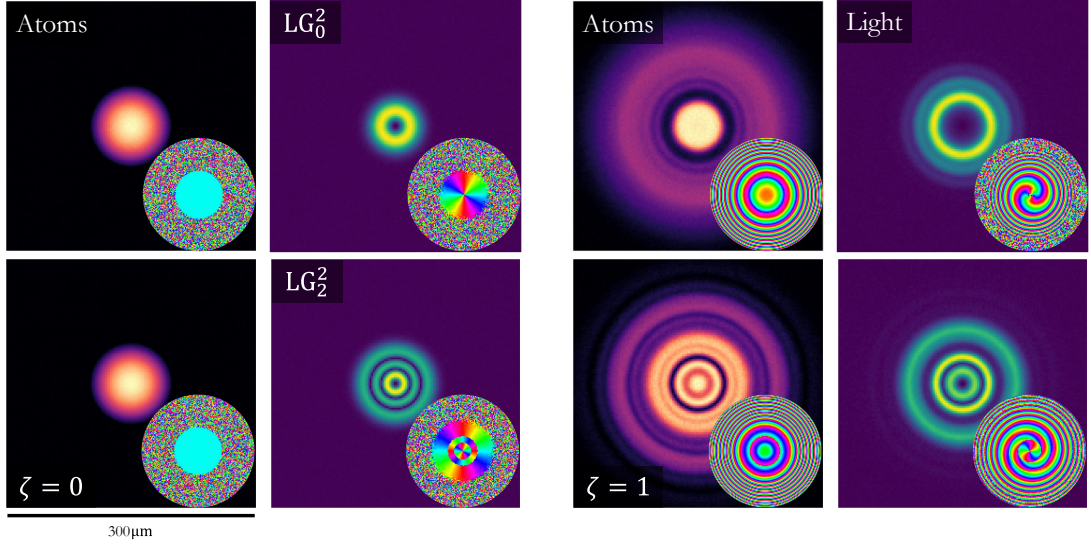
Figure 8.4: Blue-detuned propagation of various LG optical modes, as defined in Eqn. (3.38), within a BEC, at $\zeta = 0$ (left hand side) and $\zeta = 1$ (right hand side). Phase profile inset in each panel. Parameters as in Fig. 8.2.

As discussed in Chapter 3.4, OAM introduces an azimuthal velocity upon bright optical structures. To establish if such motion is transferred to the atomic field through dipole coupling, we extract one dimensional (1D) rings, $\Phi(\Upsilon)$, from the transverse fields. To quantify the rate of azimuthal flow, we evaluate the flux of probability (probability current) along these 1D fields, defined [242, 248] as

$$j(\Upsilon, \zeta) = \frac{\hbar}{2m_\Phi i} \left(\Phi^* \partial_\Upsilon \Phi - \Phi \partial_\Upsilon \Phi^* \right) \tag{8.2}$$

where m_Φ is the total field density around the extracted field ring. For both fields of

Fig. 8.2, we calculate the mean $j(\Upsilon)$ around the first optical intensity ring between $\zeta = 0 \rightarrow 1$, as shown in Fig. 8.5 for atomic (black) and optical (blue) fields.
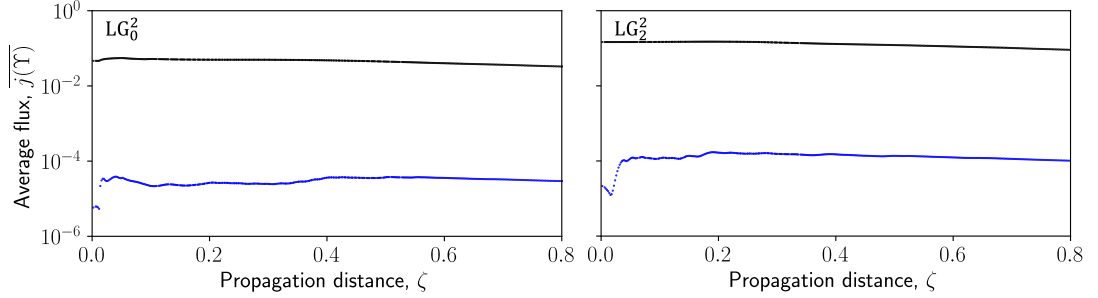
Figure 8.5: Average flux of probability around the first optical ring from the centre for blue-detuned LG_0^2 (left) and LG_2^2 (right) initial optical modes within a BEC, between $\zeta = 0 \rightarrow 1$. Optical (atomic) flux values in blue (black). Parameters as in Fig. 8.4.

A significant average flux of probability, indicative of azimuthal flow, is clear in the optical field for both panels of Fig. 8.5. The steady decay in its value reflects diffraction, with the angular velocity decreasing with ring radius. The equivalent atomic ring shows no clear rotational motion, with the flux remaining at the level of noise. For dark-seeking atoms, this optically intense ring corresponds to a region of low atomic density, and so we also evaluate the flux in areas of adjacent atomic density. We find that the average flux in these regions also remains below the noise threshold, suggesting limited OAM transfer to the atomic medium for blue-detuned co-propagation.

Red Atom-Field Detuning

The presence of OAM has far greater impact when considering bright seeking atoms when, without OAM, central collapse would occur in both fields (Fig. 8.3). The equivalent results with OAM are shown in Fig. 8.6.

Much like the blue detuned case, we initially observe optically-induced atomic reshaping, with the atomic field matching optically intense regions at $\zeta = 0.2$. We then find that the central phase singularity of the optical field prevents the mutual field collapse previously observed. Instead, we observe mutual fragmentation of transverse rings into coupled atom-light intensity clusters that propagate radially outward, similar to the fragmentation of an optical beam propagating in a self-focusing Kerr medium [148, 149].
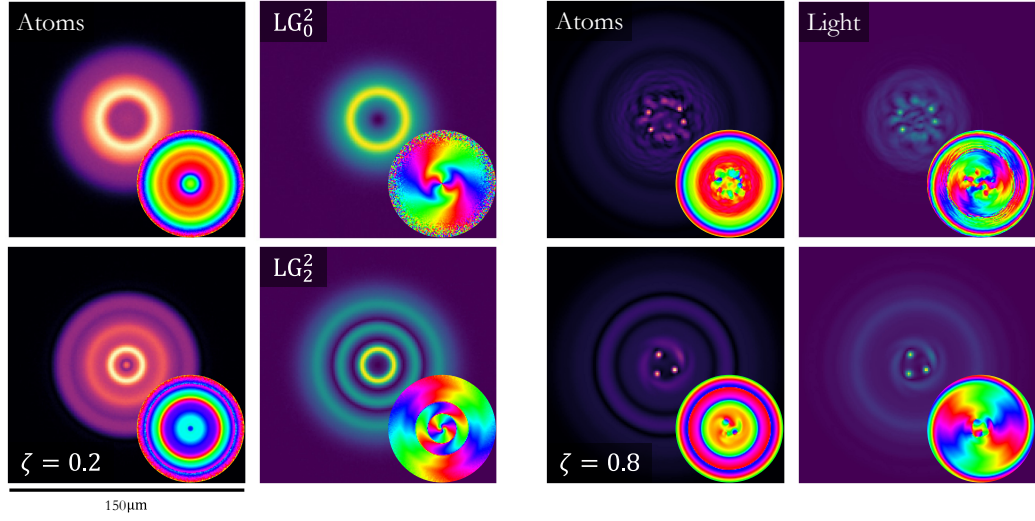
Figure 8.6: Red-detuned propagation of various LG optical modes, as defined in Eqn. (3.38), within a BEC, at $\zeta = 0.2$ (left hand side) and $\zeta = 0.8$ (right hand side). Phase profile inset in each panel. Parameters otherwise as in Fig. 8.2.

The atomic phase at $\zeta = 0.8$ in Fig. 8.6 suggests a transfer of phase to the atoms. To ascertain if azimuthal motion is also transferred to the atoms, we again calculate the flux of probability, now at the first maximal *coincident* atom-light ring from the field centre, as shown in Fig. 8.7.
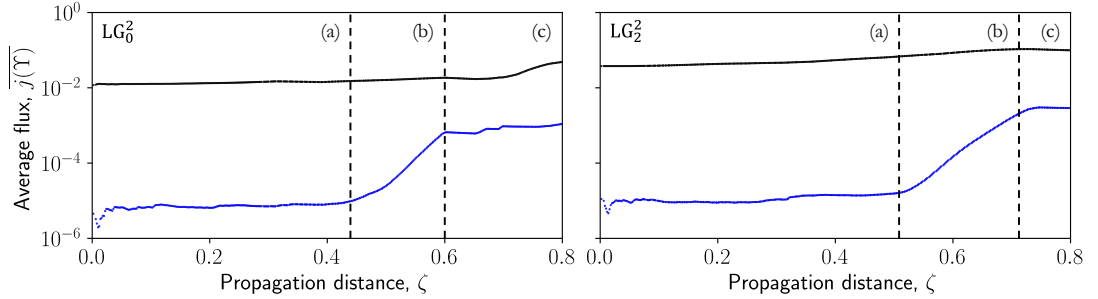
Figure 8.7: Average flux of probability around the first optical ring from the centre for red-detuned LG_0^2 (left) and LG_2^2 (right) initial optical modes within a BEC, between $\zeta = 0 \rightarrow 0.8$. Optical (atomic) flux values in blue (black). Parameters as in Fig. 8.6.

We observe a clear exponential increase of atomic flux between (a)-(b), reflecting a transfer of OAM from light to atoms leading to an azimuthal rotation around the mutually intense ring. The period (b) of exponential growth, occurring after ring formation, (a), precedes fragmentation, (c). After fragmentation, diffractive dynamics

begin to dominate, and the clusters propagate radially outwards. As the 1D reduction is on a fixed ring radius it is unable to capture the full dynamics.

Coupled Atom-Light Clusters

Given the analogy with prior studies of Kerr media [148, 149], we refine our parameter selection to optimise the fragmentation dynamics. We set $A_F = A_\psi = 9.5$, equating the initial dipole forces between fields. We also decrease the optical beam waist to $w_F = 10\mu$m, ensuring transverse capture of the optical field by the BEC whilst having $z_R \approx 0.44$mm to capture several z_R lengths during co-propagation [246, 247]. Finally, we restrict $p = 0$ for the initial optical LG mode, studying the dynamics around a single mutual intensity ring. The new initial fields for $m = 1$ are shown in Fig. 8.8.
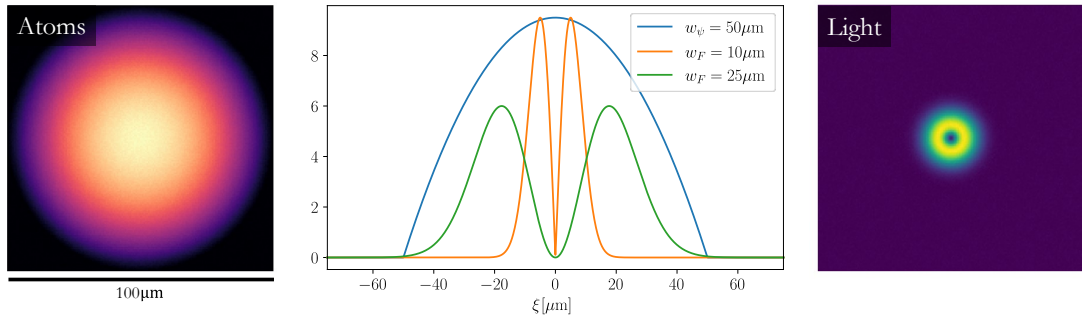
Figure 8.8: Transverse TF BEC amplitude with $w_\psi = 50.0\mu$m (left), and LG optical field amplitude for $m = 1$ and $w_F = 10\mu$m (right). Centre panel shows transverse cross sections, with comparison to $w_F = 25\mu m$, $A_F = 6$, LG_0^2 of previous section.

As with $w_F = 25\mu$m (Fig. 8.6), we find that fields configured as in Fig. 8.8 undergo a mutual localisation around the single optical ring, after which the dynamics of the BEC is closely coupled to that of the light. With the initial field amplitudes now matched, an ordered mutual fragmentation is observed, reliably forming two distinct solitons rather than filaments in spite of repulsive BEC interactions. Although both field amplitudes increase significantly within these peaks no collapse of the wave function occurs, even with negligible three-body loss, unlike without an optical vortex. Following the formation of coupled atom-light solitons, we again observe tangential ejection as shown in Fig. 8.9 [239–241].
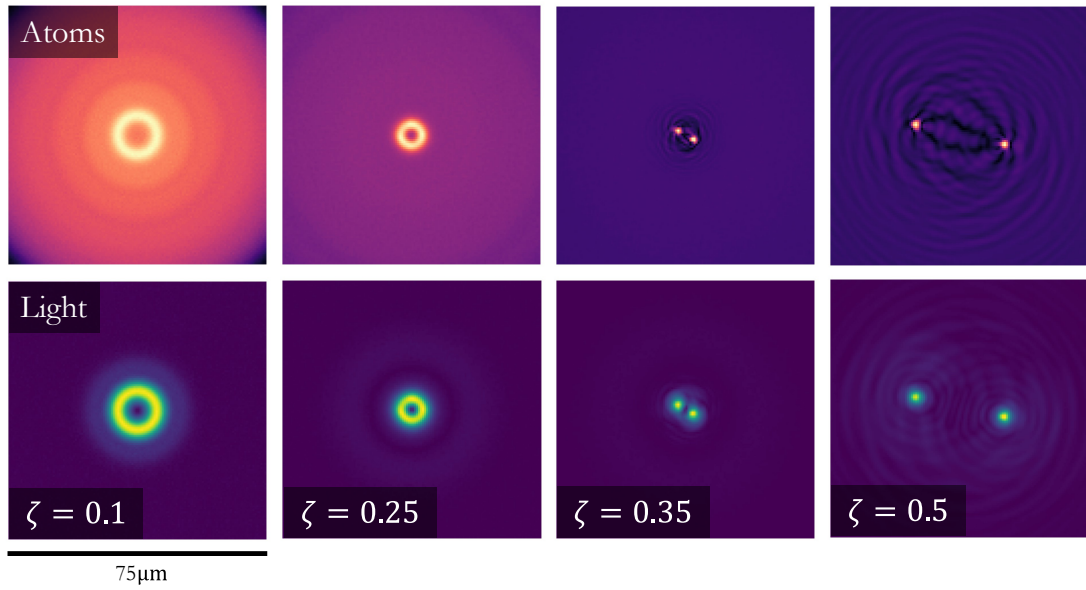
Figure 8.9: Atomic (upper) and optical (lower) intensity distributions at indicated ζ-values. Initial conditions as in Fig. 8.8.

We again apply the analogy of the 'around ring' dynamics to a 1D system to propagate homogeneous fields designed to match the rings present in the left hand panel of Fig. 8.9. We summarise these results in Fig. 8.10, which gives the dynamics of both atomic and optical 1D fields under further propagation. Like the 2D case, the fields fragment into coupled atom-light clusters which move diagonally, displaying azimuthal motion. As diffraction is not captured in this model, the clusters continue their radial progression, moving at constant angular velocity. The real part of the optical field demonstrates that each cluster forms at a local maximum, which is susceptible to growth under modulational instability for soliton formation as discussed in Chapter 4.1. In agreement with Ref. [148], we see the formation of the two solitons expected for $m = 1$. Unlike the examples of matter-wave soliton formation in ultracold atoms discussed in Chapter 4.1, there is no requirement here for attractive atomic interactions, or restriction to a single dimension for stability purposes [140–143, 146].

The behaviour of the optical field here is very similar to a vortex beam propagating in a self-focusing Kerr medium, predicted in [148, 149] and demonstrated experimentally in [60]. Such behaviour, assuming an instantaneous atomic medium, may be described
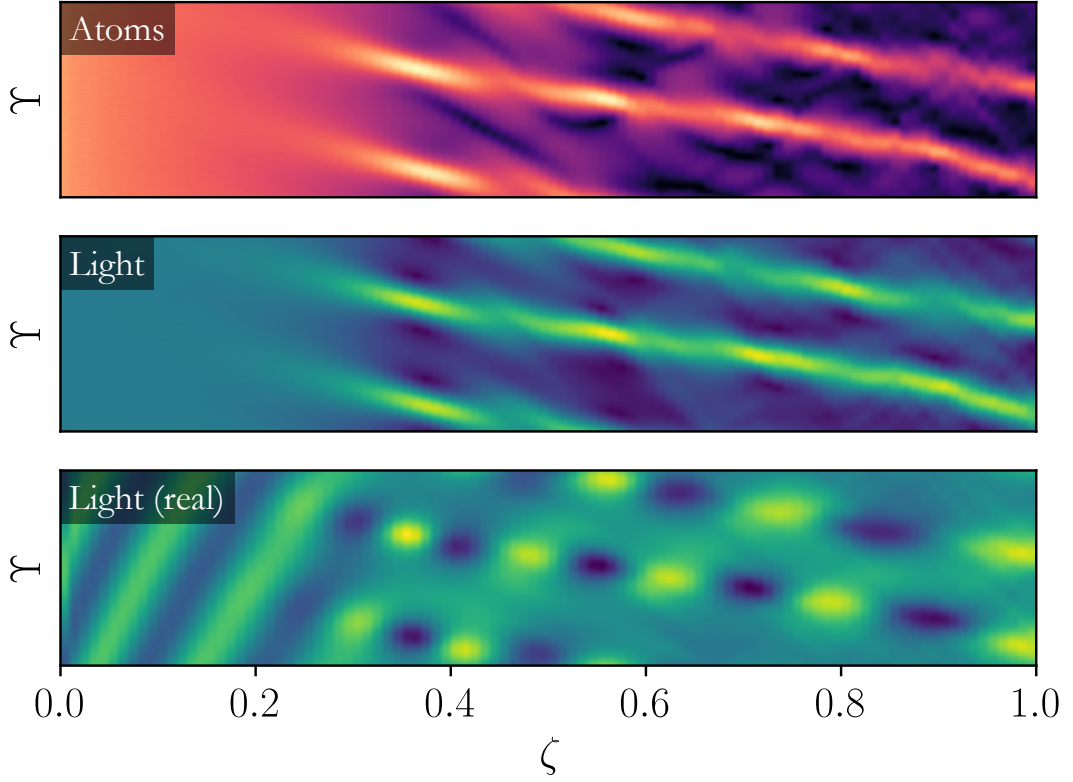
Figure 8.10: 1D 'around ring' atomic (upper), optical (centre) intensity, and real optical (lower) field distributions for $\zeta = 0 \rightarrow 1$. Initial conditions to match Fig. 8.9.

by Eqn. (5.59). With optical saturation, this relationship becomes

$$\partial_\zeta F = i\nabla_\perp^2 F + \frac{i}{\beta_{\mathrm{col}}} \left(\frac{|F|^2}{1 + \sigma_{\mathrm{sat}}|F|^2} \right) F, \qquad (8.3)$$

describing optical propagation in an effective 'saturating-Kerr' medium. We compare the evolution of identical optical fields subject to both a saturating-Kerr medium (Eqn. (8.3)) and dynamical BEC (Eqns. (7.3)-(7.4)) in Fig. 8.11, displaying in both cases the cross section of the optical field. We consider here the radially-averaged cross section, in r rather than transverse x or y, in order to capture the ejection dynamics within the cross-section regardless of 2D ejection direction. The similarity of both panels suggests that, under the considered parameters, the dynamic BEC acts as a Kerr-like superfluid [249], providing a self-focusing medium for the optical field. We note the slight ζ-mismatch between the position of strongest focusing in each panel,

which for the saturating-Kerr case is controlled solely by the strength of the Kerr non-linearity, but within the dynamical BEC case is also impacted by the time taken for the BEC to re-shape from its initial Thomas-Fermi distribution to match the position of optical intensity, a process not captured by the idealised saturating-Kerr model.
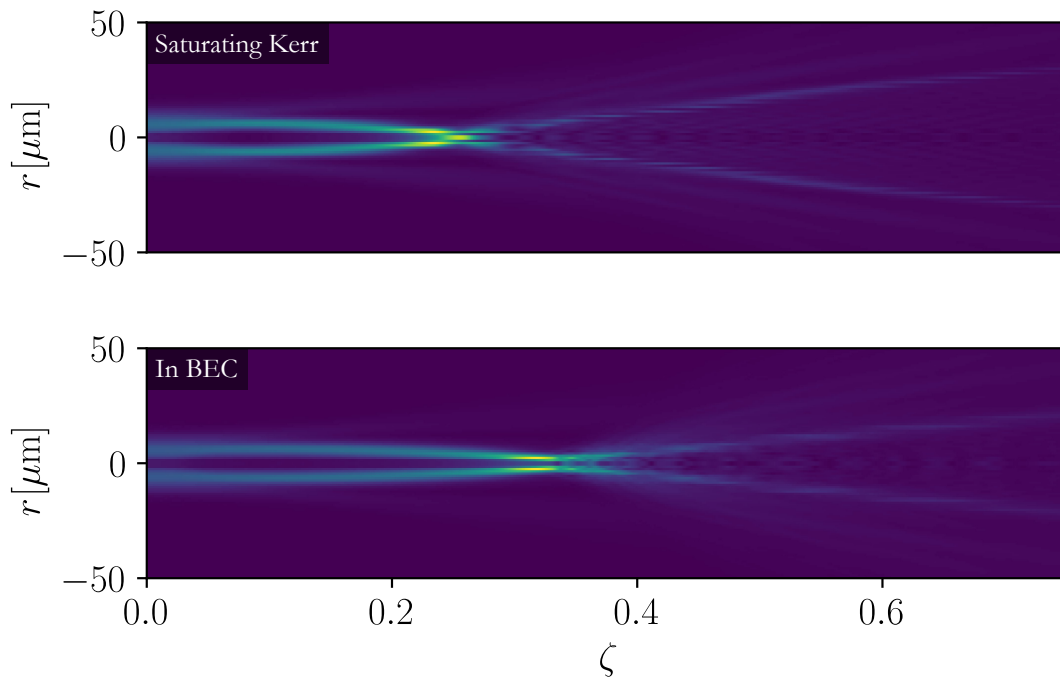
Figure 8.11: Transverse cross sections of an optical field propagating in a saturating Kerr medium (top) and within a BEC (bottom). For both, $\beta_{\mathrm{col}} = 3.5$.

We now return to considering solely the model with a dynamic BEC (Eqns. (7.3)-(7.4)) and expand the OAM selection of the initial mode. In all cases, we observe the formation of $2|m|$ coupled BEC and optical soliton peaks, following the outlined mechanism for $m = 1$. Panels (a)-(d) and (i)-(l) of Fig. 8.12 show these $2|m|$ atomic and optical solitons, respectively, at $\zeta = z_{\mathrm{R}}$. For all m-values, we see the same two distinct regimes of atomic motion described for $m = 1$, initially observing an azimuthal motion of the atomic peaks around the ring, analogous to persistent currents [217]. By extracting the fields around their radii of maximum intensity and calculating the gradient of any peak motion along these trajectories, we obtain approximations for the angular velocity of the solitons, and find that across the cases of $|m| = 1 \rightarrow 3$ this

velocity is inversely proportional to m^2 and that, in general, this 'atomic current' lasts for $\sim 0.75z_{\mathrm{R}}$, corresponding to a time period of ~ 0.1s for the selected parameters. This suggests a means of realising atomic currents within a BEC over a wide range of longitudinal propagation distances as determined by the optical Rayleigh range.
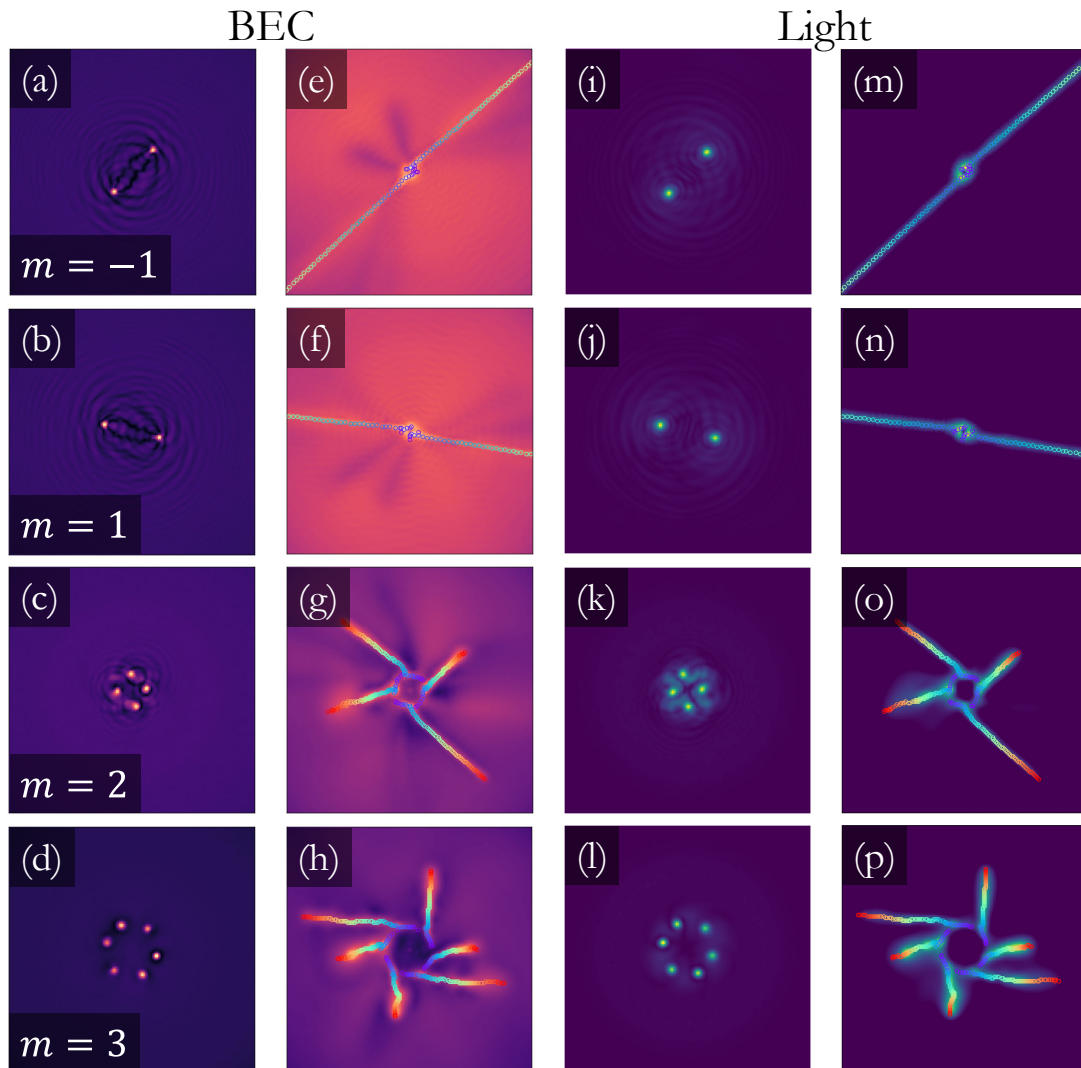
Figure 8.12: Atom-light cluster formation for $m = -1, 1, 2, 3$ (top to bottom). Panels (a)-(d) & (i)-(l): Transverse amplitude distributions of BEC and optical fields, respectively, at $\zeta = z_{\mathrm{R}}$. Panels (e)-(h) & (m)-(p): superimposed transverse BEC and optical amplitude distributions, respectively, $\zeta = 0.5z_{\mathrm{R}} \rightarrow 4z_{\mathrm{R}}$. Adapted from Ref. [239].

The atoms then enter a second regime where diffractive dynamics begins to dominate and the peaks are ejected tangentially to the ring, thus carrying away the angular

momentum [148]. This is demonstrated in panels (e)-(h) and (m)-(p) by overlaying a succession of transverse amplitude distributions from $\zeta = 0.5z_R$ to $4z_R$. We superimpose rainbow contours to highlight the propagation distance (blue at $\zeta = 0.5z_R$, red at $\zeta = 4z_R$). We find that the solitons move with a constant transverse velocity that is inversely proportional to m. This is particularly evident for the $m = -1$ and $m = 1$ cases where the solitons move in opposite directions and agrees very well with previous studies of fragmentation of OAM beams propagating in Kerr self-focusing media, predicted in Refs. [148, 149] and more recently demonstrated experimentally in Ref. [60]. The number of atomic solitons formed, and their tangential velocity, which we define simply as the speed of ejection of the solitons once their period of radial dynamics finishes, depends on the OAM of the optical input field meaning that it is possible to realise these controllable atomic transport dynamics across a wide range of longitudinal propagation distances, transverse field sizes and OAM values.

The overall behaviour of the system is summarised in Fig. 8.13, which shows in 3D (the two transverse dimensions, (ξ, η), and the propagation dimension ζ) the re-distribution of the atoms as the far-red-detuned light propagates along the length of the BEC. The atoms, initially in a Thomas-Fermi distribution, are focused onto a ring before splitting into $2|m|$ channels that twist as they propagate.
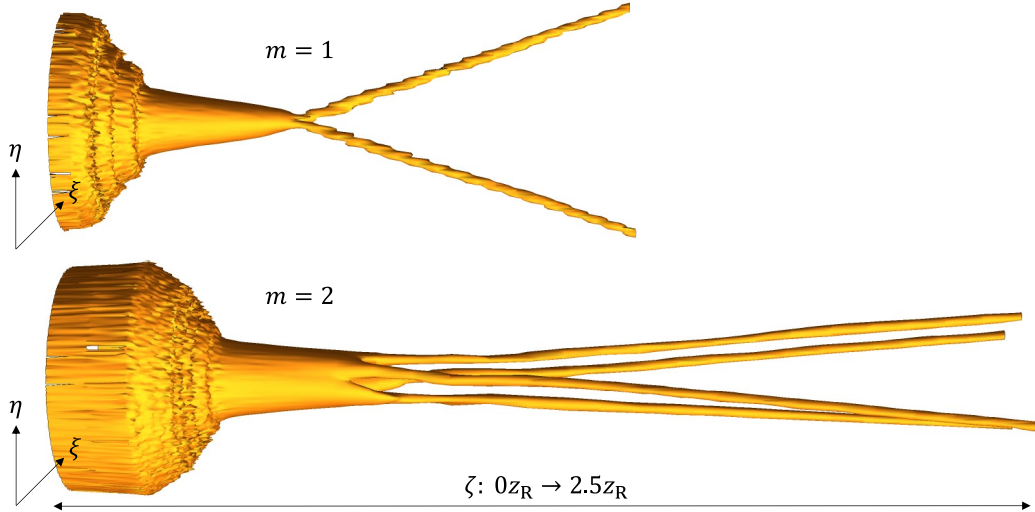
Figure 8.13: Three-dimensional (ξ, η, ζ) BEC distributions for $m = 1$ (top), and 2 (bottom), as in Fig. 8.12, between $\zeta = 0z_R \rightarrow 2.5z_R$. Transverse scales as in Fig. 8.8.

The coupled off-axis soliton formation process is robust across a wide range of OAM values, initial field amplitudes, beam sizes, and BEC scattering parameters for both weakly attractive and repulsive interactions in the range $-20a_0 < a_{gg} < 50a_0$ corresponding to $-4 < \beta_{col} < 11$. Three-body loss contributions are negligible for repulsive scattering, $\beta_{col} > 0$, but become more important for increasingly attractive scattering interactions. Both optical and atomic solitons propagate tangentially to the ring, carrying away its angular momentum, with little change to their shape or amplitude until they reach the transverse limits of the BEC [239–241].

8.2.2   Bessel-Gaussian Modes

In order to reduce diffraction and therefore increase the duration of the azimuthal rotation of the coupled atom-light solitons, we replace the LG optical mode with a matching Bessel-Gaussian mode, as defined in Eqn. (3.41). κ_{BG} is chosen so that the size of the central ring of the BG mode matches that of the equivalent LG mode, as shown in Fig. 8.14.
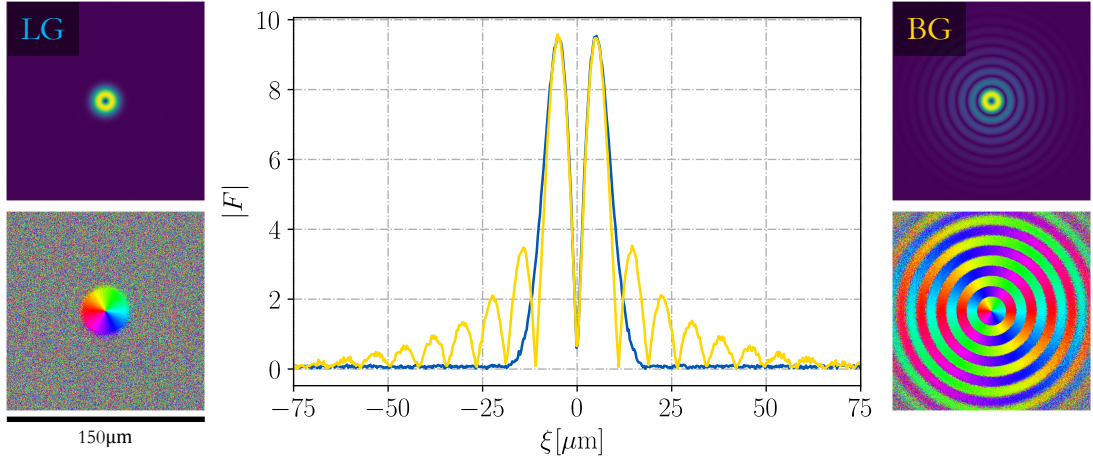
Figure 8.14: Transverse amplitude and phase distributions of a LG_1^0 mode (left, blue), as in Fig. 8.8, and matched BG mode (right, yellow). Centre shows comparison of mode cross sections.

BG beams are solutions to the paraxial wave equation that, by controlling the width of the Gaussian, encompass as limiting cases the diffraction-free Bessel beam and the Gaussian beam [122, 123]. Again, the formation of $2|m|$ coupled solitons is observed.

The diffractionless optical characteristics of the BG mode obtained when a minimum of three rings are present in the optical field, in comparison to the LG mode which diffracts, lead to a 1.2 factor increase of the length that the atoms are confined to the ring, and a decrease by more than a factor of 2 the radial spread of the solitons at $\zeta = 1$, shown in Fig. 8.15.
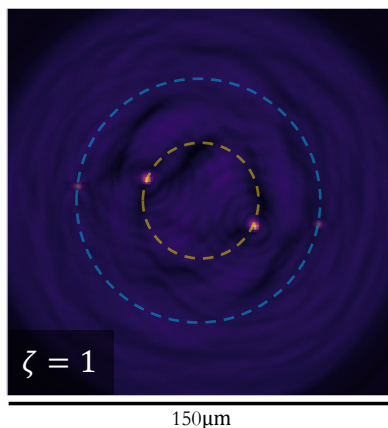
Figure 8.15: Atomic amplitude distributions, for initial modes of Fig. 8.14, at $\zeta = 1$. Soliton radius indicated for BG (yellow) and LG (blue) modes, with ratio 1:2.12.

If the scattering length of the BEC moves into moderately attractive interactions $\beta_{col} < 0$, radial soliton suppression is enhanced, with large portions of atomic density held around the optical ring. The solitons formed rotate azimuthally with constant velocity along the entire length of the atomic medium. Such a structure is reminiscent of a persistent current, with possible applications in the controllable generation of atomtronic devices such as atom-SQUIDs [198].

8.2.3 Scalar Mode Superpositions

The ability of coupled optical fields to guide ultracold atoms may be used to create counter-intuitive, customized atomic transverse distributions through tailored optical scalar mode superpositions. To exemplify the possibilities we consider two cases: creation of a ring mode of atoms, analogous to the intensity structure of a vortex soliton, and natural trapping of atomic clusters in optical darkness. In both cases, we consider 'dark-seeking' atoms arising from blue atom-field detuning.

Atomic Ring Mode Creation

To generate an atomic ring mode, we superimpose two LG modes: a Gaussian of waist $30\mu m$, and a ring mode, constructed with $p = 0$ and $m = 5$, of beam waist $60\mu m$. The initial amplitude for the Gaussian remains unchanged, with the outer ring half as intense, and $A_\psi = 0.2A_F$ to ensure the dipole forces are optically driven. The initial fields are shown in Fig 8.16.
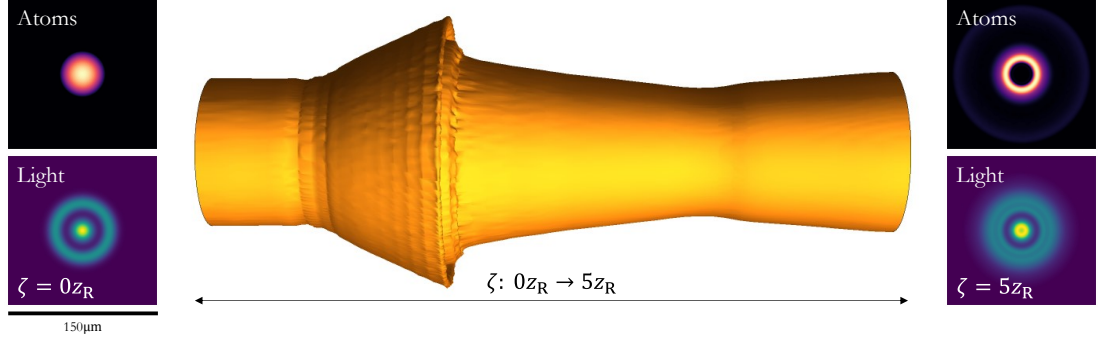
Figure 8.16: Atomic ring mode creation in optical darkness for blue atom-field detuning. Left and right: atomic (upper) and optical (lower) amplitude distributions at $\zeta = 0z_R$ (left) and $5z_R$ (right). Centre: atomic 3D distribution between $\zeta = 0z_R \rightarrow 5z_R$.

From the 3D rendering of the atomic dynamics for $\zeta = 0z_R \rightarrow 5z_R$, the BEC initially moves rapidly to optical darkness, before its repulsive interatomic collisions and natural kinetic dispersion drive it to the outer optical ring. Some atoms tunnel past this optical barrier and are ejected, but a large proportion ($\sim 75\%$) reflect back to become uniformly trapped in optical darkness, forming a uniform atomic vortex ring. This ring remains largely propagationally invariant up to $5z_R \approx 2mm$, with this mechanism effectively seeding an intensity structure akin to a 2D atomic vortex soliton [250, 251].

Dark Atomic Cluster Trapping

To generate naturally trapped atomic *clusters* in optical darkness, we superimpose two optical ring modes of beam waists $30\mu m$ and $60\mu m$, applying OAMs of $m = 2$ and 8, respectively. This generates six optical vortices around the mode minima, shown in Fig. 8.17, similar to an optical 'Ferris wheel' [63, 252]. When subjected to this initial optical field, the atomic field again moves to positions of optical darkness, in

this case forming seven clusters in the positions of the optical vortices. The atoms then begin to rotate, spiralling around the centre of each cluster in a similar manner to their red-detuned counterparts of Fig. 8.13, but in this case in atomic darkness. This phenomenon does not occur without OAM (propagating the modulus of the fields only), when the atoms are simply trapped in non-rotating clusters.
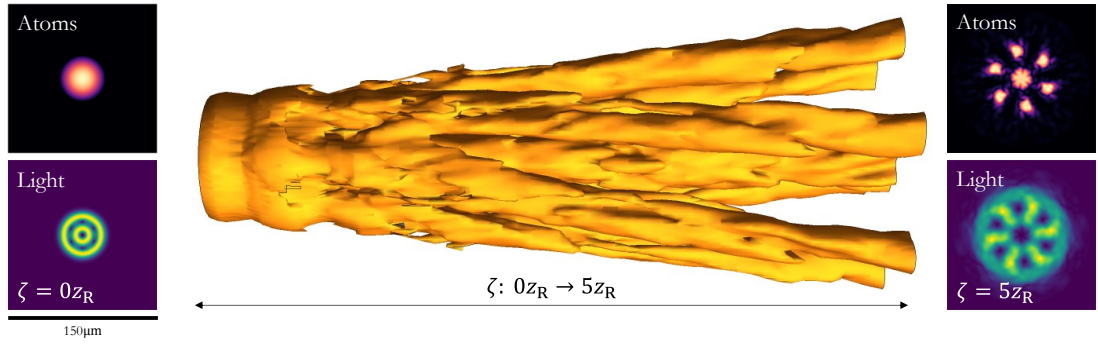
Figure 8.17: Atomic clusters trapped in optical darkness for blue atom-field detuning. Left and right: atomic (upper) and optical (lower) amplitude distributions at $\zeta = 0z_R$ (left) and $5z_R$ (right). Centre: atomic 3D distribution between $\zeta = 0z_R \rightarrow 5z_R$.

Our method therefore provides a means of re-shaping a BEC into a custom number of clusters, which are either coupled atom-light clusters in optical brightness, or atomic clusters in optical darkness. The dipole driven dynamics lead to a transfer of phase to the atoms, as summarised by Fig. 8.18, and cause the clusters to follow azimuthal rotational dynamics [242].
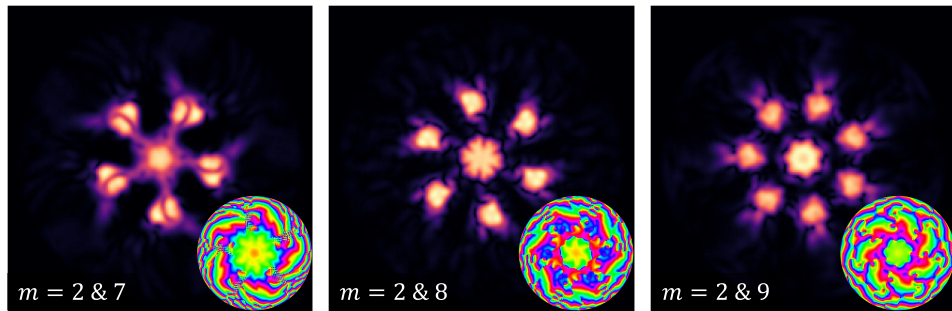
Figure 8.18: Atomic cluster amplitude and phase (inset) profiles at $\zeta = 5z_R$ for various optical OAM combinations indicated.

8.3 Conclusions and Outlook

In Chapter 8, we have built on the capacity for optically-induced atomic reshaping, showing how intensity-only optical ring modes enabled large atomic densities to be trapped in off-axis rings. By introducing structured helical phase to the optical field, cases of azimuthal atomic transport have been realised, using dipole forces to seed atomic azimuthal motion. With bright-seeking atoms, the atomic medium was observed to be acting as a Kerr-like superfluid, creating numbers of atom-light clusters proportional to $2|m|$. With dark seeking atoms, tailored scalar superpositions of optical modes were used to realise either atomic ring modes, or a customisable number of self-trapped atomic clusters, rotating due to the presence of OAM.

Our findings have immediate applications in any cases where a highly tuneable method of guiding ultracold atoms is required. This includes atomic trapping [25, 33, 253], where this method offers an alternative approach for guiding and holding atoms in positions of optical brightness or darkness, potentially offering an additional mechanism for matter wave Bessel beam creation [254]. Our results also suggest a customisable means of atomic transport [51, 243]. If additional control of the diffractive optical dynamics can be realised to extend the lifetime of such rotational behaviour, as suggested by findings with optical Bessel-Gaussian beams, atomic transverse manipulation into fixed radius rotating rings may become possible, for applications towards atomtronic device generation [198, 255, 256].

Part III

Ultracold Atomic and Optical Fields in an Optical Cavity

Chapter 9

Theory

In this chapter, we consider the evolution of coupled atomic and optical fields within a driven optical cavity. In *Section 9.1*, we introduce such a physical setup, outlining the differences with the co-propagation case considered in Chapters 5-8. In *Section 9.2*, we outline the changes to the nonlinear coupled equations required to model this system. We show that if the atomic response is instantaneous, the model again reduces to a single equation, equivalent to that for a Kerr cavity.

9.1 System of Interest

In Chapters 5-8, we considered the co-propagation of optical and ultracold atomic fields (Fig. 5.1). Now, we consider a driven optical cavity containing a stationary ultracold atomic medium. A schematic of the system of interest is given in Fig. 9.1.

An optical pump beam, F_P, enters a ring-cavity, comprising four highly reflective mirrors constructed in such a way that the circulating optical field encounters the stationary BEC, ψ, once per round trip. The BEC in the cavity takes a disk geometry in the transverse plane and is considered 'thin' in the longitudinal dimension, $L_\psi \approx 10^{-5}$m. It is held stationary in the centre of the optical cavity by additional trapping fields
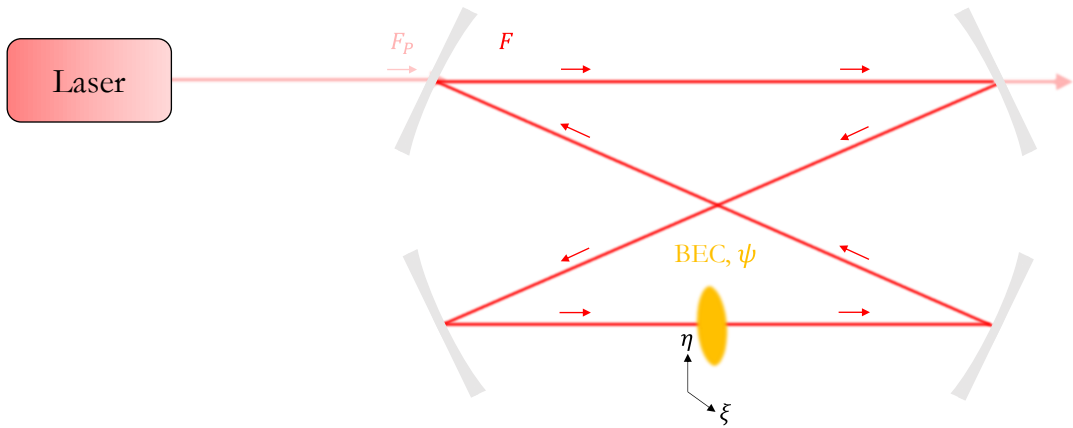
Figure 9.1: Proposed schematic of a driven optical ring cavity containing a BEC.

so that it has no mean atomic velocity, $v_a = 0$. In Chapter 10, we consider its initial structure to be homogeneous, whilst in Chapters 11-12 initial transverse structure is considered. We again consider a system of Caesium atoms, as in previous chapters, facilitating a variable scattering length. During the evolution of the optical field there is a small amount of optical field loss from the mirror interactions, but the continuously driven pump beam compensates for this during the evolution of the two fields.

We find that a transition to atom-light interactions occurring within a driven optical cavity, and the temporal control that this setup offers, opens a breadth of further realisations of atomic transport and trapping. However, before discussing them, we first consider the required alterations to the model for this second physical configuration.

9.2   Theoretical Model

To derive a model describing the interactions between the ultracold atomic and optical fields in a driven optical cavity, we follow the mean field approach of Refs. [107, 168]. First, it is necessary to re-derive the coupling between optical and atomic fields, described in Part II, for the case of a stationary ultracold atomic medium.

9.2.1 Coupling Between Optical and Atomic Fields

As outlined in Chapter 5, we consider an ultracold atomic medium consisting of ground and excited states as described by Eqns. (5.3)-(5.4), and an optical field as described by Eqn. (5.7). By making the substitution (5.8) to account for dense atomic media, we arrive at Eqns. (5.9)-(5.10), reproduced here for convenience:

$$(5.7): \quad \frac{2i\omega_\mathrm{L}n^2}{c^2}\partial_t A' = -\nabla^2 A' - \frac{\omega_\mathrm{L}^2 n^2}{c^2}A' - \frac{\omega_\mathrm{L}^2}{c^2\epsilon_0}\mu\Phi_\mathrm{g}'^*\Phi_\mathrm{e}'e^{i\Delta t}, \tag{9.1}$$

$$(5.9): \quad i\hbar\partial_t\Phi_\mathrm{g}' = -\frac{\hbar^2}{2m_\mathrm{a}}\nabla^2\Phi_\mathrm{g}' - \frac{1}{2}\mu A'^*\Phi_\mathrm{e}'e^{i\Delta t} - \frac{1}{2}\frac{\mu^2\Phi_\mathrm{g}'}{3\epsilon_0}|\Phi_\mathrm{e}'|^2 + \frac{4\pi\hbar^2 a_\mathrm{gg}}{m_\mathrm{a}}|\Phi_\mathrm{g}'|^2\Phi_\mathrm{g}',$$
$$\tag{9.2}$$

$$(5.10): \quad i\hbar\partial_t\Phi_\mathrm{e}' = -\frac{\hbar^2}{2m_\mathrm{a}}\nabla^2\Phi_\mathrm{e}' - \frac{1}{2}\mu A'\Phi_\mathrm{g}'e^{-i\Delta t} - \frac{1}{2}\frac{\mu^2\Phi_\mathrm{e}'}{3\epsilon_0}|\Phi_\mathrm{g}'|^2 - i\hbar\frac{\gamma}{2}\Phi_\mathrm{e}'. \tag{9.3}$$

As the atoms are now considered stationary, with a mean atomic velocity $v_\mathrm{a} = 0$, we now assume that the atomic ground and excited states can be written as

$$\Phi_\mathrm{g}' \to \Phi_\mathrm{g}(x,y,z,t), \tag{9.4}$$

$$\Phi_\mathrm{e}' \to \Phi_\mathrm{e}(x,y,z,t)e^{-i\Delta t} \tag{9.5}$$

where $\Delta = \omega_\mathrm{L} - \omega_\mathrm{a}$ is the detuning between the optical and atomic fields.

From Eqn. (9.5), we obtain

$$\frac{\partial\Phi_\mathrm{e}'}{\partial t} = \left(\frac{\partial\Phi_\mathrm{e}}{\partial t} - i\Delta\Phi_\mathrm{e}\right)e^{-i\Delta t},$$

and Eqns. (9.1)-(9.3) then become

$$\frac{2i\omega_\mathrm{L}n^2}{c^2}\partial_t A' = -\nabla^2 A' - \frac{\omega_\mathrm{L}^2 n^2}{c^2}A' - \frac{\omega_\mathrm{L}^2}{c^2\epsilon_0}\mu\Phi_\mathrm{g}^*\Phi_\mathrm{e}, \tag{9.6}$$

$$i\hbar\frac{\partial\Phi_\mathrm{g}}{\partial t} = -\frac{\hbar^2}{2m_\mathrm{a}}\nabla^2\Phi_\mathrm{g} - \frac{\mu}{2}A'^*\Phi_\mathrm{e} - \frac{\mu^2}{6\epsilon_0}|\Phi_\mathrm{e}|^2\Phi_\mathrm{g} + \frac{4\pi\hbar^2 a_\mathrm{gg}}{m_\mathrm{a}}|\Phi_\mathrm{g}|^2\Phi_\mathrm{g}, \tag{9.7}$$

$$i\hbar\frac{\partial\Phi_\mathrm{e}}{\partial t} = -\frac{\hbar^2}{2m_\mathrm{a}}\nabla^2\Phi_\mathrm{e} - \frac{\mu}{2}A'\Phi_\mathrm{g} - \frac{\mu^2}{6\epsilon_0}|\Phi_\mathrm{g}|^2\Phi_\mathrm{e} - i\hbar\frac{\gamma}{2}\Phi_\mathrm{e} - \hbar\Delta\Phi_\mathrm{e}. \tag{9.8}$$

As before (Eqn. (5.11)), the optical field takes the form

$$A' \to A(x, y, z, t)e^{ik_{\mathrm{L}}z},$$

with $k_{\mathrm{L}} = \omega_{\mathrm{L}}n/c$. The three field equations then become

$$\frac{2i\omega_{\mathrm{L}}n^2}{c^2}\frac{\partial A}{\partial t} = -\nabla_\perp^2 A - 2ik_{\mathrm{L}}\frac{\partial A}{\partial z} - \frac{\omega_{\mathrm{L}}^2\mu}{c^2\epsilon_0}\Phi_{\mathrm{g}}^*\Phi_{\mathrm{e}}e^{-ik_{\mathrm{L}}z}, \tag{9.9}$$

$$i\hbar\frac{\partial\Phi_{\mathrm{g}}}{\partial t} = -\frac{\hbar^2}{2m_{\mathrm{a}}}\nabla^2\Phi_{\mathrm{g}} - \frac{\mu}{2}A\Phi_{\mathrm{e}}e^{-ik_{\mathrm{L}}z} - \frac{\mu^2}{6\epsilon_0}|\Phi_{\mathrm{e}}|^2\Phi_{\mathrm{g}} + \frac{4\pi\hbar^2 a_{\mathrm{gg}}}{m_{\mathrm{a}}}|\Phi_{\mathrm{g}}|^2\Phi_{\mathrm{g}}, \tag{9.10}$$

$$i\hbar\frac{\partial\Phi_{\mathrm{e}}}{\partial t} = -\frac{\hbar^2}{2m_{\mathrm{a}}}\nabla^2\Phi_{\mathrm{e}} - \frac{\mu}{2}A\Phi_{\mathrm{g}}e^{ik_{\mathrm{L}}z} - \frac{\mu^2}{6\epsilon_0}|\Phi_{\mathrm{g}}|^2\Phi_{\mathrm{e}} - i\hbar\frac{\gamma}{2}\Phi_{\mathrm{e}} - \hbar\Delta\Phi_{\mathrm{e}}. \tag{9.11}$$

Performing an adiabatic elimination of the excited atomic state from the dynamics and again neglecting the term corresponding to spontaneous emission, we arrive at a description of the excited atomic state

$$\Phi_{\mathrm{e}} = -\frac{\mu A\Phi_{\mathrm{g}}}{2\hbar\Delta}e^{ik_{\mathrm{L}}z}\left(1 - \frac{\mu^2}{4\hbar^2\Delta^2}|A|^2 - \frac{\mu^2}{6\epsilon_0\hbar\Delta}|\Phi_{\mathrm{g}}|^2\right). \tag{9.12}$$

Details of the procedure used to reach this expression are given in Appendix B.1.

Substituting Eqn. (9.12) into the equations for the optical and ground state atomic fields, Eqns. (9.9) and (9.10), respectively,

$$i\frac{n}{c}\frac{\partial A}{\partial t} + i\frac{\partial A}{\partial z} + \frac{1}{2k_{\mathrm{L}}}\nabla_\perp^2 A = \frac{sk_{\mathrm{L}}\mu^2}{4n^2\epsilon_0\hbar|\Delta|}\left(1 - \left(\frac{\mu}{2\hbar|\Delta|}\right)^2|A|^2 - \frac{\mu^2}{6s\epsilon_0}|\Phi_{\mathrm{g}}|^2\right)|\Phi_{\mathrm{g}}|^2 A,$$

$$\tag{9.13}$$

$$i\frac{\partial\Phi_{\mathrm{g}}}{\partial t} + \frac{\hbar}{2m_{\mathrm{a}}}\nabla^2\Phi_{\mathrm{g}} = \left[s|\Delta|\left(\frac{\mu}{2\hbar|\Delta|}\right)^2\left(1 - \left(\frac{\mu}{2\hbar|\Delta|}\right)^2|A|^2 - \frac{\mu^2}{6\epsilon_0}|\Phi_{\mathrm{g}}|^2\right)|A|^2\right.$$

$$\left. - \frac{\mu^2}{6\hbar\epsilon_0}\left(\frac{\mu}{2\hbar|\Delta|}\right)^2\left(1 - \left(\frac{\mu}{2\hbar\Delta}\right)^2|A|^2 - \frac{\mu^2}{6\epsilon_0}|\Phi_{\mathrm{g}}|^2\right)^2|A|^2|\Phi_{\mathrm{g}}|^2 + \frac{4\pi\hbar a_{\mathrm{gg}}}{m_{\mathrm{a}}}|\Phi_{\mathrm{g}}|^2\right]\Phi_{\mathrm{g}},$$

$$\tag{9.14}$$

where s now represents the sign of Δ. Full details are provided in Appendix B.2.

We now introduce several re-scalings to simplify the form of Eqns. (9.13)-(9.14). We re-define a new atomic field variable, ψ, given by

$$\psi = \frac{\mu}{2n}\sqrt{\frac{k_{\mathrm{L}}}{\epsilon_0 \hbar |\Delta|}}\Phi_{\mathrm{g}}, \tag{9.15}$$

and a new optical field variable, F, given by

$$F = \frac{\mu}{2\hbar}\sqrt{\frac{1}{|\Delta|}}A. \tag{9.16}$$

Eqns. (9.13)-(9.14) then become

$$i\frac{n}{c}\frac{\partial F}{\partial t} + i\frac{\partial F}{\partial z} + \frac{1}{2k_{\mathrm{L}}}\nabla_{\perp}^2 F = s\left(1 - \frac{|F|^2}{|\Delta|}\right)|\psi|^2 F - \frac{2n^2}{3k_{\mathrm{L}}}|\psi|^4 F, \tag{9.17}$$

$$i\frac{\partial\psi}{\partial t} + \frac{\hbar}{2m_{\mathrm{a}}}\nabla^2\psi = s\left(1 - \frac{|F|^2}{|\Delta|} - \frac{2n^2}{3k_{\mathrm{L}}}|\psi|^2\right)|F|^2\psi$$

$$- \frac{2n^2}{3k_{\mathrm{L}}}\left(1 - \frac{|F|^2}{|\Delta|} - \frac{2n^2}{3k_{\mathrm{L}}}|\psi|^2\right)^2|F|^2|\psi|^2\psi + \frac{16\pi n^2\epsilon_0\hbar^2 a_{\mathrm{gg}}|\Delta|}{k_{\mathrm{L}}m_{\mathrm{a}}\mu^2}|\psi|^2\psi. \tag{9.18}$$

Finally, we introduce the parameters

$$\beta_{\mathrm{dd}} = \frac{2n^2}{3k_{\mathrm{L}}}, \tag{9.19}$$

and
$$\beta_{\mathrm{col}} = \frac{16\pi n^2\epsilon_0\hbar^2 a_{\mathrm{gg}}|\Delta|}{k_{\mathrm{L}}m_{\mathrm{a}}\mu^2}, \tag{9.20}$$

corresponding to the dipole-dipole and interatomic forces, respectively, to arrive at a set of coupled equations:

$$i\frac{n}{c}\frac{\partial F}{\partial t} + i\frac{\partial F}{\partial z} + \frac{1}{2k_{\mathrm{L}}}\nabla_{\perp}^2 F = s\left(1 - \frac{|F|^2}{|\Delta|}\right)|\psi|^2 F - \beta_{\mathrm{dd}}|\psi|^4 F, \tag{9.21}$$

$$i\frac{\partial\psi}{\partial t} + \frac{\hbar}{2m_{\mathrm{a}}}\nabla^2\psi = s\left(1 - \frac{|F|^2}{|\Delta|} - \beta_{\mathrm{dd}}|\psi|^2\right)|F|^2\psi$$

$$- \beta_{\mathrm{dd}}\left(1 - \frac{|F|^2}{|\Delta|} - \beta_{\mathrm{dd}}|\psi|^2\right)^2|F|^2|\psi|^2\psi + \beta_{\mathrm{col}}|\psi|^2\psi. \tag{9.22}$$

As in the propagation case, we consider terms in $|\Delta|^{-1}$ to be negligible, and recognise that $\beta_{dd}^2 \to 0$. This leaves us with the coupled equations

$$i\frac{n}{c}\frac{\partial F}{\partial t} + i\frac{\partial F}{\partial z} + \frac{1}{2k_L}\nabla_\perp^2 F = s|\psi|^2 F - \beta_{dd}|\psi|^4 F, \tag{9.23}$$

$$i\frac{\partial \psi}{\partial t} + \frac{\hbar}{2m_a}\nabla^2\psi = s|F|^2\psi - 2\beta_{dd}|F|^2|\psi|^2\psi + \beta_{col}|\psi|^2\psi. \tag{9.24}$$

These equations take a similar form to Eqns. (5.55)-(5.56) of Ref. [33], as derived in Part II, but contain different scalings of the fields, and different definitions of the system parameters.

9.2.2 Atom-Light Interactions in a Driven Optical Cavity

We now perform a mean field derivation, following the procedures of Refs. [107, 168] to describe the interactions of a stationary ultracold atomic medium and an optical field, as described by Eqns. (9.23)-(9.24), where the interactions occur within a driven optical cavity.

We consider a cavity of length $\mathcal{L}$, with the ultracold atomic medium of length L, where $\mathcal{L} >> L$, ensuring a BEC of disk-like geometry. For simplicity we write Eqn. (9.23) as

$$\frac{n}{c}\frac{\partial F}{\partial t} + \frac{\partial F}{\partial z} = i\nu\nabla_\perp^2 F - i\varsigma F, \tag{9.25}$$

where
$$\nu = \frac{1}{2k_L}, \tag{9.26}$$

and
$$\varsigma = s|\psi|^2 - \beta_{dd}|\psi|^4, \tag{9.27}$$

providing a generic nonlinear Schrödinger equation description of the optical field dynamics, similar to Eqn. (3.27).

The cavity is driven with an injected transverse field $F_P(x, y)$, as outlined in Fig. 9.1. The output mirror has very high reflectivity R, and so the transmittivity, T, defined as $T = 1 - R$, will be very close to 0.

Setting $z = 0$ to be the entry point to the atomic medium, we apply the longitudinal boundary condition that

$$F(x, y, 0, t) = e^{\mathcal{D}} A\left(x, y, L, t - \frac{\mathcal{L} - L}{c}\right) + \sqrt{T} F_{\mathrm{P}}(x, y), \tag{9.28}$$

where
$$\mathcal{D} = \ln \sqrt{R} - i\delta + i(\mathcal{L} - L)\nu \nabla_{\perp}^2, \tag{9.29}$$

$$\delta = \frac{(\omega_{\mathrm{c}} - \omega_{\mathrm{P}})\mathcal{L}}{c}, \tag{9.30}$$

and ω_{c} is the longitudinal cavity mode frequency closest to the input frequency ω_{P}.

We now perform the mean field transformation on temporal and longitudinal variables z and t, respectively. We define

$$z' = z, \tag{9.31}$$

$$t' = t + \left[\frac{\mathcal{L} - L}{c}\right] \frac{z}{L}. \tag{9.32}$$

The partial derivatives of these transformations are given by

$$\partial_{z'} = \partial_z - \left[\frac{\mathcal{L} - L}{c}\right] \frac{1}{L} \partial_{t'}, \tag{9.33}$$

$$\partial_{t'} = \partial_t. \tag{9.34}$$

Using Eqn. (9.28), we define
$$\Gamma = \exp\left(\frac{\mathcal{D}z}{L}\right) \tag{9.35}$$

to introduce a new circulatory optical field

$$F' = \Gamma F + \frac{\sqrt{T}z}{L} F_{\mathrm{P}}. \tag{9.36}$$

Combining Eqn. (9.25) with Eqns. (9.35)-(9.36),

$$\frac{n}{c}\partial_t F' + \partial_z F' = \frac{n}{c}\partial_t \left[\Gamma F + \frac{\sqrt{T}z}{L} F_{\mathrm{P}}\right] + \partial_z \left[\Gamma F + \frac{\sqrt{T}z}{L} F_{\mathrm{P}}\right],$$

$$= \frac{n}{c}\Gamma\partial_t F + \frac{\mathcal{D}}{L}\Gamma F + \Gamma\partial_z F + \frac{\sqrt{T}}{L}F_{\mathrm{P}},$$

$$= \frac{\mathcal{D}}{L}\Gamma F + \Gamma\left(\frac{n}{c}\partial_t F + \partial_z F\right) + \frac{\sqrt{T}}{L}F_{\mathrm{P}},$$

$$= \frac{\mathcal{D}}{L}\left(F' - \frac{\sqrt{T}z}{L}F_{\mathrm{P}}\right) + \Gamma\left(i\nu\nabla_\perp^2 F - i\varsigma F\right) + \frac{\sqrt{T}}{L}F_{\mathrm{P}}, \tag{9.37}$$

which, applying Eqns. (9.31)-(9.34), gives

$$\left(\frac{n}{c} + \left[\frac{\mathcal{L}-L}{c}\right]\frac{1}{L}\right)\partial_{t'}F' + \partial_{z'}F' = \frac{\mathcal{D}}{L}\left(F' - \frac{\sqrt{T}z}{L}F_{\mathrm{P}}\right) + \Gamma\left(i\nu\nabla_\perp^2 F - i\varsigma F\right)$$
$$+ \frac{\sqrt{T}}{L}F_{\mathrm{P}},$$

$$\Rightarrow \qquad \left[\frac{\mathcal{L}+L(n-1)}{cL}\right]\partial_{t'}F' + \partial_{z'}F' = \frac{\mathcal{D}}{L}\left(F' - \frac{\sqrt{T}z}{L}F_{\mathrm{P}}\right) + \Gamma\left(i\nu\nabla_\perp^2 F - i\varsigma F\right)$$
$$+ \frac{\sqrt{T}}{L}F_{\mathrm{P}}. \tag{9.38}$$

The mean field limit requires that T is very small, and so $\sqrt{R} \approx \sqrt{1-T} \approx 1 - T/2$ and $\ln\sqrt{R} \approx \ln(1 - T/2) \approx -T/2$. Eqn. (9.29) then becomes

$$\mathcal{D} \approx -\frac{T}{2} - i\delta + i(\mathcal{L} - L)\nu\nabla_\perp^2, \tag{9.39}$$

and Eqn. (9.35) becomes

$$\Gamma \approx 1 + \frac{\mathcal{D}z}{L}. \tag{9.40}$$

Using Eqns. (9.39)-(9.40), we may re-write Eqn. (9.38) as

$$\left[\frac{\mathcal{L}+L(n-1)}{cL}\right]\partial_{t'}F' + \partial_{z'}F' = \frac{\mathcal{D}}{L}\left(F' - \frac{\sqrt{T}z}{L}F_{\mathrm{P}}\right) + \Gamma\left(i\nu\nabla_\perp^2 F - i\varsigma F\right) + \frac{\sqrt{T}}{L}F_{\mathrm{P}},$$

$$= \frac{1}{L}\left(F' - \frac{\sqrt{T}z}{L}F_{\mathrm{P}}\right)\left(-\frac{T}{2} - i\delta + i(\mathcal{L} - L)\nu\nabla_\perp^2\right)$$

$$+ \left(i\nu\nabla_\perp^2\Gamma F - i\varsigma\Gamma F\right) + \frac{\sqrt{T}}{L}F_{\mathrm{P}},$$

and by again applying Eqn. (9.36) to the second line, we obtain

$$\left[\frac{\mathcal{L} + L(n-1)}{cL}\right]\partial_{t'}F' + \partial_{z'}F' = \frac{1}{L}\left(F' - \frac{\sqrt{T}z}{L}F_{\mathrm{P}}\right)\left(-\frac{T}{2} - i\delta + i(\mathcal{L} - L)\nu\nabla_{\perp}^2\right)$$
$$+ \left(i\nu\nabla_{\perp}^2\left(F' - \frac{\sqrt{T}z}{L}F_{\mathrm{P}}\right) - i\varsigma\left(F' - \frac{\sqrt{T}z}{L}F_{\mathrm{P}}\right)\right) + \frac{\sqrt{T}}{L}F_{\mathrm{P}}.$$

$$(9.41)$$

Considering only the first order terms in Eqn. (9.41),

$$\left[\frac{\mathcal{L} + L(n-1)}{cL}\right]\partial_{t'}F' + \partial_{z'}F' = \frac{1}{L}\left(-\frac{T}{2} - i\delta + i(\mathcal{L} - L)\nu\nabla_{\perp}^2\right)F' + i\nu\nabla_{\perp}^2 F' - i\varsigma F'$$
$$+ \frac{\sqrt{T}}{L}F_{\mathrm{P}},$$
$$= \frac{1}{L}\left(-\frac{T}{2} - i\delta\right)F' + i\frac{\mathcal{L}}{L}\nu\nabla_{\perp}^2 F' - i\varsigma F' + \frac{\sqrt{T}}{L}F_{\mathrm{P}},$$
$$= \frac{T}{2L}\left(-1 - i\frac{2\delta}{T}\right)F' + i\frac{\mathcal{L}}{L}\nu\nabla_{\perp}^2 F' - i\varsigma F' + \frac{\sqrt{T}}{L}F_{\mathrm{P}}.$$

$$(9.42)$$

Expanding Eqn. (9.42) in longitudinal Fourier modes, and retaining only the mode closest to w_{P}, where the term $\partial_{z'}F' = 0$, gives

$$\left[\frac{\mathcal{L} + L(n-1)}{c}\right]\partial_{t'}F' = \frac{T}{2}\left(-1 - i\frac{2\delta}{T}\right)F' + i\mathcal{L}\nu\nabla_{\perp}^2 F' - i\varsigma L F' + \sqrt{T}F_{\mathrm{P}},$$
$$= \frac{T}{2}\left[\left(-1 - i\frac{2\delta}{T}\right)F' + i\frac{2\mathcal{L}\nu}{T}\nabla_{\perp}^2 F' - i\frac{2L\varsigma}{T}F' + \frac{2}{\sqrt{T}}F_{\mathrm{P}}\right],$$
$$\Rightarrow \qquad \partial_{t'}F' = \kappa\left[-(1 + i\theta)F' + i\nu'\nabla_{\perp}^2 F' - i\frac{2L\varsigma}{T}F' + F_{\mathrm{P}}'\right], \qquad (9.43)$$

where we have introduced the terms

$$\kappa = \frac{cT}{2\left(\mathcal{L} + L(n-1)\right)}, \qquad (9.44)$$

$$\theta = \frac{2\delta}{T}, \qquad (9.45)$$

$$\nu' = \frac{2\mathcal{L}\nu}{T}, \qquad (9.46)$$

and
$$F_{\mathrm{P}}' = \frac{2}{\sqrt{T}} F_{\mathrm{P}} \tag{9.47}$$

to obtain a generic form of the Lugiato-Lefever equation [168].

For the specific case of a BEC, we now re-introduce the nonlinear contributions to the optical field from the atomic field in a parameter ζ, Eqn. (9.27). In this case, Eqn. (9.43) takes the form

$$\partial_{t'} F' = \kappa \left[-\left(1 + i\theta\right) F' + i\nu' \nabla_{\perp}^2 F' - i\frac{2L}{T} \left(s|\psi|^2 - \beta_{\mathrm{dd}}|\psi|^4 \right) F' + F_{\mathrm{P}}' \right]. \tag{9.48}$$

The coupled atomic field was last described in Eqn. (9.24) as

$$i\frac{\partial \psi}{\partial t} + \frac{\hbar}{2m_{\mathrm{a}}} \nabla^2 \psi = s|F|^2\psi - 2\beta_{\mathrm{dd}}|F|^2|\psi|^2\psi + \beta_{\mathrm{col}}|\psi|^2\psi.$$

We recall that the optical field was transformed from $F \to F'$ according to Eqn. (9.36), and, as we went on to expand in longitudinal modes, terms in ∂_z will be zero. Furthermore, as in the mean field limit T is small, the definition of Γ may be approximated subject to Eqn. (9.40). The second term is again neglected by the mode expansion, which leads to a simple relationship linking the two fields:

$$F' \approx F. \tag{9.49}$$

Transforming the temporal derivative of Eqn. (9.24) from $t \to t'$, and applying Eqn. (9.34), gives

$$i\partial_{t'}\psi + \frac{\hbar}{2m_{\mathrm{a}}} \nabla_{\perp}^2 \psi = s|F'|^2\psi - 2\beta_{\mathrm{dd}}|F'|^2|\psi|^2\psi + \beta_{\mathrm{col}}|\psi|^2\psi. \tag{9.50}$$

Finally, as in Part II, we introduce a term in the atomic dynamics corresponding to three-body atomic losses. The evolution of the atomic field is then given by

$$\partial_{t'}\psi = i\frac{\hbar}{2m_{\mathrm{a}}} \nabla_{\perp}^2 \psi - i \left(s|F'|^2\psi - 2\beta_{\mathrm{dd}}|F'|^2|\psi|^2\psi + \beta_{\mathrm{col}}|\psi|^2\psi - iL_3|\psi|^4\psi \right). \tag{9.51}$$

Combining Eqns. (9.48) and (9.51) provides the dynamics of a stationary ultracold atomic field and an optical field, within a driven optical cavity, described by

$$\partial_{t'} F' = \kappa \left[-(1+i\theta) F' + i\nu' \nabla_\perp^2 F' - i\frac{2L}{T} \left(s|\psi|^2 - \beta_{\mathrm{dd}}|\psi|^4 \right) F' + F'_{\mathrm{P}} \right], \tag{9.52}$$

$$\partial_{t'} \psi = i\frac{\hbar}{2m_{\mathrm{a}}} \nabla_\perp^2 \psi - i \left(s|F'|^2 \psi - 2\beta_{\mathrm{dd}}|F'|^2|\psi|^2 \psi + \beta_{\mathrm{col}}|\psi|^2 \psi - iL_3|\psi|^4 \psi \right). \tag{9.53}$$

For the consideration of spatially defined fields in later sections of this thesis, we now scale the transverse spatial variables as in Part II:

$$(\xi, \eta) = \frac{\sqrt{2}(x, y)}{w_{\mathrm{L}}}, \tag{9.54}$$

with w_{L} a characteristic waist size of the optical beam. Eqns. (9.52)-(9.53) then become

$$\partial_{t'} F' = \kappa \left[-(1+i\theta) F' + i\frac{2\nu'}{w_{\mathrm{L}}^2} \nabla_\perp^2 F' - i\frac{2L}{T} \left(s|\psi|^2 - \beta_{\mathrm{dd}}|\psi|^4 \right) F' + F'_{\mathrm{P}} \right], \tag{9.55}$$

$$\partial_{t'} \psi = i\frac{\hbar}{m_{\mathrm{a}} w_{\mathrm{L}}^2} \nabla_\perp^2 \psi - i \left(s|F'|^2 \psi - 2\beta_{\mathrm{dd}}|F'|^2|\psi|^2 \psi + \beta_{\mathrm{col}}|\psi|^2 \psi - iL_3|\psi|^4 \psi \right). \tag{9.56}$$

We also introduce a rescaled time $\tau = \kappa t'$, where for $n = 1$

$$\tau = \frac{cT}{2\mathcal{L}} t', \tag{9.57}$$

to arrive at the coupled equations

$$\partial_\tau F' = -(1+i\theta) F' + i\frac{2\nu'}{w_{\mathrm{L}}^2} \nabla_\perp^2 F' - i\frac{2L}{T} \left(s|\psi|^2 - \beta_{\mathrm{dd}}|\psi|^4 \right) F' + F'_{\mathrm{P}}, \tag{9.58}$$

$$\partial_\tau \psi = \kappa^{-1} \left[i\frac{\hbar}{m_{\mathrm{a}} w_{\mathrm{L}}^2} \nabla_\perp^2 \psi - i \left(s|F'|^2 \psi - 2\beta_{\mathrm{dd}}|F'|^2|\psi|^2 \psi + \beta_{\mathrm{col}}|\psi|^2 \psi - iL_3|\psi|^4 \psi \right) \right]. \tag{9.59}$$

By rescaling the two fields according to

$$F'' = w_{\mathrm{L}} \sqrt{\frac{m_{\mathrm{a}}}{\hbar}} F', \tag{9.60}$$

$$\psi' = w_\mathrm{L} \sqrt{k_\mathrm{L}} \psi, \tag{9.61}$$

we obtain the coupled equations

$$\partial_\tau F'' = - \left(1 + i\theta\right) F'' + i\frac{2\nu'}{w_\mathrm{L}^2} \nabla_\perp^2 F'' - i\frac{2L}{T} \frac{1}{k_\mathrm{L} w_\mathrm{L}^2} \left(s|\psi'|^2 - \frac{1}{k_\mathrm{L} w_\mathrm{L}^2} \beta_\mathrm{dd} |\psi'|^4 \right) F''$$

$$+ w_\mathrm{L} \sqrt{\frac{m_\mathrm{a}}{\hbar}} F'_\mathrm{P}, \tag{9.62}$$

$$\partial_\tau \psi' = \frac{\hbar}{m_\mathrm{a} w_\mathrm{L}^2} \kappa^{-1} \left[i\nabla_\perp^2 \psi' - i\left(s|F''|^2 \psi' - \frac{2}{k_\mathrm{L} w_\mathrm{L}^2} \beta_\mathrm{dd} |F''|^2 |\psi'|^2 \psi' + \frac{m_\mathrm{a}}{\hbar k_\mathrm{L}} \beta_\mathrm{col} |\psi'|^2 \psi' \right.\right.$$

$$\left.\left. - i\frac{m_\mathrm{a}}{\hbar k_\mathrm{L}^2 w_\mathrm{L}^2} L_3 |\psi'|^4 \psi' \right) \right]. \tag{9.63}$$

We now introduce the new parameters

$$\beta'_\mathrm{col} = \frac{m_\mathrm{a}}{\hbar k_\mathrm{L}} \beta_\mathrm{col}, \qquad \beta'_\mathrm{dd} = \frac{1}{k_\mathrm{L} w_\mathrm{L}^2} \beta_\mathrm{dd}, \qquad L'_3 = \frac{m_\mathrm{a}}{\hbar k_\mathrm{L}^2 w_\mathrm{L}^2} L_3,$$

$$\alpha_{\psi'} = \frac{\hbar}{m_\mathrm{a} w_\mathrm{L}^2}, \qquad \alpha_{F''} = \frac{2\nu'}{w_\mathrm{L}^2}, \qquad F''_\mathrm{P} = w_\mathrm{L} \sqrt{\frac{m_\mathrm{a}}{\hbar}} F'_\mathrm{P}, \tag{9.64}$$

and, for convenience, neglect prime notation to obtain coupled nonlinear equations that describe the temporal evolution of an optical field F, within a driven (F_P) optical ring cavity, which interacts with a stationary ultracold atomic field ψ once per round trip:

$$\partial_\tau F = - \left(1 + i\theta\right) F + i\alpha_F \nabla_\perp^2 F - i\frac{2L}{T k_\mathrm{L} w_\mathrm{L}^2} \left(s|\psi|^2 - \beta_\mathrm{dd} |\psi|^4 \right) F + F_\mathrm{P}, \tag{9.65}$$

$$\partial_\tau \psi = \frac{\alpha_\psi}{\kappa} \left[i\nabla_\perp^2 \psi - i\left(s|F|^2 - 2\beta_\mathrm{dd} |F|^2 |\psi|^2 + \beta_\mathrm{col} |\psi|^2 - iL_3 |\psi|^4 \right) \psi \right]. \tag{9.66}$$

The model provided by Eqns. (9.65)-(9.66) again has a '2D+1' dimensionality, as in Part II, but with the two transverse dimensions (ξ, η) now evolving in the temporal domain τ, defined in Eqns. (9.32) and (9.57). We summarise the various terms and parameters within this model in Appendix C.

We note that it is generally optimal, but not necessary, to consider $\alpha_F, \alpha_\psi/\kappa \approx 1$. Under these limits, we see that

$$\frac{2\mathcal{L}}{k_{\mathrm{L}} w_{\mathrm{L}}^2 T} = 1,$$

$$\Rightarrow \qquad\qquad \frac{\mathcal{L}}{z_{\mathrm{R}} T} = 1, \qquad\qquad (9.67)$$

and $\qquad\qquad \dfrac{2\hbar\mathcal{L}}{m_{\mathrm{a}} w_{\mathrm{L}}^2 c T} = 1, \qquad\qquad (9.68)$

which places conditions upon the experimental parameters. For example, with a selection of $\mathcal{L} \approx 10^{-2}$m, $T \approx 10^{-2}$, and $w_{\mathrm{L}} \approx 480\mu$m, α_F remains unitary with realistic parameter selections. We emphasise that this is not a physical requirement of the system, and simply represents one potential operating regime.

As in Eqn. (7.3), Eqn. (9.66) provides a Gross-Pitaevskii based description of the temporal dynamics of the ultracold atomic field ψ. Again, it includes the terms $i\nabla_\perp^2 \psi$ representing the kinetic energy contributions of the BEC atoms, $s|F|^2$ representing a dipole induced focusing or defocusing dependent on the sign of the detuning s, $\beta_{\mathrm{col}}|\psi|^2$ representing interatomic scattering between the BEC atoms controlled by β_{col}, and $-iL_3|\psi|^4$ representing the contributions of three-body atomic loss.

Eqn. (9.65) provides a Lugiato-Lefever based description of the temporal evolution of the circulating optical field F [107, 168]. As in Eqn. (7.4), it includes the term $i\nabla_\perp^2 F$ representing the field's diffraction, with $s|\psi|^2$ representing a dipole induced focusing or defocusing nonlinearity dependent on the sign of the detuning s. However, it also now includes a term in F_{P}, which represents contributions from an optical pump that drives the cavity, and the terms $[-(1 + i\theta) F]$, loss and detuning terms respectively.

9.2.3   Optical-Only Reduction

In a similar approach to that outlined in Chapter 5.2.2, Eqns. (9.65)-(9.66) may be reduced through a further adiabatic procedure that assumes an instantaneous atomic medium. Under these conditions, the atomic medium may be related to the optical

field through Eqn. (5.58):

$$|\psi|^2 = -\frac{s}{\beta_{\text{col}}}|F|^2.$$

We emphasise that, as discussed around Eqn. (5.58), restrictions upon the selections of s and β_{col} exist when applying this reduction to ensure that Eqn. (5.58) remains valid.

Substituting this into Eqn. (9.65), we obtain

$$\partial_\tau F = F_{\text{P}} - (1 + i\theta)\, F + i\nabla_\perp^2 F + i\frac{|F|^2}{\beta_{\text{col}}}F, \tag{9.69}$$

where we recognise that $s^2 \equiv 1$.

Eqn. (9.69) provides a Kerr-like description of the circulating optical field [107, 168], with the medium's nonlinear strength again proportional to $1/\beta_{\text{col}}$. When $\beta_{\text{col}} > 0$, the optical field evolves in a self-focusing Kerr cavity, and, when $\beta_{\text{col}} < 0$, the optical field evolves in a self-defocusing Kerr cavity. This relationship is analogous to the familiar Lugiato-Lefever description of optical dynamics within a driven optical cavity [168].

9.3 Conclusions and Outlook

In Chapter 9, we considered an alternative physical setup of a driven optical ring cavity containing a BEC. Following the mean-field approach, we derived Eqns. (9.65)-(9.66) that describe the evolution of the two optical and atomic fields involved.

In the remaining chapters of this section, we will consider the effects of a variety of initial field structures. We begin by considering the dynamics of both fields when initially homogeneous (Chapter 10), before considering a variety of initially structured field forms, grouped predominantly with blue atom-field detuning (Chapter 11) and then latterly red atom-field detuning (Chapter 12).

Chapter 10

Homogeneous Fields

In this chapter, we consider the coupled dynamics of atomic and optical fields under initially homogeneous conditions, with the interactions occurring within an optical cavity as described by Chapter 9. In *Section 10.1*, we report on the realisation of coupled, interleaved spontaneous pattern formation in both fields for blue atom-field detuning. In *Section 10.2*, we specifically consider regions of bistability between homogeneous and pattern states within the system, and report on several realisations of hysteresis cycles in both atomic and optical fields. In *Section 10.3*, we consider the far broader regions of monostable solutions within the system, and report on the breadth of spontaneous pattern types we realise in both atomic and optical fields. Finally, in *Section 10.4*, we report on the realisation of coupled, or interleaved, atom-light cavity solitons, for both blue and red atom-field detuning.

10.1   Spontaneous Pattern Formation

We consider the co-evolution of optical and atomic fields, described by Eqns. (9.65)-(9.66), with initially homogeneous BEC and optical pumps, similar to the procedure followed for co-propagating homogeneous fields in Chapter 6. Here, the optical pump

amplitude is decreased to $A_P = 3$ given its driven, rather than single pass, nature. We also lower the initial BEC amplitude to $A_\psi = 0.1$, thereby accounting for the updated atomic field normalisation condition of Eqn. (9.61) to maintain a similar atom number to that considered in Part II. We again apply noise to the initial BEC, ψ, and optical, F, fields at the 1% level of A_ψ in both cases (such that the initial optical field solely contains noise).

Our parameter selection remains designed to represent a BEC of Caesium atoms, allowing exploitation of the wide range of scattering lengths accessible around its Feshbach resonance [232, 238]. We initially select $\beta_{\mathrm{col}} = 0.25$, corresponding to weakly repulsive interactions of $a_{\mathrm{gg}} \approx 1.5 a_0$, to ensure that repulsive atomic interactions do not dominate the system. We maintain a three body loss selection of $L_3 \approx 10^{-4}$, and select $s = 1$, representing blue atom-field detuning, with atoms (as in the propagation case) attracted to positions of optical darkness. We begin by considering the case of $\mathcal{L} \approx 10^{-2}$m and $T \approx 10^{-2}$, such that $\kappa^{-1} \approx 10^{-8}$.

Under these conditions, the fields behave as shown in Fig. 10.1, where we observe signatures of coupled spontaneous pattern formation in both atomic and optical fields for a range of different selections of the cavity detuning parameter, θ.
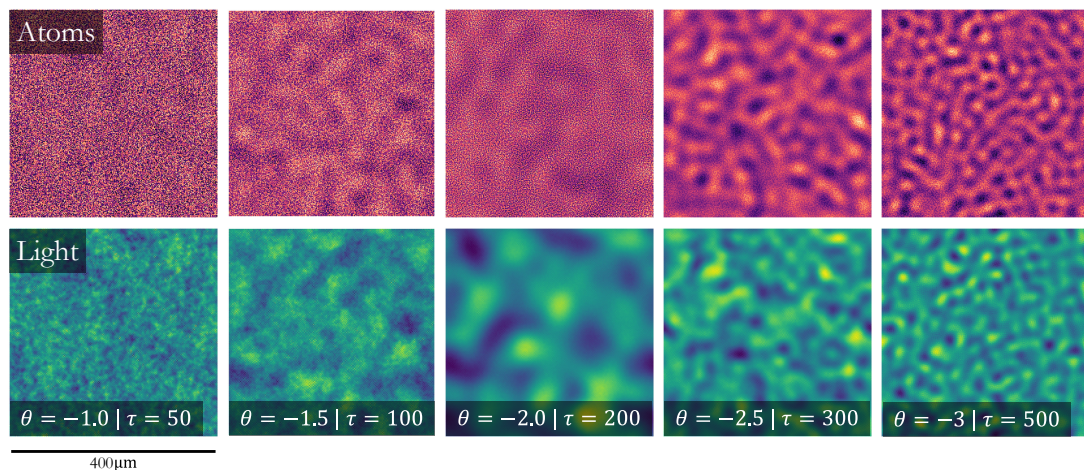
Figure 10.1: BEC (upper) and optical (lower) transverse distributions at τ and θ-values indicated. Fixed parameters: $\beta_{\mathrm{col}} = 0.25, A_P = 3, L_3 = 0.00022, s = 1, A_\psi = 0.1$. Each field is plotted between minimum and maximum amplitude.

Although pattern formation clearly occurs in Figure 10.1, their clarity is rather limited, particularly for θ selections that lie closer to zero. We find that the κ parameter within the numerical model of Eqns. (9.65)-(9.66) acts as an effective control upon the pattern clarity, with this improved the closer κ^{-1} lies to 1. From Eqn. (9.57),

$$\kappa^{-1} = \frac{2\mathcal{L}}{cT}, \qquad (10.1)$$

and it follows that the limit $\kappa^{-1} \to 1$ may be realised by either a decrease in the transmittivity of the mirrors forming the cavity (T), an increase in the length of the cavity ($\mathcal{L}$), or a combination of both.

We now justify our selection of this regime by demonstrating the potential capabilities for enhanced ultracold atomic pattern formation within it. Increasing the initial BEC amplitude to $A_\psi = 2$ to ensure that it also contributes to the dipole nonlinearity between the fields, returning the scattering length to an initially similar value to that used in Part II of $\beta_{\mathrm{col}} = 2$, corresponding to weakly repulsive interactions of $a_{\mathrm{gg}} \approx 12a_0$, and with all other procedures remaining as already outlined, we find that significantly enhanced pattern formation becomes readily accessible, as shown in Fig. 10.2 for the case of $\kappa^{-1} \approx 10^{-1}$.
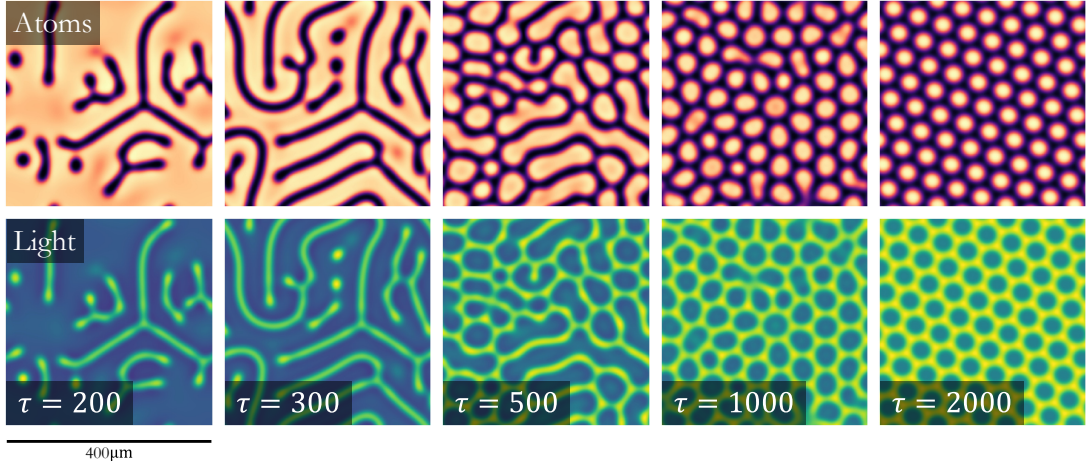
Figure 10.2: BEC (upper) and optical (lower) transverse distributions at τ-values indicated. Fixed parameters: $\theta = -1, \beta_{\mathrm{col}} = 2, A_{\mathrm{P}} = 3, L_3 = 0.00022, s = 1, A_\psi = 2$. Each field is plotted between 0 and maximum amplitude.

For this specific parameter selection, we observe a progressive pattern evolution through transient coupled spots and stripes, then labyrinths, before settling on a steady pattern of broad atomic clusters and coupled optical hexagons by $\tau = 2000$. We find that these patterns persist past $\tau = 10^4$.

We also consider the same dynamics in a one dimensional (1D) reduction, in a similar approach to that used in Ref. [155] where peaks and holes formed, providing an indication of the pattern wavelength of the full two 2D system throughout its evolution. Unlike in earlier chapters of this thesis, where a reduction to 1D reflected a reduction to a single azimuthal dimension around a transverse ring, here it simply represents a reduction to one transverse dimension, still of length 400μm, which we label as ξ. Again, we use the description provided by Eqns. (9.65)-(9.66) and identical parameters to those of Fig. 10.2. The evolution of such 1D atomic and optical fields to $\tau = 2000$ are shown in Fig. 10.3.
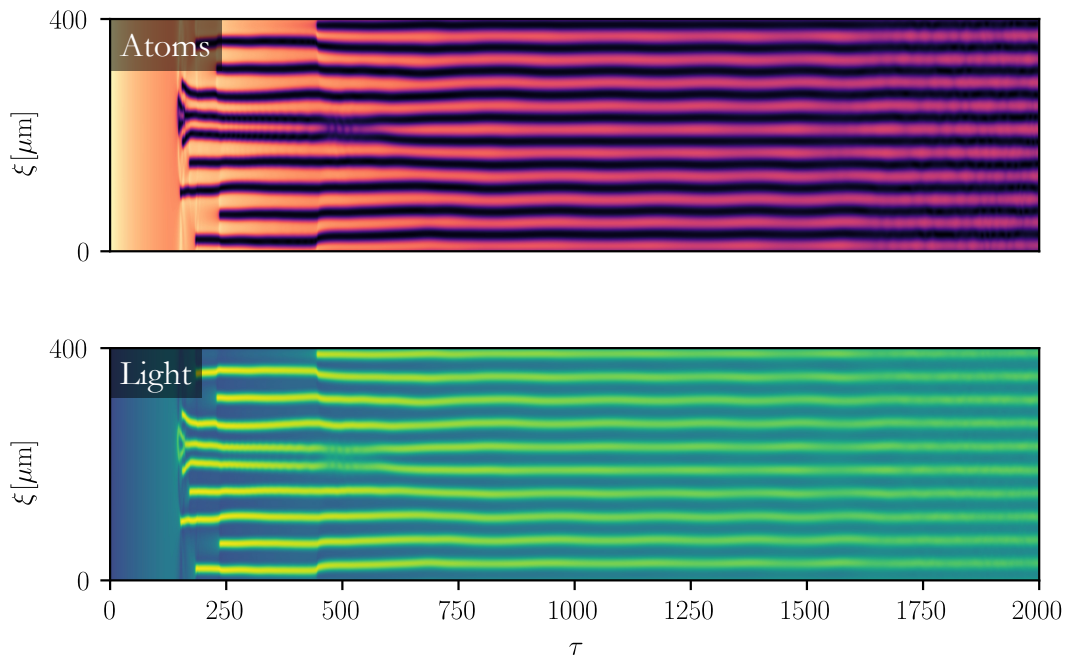
Figure 10.3: BEC (upper) and optical (lower) 1D field evolution between $\tau = 0 \rightarrow 2000$ to match 2D panels of Fig. 10.2. Fixed parameters: $\theta = -1, \beta_{\text{col}} = 2, A_{\text{P}} = 3, L_3 = 0.00022, s = 1, A_\psi = 2$. Each field is plotted between 0 and maximum amplitude.

We find that the 1D reduction here provides an excellent analogue of the full 2D process,

and observe the onset of patterns for $\tau \approx 175$ in both cases. In 2D, these patterns are spots and stripes, whereas in 1D they are a set of optical peaks and atomic minima. The region of these patterns grows in 1D, similar to 2D, with further peak-minima structures spontaneously appearing. Shortly before $\tau = 500$, the system enters a new regime in both 2D and 1D. In 2D, this corresponded to the onset of a larger, labyrinth-like pattern, with the stripes progressively joining together. In 1D, we have entered a more organised region of peak-minima structures. Over the remaining evolution to $\tau = 2000$ the spacing between the peak-minima structures in 1D steadily becomes more uniform, reflective of the 2D re-organisation into atomic cluster and optical hexagon structures, with the number of 1D structures closely matching the number of 2D cluster-hexagons.

The ability of the system to form spontaneous coupled atom-light patterns in both 2D and 1D, as demonstrated across Figs. 10.1-10.3, opens the potential of a number of physical phenomena to also be accessible within this system, including bistable solutions that demonstrate hysteresis, a plethora of transverse pattern formations across both coupled fields, and the presence of cavity solitons. Over the next sections of this chapter, we explore each case in turn.

10.2   Bistability

Considering further the presence of potential bistable solutions between homogeneous and pattern states within Eqns. (9.65)-(9.66) when $\kappa^{-1} \approx 10^{-1}$, we now use the static assumption reached in Eqn. (9.69) to obtain stationary solutions following the form

$$A_\mathrm{P} = (1 + i\theta) F_\mathrm{S} - i\frac{|F_\mathrm{S}|^2}{\beta_\mathrm{col}} F_\mathrm{S},$$

$$\Rightarrow \qquad |A_\mathrm{P}|^2 = |F_\mathrm{S}|^2 \left(1 + \left[\theta - \frac{|F_\mathrm{S}|^2}{\beta_\mathrm{col}} \right]^2 \right). \qquad (10.2)$$

As with the Lugiato-Lefever description of an optical field evolving within a self-focusing, driven optical cavity [168], these solutions provide an analytical link between the intensity of the pump $|F_\mathrm{P}|^2$ and a stationary optical field $|F_\mathrm{S}|^2$, with the self-focusing strength now given by the inverse of β_col. We therefore use Eqn. (10.2) to plot $|F_\mathrm{P}|^2$

against $|F_S|^2$ for several θ and β_{col} combinations in Fig. 10.4.
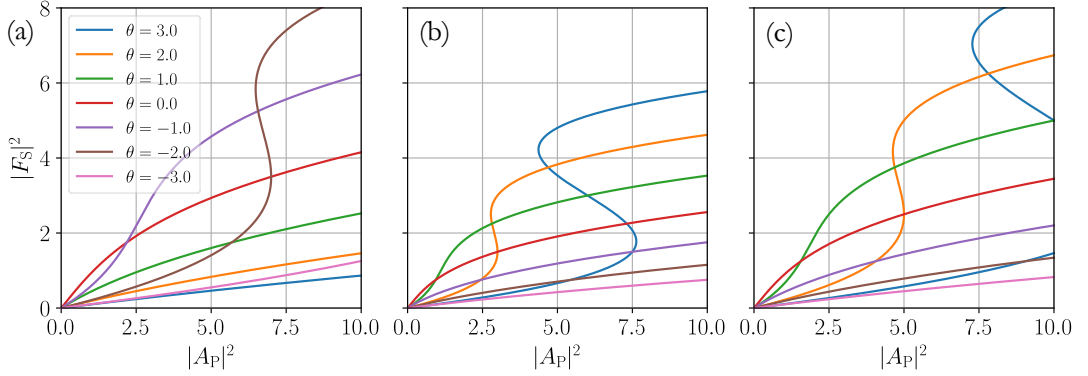
Figure 10.4: Stationary solutions of Eqn. (10.2) for indicated θ-values and $\beta_{\text{col}} =$ (a) -3.5, (b) 1.5, and (c) 2.5.

As in Ref. [168], the presence of sigmoidal curves in Fig. 10.4 suggest that, for all values of β_{col} considered, there are regions of bistability present within the system, meaning that at a certain fixed value of pump strength F_P there exists (at least) two stable solutions of the system. As can be seen from Fig. 10.4(b)-(c), the region of bistability steadily grows as $|\beta_{\text{col}}|$ increases, with the amplitude of optical pump strength required to reach bi-stable regions also growing in turn. There is also an inversion in the relationship, with positive cavity detuning selections exhibiting hysteresis when $\beta_{\text{col}} > 0$, and negative cavity detuning selections exhibiting hysteresis when $\beta_{\text{col}} < 0$.

To test whether such regions of bistability occur for the dynamically evolving BEC of Eqns. (9.65)-(9.66), we alter the cavity detuning in a cyclic progression whilst maintaining a fixed value of the input pump amplitude. The cavity detuning is increased from $\theta = -7.5 \rightarrow 7.5$ linearly over a period $\tau = 10^5$, before the identically inverse procedure is followed. We plot the average optical field intensity $|F|^2$ against θ in Fig. 10.5 for various selections of A_P.

In regions of bistability, one would expect to see that the positive and negative paths of Fig. 10.5 follow separate trajectories, with them following a similar trajectory in regions of monostability [257]. The yellow shaded region in Fig. 10.5(c), which considers the previously studied case of $A_P = 3$, shows such a divergence for small positive θ-values
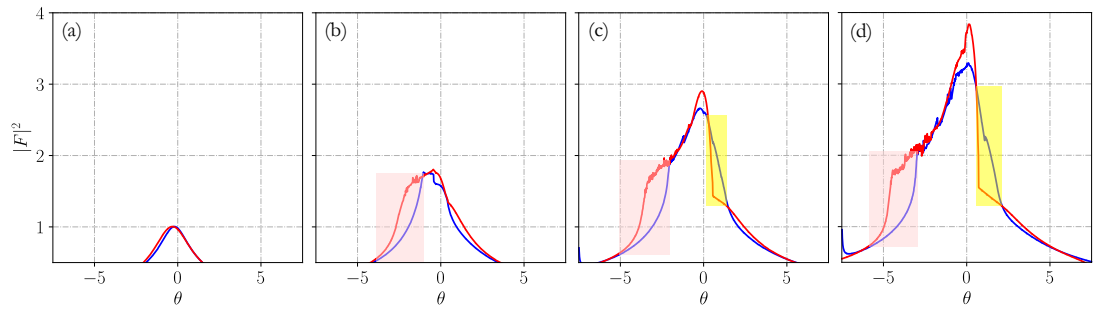
Figure 10.5: Average optical field intensity $|F|^2$ against the cavity detuning θ in the progression $\theta = -7.5 \to 7.5$ (blue) and $\theta = 7.5 \to -7.5$ (red). Windows show (fixed) $A_P =$ (a) 1.0, (b) 2.0, (c) 3.0, and (d) 4.0.

present in Fig. 10.4. The average value of the field for increasing cavity detuning (shown in blue) lies above the average value obtained when decreasing cavity detuning (shown in red). This is indicative of a bistable solution, with the lower branch corresponding to a homogeneous field jumping to a patterned state at a threshold cavity detuning. The upper branch in this region shows instead a steady decay of pattern intensity, eventually returning to homogeneous solutions and a region of monostability. In this region the system follows a hysteresis cycle; altering the cavity detuning in this region will follow the cyclic passage shown in Fig. 10.5(c).

We also find a second clear region of bistability within the system for moderately negative cavity detuning, indicated by the pink shading in Fig. 10.5(c). This time the negatively changing cavity detuning path sits above the positively changing path. Bistability was predicted for such values of θ in the case of an instantaneous BEC, but only with negative β_{col}, as shown in Fig. 10.4. We find that the alteration to dynamically evolving atoms widens this parameter space, with the system also demonstrating a hysteresis cycle in this region with $\beta_{col} = 2$.

Considering all panels of Fig. 10.5, representing equivalent studies for various static pump amplitudes, we find that the pump amplitude provides an effective control over the presence and size of bistability, and thus hysteresis behaviour, obtained. We find that for too low a pump strength, $A_P = 1$, both regions of bistability are closed, and the system is entirely monostable. As A_P is increased to $A_P = 2$, the first region clearly

visible is the region of negative detuning. It is only for $A_\mathrm{P} > 2$ that we observe a bistable regime for positive cavity detuning, indicative of the requirement for a patterned state and thus a need to exceed a threshold pump strength. This suggests that there is an analogy between changes in the pump strength and changes in the atomic scattering length in the model of Eqns. (9.65)-(9.66), given the ability of each to realise regions of bistability.

To further demonstrate the behaviour of the system, we perform an alternative cyclic operation now with the pump strength, initially increasing A_P from $|A_\mathrm{P}|^2 = 0 \to 10$ with an initial optical field of noise, each step for $\tau = 5000$ round trips. We then decrease the pump strength, returning it iteratively to $|A_\mathrm{P}|^2 = 0$ in the same number of intervals and time progression, with the initial optical field now being the previous pattern. Before each A_P change, we plot the maximal optical field power, $|F_\mathrm{max}|^2$, against $|A_\mathrm{P}|^2$, shown in Fig. 10.6.

The two trajectories of Fig. 10.6 are again indicative of a bistable solution, causing the system to follow a hysteresis cycle. When the pump power is steadily increased, as shown by the upward arrowhead markers, an initially noisy system follows a path where the maximum value of the final field amplitude is notably lower than at the equivalent pump strength of starting from a pattern state, given by the downward arrowhead markers. These two different trajectories occur as the system follows the two paths of a sigmoidal trajectory, similar to those of Fig. 10.4. When $|A_\mathrm{P}|^2 > 8$, a monostable regime is reached, indicated by the coalescing of both upward and lower cycles to form one combined trajectory.

Also shown in Fig. 10.6 are the transverse distributions of the BEC and optical fields, normalised to the same maximum amplitude, for various pump strengths. These distributions further clarify certain features. Initially, when starting from noise (lower distributions), the system follows a branch of homogeneous solutions, with the rapid jump before $|A_\mathrm{P}|^2 = 8$ corresponding to the jump to the pattern state. When starting from a pattern state (upper distributions), the system follows a different branch, with patterns organised into a much more uniform structure of peaks and holes. These
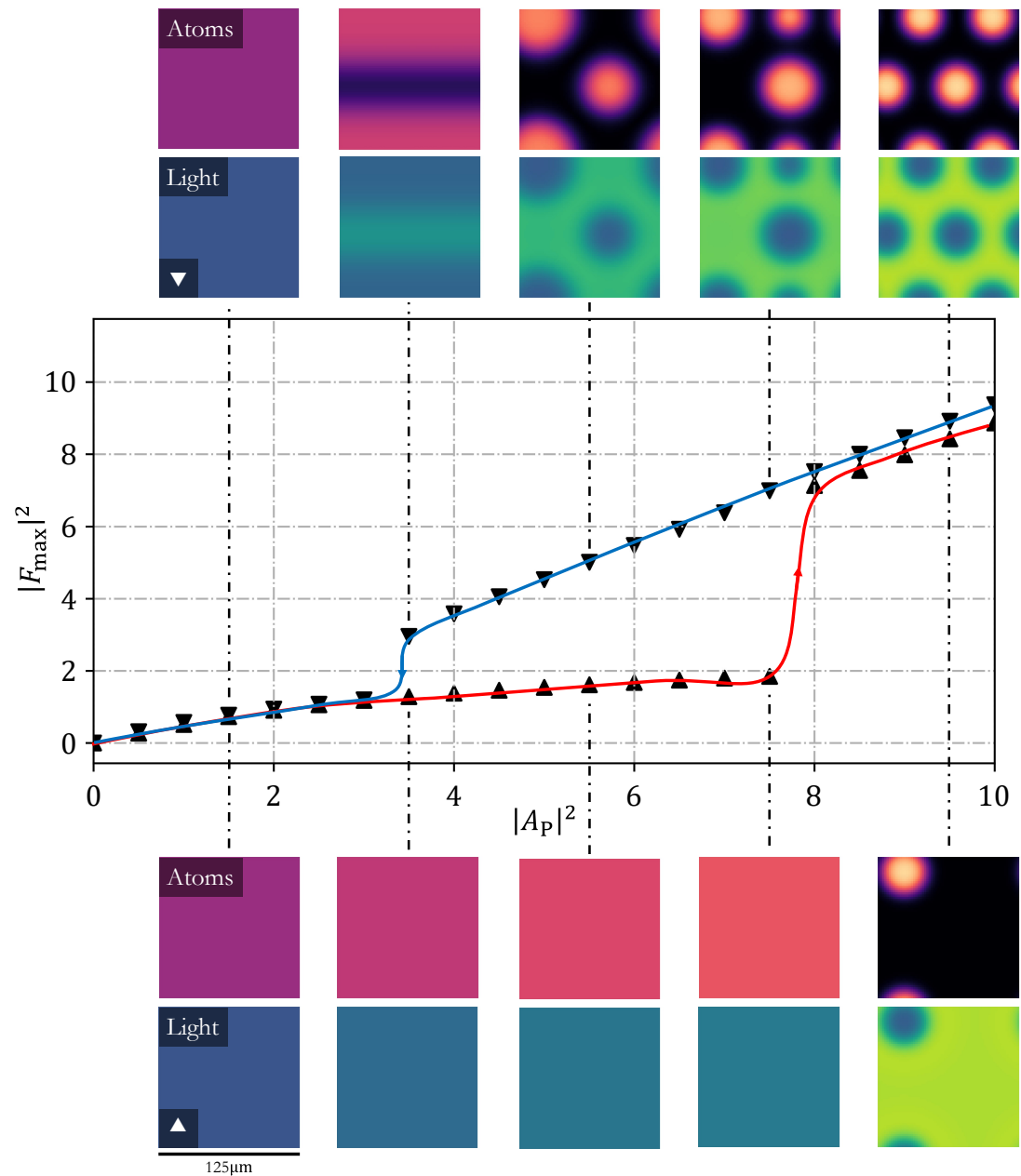
Figure 10.6: Hysteresis from Eqns. (9.65)-(9.66), for $|A_P|^2 = 0 \to 10$, at $\tau = 5000$ for each step. Central section: final maximum optical power $|F_{max}|^2$ starting from initial optical noise (up arrow) and starting from initial optical pattern (down arrow). Upper (from noise) and lower (from pattern) portions: BEC (upper rows) and optical (lower rows) transverse intensity distributions for indicated $|A_P|^2$ and $|F_{max}|^2$. Fixed parameters: $\theta = 0.4, \beta_{col} = 1.5, L_3 = 0.00022, s = 1, A_\psi = 2$. Fields plotted between 0 and maximum amplitude of all panels.

patterns also remain for much lower $|A_\mathrm{P}|^2$ values than previously, with the BEC spots steadily growing as the pump strength decreases, becoming a single stripe, and finally dropping to the homogeneous solution branch for $|A_\mathrm{P}|^2 \approx 3$. We find that larger θ-values cause the cycle to grow wider and occur at progressively higher pump strengths.

10.3 Monostable Pattern Varieties

In addition to the holes, peaks and stripes already outlined in pattern regimes, we find a far greater wealth of patterns accessible within alternative, typically monostable, regions when $\kappa^{-1} \approx 10^{-1}$. To demonstrate this, we sequentially vary a series of experimentally accessible 'control parameters' (the BEC scattering length β_col, optical pump strength A_P or cavity detuning θ), holding all other parameters values static, reporting on the patterns achieved with each change.

10.3.1 Atomic Scattering Length

We begin by considering the variety of patterns obtained as the BEC scattering length, β_col, is altered. Such a change is possible by altering the magnetic field that the atoms are subject to over time [232]. We find several transitions between different pattern regimes, as shown in Fig. 10.7, which gives the optical and BEC transverse field distributions at $\tau = 2000$.

Initially, with the BEC's scattering length weakly negative, $\beta_\mathrm{col} = -2$, the atoms are subjected to attractive interactions with one another, naturally localising. These interactions are the dominant force in the dynamics, and so the BEC organises into narrow, localised solitary peaks. With blue atom-field detuning, the optical field reorganises into a series of hole clusters in an otherwise uniform field. With $\beta_\mathrm{col} = 0$, and the BEC not being subject to any inter-atomic forces, we find that the region of coupled structure formation narrows, and the region of uniform optical field presence grows. The spatial scales of the BEC's peaks also grow, becoming broader clusters with the BEC's tendency to localise no longer a consideration.

If the BEC is subject to repulsive inter-atomic interactions, $\beta_\mathrm{col} \approx 2$, we obtain the
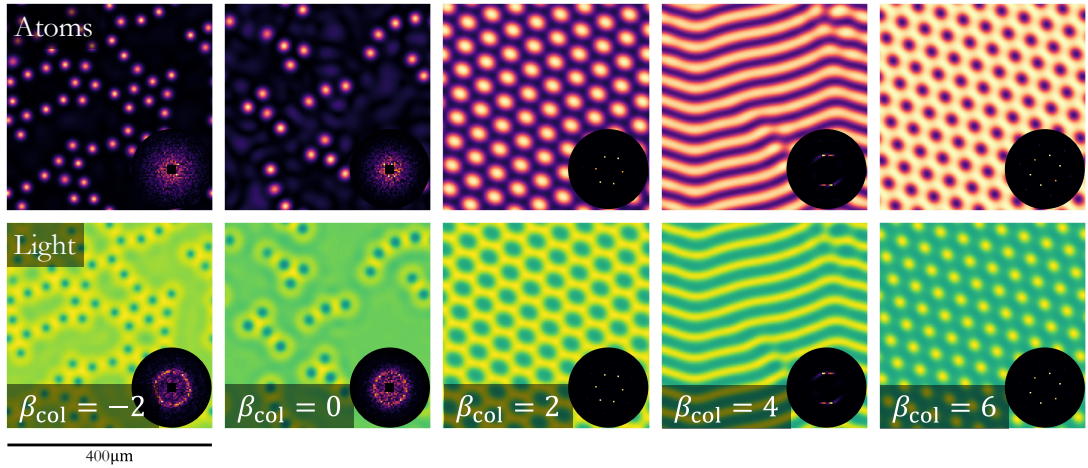
Figure 10.7: BEC (upper) and optical (lower) transverse distributions at $\tau = 2000$ for BEC scattering lengths indicated. Fixed parameters: $\theta = -1, A_{\mathrm{P}} = 3, L_3 = 0.00022, s = 1, A_\psi = 2$. Each field is plotted between 0 and maximum amplitude.

familiar broad atomic cluster and optical hexagons, as outlined in Fig. 10.7. With stronger repulsive scattering, we again transition to different pattern regimes, first passing through a region of rolls at $\beta_{\mathrm{col}} = 4$, before obtaining an organised distribution of atomic holes, with corresponding optical peaks, for $\beta_{\mathrm{col}} = 6$. Such a structure is approximately the inverse of that obtained for $\beta_{\mathrm{col}} = 2$, though the spatial scales are somewhat altered.

We emphasise that for $\beta_{\mathrm{col}} = 2 \to 6$ there are a wealth of accessible patterns, and we observe the transient dynamics of various pattern transitions across the transverse planes of both fields. We summarise such behaviour in Fig. 10.8, where we consider the evolution of the coupled fields between $\tau = 0 \to 2000$, where various pattern progressions are exhibited as the system seeks a steady state.

Considering again Fig. 10.7, we find that pattern formation remains attainable until $\beta_{\mathrm{col}} > 8$, when repulsive interactions entirely suppress formation. We also inset, for all patterns considered, the far fields of each distribution. We find that, similarly to Ref. [179], the number of peaks in the far field reflects the pattern variety, with the clarity of the far field peaks reflecting the clarity of the near field. In the majority of cases in Fig. 10.7, we obtain six far field peaks, corresponding to a hexagonal pattern
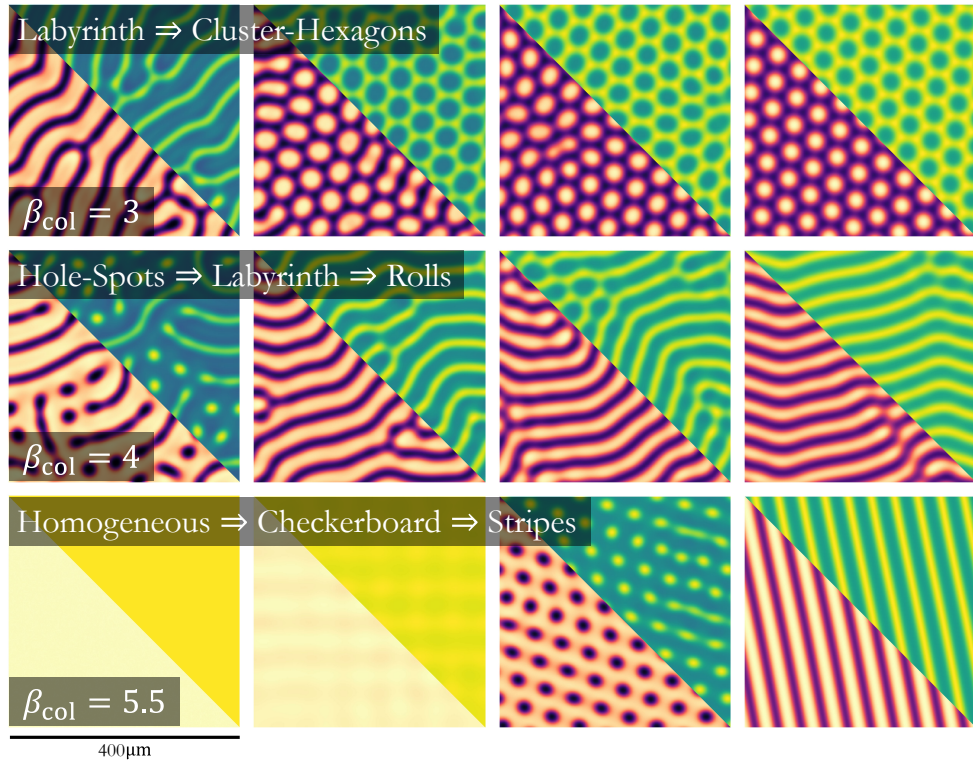
Figure 10.8: BEC (lower diagonal) and optical (upper diagonal) transverse distributions between $\tau = 0 \to 2000$ for BEC scattering lengths as indicated, displaying various transient pattern progressions. Fixed parameters: $\theta = -1, A_\mathrm{P} = 3, L_3 = 0.00022, s = 1, A_\psi = 2$. Each field is plotted between 0 and maximum amplitude.

instability seeded by quadratically nonlinear terms [171, 258, 259]. There are also cases where we observe two peaks in the far field, characteristic of the roll pattern instability observed. Significantly, we find that with excellent near-field pattern clarity (e.g. when $\beta_\mathrm{col} \geq 2$), the far field peak pattern is also present in the atomic field. In this way, the far field distributions provide an excellent means of characterising the nature and clarity of patterns in both fields.

10.3.2 Optical Pump Strength

We now return to $\beta_\mathrm{col} = 1.5$ and consider altering A_P, experimentally possible simply by altering the power of the laser providing the pump. The results of such a procedure are given in Fig. 10.9, and we observe a range of pattern varieties again across the various pump strengths.
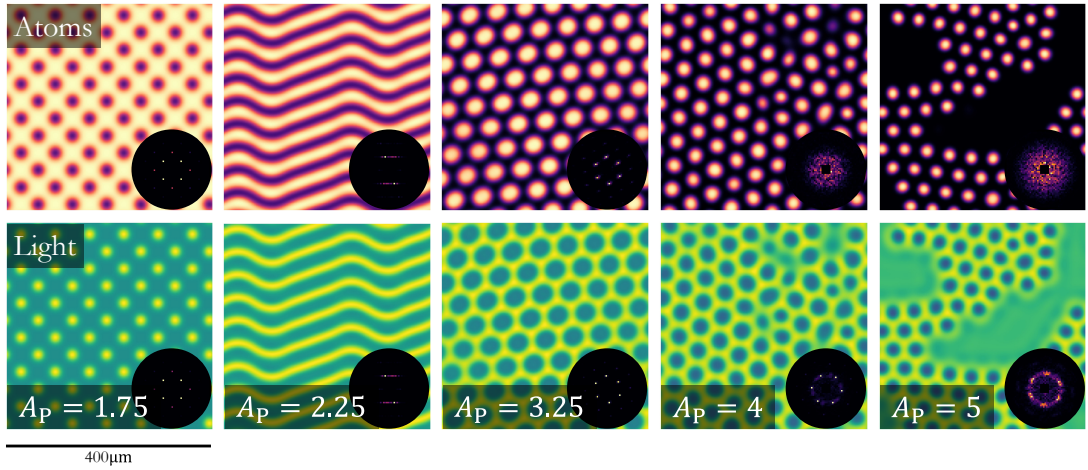
Figure 10.9: BEC (upper) and optical (lower) transverse distributions at $\tau = 2000$ for pump strengths indicated. Fixed parameters: $\theta = -1, \beta_{\mathrm{col}} = 2, L_3 = 0.00022, s = 1, A_\psi = 2$. Each field is plotted between 0 and maximum amplitude.

Initially, with the pump strength $A_{\mathrm{P}} = 1.75$, we obtain a squares pattern consisting of a uniform atomic distribution with holes corresponding to optical peaks. In this regime, the relatively weak optical pump strength is on the threshold of pattern formation, and the dipole forces between both fields are relatively equal. Such a distribution is reflected by a four-peak structure in the far-fields of both atoms and light, in excellent agreement with Ref. [179]. This structure is reasonably short-lived in terms of pump strength, and we find that by $A_{\mathrm{P}} = 2.25$, with the optical field beginning to dominate the dipole forces, we obtain instead modulated stripes in both fields, adjacent to one another, with a corresponding drop to two peaks in the far fields.

As the pump strength continues to increase and the optical field further dominates the dipole nonlinearity, we return to more familiar patterns, observing first the expected peak-hexagon combination for $A_{\mathrm{P}} \approx 3$, followed by a narrowing of the atomic pattern wavelength as the optical field becomes increasingly dominant for stronger pump powers. Again, we also see a restriction in the transverse domains of the patterns, with ever-growing homogeneous optical regions returned. In all cases, the optical far fields show six peaks that indicate a hexagonal system, with these peaks also appearing in the atomic far field when A_{P} is not significantly dominant over A_ψ.

The pattern progression of Fig. 10.9 is very similar to that observed when varying β_{col} in Fig. 10.7, suggesting that these two parameters have broadly opposite effects on the dynamics, enabling pattern variety control with either parameter. Such findings agree well with the behaviour reported in bistable regimes at Fig. 10.5, where the alterations to the pump strength had equivalent effects to those expected of the atomic scattering length under the assumption of an instantaneous BEC medium. This suggests there is a mapping between β_{col} and A_{P}, with both parameters having similar, but inverse, effects on the coupled system dynamics.

10.3.3 Cavity Detuning

We now return the value of A_{P} to 3 and study the effects of changing the cavity detuning θ. Such an alteration is possible by altering the frequency of the input pump beam in time [260]. From Eqn. (9.30), as the magnitude of the cavity detuning increases from zero, the difference between the cavity mode frequency and the input frequency grows, minimising the effectiveness of the pump on the system. We find that such changes have significant effects on the pattern varieties formed, as demonstrated in Fig. 10.10.
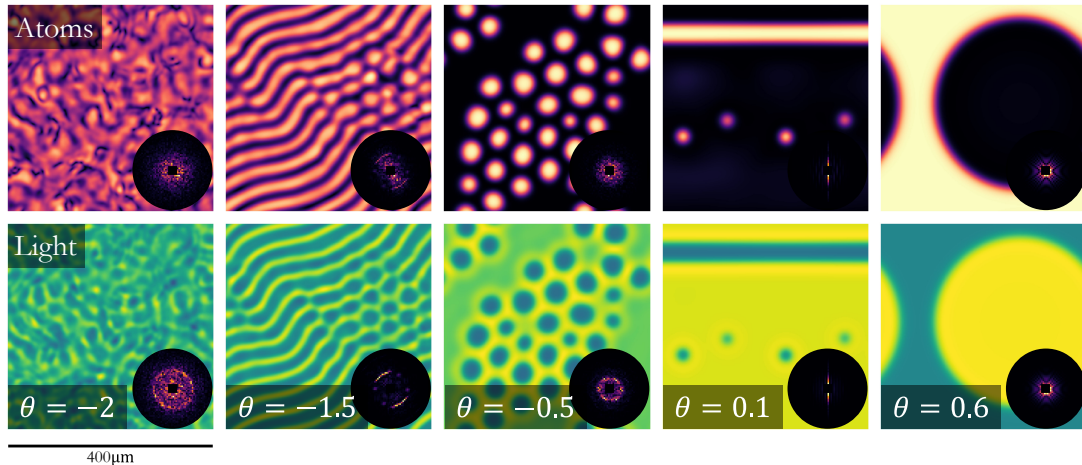
Figure 10.10: BEC (upper) and optical (lower) transverse distributions at $\tau = 2000$ for cavity detuning values indicated. Fixed parameters: $\beta_{\mathrm{col}} = 2, A_{\mathrm{P}} = 3, L_3 = 0.00022, s = 1, A_\psi = 2$. Each field is plotted between 0 and maximum amplitude.

Initially, we find for strongly negative cavity detuning a short-lived regime of pattern formation, which typically follows the procedure of atomic holes coupled to bright

optical peaks coalescing into coupled labyrinths, after which the patterns are destroyed by increasingly turbulent behaviour driven by the atomic field. For the case of $\theta = -2$ we find that the turbulent behaviour occurs for $\tau > 500$, and by $\tau = 2000$ the fields are sufficiently modulated to show little trace of the prior patterns.

As the strength of cavity detuning decreases, we find that the patterns become significantly more robust. Around $\theta = -1.5$, the fields predominantly return coupled stripes, with some evidence of a cluster-hexagon combination. This is reflected in the light's far field, which predominantly shows two peaks indicating stripes, but with a weaker series of four additional peaks indicating hexagons. With further decreases in cavity detuning, the cluster-hexagon combination becomes dominant and we pass through the outlined regime of $\theta \approx -1$, Fig. 10.2.

By $\theta \approx -0.5$ we find, analogously to other parameter alterations, the growth in spatial scales of the atomic clusters, along with the restriction of their appearance to smaller transverse regions of the total fields. However, on crossing $\theta = 0$, we find the dynamics significantly differ from previously observed patterns, and a region of strong atomic channelling is entered. The majority of atoms become enclosed in a very narrow spatial region, the parallel 'stripe' shown in Fig. 10.10, with only a small trace of the previously dominant cluster-hexagon combinations. The far field reflects these changes, with the loss of the six peaks to a dominant stripe. With further θ-increases, we find that the patterns begin to be suppressed, with the atomic stripe increasing in size. We find that during this transition a final pattern configuration is obtained around $\theta = 0.6$, where the optical field occupies a large circular domain rather than a rectangular configuration surrounding a stripe. From this point, further small increases in θ lead to the entire suppression of pattern formation, with homogeneous fields being returned for $\theta > 1$.

10.4   Cavity Solitons

We are able to realise densely localised, solitonic structures, as first introduced in Chapter 4.1, in either / both fields, depending on the parameter selection used. For blue-detuned fields, we find that these structures are restricted to the extremes of

parameter ranges, outwith the spontaneous patterns reported on. For red-detuned fields and therefore bright-seeking atoms, we find the formation of solitonic structures to be much more widespread, and thus we consider each case separately here.

10.4.1 Blue Atom-Field Detuning

As discussed around Fig. 10.7, we observe, when $\kappa^{-1} \approx 10^{-1}$, the formation of lattices of atomic peaks and optical holes when atoms naturally want to localise through attractive interatomic atomic interactions, $\beta_{\mathrm{col}} < 0$. In these regimes, the atomic structures formed are localised solitonic peaks with characteristic distribution, occurring within optical holes. We find that changes to the scattering length change many of their physical characteristics, including their intensities, widths and transverse domain coverage, which we summarise in Fig. 10.11, showing these solitonic distributions at $\tau = 1000$ for a variety of β_{col} selections.
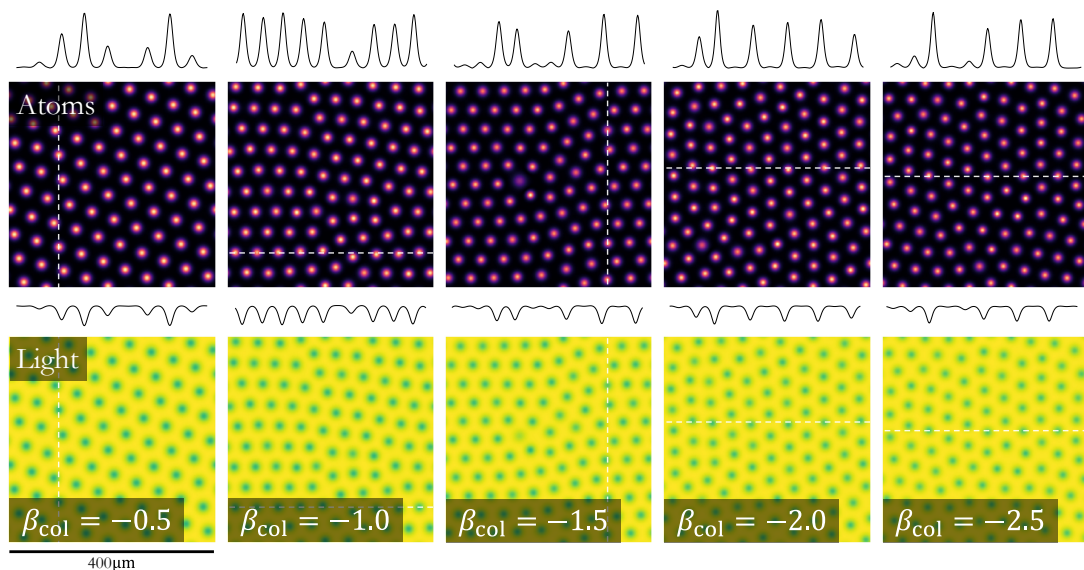
Figure 10.11: Atomic (upper) and optical (lower) transverse distributions at $\tau = 1000$ for indicated β_{col}-values, realising atomic solitonic structures with blue atom-field detuning. Fixed parameters: $A_{\mathrm{P}} = 3, L_3 = 0.00022, s = 1, A_\psi = 2$. Each field variety plotted between 0 and maximum amplitude of all panels. Position of 1D amplitude trace indicated on each panel by dotted line.

From Fig. 10.11, there is a clear narrowing of the bright atomic structures as the

scattering length decreases, indicative of the increasingly attractive atomic interactions influencing the dynamics. The combination of this force combined with the channelling of atoms into optically dark regions, thanks to the blue atom-field detuning, leads to the presence of these solitonic structures. However, these forces also contribute to disorder in the distribution of these localised structures, with some transverse regions of the field presenting a largely homogeneous optical field. The underlying pattern instability is clearly hexagonal, reflected in the far field distributions, which for all cases of Fig. 10.11 returns six peaks, as expected.

10.4.2 Red Atom-Field Detuning

We may obtain similar atomic soliton structures on considering red atom-field detuning, so that the atoms are light-seeking and will form coupled atom-light solitons. To exemplify this, we now return all other parameters to those used in Fig. 10.2, and test the cavity detuning values of θ = -2, -1, 0, 2, and 3. With blue-detuned fields one would expect turbulent behaviour, followed by interleaved spontaneous pattern formation, and finally homogeneous field return across this range. For the case of light-seeking atoms, the equivalent distributions are given in Fig. 10.12.

We obtain well organised coupled atom-light solitonic distributions for $\theta = 0$ and red atom-field detuning, shown in Fig. 10.12. These structures do not require attractive atomic interactions to form, unlike their blue-detuned atomic equivalents. Their transverse scales are similar to the blue-detuned case, suggesting that a similar mechanism lies behind their formation, with the lack of attractive atomic interactions now compensated by the switch in the nature of the dipole force between the fields.

Beyond the range $-1 < \theta < 1$, one enters new dynamical regimes, where the fields take on alternative transverse forms. When $\theta \leq -1$, this is reflected in an earlier onset of turbulence than in the blue-detuned case, and for $\theta = -1$, we observe a clearly turbulent field in a regime that supported pattern formation for blue detuning. The trace of a pattern remains visible within the optical field, reflecting this lower bound of pattern formation. However, by $\theta = -2$, evidence of patterns are lost, with both fields
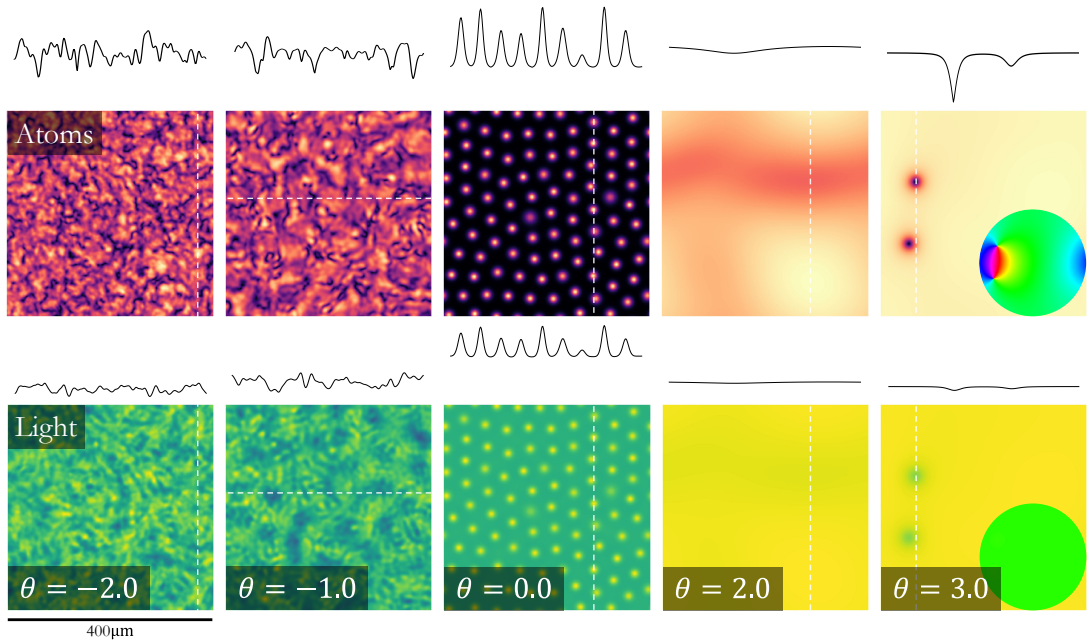
Figure 10.12: Atomic (upper) and optical (lower) transverse distributions at $\tau = 1000$ for indicated cavity detuning selections, realising turbulence, atom-light cavity solitons and isolated vortices for red atom-field detuning. Insets for $\theta = 3.0$ shows corresponding field phase distributions. Fixed parameters: $\beta_{\text{col}} = 2, A_{\text{P}} = 3, L_3 = 0.00022, s = -1, A_{\psi} = 2$. Each field variety plotted between 0 and maximum amplitude of all panels. Position of 1D amplitude trace indicated on each panel by dotted line.

simply turbulent.

When $\theta > 1$, like the blue-detuned case, the pattern forming dynamics are largely suppressed, and so the coupled solitonic structures steadily fade to broadly homogeneous fields, as shown for $\theta = 2$. However, we also observe the spontaneous formation of dark solitonic structures across both fields, as shown for $\theta = 3$, clearest in the atomic field, and somewhat visible in the optical. The phase of each field shows that these are atomic driven vortices, with two linked singularities in the atomic field but a homogeneous phase profile in the optical field.

Returning to the case of $\theta = 0$, which gives the clearest lattices of coupled solitonic structures, we find that they remain robust to a wide range of input parameters. As expected, such patterns form readily for attractive atomic interactions ($\beta_{\text{col}} < 0$) with the atoms simply reinforcing the light-seeking nature of the dipole coupling. For repulsive

interactions ($\beta_{\mathrm{col}} > 0$) they remain to $\beta_{\mathrm{col}} \approx 6$, gradually increasing in transverse size as the repulsive nature of the BEC interactions strengthens. Eventually, for $\beta_{\mathrm{col}} > 6$, their formation is entirely suppressed, and the fields remain largely homogeneous, with small fluctuations failing to form distinct patterns. Like the blue-detuned case, altering the optical pump strength has the broadly opposite effect to changing the atomic scattering length, with a minimum threshold of $A_{\mathrm{P}} \approx 2.5$ to obtain patterns, beneath which one again obtains homogeneous fields with small fluctuations. As the pump strength increases above threshold, the solitonic structures become further localised, narrowing in transverse size and increasing in amplitude in a way analogous to increasingly attractive atomic interactions.

Finally, we note that, much as was the case for blue-detuned fields, when $\kappa^{-1} \approx 10^{-8}$ we obtain signatures of the richer dynamics outlined in Fig. 10.12. We summarise this in Fig. 10.13, which considers the equivalent case to Fig. 10.1, with identical physical parameters, for red atom-field detuning. There is a transition from a region of largely suppressed pattern formation when $\theta \lesssim -2.0$, to relatively organised coincident pattern formation when $\theta \approx 0$, which then leads to the formation of isolated, mutual cavity solitons that originate from these structures when $\theta \gtrsim 2.0$.
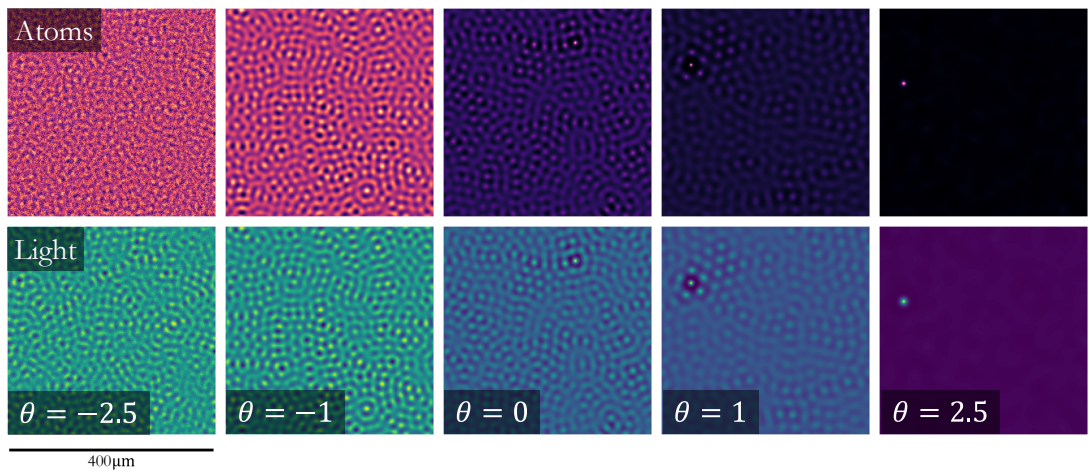
Figure 10.13: BEC (upper) and optical (lower) transverse distributions at $\tau = 1000$ for θ-values indicated. Fixed parameters: $\beta_{\mathrm{col}} = 0.25, A_{\mathrm{P}} = 3, L_3 = 0.00022, s = -1, A_\psi = 0.1$. Each field is plotted between minimum and maximum amplitude.

10.5   Conclusions and Outlook

We have considered the co-evolution of initially homogeneous ultracold atomic and optical fields within a driven optical cavity. With blue atom-field detuning, and therefore dark-seeking atoms, signatures of spontaneous coupled pattern formation across both fields were found. By considering the model parameter $\kappa^{-1} \to 1$, attainable through alterations to the mirror reflectivity, cavity length, or both, the pattern formation dynamics have been optimised. We demonstrated that the system may exhibit both bistable and monostable regions, and hysteresis cycles in bistable regimes and a wealth of pattern varieties in monostable regimes were shown. Outside of pattern formation, we reported on the ability to obtain atomic cavity solitons. For red atom-field detuning (light-seeking atoms), far wider regimes of coupled cavity soliton generation were found.

These findings may guide the realisation of a wealth of pattern varieties within a BEC that is more varied than those currently demonstrated [183, 184, 187, 188], whilst also requiring a relatively straight forward ultracold atomic setup. Additionally, there are clear links to ongoing research in the demonstration and application of hysteresis cycles within ultracold matter [196]. If these hysteresis cycles, arising through pattern formation, are realisable on spatially defined, physical atomic and optical profiles, there may be the potential to apply these cycles in the field of atomtronics [198], building on the control applications hysteresis enables within conventional electronics [261–264]. Significant applications also become possible in areas such as BEC atomic manipulation [25, 33, 253], and for guiding and trapping atoms to dark-regions, less vulnerable to optically-induced heating from a coincident beam [265].

Chapter 11

Structured Fields I: Spatial Patterns and Vortex Lattices

In this chapter, we build on the results of Chapter 10, and in *Section 11.1* consider spontaneous pattern formation on initially spatially structured fields. For blue atom-field detuning, the ultracold atoms are trapped in clusters in optical darkness, and in *Section 11.2* we introduce OAM to such structures, realising rotating optical and atomic patterns before increasing the OAM to obtain asymmetrical atomic reshaping and atomic vortex formation. Finally, in *Section 11.3*, we consider this approach as a mechanism for vortex lattice formation of any desired vortex order within a BEC.

11.1 Spatially Defined Spontaneous Patterns

We now seek to replicate the spontaneous pattern formation discussed in Chapter 10.1, but with atomic and optical fields possessing structured spatial intensity. Such pattern formation dynamics have the strict condition that a large enough overlapping area is provided, where both fields have amplitudes of sufficient magnitude, across a sufficiently large transverse region, in order to replicate the dynamics previously discussed.

For the ultracold atomic field, we return to considering an initial Thomas-Fermi distribution, Eqn. (2.17). To ensure optimal overlap, we utilise an optical pump given by a 'top-hat'-style distribution [174]. We define this here as

$$F_{\mathrm{P}}(r) = A_{\mathrm{P}} \left[\frac{1}{2} \Big(1 - \tanh\big(S\,(r - w_{F'}) \big) \Big) \right], \tag{11.1}$$

where S represents the steepness of the edges of the top-hat, $w_{F'} = w_F/w_{\mathrm{L}}$, and w_F represents the physical transverse size of the optical pump. We set $w_F = w_\psi = 200\mu$m to ensure that the transverse diameter of the optical pump matches the transverse diameter of the BEC. The initial optical field itself, as standard, remains simply noise. Such fields are shown in the first column of Fig. 11.1.

We consider both positive and negative values of s, representing blue and red atom-field detuning, respectively. All other system parameters remain unchanged from the selections discussed in Chapter 10.1 and 10.4. Depending on the selection of κ, we find that the range of patterns reported in Chapter 10 may also be realised on initially spatially defined fields, and so we consider one case of each detuning in turn below, enabling comparison with their homogeneous field equivalents.

11.1.1 Blue Atom-Field Detuning

For blue atom-field detuning, and dark-seeking atoms, one would expect to see the formation of coincident patterns similar to those of Chapter 10.1. Under the limits of both $\kappa^{-1} \approx 10^{-8}$ and $\kappa^{-1} \approx 10^{-1}$, we again obtain similar structures across both spatially defined fields, as shown in Fig. 11.1. As in Chapter 10, the pattern clarity is significantly enhanced for the larger selection of κ^{-1}, and so we continue to focus our discussion on that case.

There are notable differences between the patterns of Fig. 11.1 and their homogeneous equivalents (Fig. 10.1 for $\kappa^{-1} \approx 10^{-8}$ and Fig. 10.2 for $\kappa^{-1} \approx 10^{-1}$). The hexagonal-hole patterns are distinctly more circular than the transverse patterns formed on homogeneous fields. This reflects the change in initial conditions: a circularly bounded optical pump leading to circular patterns. Atoms on the outer edge of the optical pump are
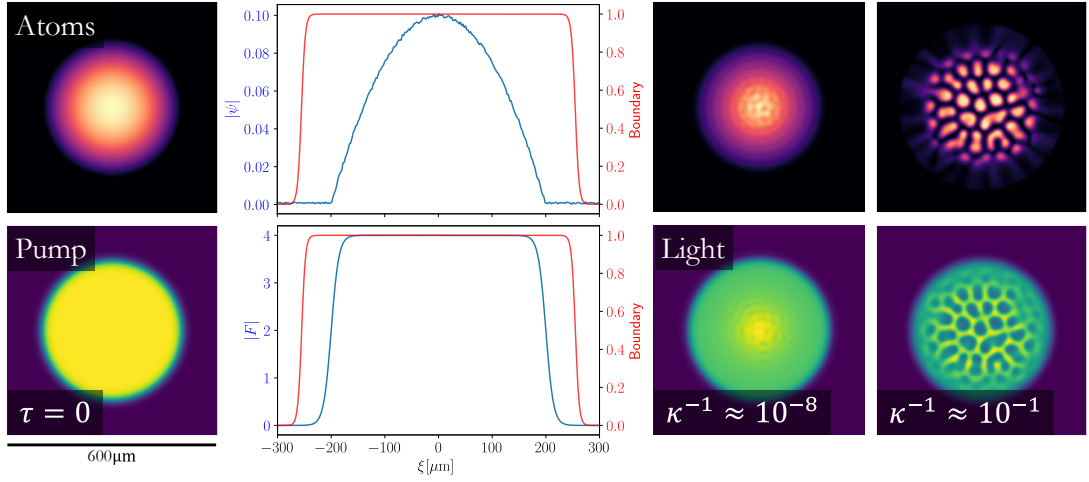
Figure 11.1: Blue-detuned pattern formation on spatially bounded initial atomic (upper) and optical (lower) fields (left) and associated cross sections with absorbing boundary location (centre left) for varying κ selection. $w_\psi = w_F = 200\mu$m, with parameters otherwise as in Fig. 10.1 ($\kappa^{-1} \approx 10^{-8}$, $\theta = -4$) and Fig. 10.2 ($\kappa^{-1} \approx 10^{-1}$, $\theta = -1$).

able to tunnel out of the spatial domain of the pump through their kinetic energy contributions and tendency to move towards dark regions, being lost from the system through the absorbing boundaries. We are able to largely eliminate this atomic loss and sustain pattern formation on spatially defined fields if the dipole force upon the atoms is increased relative to their kinetic term. An optical pump with $A_{\mathrm{P}} = 4$, with all other conditions maintained as in Fig. 11.1, meets this criterion and sustains pattern formation, as shown in Fig. 11.2.

For both pump strengths, we note that the entire formation procedure happens quicker in the case of spatially defined fields, as the dark-seeking atoms are subject to an additional intensity gradient in this configuration, and they are driven to regions of darkness in the optical field. The forces arising from this motion cause the fields to mutually structure significantly quicker than in the homogeneous case, with the fields developing interleaved spots and stripes by $\tau = 50$, and signatures of cluster patterns by $\tau = 100$, with homogeneous equivalents at $\tau \approx 150$ and $\tau \approx 350$, respectively.
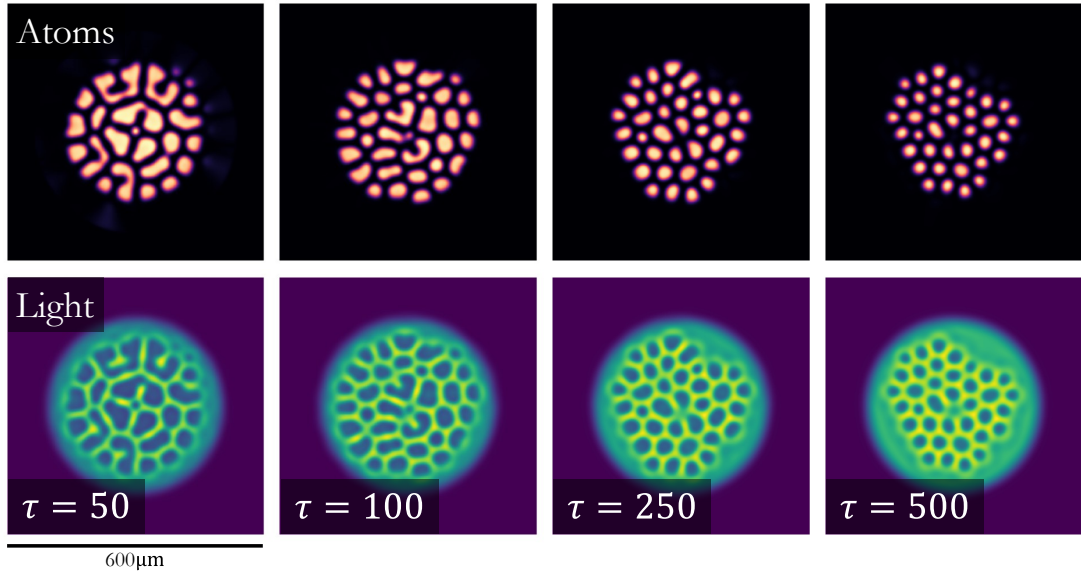
Figure 11.2: Blue-detuned pattern formation on spatially bounded initial atomic (upper) and optical (lower) fields between $\tau = 0 \to 500$, using a stronger optical pump than in Fig. 11.1. Fixed parameters: $\beta_{\text{col}} = 2, \theta = -1, L_3 = 0.00022, s = 1, A_{\text{P}} = 4, A_\psi = 2, w_\psi = w_F = 200\mu$m.

11.1.2 Red Atom-Field Detuning

Now considering red atom-field detuning, we return the pump strength to $A_{\text{P}} = 3$, and set the cavity detuning to $\theta = 0$, matching the procedure to obtain coupled atom-light cavity solitons on homogeneous fields outlined in Fig. 10.12. All other aspects remain the same as in the preceding blue-detuned pattern case. As expected, we obtain coupled atom-light solitons across the bright area of the top hat, Fig. 11.3.

The coupled atom-light solitons that appear in this case again follow a radial distribution, organising into approximate ring structures, of increasing width, reflective of the circular boundary of the optical pump. Similar to their homogeneous counterparts, formation occurs swiftly as the strength of the optical field circulating within the cavity increases, being aided by the light-seeking nature of the atoms. Unlike the blue-detuned case, a pump strength of $A_{\text{P}} = 3$ is sufficient to overcome the atomic kinetic energy contributions and realise the expected coupled cavity soliton formation.

Transverse structures like those in Fig. 11.3 have analogues in many systems, including
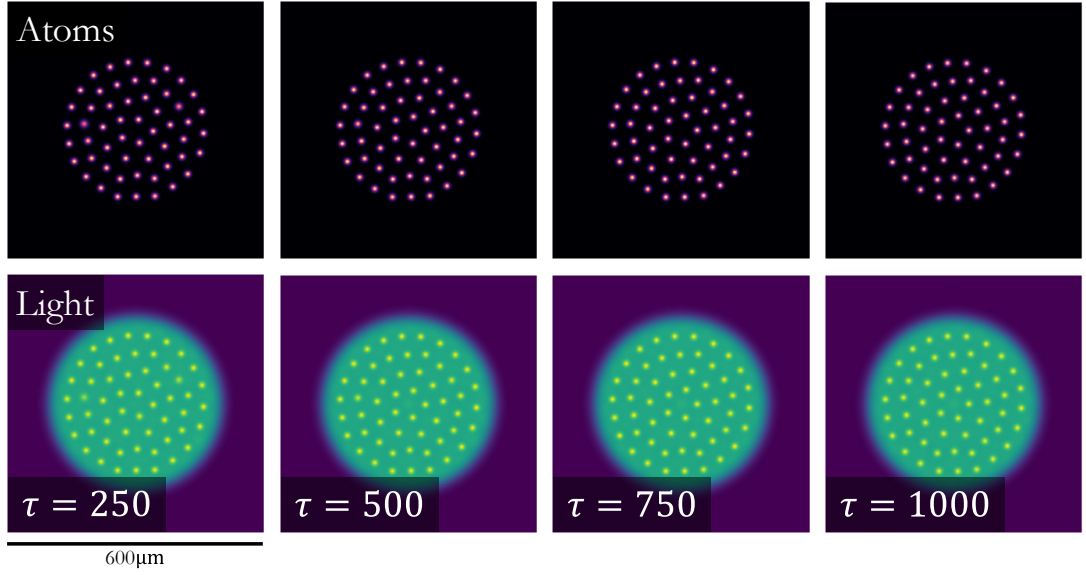
Figure 11.3: Red-detuned pattern formation on spatially structured initial atomic (upper) and optical (lower) fields between $t = 0 \rightarrow 1000$, comparable with homogeneous field equivalent in Fig. 10.12. Fixed parameters: $\beta_{\mathrm{col}} = 2, \theta = 0, L_3 = 0.00022, s = -1, A_{\mathrm{P}} = 3, A_{\psi} = 2, w_{\psi} = w_F = 200\mu\mathrm{m}$.

those recently studied in a variety of optical cavity configurations with a cold atomic medium, for example in Refs. [61, 178, 179]. Throughout the rest of this chapter, we restrict ourselves to further exploration of the blue-detuned, dark-seeking atomic case, but we return to considerations of a red-detuned, light-seeking cavity in Chapter 12.

11.2   Azimuthal Motion

Focusing on the dark atom trapping with blue detuning (Fig. 11.2), we now consider the effects of adding an azimuthal velocity to the pumped optical field through OAM [36]. Following the example of Ref. [174], the pumped optical field becomes

$$F_{\mathrm{P}}(r, m) = A_{\mathrm{P}} \left[\frac{1}{2} \Big(1 - \tanh\big(S\left(r - w_{F'}\right)\big) \Big) \right] e^{im\varphi}, \tag{11.2}$$

where m is an integer representing the desired OAM index of the pump field, applied using a spatial light modulator on the pump before it enters the cavity, as shown in Fig. 9.1.

11.2.1 Small OAM Indices

We initially study small m values in the range $-2 \leq m \leq 2$, applying the additional OAM to the pump beam, which otherwise remains unchanged in transverse size and amplitude. The results are shown in Fig. 11.4, which presents transverse intensity distributions of both fields at both $\tau = 250$ (left) and $\tau = 300$ (right), along with the continuous temporal evolution of each field around an unwrapped ring of 100μm radius (the radial centre of each field, marked for $m = 0$) between $\tau = 0 \rightarrow 500$, for all outlined m-values.
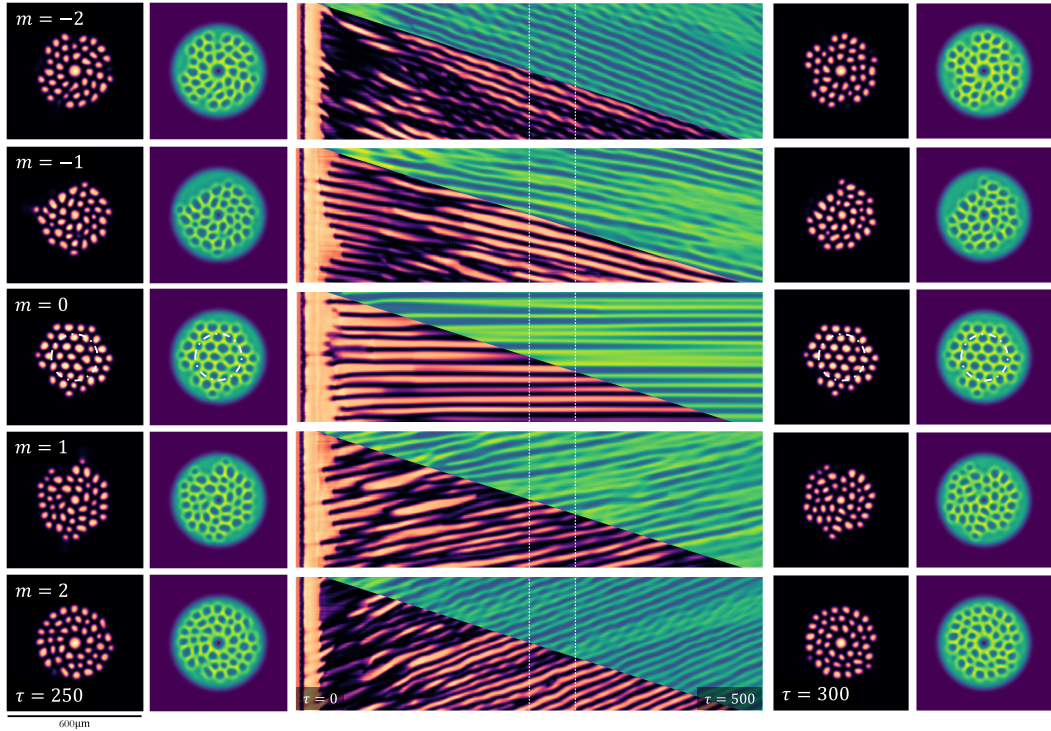
Figure 11.4: Rotating (when $m \neq 0$) atomic (left panel / left diagonal) and optical (right panel / right diagonal) patterns when the optical pump is seeded with OAM $m = -2 \rightarrow 2$ (top to bottom). Left panels at $\tau = 250$, right panels at $\tau = 300$ (indicated on central panel). Central panel shows the temporal evolution for $\tau = 0 \rightarrow 500$ of a ring of radius 100μm from the centre of each field, dotted for $m = 0$. Fixed parameters: $\beta_{\text{col}} = 2, \theta = -1, L_3 = 0.00022, s = 1, A_{\text{P}} = 4, A_\psi = 2, w_\psi = w_F = 200\mu$m.

From Fig. 11.4, the familiar interleaved patterns again form between both optical and BEC fields in regions of strong field intensities for all m-values. However, with $m \neq 0$, there are some clear differences in the patterns. With OAM present, a phase singu-

larity develops in the optical field, creating a new regime of coupled dynamics where previously there were simply hexagon-cluster patterns. Now, the optical field forms a large central dark region which the dark-seeking BEC atoms move to fill. In this way, a naturally occurring BEC trap has formed, within which the atoms are tightly held for long time periods. As $|m|$ increases, the size of the optical field phase singularity increases, and thus the total transverse proportion of the trapped BEC cluster grows noticeably.

Another notable alteration to the dynamics when OAM is included in the pump field is the seeding of azimuthal motion in both BEC and optical fields. As was shown in Ref. [174], the presence of OAM within a driven, self-focusing optical cavity leads to an azimuthal motion of any optical intensity structures formed. Here, such motion is clearest from the central column of Fig. 11.4, which shows the temporal evolution of a central ring in both fields. For $m = 0$ it may be noted that, although there are fluctuations in the placement of peaks owing to the settling of patterns with time, there is no prevailing diagonal motion, which would be indicative of angular momentum. When $m \neq 0$, a diagonal motion is clear. This indicates a transfer of angular momentum from the pump field to both the optical field and the BEC, and radial transport of the BEC atomic clusters at constant angular velocity. As the blue-detuned atoms are held in positions of optical minima, we find that they are effectively 'pushed' radially by neighbouring regions of (typically hexagonal) optical intensity.

11.2.2   Larger OAM Indices

We now consider the application of larger m-indices upon the optical pump. As previously highlighted, when m increases, the size of the phase singularity at the centre of the pump also increases. As both optical and BEC fields are spatially bounded, rather than homogeneous as in Chapter 10, there is a limit to the transverse area that patterns can form upon, and as m increases we find that the pattern formation, rotational, and kinetic nonlinear forces all combine to present a novel means of exotic transverse reshaping of a BEC. This is summarised in Fig. 11.5, which gives the transverse fields at $\tau = 50$ for a variety of larger OAM indices $m = 6 \rightarrow 12$.
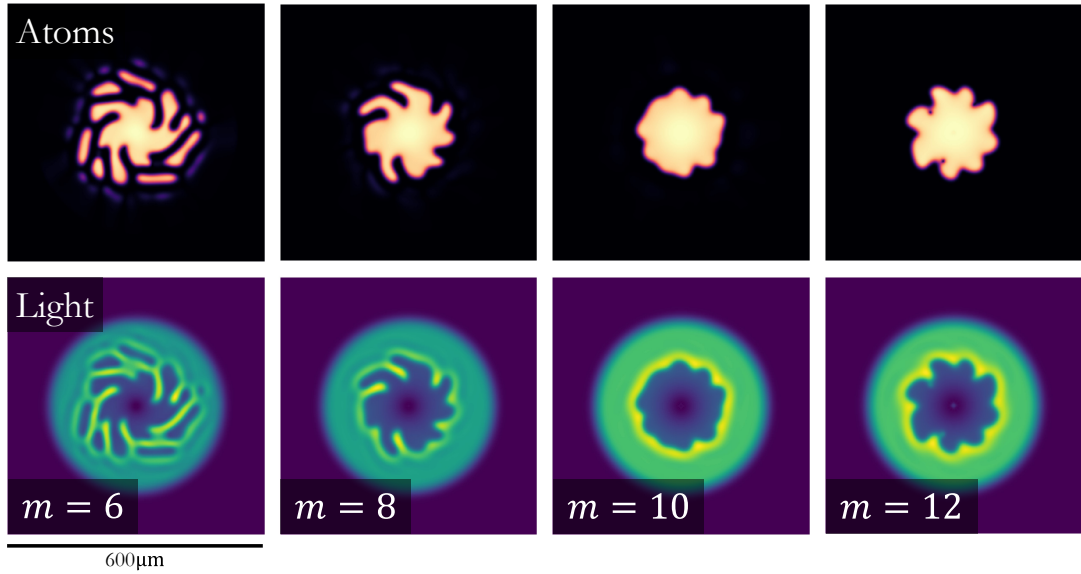
Figure 11.5: Transverse atomic (upper) and optical (lower) profiles, demonstrating exotic BEC reshaping at $\tau = 50$ for optical pumps with $m = 6 \rightarrow 12$ left to right. Fixed parameters: $\beta_{\mathrm{col}} = 2, \theta = -1, L_3 = 0.00022, s = 1, A_{\mathrm{P}} = 4, A_\psi = 2, w_\psi = w_F = 200\mu$m.

We find that at these larger $|m|$, the BEC transverse distribution rapidly reshapes into striking asymmetrical transverse distributions. In all cases considered in Fig. 11.5, the previously uniform Thomas-Fermi BEC distribution has localised more centrally, with additional protruding 'arms' spreading from the centre of the field towards the outer edges. These structures arise from the interplay in the optical field between the central phase singularity, which continues to expand spatially with increased m, and the tendency of the two fields to form coupled patterns from the dipole forces wherever the field amplitudes allow. This leads to a new regime where in part of the field 'snaking' structures are observed, a region in which distinct patterns do not quite form, but a highly asymmetric BEC cluster sits adjacent to optical regions of twisting labyrinth-like stripe patterns. The breaking of radial symmetry is an effect of the OAM of the optical pump which causes a rotation of both optical and atomic fields.

11.3   Vortex Lattices

In Fig. 11.5, for $m = 12$ two atomic 'holes' are formed. For greater τ, the number of holes increases until reaching a steady value, and by $\tau = 500$ such structures are observed for all m values considered in Fig. 11.5. To demonstrate the formation mechanism, we now plot the transverse field profiles for $m = 12$ to $\tau = 500$, showing in Fig. 11.6 the eventual formation of six atomic holes, rotating in an otherwise uniform atomic distribution naturally trapped within the central vortex of the optical field.
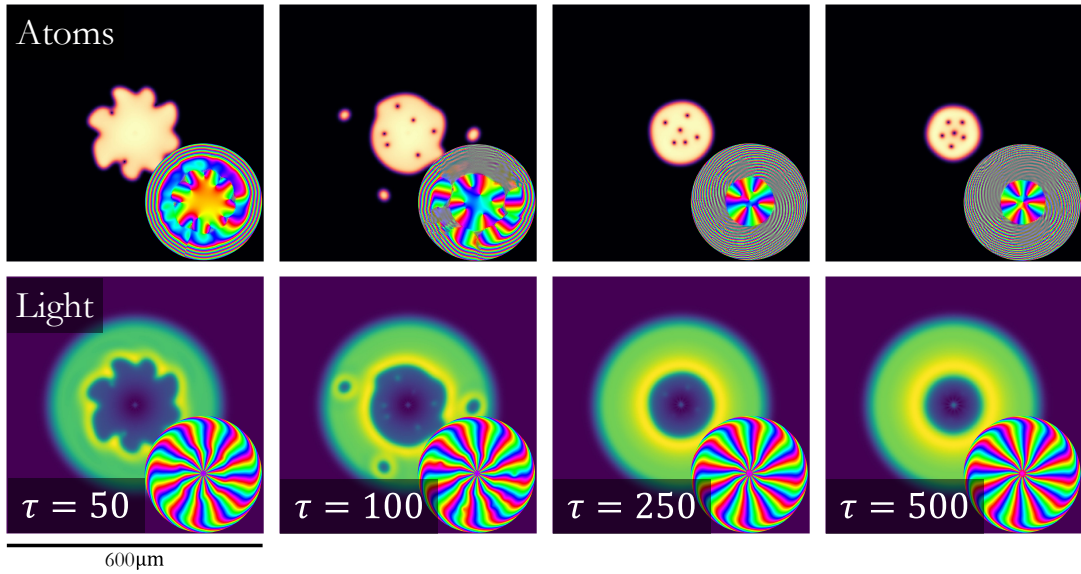
Figure 11.6: Transverse atomic (upper) and optical (lower) profiles, demonstrating the formation and natural trapping of atomic holes between $\tau = 50 \rightarrow 500$ for an optical pump with $m = 12$. Fixed parameters: $\beta_{\text{col}} = 2, \theta = -1, L_3 = 0.00022, s = 1, A_{\text{P}} = 4, A_\psi = 2, w_\psi = w_F = 200\mu\text{m}$.

Fig. 11.6 suggests that, for this particular selection of m, not only does the number of atomic vortices settle for longer run times, but that these structures appear to spatially self-organise, with an isolated hole in the centre of the field and five fairly equally spaced holes surrounding it radially. Most notable, however, are the corresponding atomic field phase portraits, which demonstrate that these are not only atomic holes with a lack of atoms, but in fact well defined BEC vortices, with a corresponding phase singularity at each field minimum. Additionally, these singularities demonstrate a transfer of OAM

from the optical field to the BEC, with a 2π phase wrap occurring at each BEC vortex. This leads to a rapid azimuthal rotation of the vortices (and the uniformly distributed atoms surrounding them), with the direction of rotation controlled by the sign of m applied to the optical pump. Though they rotate rapidly, the vortex structures formed appear robust to this motion, maintaining their spatial structures for $\tau > 10^4$. To demonstrate this, we again increase the m-index of the optical pump to higher values, and allow the fields to evolve to $\tau = 2500$. Such atomic fields for $m = 15 \rightarrow 30$ are shown in Fig. 11.7.

$m = 15$ $\qquad$ $m = 20$ $\qquad$ $m = 25$ $\qquad$ $m = 30$

600µm
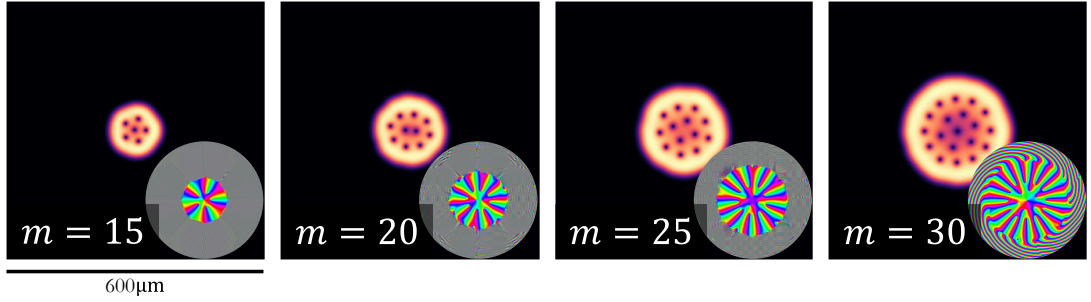
Figure 11.7: Transverse atomic field profiles, demonstrating the formation of rotating atomic vortex lattices at $\tau = 2500$ for optical pumps with $m = 15 \rightarrow 30$. Fixed parameters: $\beta_{\rm col} = 2, \theta = -1, L_3 = 0.00022, s = 1, A_{\rm P} = 4, A_\psi = 2, w_\psi = w_F = 200\mu$m.

In all cases of Fig. 11.7, we see a clear organisation in the vortex lattices by $\tau = 2500$, creating two or three rings of rotating vortices depending on the total number of vortices present within the field. This suggests that, as a cascading effect of the pump's OAM seeding azimuthal motion in bright optical regions, the subsequent motion of atoms trapped in adjacent positions of optical darkness leads to the development of vortices arising from this quantised circulation induced in the atomic field. In the correspond phase profiles, we again see a clear transfer of phase between optical and atomic fields, and each vortex position has a clear 2π phase wrap, as in the case with $m = 12$ in Fig. 11.6.

In Fig. 11.7, we also observe a clear dependence on the total number of vortices formed in the atomic field, which we label $N_{\rm v}$, with the OAM index m of the optical pump. This relationship is shown in Fig. 11.8, where $N_{\rm v}$ is plotted against m for both positive (red

markers) and negative (blue markers) values of m between $|m| = 0 \rightarrow 40$, indicating the direction of azimuthal rotation of the vortices with the marker head.
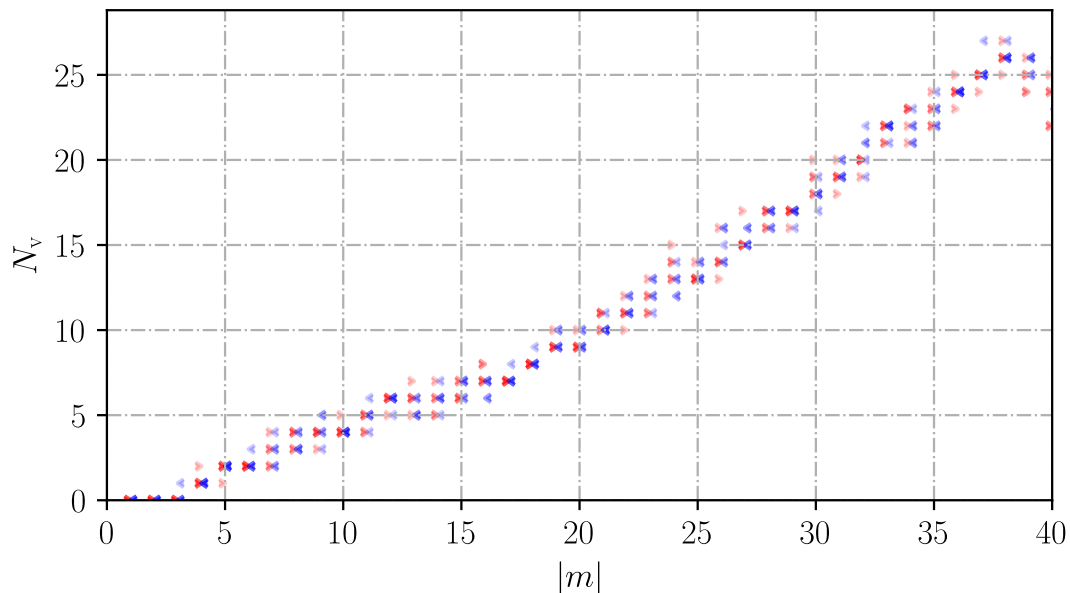
Figure 11.8: Observed number of vortices N_v for $|m| = 0 \rightarrow 40$. Red (blue) arrowheads represent positive (negative) m-value results, with the arrowhead pointing in the direction of azimuthal motion of the vortices. Fixed parameters as in Fig. 11.5.

Across all m-values considered, we find that the number of vortices that will be formed increases with increasing $|m|$. There is no clear upper bound to the size of vortex lattice formed with this method, beyond the obvious requirement to ensure that as the transverse size of the optical vortex increases with larger OAM, the transverse domain of the optical pump should increase accordingly to ensure that the entire vortex core of the beam is captured within the considered domain.

11.4   Conclusions and Outlook

In Chapter 11, we demonstrated the spontaneous pattern formation first reported in Chapter 10 on spatially structured atomic and optical fields, assuming a large enough transverse overlap at sufficient values of A_P and A_ψ. Introducing OAM to the optical pump, we seeded an azimuthal motion of these patterns in both fields, with the atomic

clusters formed being 'pushed' around by the surrounding optical maxima, whilst remaining themselves in dark optical regions. With higher OAM indices, we demonstrated the unusual transverse reshaping of large ultracold atomic distributions, and demonstrated the ability to form vortex lattices, of vortex number related to the OAM of the optical pump, within ultracold atoms trapped in the central optical singularity.

The findings we report here have many potential applications, including in generating patterns within a simpler BEC setup than in existing approaches whilst simultaneously realising a richer range of pattern formats than previously observed [183, 184, 187–190]. Additionally, there are significant potential applications in areas such as BEC transverse atomic manipulation [266], and for guiding and trapping atoms, transporting them in dark-regions without the impact of optical heating from a coincident bright optical region [51, 243, 266].

Most important, however, is the ability of our method to spontaneously generate vortex arrays in BECs, without the requirement for an external stirring potential [204, 209, 210, 267], and with the number of vortices within the array related to the OAM of the optical pump. This alternative approach to vortex array formation allows for potential applications in advancing quantum simulations in areas including modelling the behaviour of vortex matter within superconductors [268], cosmology [269], and quantum droplets [270].

Chapter 12

Structured Fields II: Atomic Persistent Currents

In this chapter, we explore further the formation of coupled atom-light Turing patterns, reported in Chapter 11.1.2 with red detuned fields. In *Section 12.1*, we consider such patterns with ring shaped optical pumps, before introducing OAM in *Section 12.2*, generating ultracold atomic persistent currents. In *Section 12.3*, we consider dynamic variation, before exploring alternative transverse current forms in *Section 12.4*, including co- or counter-rotating current superpositions: an 'atomic peppermill'. Finally, in *Section 12.5*, we consider altering the cavity detuning to realise a mechanism to obtain either coupled peak lattices, cavity solitons, or uniformly rotating rings. On top hat pumps, we introduce radial and azimuthal phase gradients to realise spiralling atomic cavity solitons.

12.1   Static Turing patterns

We now consider the formation of coupled atom-light structures within a driven optical cavity, as suggested in Chapter 11.1.2. We consider these structures forming around a

radial ring of intensity, and as such the pump becomes

$$F_{\mathrm{P}}\left(r\right) = \mathrm{LG}_0^m\left(r\right),$$

where
$$\mathrm{LG}_0^m\left(r\right) = A_{\mathrm{P}} r^{|m|} e^{-r^2/\left(2w_{F'}^2\right)}, \tag{12.1}$$

equivalent to Eqn. (3.38) after transverse scaling, taking $p = 0$, and disregarding OAM. We allow for an optical beam of beam waist w_F different to the domain transverse scaling size w_{L} through the relationship $w_{F'} = w_F/w_{\mathrm{L}}$, giving an intensity profile equivalent to a Laguerre-Gaussian mode, but with homogeneous phase profile. The initial BEC is a Thomas-Fermi distribution (Eqn. (2.17)).

We select $w_F = 40\mu$m and $w_\psi = 50\mu$m to ensure an overlap between the optical pump and the transverse BEC domain. The initial optical field is simply noise at the 1% level of the maximal pump amplitude. Both initial BEC and optical pump fields have maximal amplitudes A_ψ and A_{P}, respectively, where we select $A_\psi = 0.1, A_{\mathrm{P}} = 4$. The atomic parameters selected continue to represent a Caesium BEC, and we consider $\beta_{\mathrm{col}} \approx 2$, representing weakly repulsive interactions of $a_{\mathrm{gg}} \approx 12a_0$, with a_0 the Bohr radius. All other system parameters remain as considered within Chapters 10-11 for the case of $\kappa^{-1} \approx 10^{-8}$, giving an initial atomic field and optical pump field as shown in the left column of Fig. 12.1.
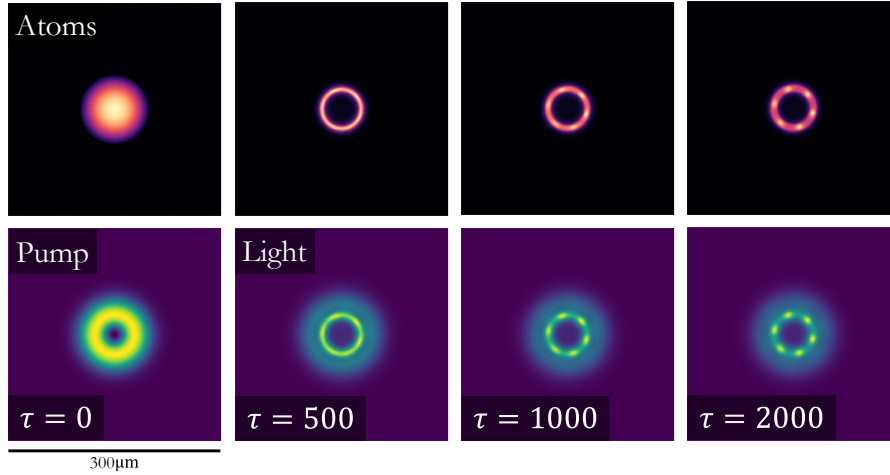
Figure 12.1: BEC (upper) and optical (lower) field transverse distributions between $\tau = 0 \rightarrow 2000$. Parameters: $\theta = 0, A_\psi = 0.1, A_{\mathrm{P}} = 4, w_\psi = 50\mu$m, $w_F = 40\mu$m.

As these fields evolve within the driven optical cavity, the atomic field initially moves to the optical field ring. Both rings then undergo mutual pattern formation, forming coupled atom-light structures in a similar mechanism to that of Section 11.1.2. For the system outlined above, this process begins around $\tau = 500$, with six evenly spaced peaks apparent by $\tau = 1000$. The system dynamics are largely confined to a single radial ring, and so we consider the continuous evolution around this ring of radius R, unwrapped as a 1D distribution, in both fields in Fig. 12.2, which shows the initial atomic ring formation, mutual fragmentation, and peak evolution of Fig. 12.1.
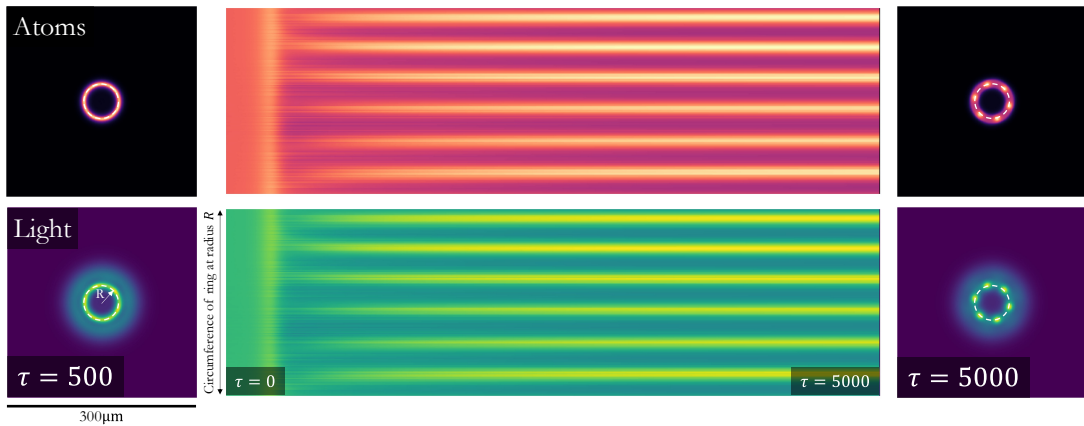
Figure 12.2: BEC (upper) and optical (lower) field evolution between $\tau = 0 \rightarrow 5000$ around an 'unwrapped' maximum intensity ring (centre) and transverse profiles at $\tau = 500$ (left) and $\tau = 5000$ (right), with position of maximum intensity ring indicated. Parameters: $\theta = 0, A_\psi = 0.1, A_P = 4, w_\psi = 50\mu m, w_F = 40\mu m$.

These dynamics are a further manifestation of Turing pattern formation [174], now occurring coincidently in the atomic field with red field detuning. Like previous chapters, we again find that changes to the pump strength A_P enable control over the temporal scale of formation, and clarity of, the patterns, with a larger A_P quickly forming patterns of increased clarity, and a smaller A_P more slowly forming patterns of decreased clarity. Below a threshold A_P, pattern formation is entirely suppressed to deliver a uniform atomic ring.

12.2 Introducing OAM

We now consider introducing OAM through a helical phase profile, $\exp\left(im\varphi\right)$. The optical pump becomes

$$F_{\mathrm{P}}\left(r,\varphi\right) = \mathrm{LG}_0^m\left(r,\varphi\right),$$

where
$$\mathrm{LG}_0^m\left(r,\varphi\right) = A_{\mathrm{P}}r^{|m_{\mathrm{P}}|}e^{-r^2/\left(2w_{F'}^2\right)}e^{im\varphi}, \tag{12.2}$$

equivalent to Eqn. (3.38) after transverse scaling and taking $p = 0$. Here, m_{P} enables a mode transverse size different to the OAM of the pump if $m_{\mathrm{P}} \neq m$. For ease of comparison we fix $m_{\mathrm{P}} = 2$, altering the OAM index, m, to ensure that patterns form on the same ring profile irrespective of the applied OAM.

On introducing a helical phase profile, we again find similar initial dynamics, and coupled atomic and optical radial rings undergo pattern formation. With OAM introduced, the lattices rotate with their speed controlled by the OAM; in Fig. 12.3 rotating lattices of seven and eight atom-light clusters with $m = 1$ and 2, respectively, are seen to form on otherwise identical rings.
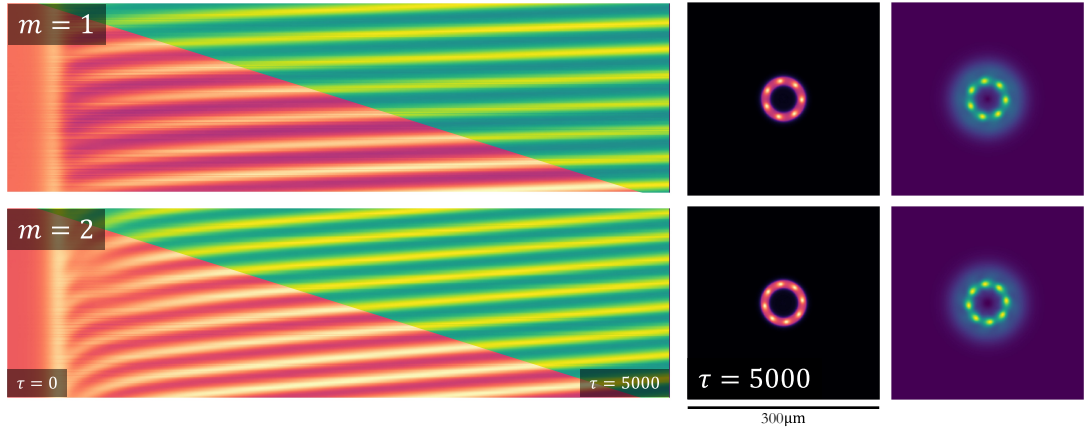
Figure 12.3: Atomic and optical ring evolution between $\tau = 0 \rightarrow 5000$ (left), and field transverse profiles at $\tau = 5000$ (right), for optical pumps with $m = 1$ (upper) and 2 (lower). Parameters: $\theta = 0, A_\psi = 0.1, A_{\mathrm{P}} = 4, w_\psi = 50\mu$m, $w_F = 40\mu$m.

These dynamics strongly suggest that the BEC is again acting as a Kerr-like superfluid [174], as was the case for co-propagating fields in Chapter 8. We find that these

atomic rotational dynamics persist, as shown in Fig. 12.4 for the $m = 2$ configuration at $\tau = 10^5$, where we note the eventual settling on a lattice of nine peaks, with the rotation speed unchanged throughout. This rotating atomic lattice is a form of atomic *persistent current* of constant azimuthal rotation, and we find no evidence of an upper current lifetime before the typical BEC lifetime. Typically, the only conditions required to be satisfied for the creation of such a current are an optical pump of $A_{\mathrm{P}} \gtrsim 2A_\psi$ and field widths such that $(w_F/w_\psi) \gtrsim 0.5$ [271, 272].
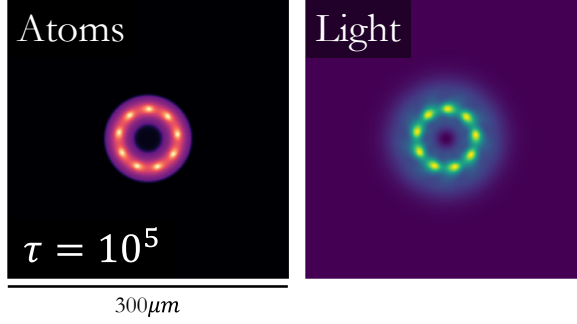
Figure 12.4: BEC (left) and optical (right) amplitude distributions at $\tau = 10^5$. Initial fields and parameters as $m = 2$ in Fig. 12.3.

As in the Kerr case, the velocity of the atomic current may be related to the OAM of the input light. Considering the initial optical fields as a ring of fixed radius R, expressing the transverse Laplacian in polar coordinates (R, φ) with R a constant such that $\partial_R \to 0$, Eqns. (9.65)-(9.66) may be written in one transverse dimension (1D):

$$\partial_\tau \psi = \frac{i}{R^2} \frac{\partial^2 \psi}{\partial \varphi^2} - i \left(s|F|^2 + \beta_{\mathrm{col}}|\psi|^2 - iL_3|\psi|^4 \right) \psi, \tag{12.3}$$

$$\partial_\tau F = F_{\mathrm{P}} - (1 + i\theta) F + \frac{i}{R^2} \frac{\partial^2 F}{\partial \varphi^2} - is|\psi|^2 F. \tag{12.4}$$

The evolution of 1D uniform fields, described by Eqns. (12.3)-(12.4), successfully predicts the number of 2D peaks, their widths, and rotation speed.

By assuming an instantaneous atomic medium with $|\psi|^2 = -(s|F|^2)/(\beta_{\mathrm{col}})$, Eqn. (12.4) becomes

$$\partial_\tau F = F_{\mathrm{P}} - (1 + i\theta) F + \frac{i}{R^2} \frac{\partial^2 F}{\partial \varphi^2} + i \frac{|F|^2}{\beta_{\mathrm{col}}} F. \tag{12.5}$$

143

Following the procedures of Ref. [174], Eqn. (12.5) will involve a pump that carries OAM, and will therefore have solutions which take the form

$$F(m, \tau) \rightarrow \mathcal{F}(m, \tau)e^{im\varphi}, \tag{12.6}$$

meaning that Eqn. (12.5) becomes

$$\partial_\tau \mathcal{F} + \frac{2m}{R^2}\partial_\varphi \mathcal{F} = F_{\mathrm{P}} - \left[1 + i\left(\theta + \frac{m^2}{R^2}\right)\right]\mathcal{F} + \frac{i}{R^2}\frac{\partial^2 \mathcal{F}}{\partial \varphi^2} + i\frac{|\mathcal{F}|^2}{\beta_{\mathrm{col}}}\mathcal{F}. \tag{12.7}$$

If we consider the travelling solutions of Eqn. (12.7) of the form $F(q)$ to depend on φ and τ through $q = \varphi - \omega\tau$, then we may write that

$$\partial_\tau \mathcal{F} + \frac{2m}{R^2}\partial_\varphi \mathcal{F} = \partial_q \mathcal{F}(q)\left(-\omega + \frac{2m}{R^2}\right). \tag{12.8}$$

The bracket on the right hand side of Eqn. (12.8) is zero when

$$\omega = \frac{2m}{R^2}, \tag{12.9}$$

providing a prediction for the angular velocity, ω, of solutions satisfying Eqn. (12.5).

Eqn. (12.9) suggests that the characteristics of the current may be altered by the OAM and waist size of the pump. Testing this in Fig. 12.5, we form, in 2D, a range of current configurations, using a LG mode as the optical pump with various OAM selections and beam waists, before calculating the average current velocity in each case.

Applying Eqn. (12.9) to an LG mode, which increases its transverse size as m increases, one would expect the same angular velocity for each m [174]. However, in Fig. 12.5, we observe notable variation of ω with m for the various beam waists, suggesting that the atomic field introduces a 'drag' upon the idealised optical dynamics within a Kerr medium, in a similar way to that observed in cold atoms [61]. Further investigation is required to quantify this drag factor, but we note that, in the case of $\kappa^{-1} \approx 10^{-1}$, little atomic drag is observed, with the current velocity instead closely following the relationship of Eqn. (12.5). We also note that, as expected, the average current velocity
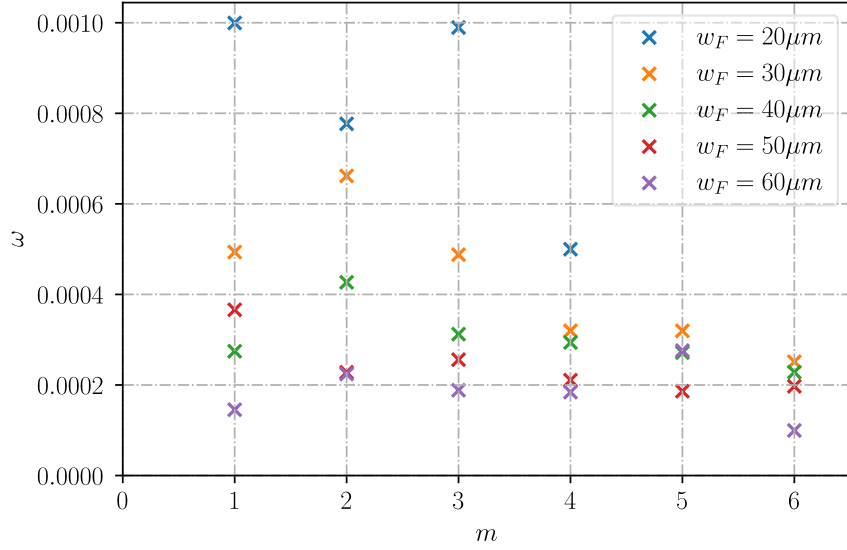
Figure 12.5: Atomic current velocities when using pumps of a LG mode with $m = 1 \rightarrow 6$ and $w_F = 20 \rightarrow 60\mu$m. Parameters as in Fig. 12.3.

decreases with increasing R. Taking the results for $w_F = 40\mu$m and converting τ to physical units through Eqns. (9.32) and (9.57), we calculate an approximate rotation speed of 2ms^{-1} across the considered m-values and their respective ring sizes.

This approach therefore enables the creation of an atomic current, of customisable velocity and rotation direction, related to the OAM and radius of the pump. As will be shown in the next section, this enables *dynamic* control of the direction, size, and strength of the current, providing a simple way to tailor ultracold atomic currents.

12.3 Dynamic Current Reconfigurability

In this section, we outline three examples of *dynamic* atomic persistent current formation as an indication of the possibilities opened by our proposed mechanism.

12.3.1 Direction Switching Atoms

We first consider switching the direction of current rotation throughout its evolution. It is readily possible to switch the OAM applied to a pump by dynamically changing the hologram applied to an SLM [120, 121]. As the sign of the OAM directly alters the

phase ramp, which in turn alters the direction of atomic rotation, this allows dynamic switching of the current direction [272].

We again consider the $m = 2$ case of Fig. 12.3, but now switch the OAM of the pump between $m = 2, -2, 2, ...$ at $\tau = 0, 2000, 4000, ...$. This results in the current dynamics given in Fig. 12.6, which shows the rotational motion around a ring of maximum radial intensity, with the phase switching positions indicated by small arrows.
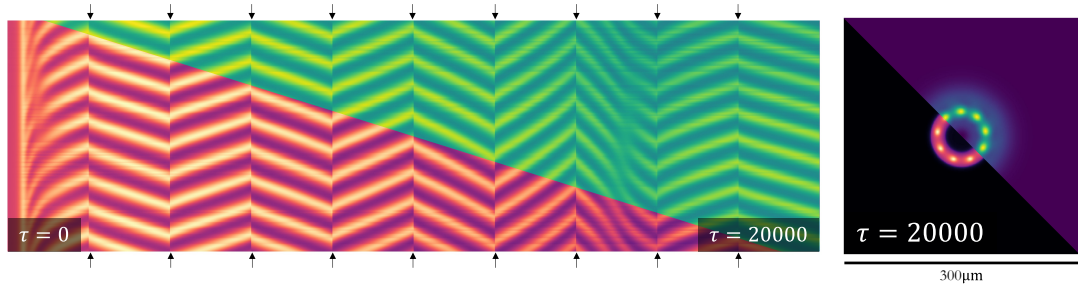
Figure 12.6: Atomic (lower) and optical (upper diagonal) fields between $\tau = 0 \rightarrow 20000$ around the current ring (left), and at $\tau = 20000$ (right), for a pump switching between $m = \pm 2$ at intervals of $\tau = 2000$ (each arrow). Other parameters as Fig. 12.3.

Fig. 12.6 demonstrates that altering the pump's OAM provides an excellent mechanism to switch the rotational direction of the current at any time after lattice formation. The transition from eight to nine lattices around $\tau = 15000$ (as discussed around Fig. 12.4) is still observed in this case, regardless of any change to the pump's OAM. Crucially, this means that the ability to change the direction of the current will have no impact upon the lattice structure outside its motion, as demonstrated by the final field amplitude distributions at $\tau = 20000$.

12.3.2 Accelerating Atoms

As well as switching the sign of the OAM applied to the pump, we may also change its magnitude using a SLM [120, 121]. For a pump of a fixed radius, increasing the OAM will lead to an acceleration in the rotational motion of the atomic current.

To demonstrate this, we ramp the change of OAM over a time period, providing an acceleration upon the atoms, rather than an immediate motion switch. We consider, between $\tau = 0 \rightarrow 10000$, an initially stationary lattice of peaks ($m = 0$), with the

pump then increased to $m = 1$ uniformly over a period of $\tau = 500$. The results of this procedure are shown in Fig. 12.7, with the arrows now indicating the onset and end of the phase ramp (i.e. the final / initial times where the optical pump has an OAM of $m = 0$ / $m = 1$).
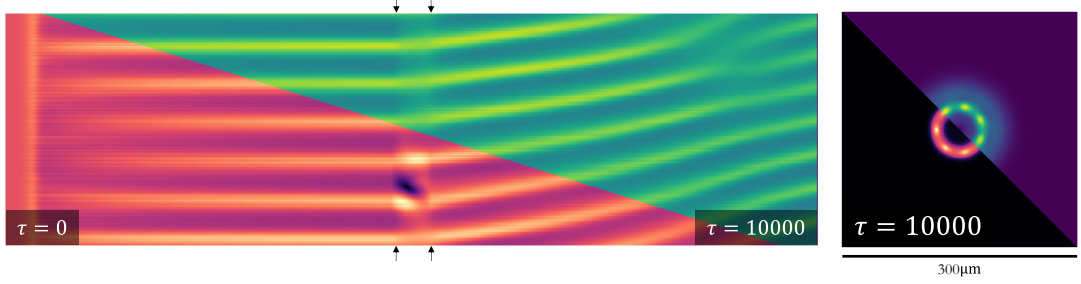
Figure 12.7: Atomic (lower) and optical (upper diagonal) fields between $\tau = 0 \rightarrow 10000$ around the current ring (left), and at $\tau = 10000$ (right), for a pump changing from $m = 0 \rightarrow 1$ in the central $\tau = 500$ interval (arrows). Other parameters as Fig. 12.3.

An acceleration of the atom-light lattice peaks from their stationary state to the expected $m = 1$ velocity is observed, at which point they settle upon a fixed velocity. The introduction of OAM in the pump leads to a temporary minimum being created around the ring as the phase singularity forms in the optical field, leading to a restriction and redistribution of the lower two peaks. After the singularity has formed in the optical field, the lattice settles and we observe six evenly distributed peaks, now also rotating. For the peaks unaffected by the optically-induced temporary redistribution, a clear acceleration is observed as they commence a radial motion. For further evolution as an $m = 1$ current, the upper peaks fragment, forming an additional peak to obtain a final lattice of seven rotating peaks, as previously obtained with $m = 1$ in Fig. 12.3.

12.3.3 Decelerating Atoms

Finally we exemplify the deceleration of an initially rotating current lattice. To realise this, we perform roughly the inverse procedure of that used to obtain accelerating atoms, ramping down the optical pump driving the cavity from an initial $m = 1$ state to a final $m = 0$ state. We select a different temporal period to demonstrate the flexibility of this method, and consider ramping the phase over a central $\tau = 25$ period,

significantly quicker than previously considered.   The result of such a procedure is shown in Fig. 12.8.
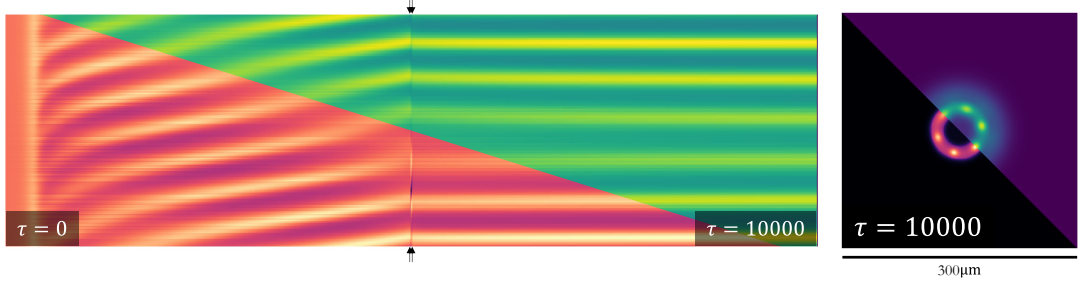
Figure 12.8: Atomic (lower) and optical (upper diagonal) fields between $\tau = 0 \to 10000$ around the current ring (left), and at $\tau = 10000$ (right), for a pump changing from $m = 1 \to 0$ in the central $\tau = 25$ interval (arrows). Other parameters as Fig. 12.3.

With the pump initially at $m = 1$, we observe the formation of an atom-light lattice of six peaks that rotates at the expected rate. Slightly before $\tau = 5000$, with the phase of the optical pump progressively being ramped down, we see a rapid deceleration of the peaks, with the position of phase interference temporarily impacting the behaviour of some lower peaks, though this impact is much less clear here than with accelerating atoms due to the more rapid ramp rate. As the $m = 0$ pump becomes dominant, the lattice positions self-regulate to realise six evenly distributed lattice peaks that no longer exhibit rotational motion.

12.4   Transverse Current Alterations

Having shown that we can tailor the 'switching' on or off of azimuthal atomic motion whenever desired simply by altering the OAM of the optical pump driving the cavity, we now focus on altering the *transverse* current characteristics.

12.4.1   Lattice Number

Considering again the 1D description of Eqn. (12.5), its stationary solutions will satisfy

$$F_{\mathrm{P}} = \left(1 + i\left[\theta + \frac{m^2}{R^2} + \frac{|F|^2}{\beta_{\mathrm{col}}}\right]\right)F. \tag{12.10}$$

Following Ref. [174], these solutions will have a number of lattice peaks, N_P, given by

$$N_P = \sqrt{\frac{2|F|^2}{\beta_{\text{col}}}R^2 - m^2},$$

(12.11)

for the case of $\theta = 0$.

We test Eqn. (12.11) against a variety of pumps of waist $w_F \equiv R = 15 \rightarrow 80\mu$m, fixing the BEC to $w_\psi = 100\mu$m to ensure atomic coverage across all optical modes. For each selected w_F, we plot the result of several runs, reflecting the variation of the exact number of peaks in the lattice obtained from each run. Plotting the obtained current lattice number, N_P, against w_F in the left hand side of Fig. 12.9, the expected dependence on $R \equiv w_F$ from Eqn. (12.11) is observed.
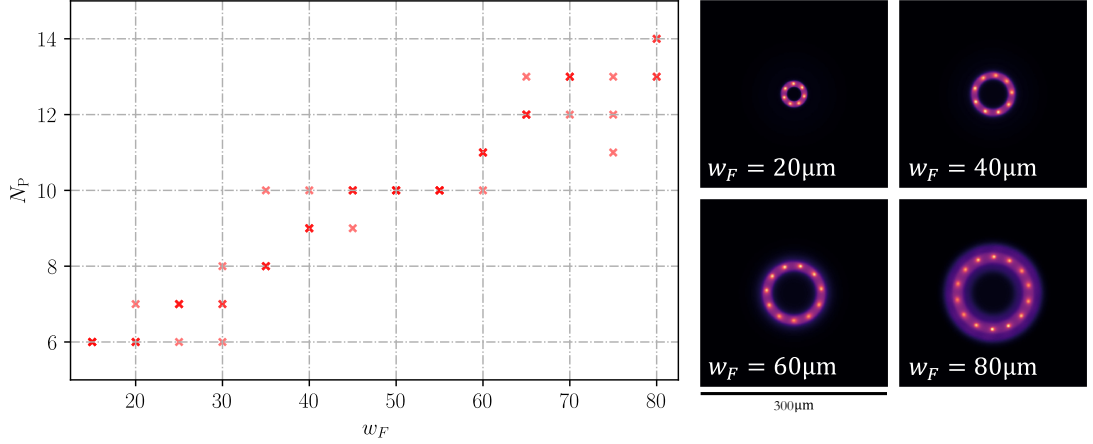
Figure 12.9: Left: number of lattice peaks N_P obtained in an atomic persistent current for different pump waist sizes $w_F = 15 \rightarrow 80\mu$m when $m = 2$. Right: selected 2D transverse atomic currents for indicated w_F. Other parameters as in Fig. 12.4.

It may be noted that $w_F \approx 15\mu$m acts as a minimum optical beam waist for Turing pattern formation for this initial field and parameter combination, beneath which the pattern wavelength is mismatched with respect to the ring size, returning instead a uniform ring. On the right hand side of Fig. 12.9 we indicate selected transverse forms of atomic currents for the considered values of w_F, demonstrating the range of lattice numbers attainable.

12.4.2   Dynamically Varying Waist Sizes

Building on the ability to change the velocity characteristics of the atomic current through the optical pump driving the cavity, we now consider similar dynamic changes to the pump's beam waist [272]. In this case, we again consider evolving a pump as outlined for $m = 2$ in Fig. 12.3, now to $\tau = 30000$, and change its beam waist from $w_F = 40 \to 60\mu$m between $\tau = 5000 \to 15000$. The results are shown in Fig. 12.10, where we show the evolution around both rings.
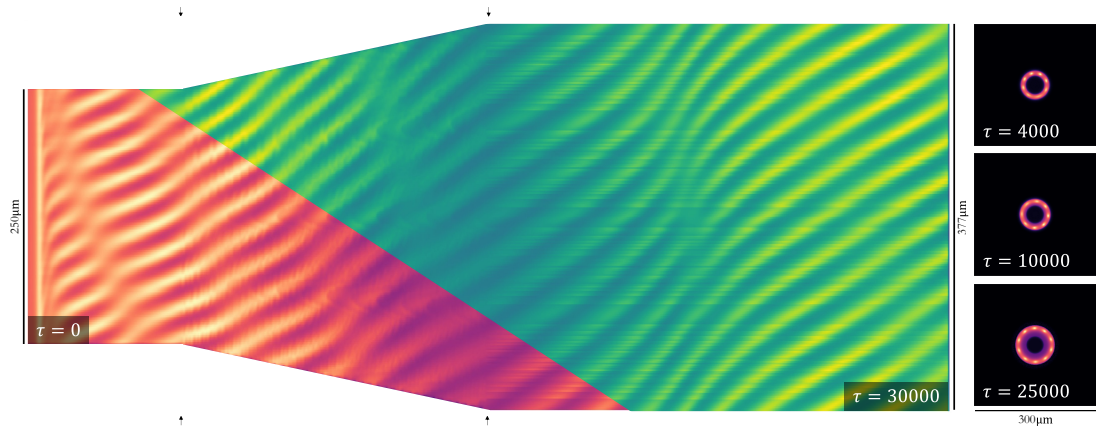
Figure 12.10:   Atomic (lower) and optical (upper diagonal) field evolution between $\tau = 0 \to 30000$ around a maximum intensity ring (left), and selected atomic transverse amplitude distributions (right), for an optical pump uniformly changing from $w_F = 40 \to 60\mu$m between $\tau = 5000 \to 15000$ (indicated by arrows). Other parameters as in Fig. 12.4.

From Fig. 12.10, dynamically altering the pump's waist size leads to the expected dynamic alterations in the position of the atomic patterns in the transverse field. We observe an excellent transport of atoms, with the lattice moving entirely from the 40μm radius ring to the 60μm ring by $\tau = 30000$, reflected in the relative fade and growth in the upper and lower ring evolution, respectively. Furthermore, as the lattice moves radially outwards, the spacing between peaks self-regulates through instances of peak splitting, and by the end of the evolution period we observe the formation of a further two peaks, in agreement with Fig. 12.9, despite having not followed the idealised formation mechanism.

The same approach also works for decreasing the transverse waist size of the atomic

current, as demonstrated in Fig. 12.11, where we alter the beam waist from $w_F = 40 \to 20\mu$m between $\tau = 3000 \to 7000$. In this case, as well as the transverse size of the current decreasing as expected, we also observe a period of peak merging, eventually returning seven uniformly spaced rotating peaks around the atomic current, in agreement with Fig. 12.9.

Figure 12.11: Atomic (lower) and optical (upper diagonal) field evolution between $\tau = 0 \to 20000$ around a maximum intensity ring (left), and atomic transverse amplitude distributions (right), for an optical pump uniformly changing from $w_F = 40 \to 20\mu$m between $\tau = 3000 \to 7000$ (indicated by arrows). Other parameters as in Fig. 12.4.

This method of altering the pump's waist size therefore provides another dynamic means of tailoring the transverse size of any atomic current formed.

12.4.3 Atomic Peppermill

Having shown how the optical pump may be used to control the size, velocity, and directional characteristics of the atomic current formed, we now consider creating multiple concentric currents by using a customised SLM that superimposes a number of optical rings with sufficiently different OAM-values to prevent overlap [174]. The optical pump becomes a superposition of LG modes, each of which has an independent phase applied. These scalar modes are then summed to form the total pump that enters the cavity. Fig. 12.12 exemplifies three such setups, showing the optical pump (top row) and the resultant field profiles after evolution to $\tau = 10^4$ (bottom row), where the flow direction of any atomic current is indicated with an arrow.

As a result of the m and w_F selections, the rings may counter-rotate (left), co-rotate anti-clockwise (centre), or co-rotate clockwise (right), with the respective speeds of
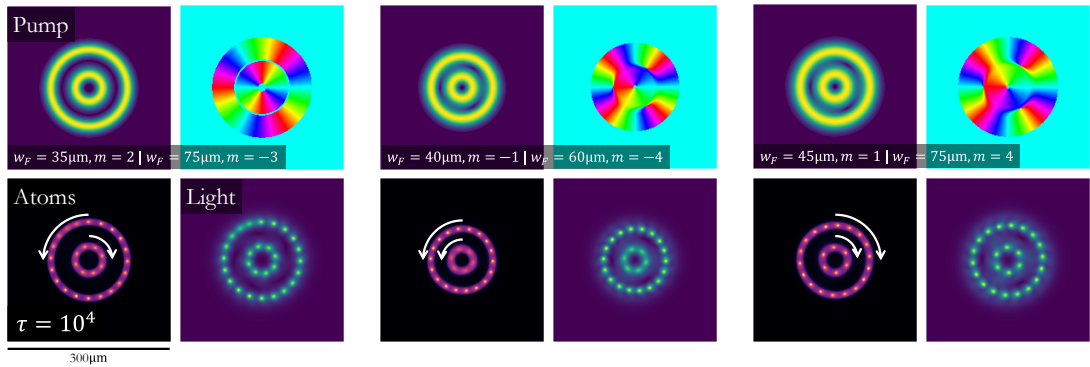
Figure 12.12: Top row: optical pump amplitude (left) and phase (right). Bottom row: BEC (left) and optical (right) amplitude at $\tau = 10^4$, arrow indicating current direction. Pump parameters indicated beneath top row of each set of four panels. Other parameters as in Fig. 12.4.

each ring continuing to observe Eqn. (12.9). We coin the term 'atomic peppermills' to describe such structures, which are an extension of those previously observed inside an optical Kerr cavity [174]. Our method realises *independent* control over each atomic current ring through the optical pump. We emphasise that, similarly to previous sections of this chapter, our selection of optical pump here is simply indicative, with a far wider range of transverse setups, sizes and rotational directions available by changing the respective control parameters outlined.

12.5   Cavity Solitons

Throughout this chapter, we have reported on various realisations of atomic persistent currents with increasing dynamical complexity, considered without cavity detuning ($\theta = 0$). Previous studies using the Lugiato-Lefever equation have shown that such pattern formation is related to the cavity detuning, which modifies the dominant pattern wavevector as the difference between ω_c and ω_P in Eqn. (9.30) grows, and so in this section we consider the alternative cases of $\theta \neq 0$.

12.5.1 Solitons on a Ring

We return to the setup of Fig. 12.4, where an LG pump led to the formation of a single rotating atom-light lattice. By changing the cavity detuning such that $\theta < 0$, we find that the only effect is that the clarity of the rotating patterns decreases. For $\theta \lesssim -1.5$, the lattice formation is inhibited and both fields simply return uniform rings without any evidence of current formation.

By increasing the cavity detuning to moderately positive values however, we may realise rotating atomic currents with a wide range of lattice numbers, or uniform rings of (rotating) atomic current, *without* requiring a change in the beam waist of the optical pump. Considering Eqn. (12.10), when $\theta \neq 0$ the number of lattice peaks, N_{P}, of this solution may be written as [174]

$$N_{\mathrm{P}} = \sqrt{\left(\frac{2|F|^2}{\beta_{\mathrm{col}}} - \theta\right) R^2 - m^2}. \tag{12.12}$$

This suggests that, as θ increases, we would expect the pattern formation to remain, but with a decreasing number of peaks as θ increases, before eventually entering a regime of no peak formation. In Fig. 12.13, we therefore consider several positive θ-values to test this prediction, as indicated in the panels.
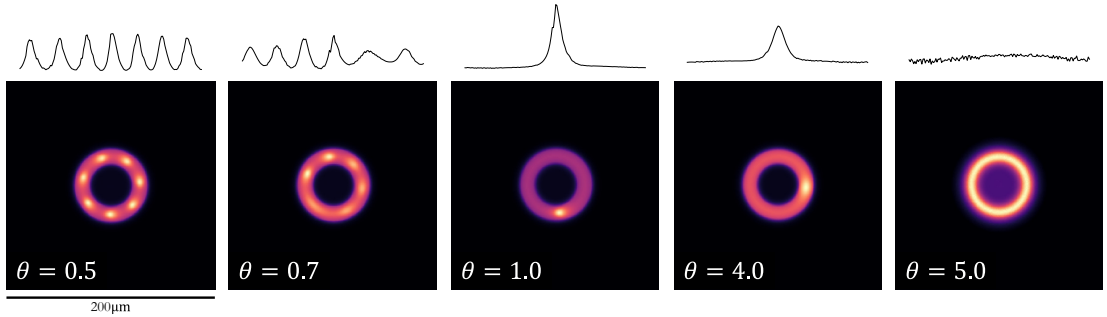
Figure 12.13: BEC transverse amplitude distributions at $\tau = 10^4$ for $\theta = 0.5$, 0.7, 1.0, 4.0, and 5.0 left to right. Other parameters as Fig. 12.4. 1D radial profiles around the maximum intensity ring of the atomic field included above 2D panels.

Such changes to the cavity detuning lead to a transition through atomic lattices of lessening peak numbers, to isolated solitary peak(s) with recognisable tails in the op-

tical field, to a uniform atomic ring: a rotating, uniform ultracold atomic ring, with many analogies in nature [199]. For fields as described here, we find that we obtain cavity solitons between $\theta = 1.0 \rightarrow 4.0$, but these values vary according to the initial fields and transverse current sizes. Our method therefore provides a means of current generation, not only of any desired speed and transverse size, but also with the capacity to determine whether the current forms on a customisable number of peaks, or entirely uniform, intensity structure.

12.5.2 Spiralling Solitons

We may also obtain cavity solitons, equivalent to those obtained on Laguerre-Gaussian modes, when we alter the optical pump to a top hat field, as defined by Eqn. (11.2). We maintain $m = 2$, but increase $w_F = w_\psi = 100\mu$m and select $\theta = 1.5$ to obtain, as expected by this detuning selection, a single rotating cavity soliton, now on a broader transverse background than when using a ring-based optical pump. The initial atomic field, pump, and coupled atom-light fields at $\tau = 10000$ are shown in Fig. 12.14.
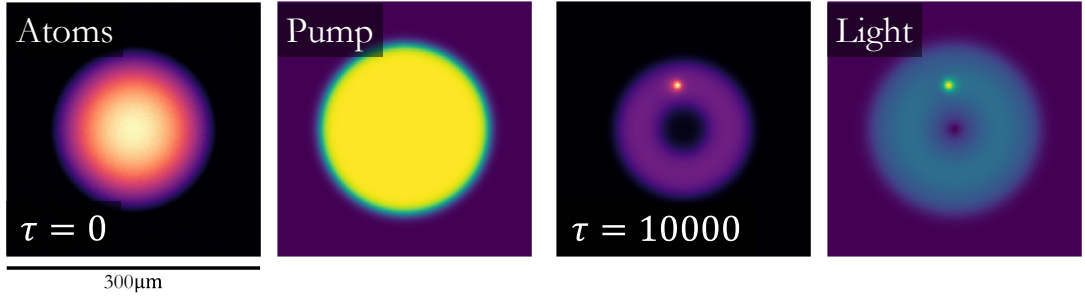
Figure 12.14: Atom-light cavity soliton formation on a top hat pump, with $w_F = w_\psi = 100\mu$m and $\theta = 1.5$. Left pair: initial atomic and optical pump. Right pair: Atomic and optical fields at $\tau = 10000$. Other parameters as in Fig. 12.4.

We may introduce an additional, radial, phase gradient into the top hat pump by altering Eqn. (11.2) into the form

$$F_{\mathrm{P}}(r, m) = A_{\mathrm{P}} \left[\frac{1}{2}\left(1 - \tanh\big(S\left(r - w_{F'}\right)\big)\right)\right] e^{i(m\varphi + \alpha r)}, \qquad (12.13)$$

where α represents the strength of the applied gradient. Throughout, we consider

$|\alpha| \leq 0.1$, ensuring that it contributes to, but does not overwhelm, the system dynamics.

When $\alpha > 0$, the phase gradient transports the atom-light soliton radially out from the centre of the field, only stopping on reaching the edge of the pump. The speed at which this alteration in radial position occurs is also, as expected, controlled by the size of α. Fig. 12.15 exemplifies dynamics where we evolve the final fields of Fig. 12.14 for a further $\tau = 10^5$ period with different applied α values left to right, in each case displaying the superposition of the fields across this temporal range to allow for the azimuthal motion of the soliton to be tracked.
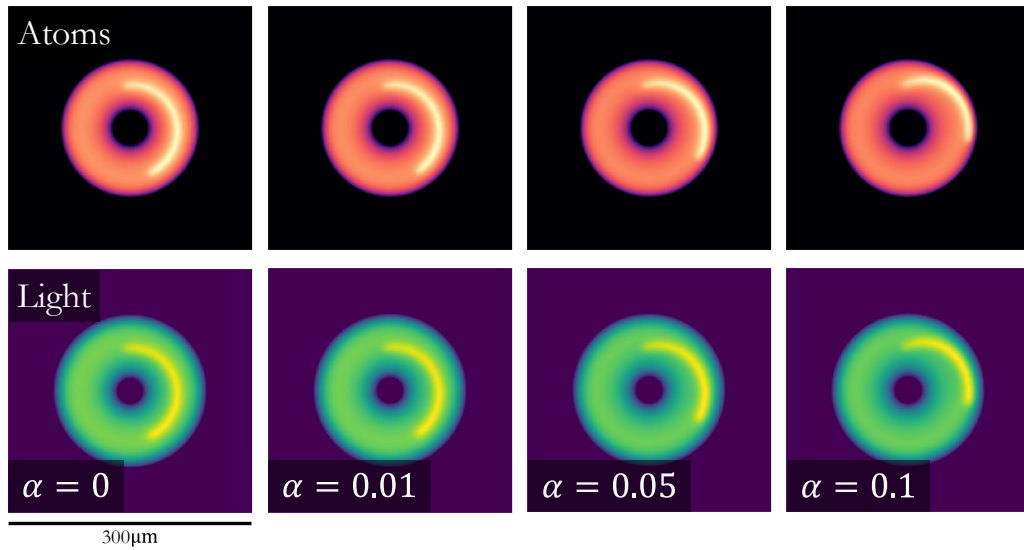
Figure 12.15: Superimposed atomic (upper) and optical (lower) fields over a $\tau = 10^5$ period for positive α phase gradients indicated applied to the optical pump. Initial fields from right hand of Fig. 12.14. Parameters otherwise as Fig. 12.14.

When $\alpha = 0$, the coupled soliton rotates azimuthally around a fixed ring radius. As α increases, the strength of the phase gradient steadily increases, and with a larger radial phase gradient there is a faster outward radial motion of the soliton, leading to an outward spiralling of the coupled structure. Due to its increasing ring radius, the velocity of the soliton slows, and the radial distance travelled progressively decreases as α increases. By $\alpha = 0.05$, the soliton reaches the outer transverse edge of the pump's domain within the considered evolution period, and so the gradient causes it to simply continue rotating around this extreme radius with further evolution.

If $\alpha < 0$, the radial phase gradient now causes the solitons to spiral inward, shown in Fig. 12.16, which again evolves the fields of Fig. 12.14 for a further $\tau = 10^5$ period.
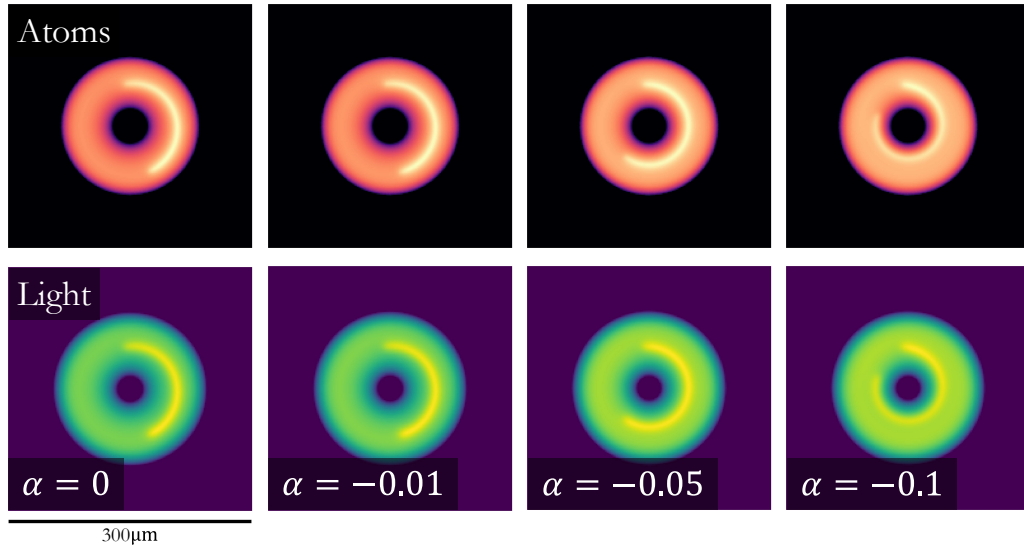
Figure 12.16: Superimposed atomic (upper) and optical (lower) fields over a $\tau = 10^5$ period for negative α phase gradients indicated applied to the optical pump. Initial fields from right hand of Fig. 12.14. Parameters otherwise as Fig. 12.14.

Again, as the magnitude of α increases, the strength of the gradient increases, which in this case leads to an inward spiralling motion of the solitons due to the negative value of α. With a weak gradient of $\alpha = -0.01$ there is little inward spiralling observed, but as α decreases, we observe a dramatic inward spiralling of the solitary peak as it falls into the centre of the field, gaining a quicker azimuthal velocity, before rotating around the central optical phase singularity. The effect of an increased strength of $\alpha = -0.1$ is apparent here too, with the final radius upon which the soliton rotates notably narrower and closer to the central singularity than the $\alpha = -0.05$ case.

12.6 Conclusions and Outlook

In Chapter 12, the formation of coupled atom-light lattices of Turing patterns have been investigated, enabled by red atom-field detuning and the dipole forces between the two fields. With OAM in the optical pump, rotational motion was added to these patterns, and the transfer of rotational motion arising from the optical pump's helical

phase to both the optical and atomic fields was observed. We propose this as a method for atomic persistent current formation, producing a highly tuneable current without the need for complex trapping potentials.

As the behaviour of the atomic current depends on the optical pump, we outlined the capacity for direction switching, accelerating, and decelerating atomic currents, as well as alterations in the number of lattice peaks. Building on this, the ability to superimpose several current rings was demonstrated, the speed, size, and direction of which can be controlled independently, forming an 'atomic peppermill' superposition of currents. Achieving such structures, with the level of control outlined here, would be highly challenging using current trap-based setups.

Finally, it has been demonstrated that changes to the cavity detuning provide a mechanism to change the intensity structure of the current, obtaining either coupled lattices, small numbers of coupled cavity solitons, or uniformly rotating rings. On broader optical top hat pumps, phase gradients have been applied to the optical pump to obtain spiralling inward or outward atom-light cavity solitons.

As such, our method provides a means of dynamically reconfigurable ultracold atomic current generation of a desired speed, size, and atom number, on either lattice or uniform intensity structures. This complete control, building on prior work [61, 174, 273], enhances the capabilities of existing approaches to ultracold atomic persistent current generation, in particular with the now possible realisation of dynamically reconfigurable dynamics, with obvious links to the field of atomtronic current generation [197, 198].

In addition to enhanced control of a single current ring, our method also allows for the superposition of currents, a challenging prospect with conventional trapping approaches [206, 207, 219, 222, 274] - an 'atomic peppermill', a red-detuned equivalent of the 'optical revolver' of Ref. [252], demonstrating the powerful ability of our method to superimpose several transverse currents. The independent control over each current ring that our method allows has many potential applications, including in simultaneous or interleaved cog-like atomic SQUIDs for atomtronics [197, 198], and current interactions for phase-slip qubit realisation [275, 276].

Part IV

Conclusions

Findings Within This Thesis

Throughout this thesis, we have considered various approaches to study the capacity of light to control the behaviour of ultracold atoms. In the majority of cases, we have specifically considered *structured* light - light structured in both intensity and phase such that the atoms are subjected to phase gradients, in addition to confinement and transport through the typical intensity gradient-based approach.

We studied two physical configurations within which such atom-light interactions can occur. The first, considered in Part II, was the co-propagation of ultracold matter waves and optical fields, initially focusing upon extending the viability of existing models in the literature describing mutual self-structuring of homogeneous atomic and optical fields, through the dipole force felt by each from the other, into coupled filamentation patterns [32, 33]. The nature of these coupled patterns was controlled by the detuning between the fields, enabling light- or dark-seeking atoms with a selection of red- or blue-atom-field detuning, respectively.

We extended these studies to fields with intensity structure, again obtaining coupled patterns as expected from Ref. [33]. With the addition of further nonlinear terms to the model, we presented a means of avoiding subsequent numerical collapse whilst still exhibiting self-structuring. Crucially, such a model leads to subsequent stable co-propagation, allowing the investigation of these dipole-led interactions between the fields at significantly longer co-propagation scales.

Applying the extended model to structured optical fields, we presented cases of coupled field dynamics where the optical field acted as a highly effective mechanism to guide the co-propagating ultracold atomic beam. We outlined a number of configurations in which atoms may be trapped in optical brightness or darkness, with the precise configuration of this atomic trapping defined by the distribution of the optical field and field detuning selection. Notably, we outlined a scheme by which, using Laguerre-Gaussian optical rings and red atom-field detuning (bright-seeking atoms), Kerr-like fragmentation in both fields permitted the formation of coupled atom-light clusters, which behaved like

spatial optical solitons [148, 149]. Crucially, the number of coupled clusters formed was exclusively determined by the OAM of the optical beam: for a beam of OAM $\pm m$, one obtained $2|m|$ clusters in each field. This approach thus provides a simple means of confining an ultracold atomic beam into a pre-determined number of clusters. Additionally, the clusters were shown to begin to rotate before eventual ejection: a mechanism of OAM rotational transfer from the optical to the atomic field. Alternatively, with blue atom-field detuning, we outlined a means of producing broader atomic clusters, now in positions of optical darkness, through the scalar superposition of LG optical beams. In this case, the clusters rotated around their centres, 'pushed' by the surrounding optical field. For both the blue- and red-detuned cases, we realised a method of atomic cluster generation, of customisable number determined purely through the initial optical field's characteristics: a powerful mechanism of atomic confinement and trapping.

In Part III, we considered atom-light interactions within a driven optical cavity. With the optical field now circulatory and encountering the atomic medium on many occasions, additional temporal control of the dynamics was realised, along with greater capacity to design the transverse characteristics of the atomic medium. Initially, we outlined an updated numerical description of the involved atom-light interactions within a driven optical cavity, based around a Lugiato-Lefever description of the optical dynamics [168]. In this case, the ultracold atomic medium was considered static in the centre of the cavity, rather than co-propagating with an optical field as in Part II. The nature of atom-field interactions remained determined by the atom-field detuning, enabling similar differentiation between light- and dark-seeking atoms as in Part II.

Before considering structured optical and atomic fields, we first studied the dynamics of homogeneous fields, similar to the procedure followed for co-propagating fields. Within a driven optical cavity, coupled patterns were again obtained, but their dynamics were significantly richer, and we observed the formation of spontaneous Turing-like patterns with blue atom-field detuning [153]. Observing both bistable and monostable regimes within the system, we demonstrated that bistable regimes permit hysteresis behaviour between a homogeneous and patterned state in both atomic and optical fields. Within

monostable regimes, we demonstrated a wide breadth of possible pattern varieties across both fields. Additionally, we demonstrated the formation of atomic cavity solitons, restricted to regions of attractive interatomic BEC interactions for blue atom-field detuning, but far more widespread for the case of red atom-field detuning, and therefore light-seeking atoms.

Moving to initially structured optical and atomic fields, we initially considered a direct extension of the coupled Turing pattern formation, and demonstrated their presence for spatially structured fields in the form of optical 'top hat' modes. By introducing a structured optical phase to the optical pump through OAM, the patterns azimuthally rotated with their rotation rate and direction determined by the OAM index, m. Considering larger values of $|m|$ we demonstrated that the interplay of nonlinear forces leads to a complex transverse reshaping of the ultracold atomic field, providing a highly effective atomic trap in the central portion of the optical field. At longer run times, we observed that the OAM of the optical field becomes completely transferred to the atomic field, and that such rotational atomic motion leads to the formation of atomic vortices, unique to the atomic field. The vortices formed organised themselves into grid-like, rotating structures, with the total number of vortices proportional to the OAM of the optical pump.

Finally, we considered an alternative formation mechanism for Turing patterns, occurring as a lattice of peaks atop an off-axis ring of optical intensity. With Laguerre-Gaussian optical pumps, we confirmed that, akin to behaviour within a self-focusing Kerr cavity, atom-light interactions within a driven optical cavity of this nature will lead to the formation of rotating Turing patterns [174]. With red atom-field detuning the atoms are captured by the light, and also rotate around the ring of fixed radius: a form of atomic persistent current, guided by the optical field. Like the Kerr case, we reported that the characteristics of these currents are set by the OAM and ring radius selections.

Crucially, we also reported on the *dynamic* capabilities of this method of atomic persistent current generation. Through alterations to the profile of the optical pump in time,

161

we established that it was variously possible to: switch the direction of the rotation of the current; accelerate the current from a stationary configuration; decelerate the current to a stationary configuration; or progressively vary the transverse size of the current, leading to the formation of additional lattices from the previous background of the ring structure as appropriate. Alternatively, with an optical pump of a scalar superposition of LG modes, we outlined that an 'atomic peppermill' - a co- or counter-rotating transverse current distribution (depending on the OAM index selection) was also possible.

A final capability of this method of current generation was outlined through its dependence on the cavity detuning. We showed that with increased cavity detuning, it was possible to alter the lattice structure without adapting its ring size, realising transitions from evenly distributed lattices to small numbers of cavity solitons and uniformly rotating current rings. Employing this technique to realise isolated atomic cavity solitons on optical top hat pumps, we used an additional phase gradient within the pump to cause inward or outward spiralling of the atomic cavity solitons, observing the expected variation in its velocity as its ring radius altered.

Prospective Applications

The work within this thesis was designed to explore the capacity of light, typically structured in both intensity and phase, to control the behaviour of ultracold atoms. We have realised many such methods of control and this work is potentially applicable in a variety of settings, which we now consider.

The primary findings of the co-propagation scheme outlined the ability of ultracold atoms to be directed towards positions of optical intensity or darkness depending on the nature of the field detuning. Such a mechanism may be applied in the field of atomic trapping, where the ability to trap atoms in particular spatial regions is sought [25, 33, 253]. Specifically for the trapping of atomic clusters within the dark optical regime demonstrated here, there are additional attractions to this scheme, given the thermal-free properties of regions outside of optical intensity [63, 265]. Alternatively, with the

scheme outlined for the generation of coupled atom-light solitons with red atom-field detuning, there are clear applications to the fields of atomic transport, forming a predetermined number of solitons in a typically prohibitive regime, with expectation of their rotational and ejection characteristics [51, 243].

There are many additional applications for the light-induced control of ultracold atomic dynamics outlined within a driven optical cavity. Again, atomic transport was realised to dark optical regions within Turing patterns on homogeneous fields. However, unlike in the co-propagation case, OAM was shown to add rotational dynamics to these atoms confined in darkness, with the rotational characteristics set by the optical pump. This scheme again opens further applications available for atomic trapping, manipulation, and transport in thermal-free regions of the field [25, 33, 51, 63, 243, 253, 265, 266].

With red atom-field detuning, we outlined the capacity to create ultracold atomic persistent currents. Such a continuous flow of neutral atoms, acting as an effective current, is highly applicable to the field of atomtronics, with this optically-led formation process acting as an alternative to the typically used static trapping field approach to create structures analogous to atomtronic superconducting quantum interference devices (SQUIDs) [197, 198]. Many of the structures that we outlined, such as the 'atomic peppermill' realised through scalar superpositions of optical LG modes, are significantly more complex transverse forms than those accessible through trapping-based approaches [64, 206, 207, 219, 222, 274], with applications in studying the interactions between current rings for phase-slip qubit realisation [275, 276]. Crucially, our approach also enables the formation of a *dynamic* atomic current, in an approach prohibited when using static trapping fields. This opens the exciting prospect of future atomtronic devices, enabled through the guiding of a structured optical beam within a cavity, adapting itself dynamically in time to suit various current requirements.

In addition to these numerous applications of light-induced control of ultracold atomic dynamics, additional applications outside of this immediate scope may be conceived. Fundamentally, the additional control of ultracold atomic dynamics with structured light promises to advance a range of areas of ultracold atomic sciences. Areas include

163

quantum and superfluid simulation [20] and quantum computation [277]. Additionally, there are applications within fundamental BEC research [78], particularly considering the ability of structured light to seed the creation of atomic solitons in repulsive, typically prohibitive, regimes [146, 278].

We have demonstrated in this work an alternative approach to realise a wide range of ultracold atomic Turing patterns, by applying a driven optical cavity. Such an approach utilises a far more straightforward BEC setup than currently outlined, with prior observations of ultracold atomic Turing patterns occurring in configurations including ferromagnetic [183], polariton [184], or dipolar [187–190] condensates. By using the coupling to the optical field to realise the required activator-inhibitor conditions, we may observe Turing patterns in a straightforward, single-species, single-component condensate, in addition to a wider diversity of patterns than those previously reported.

We also outlined that Turing patterns, under appropriate conditions, may realise hysteresis cycles within ultracold atoms. Though such behaviour has previously been demonstrated [196], its realisation here, in a system that may be seeded with angular momentum towards atomtronic applications [197, 198], opens the possibility of the direct application of hysteresis cycles for atomtronics. Building on the applications of hysteresis within electronic systems [261–264], similar applications may be enabled through this approach to an atomic current.

Finally, our work outlined an alternative approach to the formation of organised vortex arrays within ultracold atoms without the requirement to use trapped atoms subjected to a stirring potential [204, 209, 210, 267] if the atoms are guided by a coupled optical field carrying OAM within a driven optical cavity. We also demonstrated that such an approach defines the eventual properties of the array, with the OAM index of the optical pump related to the final number of vortices obtained and large numbers of vortices becoming accessible through this method. Such an alternative method, with its additional array control, may enable advancements in the modelling of vortex matter within superconductors [268], cosmology [269], or quantum droplets [270].

Future Research Directions

There are a number of lines indicated for future research. Most obviously, the results presented here should be experimentally realised, using the schemes as outlined in Chapters 5 and 9. Though certain results related to those of this thesis have been verified in a range of alternative media, including in hot atomic vapours [60, 150, 176], nonlinear colloidal suspensions [151, 152], or cold atoms [178, 181, 182], it is our hope that, building on such realisations, the results presented here will be applied experimentally to realise the additional benefits of such processes unique to the *ultracold* atomic realm.

Moving forward, further numerical study should focus on the specific application of the findings outlined in Part III to the atomtronic field. Particular focus should be given to the adaptation of this scheme for atomtronic SQUID-like devices, given the relative ease of atomic persistent current geometry realisation for light-seeking atoms. Studies to discern the particular transverse current geometries enabled by the *dynamic* capabilities of the methods outlined here should also be conducted. Additionally, work should focus on alternative current configurations, particularly for rotating dark-seeking atoms trapped in Turing patterns, free from coincident optical heating.

A further form of structured light is possible, outside of the scope of this thesis. A vector superposition of orthogonally polarized OAM beams may provide structured polarization, in addition to the structured intensity and phase considered within this work. Such light, typically referred to as fully structured light [39], should also be considered in the atom-light configurations outlined within this work. Light with structured polarization propagating within a Kerr medium leads to more stable propagation, delaying fragmentation similar to that reported in this thesis [60, 279]. Additionally, within a self-focusing Kerr cavity, it enables additional customisation over the transverse and rotational characteristics of the dynamics [174]. If such benefits were realised when this light interacts with ultracold atoms, the resulting atomic dynamics may also be significantly more rich and applicable for application in fields such as atomtronics, and as such this promises a potentially fruitful vein of research.

Finally, work should consider more complex BEC varieties than the single-species, single-component condensate considered in this thesis. Though the simplicity of such a condensate is beneficial in potentially realising the results presented here, a number of additional dynamical considerations may be introduced by using condensate varieties such as dipolar quantum mixtures and spinor condensates [18]. By introducing a multi-species BEC, and then subjecting it to interaction with structured light in the ways considered here, the additional interactions between atomic components may be used as a tool to alter factors such as the number of atomic clusters realised, or their transverse behaviour under evolution, in addition to other unforeseen benefits through alteration to the dynamics obtained.

Part V

Appendix

Appendix A

Additional Propagation Model Derivation Details

This section contains fuller details of procedures followed when deriving the propagation model outlined in Chapter 5.2.

A.1   Polarization Corrections for Dense Atomic Media

We proceed from Eqn. (5.8), the point at which we make the substitution

$$A^{'} \rightarrow A^{'} + \frac{P^{'}}{3\epsilon_0}$$

into the atomic wavefunctions (Eqns. (5.3)-(5.4)) in order to include corrections due to induced polarization in dense atomic media [30, 31, 229]. The atomic equations now take the form

$$i\hbar\partial_t\Phi^{'}_{\mathrm{g}} = -\frac{\hbar^2}{2m_{\mathrm{a}}}\nabla^2\Phi^{'}_{\mathrm{g}} - \frac{1}{2}\mu\left(A^{'*} + \frac{P^{'*}}{3\epsilon_0}\right)\Phi^{'}_{\mathrm{e}}e^{i\Delta t} + \frac{4\pi\hbar^2 a_{\mathrm{gg}}}{m_{\mathrm{a}}}|\Phi^{'}_{\mathrm{g}}|^2\Phi^{'}_{\mathrm{g}},$$

$$i\hbar\partial_t\Phi^{'}_{\mathrm{e}} = -\frac{\hbar^2}{2m_{\mathrm{a}}}\nabla^2\Phi^{'}_{\mathrm{e}} - \frac{1}{2}\mu\left(A^{'} + \frac{P^{'}}{3\epsilon_0}\right)\Phi^{'}_{\mathrm{g}}e^{-i\Delta t} - i\hbar\frac{\gamma}{2}\Phi^{'}_{\mathrm{e}},$$

$$i\hbar\partial_t\Phi'_{\mathrm{g}} = -\frac{\hbar^2}{2m_{\mathrm{a}}}\nabla^2\Phi'_{\mathrm{g}} - \frac{1}{2}\mu\left(A'^* + \frac{\mu\Phi'_{\mathrm{g}}\Phi'^*_{\mathrm{e}}e^{-i\Delta t}}{3\epsilon_0}\right)\Phi'_{\mathrm{e}}e^{i\Delta t} + \frac{4\pi\hbar^2 a_{\mathrm{gg}}}{m_{\mathrm{a}}}|\Phi'_{\mathrm{g}}|^2\Phi'_{\mathrm{g}},$$

$$i\hbar\partial_t\Phi'_{\mathrm{e}} = -\frac{\hbar^2}{2m_{\mathrm{a}}}\nabla^2\Phi'_{\mathrm{e}} - \frac{1}{2}\mu\left(A' + \frac{\mu\Phi'^*_{\mathrm{g}}\Phi'_{\mathrm{e}}e^{i\Delta t}}{3\epsilon_0}\right)\Phi'_{\mathrm{g}}e^{-i\Delta t} - i\hbar\frac{\gamma}{2}\Phi'_{\mathrm{e}},$$

$$i\hbar\partial_t\Phi'_{\mathrm{g}} = -\frac{\hbar^2}{2m_{\mathrm{a}}}\nabla^2\Phi'_{\mathrm{g}} - \frac{1}{2}\mu A'^*\Phi'_{\mathrm{e}}e^{i\Delta t} - \frac{1}{2}\frac{\mu^2\Phi'_{\mathrm{g}}}{3\epsilon_0}|\Phi'_{\mathrm{e}}|^2 + \frac{4\pi\hbar^2 a_{\mathrm{gg}}}{m_{\mathrm{a}}}|\Phi'_{\mathrm{g}}|^2\Phi'_{\mathrm{g}}, \qquad (\mathrm{A.1})$$

$$i\hbar\partial_t\Phi'_{\mathrm{e}} = -\frac{\hbar^2}{2m_{\mathrm{a}}}\nabla^2\Phi'_{\mathrm{e}} - \frac{1}{2}\mu A'\Phi'_{\mathrm{g}}e^{-i\Delta t} - \frac{1}{2}\frac{\mu^2\Phi'_{\mathrm{e}}}{3\epsilon_0}|\Phi'_{\mathrm{g}}|^2 - i\hbar\frac{\gamma}{2}\Phi'_{\mathrm{e}}, \qquad (\mathrm{A.2})$$

where Eqns. (A.1)-(A.2) are Eqns. (5.9)-(5.10) of Chapter 5.2.

A.2 Rotating Wave Procedure

We consider the simplification of Eqns. (5.22)-(5.24). We identify that, when $\Delta' = \Delta - k_{\mathrm{L}}v_{\mathrm{a}}$, $\Delta >> k_{\mathrm{L}}v_{\mathrm{a}}$ and thus $\exp(\Delta') \approx \exp(\Delta)$, and so write

$$\hbar\omega\Phi_{\mathrm{g}}e^{i(k_{\mathrm{a}}z-\omega t)} = -\frac{\hbar^2}{2m_{\mathrm{a}}}\left[\nabla^2_\perp\Phi_{\mathrm{g}} + 2ik_{\mathrm{a}}\partial_z\Phi_{\mathrm{g}} - k_{\mathrm{a}}^2\Phi_{\mathrm{g}}\right]e^{i(k_{\mathrm{a}}z-\omega t)} - \frac{1}{2}\mu A^*\Phi_{\mathrm{e}}e^{i(k_{\mathrm{a}}z-\omega t)}$$
$$- \frac{1}{2}\frac{\mu^2\Phi_{\mathrm{g}}}{3\epsilon_0}|\Phi_{\mathrm{e}}|^2e^{i(k_{\mathrm{a}}z-\omega t)} + \frac{4\pi\hbar^2 a_{\mathrm{gg}}}{m_{\mathrm{a}}}|\Phi_{\mathrm{g}}|^2\Phi_{\mathrm{g}}e^{i(k_{\mathrm{a}}z-\omega t)},$$

$$\hbar(\omega + \Delta')\Phi_{\mathrm{e}}e^{i((k_{\mathrm{L}}+k_{\mathrm{a}})z-(\omega+\Delta')t)} = -\frac{\hbar^2}{2m_{\mathrm{a}}}\left[\nabla^2_\perp\Phi_{\mathrm{e}} + 2i(k_{\mathrm{L}} + k_{\mathrm{a}})\partial_z\Phi_{\mathrm{e}}\right.$$
$$\left.- (k_{\mathrm{L}} + k_{\mathrm{a}})^2\Phi_{\mathrm{e}}\right]e^{i((k_{\mathrm{L}}+k_{\mathrm{a}})z-(\omega+\Delta')t)} - \frac{1}{2}\mu A\Phi_{\mathrm{g}}e^{i((k_{\mathrm{L}}+k_{\mathrm{a}})z-(\omega+\Delta')t)}$$
$$- \frac{1}{2}\frac{\mu^2\Phi_{\mathrm{e}}}{3\epsilon_0}|\Phi_{\mathrm{g}}|^2e^{i((k_{\mathrm{L}}+k_{\mathrm{a}})z-(\omega+\Delta')t)} - i\hbar\frac{\gamma}{2}\Phi_{\mathrm{e}}e^{i((k_{\mathrm{L}}+k_{\mathrm{a}})z-(\omega+\Delta')t)},$$

$$\frac{2i\omega_{\mathrm{L}}n^2}{c^2}\partial_t A e^{ik_{\mathrm{L}}z} = -\left[\nabla^2_\perp A + 2ik_{\mathrm{L}}\partial_z A - k_{\mathrm{L}}^2 A\right]e^{ik_{\mathrm{L}}z} - \frac{\omega_{\mathrm{L}}^2 n^2}{c^2}A e^{ik_{\mathrm{L}}z} - \frac{\omega_{\mathrm{L}}^2}{c^2\epsilon_0}\mu\Phi^*_{\mathrm{g}}\Phi_{\mathrm{e}}e^{ik_{\mathrm{L}}z},$$

which, on cancelling the exponents, gives

$$\hbar\omega\Phi_{\mathrm{g}} = -\frac{\hbar^2}{2m_{\mathrm{a}}}\left[\nabla^2_\perp\Phi_{\mathrm{g}} + 2ik_{\mathrm{a}}\partial_z\Phi_{\mathrm{g}} - k_{\mathrm{a}}^2\Phi_{\mathrm{g}}\right] - \frac{1}{2}\mu A^*\Phi_{\mathrm{e}} - \frac{1}{2}\frac{\mu^2}{3\epsilon_0}|\Phi_{\mathrm{e}}|^2\Phi_{\mathrm{g}}$$
$$+ \frac{4\pi\hbar^2 a_{\mathrm{gg}}}{m_{\mathrm{a}}}|\Phi_{\mathrm{g}}|^2\Phi_{\mathrm{g}},$$

$$\hbar(\omega + \Delta')\Phi_{\mathrm{e}} = -\frac{\hbar^2}{2m_{\mathrm{a}}} \left[\nabla_{\perp}^2 \Phi_{\mathrm{e}} + 2i(k_{\mathrm{L}} + k_{\mathrm{a}})\partial_z \Phi_{\mathrm{e}} - (k_{\mathrm{L}} + k_{\mathrm{a}})^2 \Phi_{\mathrm{e}} \right] - \frac{1}{2}\mu A \Phi_{\mathrm{g}}$$
$$- \frac{1}{2}\frac{\mu^2}{3\epsilon_0}|\Phi_{\mathrm{g}}|^2 \Phi_{\mathrm{e}} - i\hbar \frac{\gamma}{2}\Phi_{\mathrm{e}},$$

$$\frac{2i\omega_{\mathrm{L}} n^2}{c^2}\partial_t A = -\left(\nabla_{\perp}^2 A + \frac{2i\omega_{\mathrm{L}} n}{c}\partial_z A - \frac{w_{\mathrm{L}}^2 n^2}{c^2}A \right) - \frac{\omega_{\mathrm{L}}^2 n^2}{c^2}A - \frac{\omega_{\mathrm{L}}^2}{c^2 \epsilon_0}\mu \Phi_{\mathrm{g}}^* \Phi_{\mathrm{e}}.$$

With $k_{\mathrm{L}} = \omega_{\mathrm{L}} n/c$, $k_{\mathrm{a}} = m_{\mathrm{a}} v_{\mathrm{a}}/\hbar$ and $\hbar\omega = m_{\mathrm{a}} v_{\mathrm{a}}^2/2$, we obtain

$$i\frac{\hbar^2 k_{\mathrm{a}}}{m_{\mathrm{a}}}\partial_z \Phi_{\mathrm{g}} = -\frac{\hbar^2}{2m_{\mathrm{a}}}\left(\nabla_{\perp}^2 \Phi_{\mathrm{g}} - k_{\mathrm{a}}^2 \Phi_{\mathrm{g}} \right) - \hbar\omega \Phi_{\mathrm{g}} - \frac{1}{2}\mu A^* \Phi_{\mathrm{e}} - \frac{1}{2}\frac{\mu^2}{3\epsilon_0}|\Phi_{\mathrm{e}}|^2 \Phi_{\mathrm{g}}$$
$$+ \frac{4\pi\hbar^2 a_{\mathrm{gg}}}{m_{\mathrm{a}}}|\Phi_{\mathrm{g}}|^2 \Phi_{\mathrm{g}}, \tag{A.3}$$

$$i\frac{\hbar^2 (k_{\mathrm{L}} + k_{\mathrm{a}})}{m_{\mathrm{a}}}\partial_z \Phi_{\mathrm{e}} = -\frac{\hbar^2}{2m_{\mathrm{a}}}\left(\nabla_{\perp}^2 \Phi_{\mathrm{e}} - (k_{\mathrm{L}} + k_{\mathrm{a}})^2 \Phi_{\mathrm{e}} \right) - \hbar(\omega + \Delta')\Phi_{\mathrm{e}} - \frac{1}{2}\mu A \Phi_{\mathrm{g}}$$
$$- \frac{1}{2}\frac{\mu^2}{3\epsilon_0}|\Phi_{\mathrm{g}}|^2 \Phi_{\mathrm{e}} - i\hbar\frac{\gamma}{2}\Phi_{\mathrm{e}}, \tag{A.4}$$

$$\frac{2i\omega_{\mathrm{L}} n}{c}\left(\frac{n}{c}\partial_t A + \partial_z A \right) = -\nabla_{\perp}^2 A - \frac{\omega_{\mathrm{L}}^2}{c^2 \epsilon_0}\mu \Phi_{\mathrm{g}}^* \Phi_{\mathrm{e}}, \tag{A.5}$$

where Eqns. (A.3)-(A.5) are Eqns. (5.25)-(5.27) of Chapter 5.2.

A.3 Dimensional Scalings

We apply the scalings of Eqns. (5.35)-(5.36) to Eqns. (5.32)-(5.34):

$$i\frac{\hbar^2 k_{\mathrm{a}}}{m_{\mathrm{a}}}\frac{1}{k_{\mathrm{L}} w_{\mathrm{L}}^2}\partial_\zeta \Phi_{\mathrm{g}} = -\frac{\hbar^2}{2m_{\mathrm{a}}}\left(\frac{2}{w_{\mathrm{L}}^2}\nabla_{\perp}^2 \Phi_{\mathrm{g}} - k_{\mathrm{a}}^2 \Phi_{\mathrm{g}} \right) - \hbar\omega \Phi_{\mathrm{g}} - \frac{1}{2}\mu A^* \Phi_{\mathrm{e}}$$
$$- \frac{1}{2}\frac{\mu^2}{3\epsilon_0}|\Phi_{\mathrm{e}}|^2 \Phi_{\mathrm{g}} + \frac{4\pi\hbar^2 a_{\mathrm{gg}}}{m_{\mathrm{a}}}|\Phi_{\mathrm{g}}|^2 \Phi_{\mathrm{g}},$$

$$i\frac{\hbar^2 (k_{\mathrm{L}} + k_{\mathrm{a}})}{m_{\mathrm{a}}}\frac{1}{k_{\mathrm{L}} w_{\mathrm{L}}^2}\partial_\zeta \Phi_{\mathrm{e}} = -\frac{\hbar^2}{2m_{\mathrm{a}}}\left(\frac{2}{w_{\mathrm{L}}^2}\nabla_{\perp}^2 \Phi_{\mathrm{e}} - (k_{\mathrm{L}} + k_{\mathrm{a}})^2 \Phi_{\mathrm{e}} \right) - \hbar(\omega + \Delta)\Phi_{\mathrm{e}} - \frac{1}{2}\mu A \Phi_{\mathrm{g}}$$
$$- \frac{1}{2}\frac{\mu^2}{3\epsilon_0}|\Phi_{\mathrm{g}}|^2 \Phi_{\mathrm{e}} - i\hbar\frac{\gamma}{2}\Phi_{\mathrm{e}},$$

$$\frac{2i\omega_{\mathrm{L}} n}{c}\frac{1}{k_{\mathrm{L}} w_{\mathrm{L}}^2}\partial_\zeta A = -\frac{2}{w_{\mathrm{L}}^2}\nabla_{\perp}^2 A - \frac{\omega_{\mathrm{L}}^2}{c^2 \epsilon_0}\mu \Phi_{\mathrm{g}}^* \Phi_{\mathrm{e}},$$

Appendix A: Additional Propagation Model Derivation Details

$$i\frac{\hbar^2 k_{\mathrm{a}}}{m_{\mathrm{a}} k_{\mathrm{L}} w_{\mathrm{L}}^2}\partial_\zeta \Phi_{\mathrm{g}} = -\frac{\hbar^2}{m_{\mathrm{a}} w_{\mathrm{L}}^2}\nabla_\perp^2 \Phi_{\mathrm{g}} + \frac{\hbar^2 k_{\mathrm{a}}^2}{2m_{\mathrm{a}}}\Phi_{\mathrm{g}} - \hbar\omega\Phi_{\mathrm{g}} - \frac{1}{2}\mu A^* \Phi_{\mathrm{e}} - \frac{1}{2}\frac{\mu^2}{3\epsilon_0}|\Phi_{\mathrm{e}}|^2 \Phi_{\mathrm{g}}$$
$$+ \frac{4\pi\hbar^2 a_{\mathrm{gg}}}{m_{\mathrm{a}}}|\Phi_{\mathrm{g}}|^2 \Phi_{\mathrm{g}},$$

$$i\frac{\hbar^2 (k_{\mathrm{L}}+k_{\mathrm{a}})}{m_{\mathrm{a}} k_{\mathrm{L}} w_{\mathrm{L}}^2}\partial_\zeta \Phi_{\mathrm{e}} = -\frac{\hbar^2}{m_{\mathrm{a}} w_{\mathrm{L}}^2}\nabla_\perp^2 \Phi_{\mathrm{e}} + \frac{\hbar^2 (k_{\mathrm{L}}+k_{\mathrm{a}})^2}{2m_{\mathrm{a}}}\Phi_{\mathrm{e}} - \hbar(\omega+\Delta)\Phi_{\mathrm{e}} - \frac{1}{2}\mu A \Phi_{\mathrm{g}}$$
$$- \frac{1}{2}\frac{\mu^2}{3\epsilon_0}|\Phi_{\mathrm{g}}|^2 \Phi_{\mathrm{e}} - i\hbar\frac{\gamma}{2}\Phi_{\mathrm{e}},$$

$$\frac{2i}{w_{\mathrm{L}}^2}\partial_\zeta A = -\frac{2}{w_{\mathrm{L}}^2}\nabla_\perp^2 A - \frac{\omega_{\mathrm{L}}^2}{c^2 \epsilon_0}\mu \Phi_{\mathrm{g}}^* \Phi_{\mathrm{e}},$$

$$i\partial_\zeta \Phi_{\mathrm{g}} = \frac{m_{\mathrm{a}} w_{\mathrm{L}}^2}{\hbar^2}\left(-\frac{\hbar^2}{m_{\mathrm{a}} w_{\mathrm{L}}^2}\nabla_\perp^2 \Phi_{\mathrm{g}} + \frac{\hbar^2 k_{\mathrm{a}}^2}{2m_{\mathrm{a}}}\Phi_{\mathrm{g}} - \hbar\omega\Phi_{\mathrm{g}} - \frac{1}{2}\mu A^* \Phi_{\mathrm{e}} \right.$$
$$\left. - \frac{1}{2}\frac{\mu^2}{3\epsilon_0}|\Phi_{\mathrm{e}}|^2 \Phi_{\mathrm{g}} + \frac{4\pi\hbar^2 a_{\mathrm{gg}}}{m_{\mathrm{a}}}|\Phi_{\mathrm{g}}|^2 \Phi_{\mathrm{g}} \right),$$

$$i\partial_\zeta \Phi_{\mathrm{e}} = \frac{m_{\mathrm{a}} w_{\mathrm{L}}^2}{\hbar^2}\left(-\frac{\hbar^2}{m_{\mathrm{a}} w_{\mathrm{L}}^2}\nabla_\perp^2 \Phi_{\mathrm{e}} + \frac{\hbar^2 (k_{\mathrm{L}}+k_{\mathrm{a}})^2}{2m_{\mathrm{a}}}\Phi_{\mathrm{e}} - \hbar(\omega+\Delta)\Phi_{\mathrm{e}} \right.$$
$$\left. - \frac{1}{2}\mu A \Phi_{\mathrm{g}} - \frac{1}{2}\frac{\mu^2}{3\epsilon_0}|\Phi_{\mathrm{g}}|^2 \Phi_{\mathrm{e}} - i\hbar\frac{\gamma}{2}\Phi_{\mathrm{e}} \right),$$

$$i\partial_\zeta A = -\nabla_\perp^2 A - \frac{\omega_{\mathrm{L}}^2 w_{\mathrm{L}}^2 \mu}{2c^2 \epsilon_0}\Phi_{\mathrm{g}}^* \Phi_{\mathrm{e}},$$

$$i\partial_\zeta \Phi_{\mathrm{g}} = -\nabla_\perp^2 \Phi_{\mathrm{g}} + \frac{k_{\mathrm{a}}^2 w_{\mathrm{L}}^2}{2}\Phi_{\mathrm{g}} - \frac{m_{\mathrm{a}} w_{\mathrm{L}}^2 \omega}{\hbar}\Phi_{\mathrm{g}} - \frac{m_{\mathrm{a}} w_{\mathrm{L}}^2 \mu}{2\hbar^2}A^* \Phi_{\mathrm{e}}$$
$$- \frac{m_{\mathrm{a}} w_{\mathrm{L}}^2 \mu^2}{6\hbar^2 \epsilon_0}|\Phi_{\mathrm{e}}|^2 \Phi_{\mathrm{g}} + 4\pi w_{\mathrm{L}}^2 a_{\mathrm{gg}}|\Phi_{\mathrm{g}}|^2 \Phi_{\mathrm{g}}, \tag{A.6}$$

$$i\partial_\zeta \Phi_{\mathrm{e}} = -\nabla_\perp^2 \Phi_{\mathrm{e}} + \frac{w_{\mathrm{L}}^2 (k_{\mathrm{L}}+k_{\mathrm{a}})^2}{2}\Phi_{\mathrm{e}} - \frac{m w_{\mathrm{L}}^2}{\hbar}(\omega+\Delta)\Phi_{\mathrm{e}}$$
$$- \frac{m_{\mathrm{a}} w_{\mathrm{L}}^2 \mu}{2\hbar^2}A \Phi_{\mathrm{g}} - \frac{m_{\mathrm{a}} w_{\mathrm{L}}^2 \mu^2}{6\hbar^2 \epsilon_0}|\Phi_{\mathrm{g}}|^2 \Phi_{\mathrm{e}} - i\frac{m_{\mathrm{a}} w_{\mathrm{L}}^2 \gamma}{2\hbar}\Phi_{\mathrm{e}}, \tag{A.7}$$

$$i\partial_\zeta A = -\nabla_\perp^2 A - \frac{\omega_{\mathrm{L}}^2 w_{\mathrm{L}}^2 \mu}{2c^2 \epsilon_0}\Phi_{\mathrm{g}}^* \Phi_{\mathrm{e}}, \tag{A.8}$$

where Eqns. (A.6)-(A.8) are Eqns. (5.37)-(5.39) of the main text.

A.4 Optical Field Transformations

We apply the optical field transformation, defined in Eqn. (5.40) as

$$F = \frac{\mu A}{2\hbar} \frac{k_{\mathrm{L}} w_{\mathrm{L}}^2}{v_{\mathrm{a}}} \frac{1}{\sqrt{|\delta|}},$$

$$\Rightarrow \qquad A = \frac{2\hbar v_{\mathrm{a}} \sqrt{|\delta|}}{\mu k_{\mathrm{L}} w_{\mathrm{L}}^2} F,$$

successively to the three fields.

A.4.1 Optical Field

Using a slightly rearranged version of Eqn. (5.39), the description of the optical field becomes (taking $n = 1$)

$$(i\partial_\zeta + \nabla_\perp^2) \frac{2\hbar v_{\mathrm{a}} \sqrt{|\delta|}}{\mu k_{\mathrm{L}} w_{\mathrm{L}}^2} F = -\frac{\omega_{\mathrm{L}}^2 w_{\mathrm{L}}^2 \mu}{2c^2 \epsilon_0} \Phi_{\mathrm{g}}^* \Phi_{\mathrm{e}},$$

$$\Rightarrow \qquad (i\partial_\zeta + \nabla_\perp^2) F = -\frac{\mu^2 k_{\mathrm{L}} \omega_{\mathrm{L}}^2 w_{\mathrm{L}}^4}{4c^2 \hbar \epsilon_0 \sqrt{|\delta|}} \frac{1}{v_{\mathrm{a}}} \Phi_{\mathrm{g}}^* \Phi_{\mathrm{e}},$$

$$v_{\mathrm{a}} = \frac{k_{\mathrm{a}} \hbar}{m_{\mathrm{a}}} \Rightarrow \qquad (i\partial_\zeta + \nabla_\perp^2) F = -\frac{\mu^2 k_{\mathrm{L}} \omega_{\mathrm{L}}^2 w_{\mathrm{L}}^4}{4c^2 \hbar \epsilon_0 \sqrt{|\delta|}} \frac{m_{\mathrm{a}}}{k_{\mathrm{a}} \hbar} \Phi_{\mathrm{g}}^* \Phi_{\mathrm{e}}, \qquad (\mathrm{A.9})$$

$$\omega_{\mathrm{L}} = \frac{k_{\mathrm{L}} c}{n}, k_{\mathrm{a}} = k_{\mathrm{L}} \Rightarrow \qquad (i\partial_\zeta + \nabla_\perp^2) F = -\frac{k_{\mathrm{L}}^2 c^2}{n^2} \frac{\mu^2 w_{\mathrm{L}}^4 m_{\mathrm{a}}}{4c^2 \hbar^2 \epsilon_0 \sqrt{|\delta|}} \Phi_{\mathrm{g}}^* \Phi_{\mathrm{e}},$$

$$= -\frac{k_{\mathrm{L}}^2 w_{\mathrm{L}}^4 m_{\mathrm{a}} \mu^2}{4\epsilon_0 \hbar^2 \sqrt{|\delta|}} \Phi_{\mathrm{g}}^* \Phi_{\mathrm{e}}. \qquad (\mathrm{A.10})$$

Eqn. (A.10) is both Eqn. (5.44) of Section 5.2 and Eqn. (5c) of Ref. [33].

A.4.2 Ground State Atomic Field

Using Eqn. (5.37), the description of the atomic ground state is now given by

$$(i\partial_\zeta + \nabla_\perp^2)\Phi_{\mathrm{g}} = \frac{k_{\mathrm{a}}^2 w_{\mathrm{L}}^2}{2} \Phi_{\mathrm{g}} - \frac{m_{\mathrm{a}} w_{\mathrm{L}}^2 \omega}{\hbar} \Phi_{\mathrm{g}} - \frac{m_{\mathrm{a}} w_{\mathrm{L}}^2 \mu}{2\hbar^2} A^* \Phi_{\mathrm{e}}$$

$$- \frac{m_{\mathrm{a}} w_{\mathrm{L}}^2 \mu^2}{6\hbar^2 \epsilon_0} |\Phi_{\mathrm{e}}|^2 \Phi_{\mathrm{g}} + 4\pi w_{\mathrm{L}}^2 a_{\mathrm{gg}} |\Phi_{\mathrm{g}}|^2 \Phi_{\mathrm{g}},$$

$$\Rightarrow \quad (i\partial_\zeta + \nabla_\perp^2)\Phi_g = \frac{k_a^2 w_L^2}{2}\Phi_g - \frac{m_a w_L^2 \omega}{\hbar}\Phi_g - \frac{m_a w_L^2 \mu}{2\hbar^2}\frac{2\hbar v_a \sqrt{|\delta|}}{\mu k_L w_L^2}F^*\Phi_e$$

$$- \frac{m_a w_L^2 \mu^2}{6\hbar^2 \epsilon_0}|\Phi_e|^2\Phi_g + 4\pi w_L^2 a_{gg}|\Phi_g|^2\Phi_g,$$

$$\hbar\omega = \frac{m_a v_a^2}{2} \Rightarrow \qquad = \frac{k_a^2 w_L^2}{2}\Phi_g - \frac{m_a w_L^2}{\hbar}\frac{m_a v_a^2}{2\hbar}\Phi_g - \frac{m_a v_a \sqrt{|\delta|}}{k_L \hbar}F^*\Phi_e$$

$$- \frac{m_a w_L^2 \mu^2}{6\hbar^2 \epsilon_0}|\Phi_e|^2\Phi_g + 4\pi w_L^2 a_{gg}|\Phi_g|^2\Phi_g,$$

$$k_a = \frac{m_a v_a}{\hbar} \Rightarrow \qquad = \frac{k_a^2 w_L^2}{2}\Phi_g - \frac{m_a^2 w_L^2 v_a^2}{2\hbar^2}\Phi_g - \frac{k_a \sqrt{|\delta|}}{k_L}F^*\Phi_e$$

$$- \frac{m_a w_L^2 \mu^2}{6\hbar^2 \epsilon_0}|\Phi_e|^2\Phi_g + 4\pi w_L^2 a_{gg}|\Phi_g|^2\Phi_g,$$

$$k_a = k_L \Rightarrow \qquad = \frac{k_a^2 w_L^2}{2}\Phi_g - \frac{k_a^2 w_L^2}{2}\Phi_g - \sqrt{|\delta|}F^*\Phi_e - \frac{m_a w_L^2 \mu^2}{6\hbar^2 \epsilon_0}|\Phi_e|^2\Phi_g$$

$$+ 4\pi w_L^2 a_{gg}|\Phi_g|^2\Phi_g,$$

$$= -\sqrt{|\delta|}F^*\Phi_e - \frac{m_a w_L^2 \mu^2}{6\hbar^2 \epsilon_0}|\Phi_e|^2\Phi_g + 4\pi w_L^2 a_{gg}|\Phi_g|^2\Phi_g,$$

$$\Rightarrow \quad (i\partial_\zeta + \nabla_\perp^2)\Phi_g = -\sqrt{|\delta|}F^*\Phi_e + \frac{m_a w_L^2}{\hbar^2}\left(-\frac{\mu^2}{6\epsilon_0}|\Phi_e|^2 + \frac{4\pi\hbar^2 a_{gg}}{m_a}|\Phi_g|^2\right)\Phi_g.$$

$$(A.11)$$

Eqn. (A.11) is both Eqn. (5.42) of Section 5.2 and Eqn. (5a) of Ref. [33].

A.4.3 Excited State Atomic Field

Using Eqn. (5.38), the description of the atomic excited state becomes

$$(i\partial_\zeta + \nabla_\perp^2)\Phi_e = \frac{w_L^2(k_L + k_a)^2}{2}\Phi_e - \frac{m_a w_L^2}{\hbar}(\omega + \Delta)\Phi_e$$

$$- \frac{m_a w_L^2 \mu}{2\hbar^2}A\Phi_g - \frac{m_a w_L^2 \mu^2}{6\hbar^2 \epsilon_0}|\Phi_g|^2\Phi_e - i\frac{m_a w_L^2 \gamma}{2\hbar}\Phi_e,$$

$$\Rightarrow \qquad = \frac{w_L^2(k_L + k_a)^2}{2}\Phi_e - \frac{m_a w_L^2}{\hbar}(\omega + \Delta)\Phi_e$$

$$- \frac{m_a w_L^2 \mu}{2\hbar^2}\frac{2\hbar v_a \sqrt{|\delta|}}{\mu k_L w_L^2}F\Phi_g - \frac{m_a w_L^2 \mu^2}{6\hbar^2 \epsilon_0}|\Phi_g|^2\Phi_e$$

$$- i\frac{m_a w_L^2 \gamma}{2\hbar}\Phi_e,$$

$$\Rightarrow \qquad = \frac{w_L^2(k_L + k_a)^2}{2}\Phi_e - \frac{m_a w_L^2}{\hbar}(\omega + \Delta)\Phi_e$$
$$- \frac{m_a v_a \sqrt{|\delta|}}{k_L \hbar}F\Phi_g - \frac{m_a w_L^2 \mu^2}{6\hbar^2 \epsilon_0}|\Phi_g|^2\Phi_e - i\frac{m_a w_L^2 \gamma}{2\hbar}\Phi_e,$$

$$k_a = \frac{m_a v_a}{\hbar} \Rightarrow \quad (i\partial_\zeta + \nabla_\perp^2)\Phi_e = \frac{w_L^2(k_L + k_a)^2}{2}\Phi_e - \frac{m_a w_L^2}{\hbar}(\omega + \Delta)\Phi_e - \frac{k_a \sqrt{|\delta|}}{k_L}F\Phi_g$$
$$- \frac{m_a w_L^2 \mu^2}{6\hbar^2 \epsilon_0}|\Phi_g|^2\Phi_e - i\frac{m_a w_L^2 \gamma}{2\hbar}\Phi_e,$$

$$k_a = k_L \Rightarrow \qquad = \frac{w_L^2(k_L + k_a)^2}{2}\Phi_e - \frac{m_a w_L^2}{\hbar}(\omega + \Delta)\Phi_e - \sqrt{|\delta|}F\Phi_g$$
$$- \frac{m_a w_L^2 \mu^2}{6\hbar^2 \epsilon_0}|\Phi_g|^2\Phi_e - i\frac{m_a w_L^2 \gamma}{2\hbar}\Phi_e,$$

$$\Rightarrow \quad (i\partial_\zeta + \nabla_\perp^2)\Phi_e = \frac{w_L^2(k_L + k_a)^2}{2}\Phi_e - \frac{m_a w_L^2}{\hbar}(\omega + \Delta)\Phi_e - \sqrt{|\delta|}F\Phi_g$$
$$- \frac{m_a w_L^2 \mu^2}{6\hbar^2 \epsilon_0}|\Phi_g|^2\Phi_e - i\frac{m_a w_L^2 \gamma}{2\hbar}\Phi_e. \qquad (A.12)$$

The first two right hand terms of Eqn. (A.12) may be written as

$$= \frac{w_L^2(k_L + k_a)^2}{2}\Phi_e - \frac{m_a w_L^2}{\hbar}(\omega + \Delta)\Phi_e,$$

$$\hbar\omega = \frac{m_a v_a^2}{2} \Rightarrow \qquad = \frac{w_L^2}{2}k_L^2\Phi_e + w_L^2 k_L k_a \Phi_e + \frac{w_L^2}{2}k_a^2\Phi_e - \frac{m_a w_L^2}{\hbar}\left(\frac{m_a v_a^2}{\hbar} + \Delta\right)\Phi_e,$$

$$\Rightarrow \qquad = \frac{w_L^2}{2}k_L^2\Phi_e + w_L^2 k_L k_a \Phi_e + \frac{w_L^2}{2}k_a^2\Phi_e - \frac{m_a^2 w_L^2 v_a^2}{\hbar^2}\Phi_e - \frac{m_a w_L^2}{\hbar}\Delta\Phi_e,$$

$$k_a = \frac{m_a v_a}{\hbar} \Rightarrow \qquad = \frac{w_L^2}{2}k_L^2\Phi_e + w_L^2 k_L k_a \Phi_e + \frac{w_L^2}{2}k_a^2\Phi_e - k_a^2 w_L^2\Phi_e - \frac{m_a w_L^2}{\hbar}\Delta\Phi_e,$$

$$\Rightarrow \qquad = \frac{w_L^2}{2}k_L^2\Phi_e + w_L^2 k_L k_a \Phi_e - \frac{w_L^2}{2}k_a^2\Phi_e - \frac{m_a w_L^2}{\hbar}\Delta\Phi_e,$$

$$k_a = k_L \Rightarrow \qquad = w_L^2 k_L k_a \Phi_e - \frac{m_a w_L^2}{\hbar}\Delta\Phi_e.$$

Applying this to Eqn. (A.12) gives

$$(i\partial_\zeta + \nabla_\perp^2)\Phi_e = -\sqrt{|\delta|}F\Phi_g - \frac{m_a w_L^2 \mu^2}{6\hbar^2 \epsilon_0}|\Phi_g|^2\Phi_e + \frac{m_a w_L^2}{\hbar}\left(\frac{\hbar k_L k_a}{m_a} - \Delta - i\frac{\gamma}{2}\right)\Phi_e. \quad (A.13)$$

Rearranging the bracketed right hand terms of Eqn. (A.13),

$$= \frac{m_a w_L^2}{\hbar}\left(\frac{\hbar k_L k_a}{m_a} - \Delta - i\frac{\gamma}{2}\right)\Phi_e,$$

$$\Rightarrow \qquad = w_{\mathrm{L}}^2 \left(k_{\mathrm{L}} k_{\mathrm{a}} - \frac{m_{\mathrm{a}} \Delta}{\hbar} - i \frac{m_{\mathrm{a}} \gamma}{2\hbar} \right) \Phi_{\mathrm{e}},$$

$$\Rightarrow \qquad = k_{\mathrm{L}}^2 w_{\mathrm{L}}^2 \left(\frac{k_{\mathrm{a}}}{k_{\mathrm{L}}} - \frac{m_{\mathrm{a}} \Delta}{\hbar k_{\mathrm{L}}^2} - i \frac{m_{\mathrm{a}} \gamma}{2\hbar k_{\mathrm{L}}^2} \right) \Phi_{\mathrm{e}},$$

$$k_{\mathrm{a}} = k_{\mathrm{L}}, \omega_{\mathrm{R}} = \frac{\hbar k_{\mathrm{L}}^2}{2m_{\mathrm{a}}} \Rightarrow \qquad = k_{\mathrm{L}}^2 w_{\mathrm{L}}^2 \left(1 - \frac{\Delta}{2\omega_{\mathrm{R}}} - i \frac{m_{\mathrm{a}} \gamma}{2\hbar k_{\mathrm{L}}^2} \right) \Phi_{\mathrm{e}},$$

and so Eqn. (A.13) becomes

$$(i\partial_\zeta + \nabla_\perp^2)\Phi_{\mathrm{e}} = -\sqrt{|\delta|}F\Phi_{\mathrm{g}} - \frac{m_{\mathrm{a}} w_{\mathrm{L}}^2}{\hbar^2} \frac{\mu^2}{6\epsilon_0}|\Phi_{\mathrm{g}}|^2\Phi_{\mathrm{e}} - k_{\mathrm{L}}^2 w_{\mathrm{L}}^2 \left(\frac{\Delta}{2\omega_{\mathrm{R}}} - 1 + i\frac{m_{\mathrm{a}} \gamma}{2\hbar k_{\mathrm{L}}^2} \right) \Phi_{\mathrm{e}}. \quad \text{(A.14)}$$

Finally, if we let $\delta = k_{\mathrm{L}}^2 w_{\mathrm{L}}^2 \left(\frac{\Delta}{2\omega_{\mathrm{R}}} - 1 \right)$, as in Ref. [33], we obtain

$$(i\partial_\zeta + \nabla_\perp^2)\Phi_{\mathrm{e}} = -\sqrt{|\delta|}F\Phi_{\mathrm{g}} - \frac{m_{\mathrm{a}} w_{\mathrm{L}}^2}{\hbar^2} \frac{\mu^2}{6\epsilon_0}|\Phi_{\mathrm{g}}|^2\Phi_{\mathrm{e}} - \delta \left(1 + i\frac{m_{\mathrm{a}} w_{\mathrm{L}}^2}{\hbar} \frac{\gamma}{2\delta} \right) \Phi_{\mathrm{e}}. \quad \text{(A.15)}$$

Eqn. (A.15) is both Eqn. (5.43) of Chapter 5.2 and Eqn. (5b) of Ref. [33].

A.5 Adiabatic Elimination of Excited Atomic State

Proceeding from Eqns. (5.42)-(5.44), neglecting the final term in Eqn. (5.43) assuming large detuning and under a first order adiabatic assumption, we obtain

$$i\partial_\zeta \Phi_{\mathrm{g}} = -\sqrt{|\delta|}F^*\Phi_{\mathrm{e}} + \frac{m_{\mathrm{a}} w_{\mathrm{L}}^2}{\hbar^2} \left(-\frac{\mu^2}{6\epsilon_0}|\Phi_{\mathrm{e}}|^2 + \frac{4\pi\hbar^2 a_{\mathrm{gg}}}{m_{\mathrm{a}}}|\Phi_{\mathrm{g}}|^2 \right) \Phi_{\mathrm{g}}, \quad \text{(A.16)}$$

$$i\partial_\zeta \Phi_{\mathrm{e}} = -\sqrt{|\delta|}F\Phi_{\mathrm{g}} - \frac{m_{\mathrm{a}} w_{\mathrm{L}}^2}{\hbar^2} \frac{\mu^2}{6\epsilon_0}|\Phi_{\mathrm{g}}|^2\Phi_{\mathrm{e}} - \delta\Phi_{\mathrm{e}}, \quad \text{(A.17)}$$

$$i\partial_\zeta F = -\frac{k_{\mathrm{L}}^2 w_{\mathrm{L}}^4 m_{\mathrm{a}} \mu^2}{4\epsilon_0 \hbar^2 \sqrt{|\delta|}} \Phi_{\mathrm{g}}^* \Phi_{\mathrm{e}}. \quad \text{(A.18)}$$

Writing Eqn. (A.17) as

$$\left(\frac{m_{\mathrm{a}} w_{\mathrm{L}}^2}{\hbar^2} \frac{\mu^2}{6\epsilon_0}|\Phi_{\mathrm{g}}|^2 + \delta \right) \Phi_{\mathrm{e}} = -\sqrt{|\delta|}F\Phi_{\mathrm{g}} - i\partial_\zeta \Phi_{\mathrm{e}},$$

$$\Rightarrow \qquad \Phi_{\mathrm{e}} = -\alpha\sqrt{|\delta|}F\Phi_{\mathrm{g}} - i\alpha\partial_\zeta \Phi_{\mathrm{e}}, \quad \text{(A.19)}$$

with

$$\alpha^{-1} = \delta + \frac{m_{\mathrm{a}} w_{\mathrm{L}}^2}{\hbar^2} \frac{\mu^2}{6\epsilon_0} |\Phi_{\mathrm{g}}|^2, \tag{A.20}$$

we recognise that Eqn. (A.19) takes a similar form to Eqn. (19) of Ref. [280]. We then identify a zero order term of

$$\Phi_{\mathrm{e}} = -\alpha \sqrt{|\delta|} F \Phi_{\mathrm{g}} \tag{A.21}$$

which leads to a definition of $\partial_\zeta \Phi_{\mathrm{e}}$ given by

$$\partial_\zeta \Phi_{\mathrm{e}} \;\; = -\alpha \sqrt{|\delta|} \left[\Phi_{\mathrm{g}} \partial_\zeta F + F \partial_\zeta \Phi_{\mathrm{g}}\right]. \tag{A.22}$$

From Eqn. (A.16),

$$\partial_\zeta \Phi_{\mathrm{g}} = i \sqrt{|\delta|} F^* \Phi_{\mathrm{e}} - i \frac{m_{\mathrm{a}} w_{\mathrm{L}}^2}{\hbar^2} \left(-\frac{\mu^2}{6\epsilon_0}|\Phi_{\mathrm{e}}|^2 + \frac{4\pi \hbar^2 a_{\mathrm{gg}}}{m}|\Phi_{\mathrm{g}}|^2\right)\Phi_{\mathrm{g}},$$

$$\Rightarrow \qquad \partial_\zeta \Phi_{\mathrm{g}} \approx i \sqrt{|\delta|} F^* \Phi_{\mathrm{e}} + i \frac{m_{\mathrm{a}} w_{\mathrm{L}}^2 \mu^2}{6\epsilon_0 \hbar^2}|\Phi_{\mathrm{e}}|^2 \Phi_{\mathrm{g}}, \tag{A.23}$$

and from Eqn. (A.18),

$$\partial_\zeta F = i \frac{k_{\mathrm{L}}^2 w_{\mathrm{L}}^4 m_{\mathrm{a}} \mu^2}{4\epsilon_0 \hbar^2 \sqrt{|\delta|}} \Phi_{\mathrm{g}}^* \Phi_{\mathrm{e}}. \tag{A.24}$$

Applying Eqns. (A.23)-(A.24) to Eqn. (A.22),

$$\partial_\zeta \Phi_{\mathrm{e}} = -\alpha \sqrt{|\delta|} \left[\Phi_{\mathrm{g}}\left(i\frac{k_{\mathrm{L}}^2 w_{\mathrm{L}}^4 m_{\mathrm{a}} \mu^2}{4\epsilon_0 \hbar^2 \sqrt{|\delta|}}\Phi_{\mathrm{g}}^* \Phi_{\mathrm{e}}\right) + F\left(i\sqrt{|\delta|}\Omega^* \Phi_{\mathrm{e}} + i\frac{m_{\mathrm{a}} w_{\mathrm{L}}^2 \mu^2}{6\epsilon_0 \hbar^2}|\Phi_{\mathrm{e}}|^2 \Phi_{\mathrm{g}}\right)\right],$$

$$\Rightarrow \qquad = -i\alpha\sqrt{|\delta|}\left[\frac{k_{\mathrm{L}}^2 w_{\mathrm{L}}^4 m_{\mathrm{a}} \mu^2}{4\epsilon_0 \hbar^2 \sqrt{|\delta|}}|\Phi_{\mathrm{g}}|^2 + \sqrt{|\delta|}|F|^2 + \frac{m_{\mathrm{a}} w_{\mathrm{L}}^2 \mu^2}{6\epsilon_0 \hbar^2}|\Phi_{\mathrm{e}}|\Phi_{\mathrm{g}} F\right]|\Phi_{\mathrm{e}}|. \tag{A.25}$$

Substituting Eqn. (A.25) into Eqn. (A.17),

$$-\sqrt{|\delta|}F\Phi_g - \frac{m_a w_L^2}{\hbar^2}\frac{\mu^2}{6\epsilon_0}|\Phi_g|^2 \Phi_e - \delta\Phi_e = \alpha\sqrt{|\delta|}\left[\frac{k_L^2 w_L^4 m_a \mu^2}{4\epsilon_0 \hbar^2 \sqrt{|\delta|}}|\Phi_g|^2\right.$$

$$\left. + \sqrt{|\delta|}|F|^2 + \frac{m w_L^2 \mu^2}{6\epsilon_0 \hbar^2}|\Phi_e|\Phi_g F\right]|\Phi_e|. \tag{A.26}$$

Recognising that, in Eqn. (A.20), the term in δ dominates over the term in $|\Phi_{\text{g}}|^2$,

$$\alpha^{-1} \approx \delta, \tag{A.27}$$

and Eqn. (A.26) becomes

$$-\sqrt{|\delta|}F\Phi_{\text{g}} - \frac{m_{\text{a}}w_{\text{L}}^2}{\hbar^2}\frac{\mu^2}{6\epsilon_0}|\Phi_{\text{g}}|^2\Phi_{\text{e}} - \delta\Phi_{\text{e}} = \frac{1}{\sqrt{|\delta|}}\left[\frac{k_{\text{L}}^2 w_{\text{L}}^4 m_{\text{a}}\mu^2}{4\epsilon_0\hbar^2\sqrt{|\delta|}}|\Phi_{\text{g}}|^2\right.$$
$$\left. + \sqrt{|\delta|}|F|^2 + \frac{m_{\text{a}}w_{\text{L}}^2\mu^2}{6\epsilon_0\hbar^2}|\Phi_{\text{e}}|\Phi_{\text{g}}F\right]|\Phi_{\text{e}}|,$$

$$\Rightarrow \qquad -|\delta|F\Phi_{\text{g}} - \sqrt{|\delta|}\frac{m_{\text{a}}w_{\text{L}}^2}{\hbar^2}\frac{\mu^2}{6\epsilon_0}|\Phi_{\text{g}}|^2\Phi_{\text{e}} - \delta\sqrt{|\delta|}\Phi_{\text{e}} = \frac{k_{\text{L}}^2 w_{\text{L}}^4 m_{\text{a}}\mu^2}{4\epsilon_0\hbar^2\sqrt{|\delta|}}|\Phi_{\text{g}}|^2|\Phi_{\text{e}}|$$
$$+ \sqrt{|\delta|}|F|^2|\Phi_{\text{e}}| + \frac{m_{\text{a}}w_{\text{L}}^2\mu^2}{6\epsilon_0\hbar^2}\Phi_{\text{g}}F|\Phi_{\text{e}}|^2. \tag{A.28}$$

Now using Eqn. (A.21),

$$|\Phi_{\text{e}}|^2 = |\alpha|^2|\delta||F|^2|\Phi_{\text{g}}|^2,$$
$$\Rightarrow \qquad = \frac{|F|^2|\Phi_{\text{g}}|^2}{|\delta|}. \tag{A.29}$$

Eqn. (A.29) is Eqn. (5.46) of Chapter 5.2. Applying it to Eqn. (A.28) gives

$$-|\delta|F\Phi_{\text{g}} - \frac{m_{\text{a}}w_{\text{L}}^2\mu^2}{6\epsilon_0\hbar^2|\delta|}|\Phi_{\text{g}}|^2|F|^2\Phi_{\text{g}}F = \sqrt{|\delta|}\left(\delta + \frac{m_{\text{a}}w_{\text{L}}^2}{\hbar^2}\frac{\mu^2}{6\epsilon_0}|\Phi_{\text{g}}|^2\right.$$
$$\left. + \frac{k_{\text{L}}^2 w_{\text{L}}^4 m_{\text{a}}\mu^2}{4\epsilon_0\hbar^2|\delta|}|\Phi_{\text{g}}|^2 + |F|^2\right)|\Phi_{\text{e}}|,$$

$$\Rightarrow \qquad -|\delta|F\Phi_{\text{g}} = \sqrt{|\delta|}\left(\delta + \frac{m_{\text{a}}w_{\text{L}}^2}{\hbar^2}\frac{\mu^2}{6\epsilon_0}|\Phi_{\text{g}}|^2 + |F|^2\right)|\Phi_{\text{e}}|,$$
$$\tag{A.30}$$

where we have identified that the two terms in $1/|\delta|$ may be neglected.

From Eqn. (A.30), we may reach a description of the atomic excited state, under an adiabatic assumption, given by

$$-|\delta|F\Phi_{\mathrm{g}} = s|\delta|\sqrt{|\delta|}\left(1 + \frac{1}{s|\delta|}\left(\frac{m_{\mathrm{a}}w_{\mathrm{L}}^2}{\hbar^2}\frac{\mu^2}{6\epsilon_0}|\Phi_{\mathrm{g}}|^2 + |F|^2\right)\right)|\Phi_{\mathrm{e}}|,$$

$$\Rightarrow \qquad |\Phi_{\mathrm{e}}| = -\frac{s|\delta|}{\delta\sqrt{|\delta|}\left(1 + \frac{1}{s|\delta|}\left(\frac{m_{\mathrm{a}}w_{\mathrm{L}}^2}{\hbar^2}\frac{\mu^2}{6\epsilon_0}|\Phi_{\mathrm{g}}|^2 + |F|^2\right)\right)}F\Phi_{\mathrm{g}},$$

$$= -\frac{s}{\sqrt{|\delta|}\left(1 + \frac{1}{s|\delta|}\left(\frac{m_{\mathrm{a}}w_{\mathrm{L}}^2}{\hbar^2}\frac{\mu^2}{6\epsilon_0}|\Phi_{\mathrm{g}}|^2 + |F|^2\right)\right)}F\Phi_{\mathrm{g}},$$

$$\approx -\frac{sF\Phi_{\mathrm{g}}}{\sqrt{|\delta|}}\left(1 - \frac{1}{|\delta|}\left(\frac{sm_{\mathrm{a}}w_{\mathrm{L}}^2}{\hbar^2}\frac{\mu^2}{6\epsilon_0}|\Phi_{\mathrm{g}}|^2 + |F|^2\right)\right),$$

$$\Rightarrow \qquad \Phi_{\mathrm{e}} = -\frac{sF\Phi_{\mathrm{g}}}{\sqrt{|\delta|}}\left(1 - \frac{1}{|\delta|}\left(\frac{sm_{\mathrm{a}}w_{\mathrm{L}}^2}{\hbar^2}\frac{\mu^2}{6\epsilon_0}|\Phi_{\mathrm{g}}|^2 + |F|^2\right)\right), \qquad (A.31)$$

where s represents the sign of δ, and as such $s^2 \equiv 1$. Eqn. (A.31) is equivalent to both Eqn. (5.45) of Chapter 5.2 and Eqn. (7) of Ref. [33].

A.6 Atomic Field Transformations

A.6.1 Atomic Field

Applying the atomic field transformations outlined in Eqns. (5.48)-(5.49) to Eqn. (5.47),

$$(i\partial_\zeta + \nabla_\perp^2)\Phi_{\mathrm{g}} = s|F|^2\Phi_{\mathrm{g}} - \frac{s|F|^2}{|\delta|}\left(\frac{sm_{\mathrm{a}}w_{\mathrm{L}}^2}{\hbar^2}\frac{\mu^2}{6\epsilon_0}|\Phi_{\mathrm{g}}|^2 + |F|^2\right)\Phi_{\mathrm{g}}$$
$$+ \frac{m_{\mathrm{a}}w_{\mathrm{L}}^2}{\hbar^2}\left(-\frac{\mu^2}{6\epsilon_0}\frac{|F|^2}{\delta}|\Phi_{\mathrm{g}}|^2 + \frac{4\pi\hbar^2 a_{\mathrm{gg}}}{m}|\Phi_{\mathrm{g}}|^2\right)\Phi_{\mathrm{g}},$$

$$\Rightarrow \quad (i\partial_\zeta + \nabla_\perp^2)\psi = s|F|^2\psi - \frac{s|F|^2}{|\delta|}\left(\frac{sm_{\mathrm{a}}w_{\mathrm{L}}^2}{\hbar^2}\frac{\mu^2}{6\epsilon_0}\frac{4\hbar^2}{k_{\mathrm{L}}^2 w_{\mathrm{L}}^4\mu^2}\frac{\epsilon_0|\delta|}{m_{\mathrm{a}}}|\psi|^2 + |F|^2\right)\psi$$
$$+ \frac{m_{\mathrm{a}}w_{\mathrm{L}}^2}{\hbar^2}\left(-\frac{\mu^2}{6\epsilon_0}\frac{|F|^2}{\delta}\frac{4\hbar^2}{k_{\mathrm{L}}^2 w_{\mathrm{L}}^4\mu^2}\frac{\epsilon_0|\delta|}{m_{\mathrm{a}}}|\psi|^2 + \frac{4\pi\hbar^2 a_{\mathrm{gg}}}{m_{\mathrm{a}}}\frac{4\hbar^2}{k_{\mathrm{L}}^2 w_{\mathrm{L}}^4\mu^2}\frac{\epsilon_0|\delta|}{m_{\mathrm{a}}}|\psi|^2\right)\psi,$$

$$= s|F|^2\psi - \frac{s|F|^2}{|\delta|}\left(\frac{2s|\delta|}{3k_{\mathrm{L}}^2 w_{\mathrm{L}}^2}|\psi|^2 + |F|^2\right)\psi$$
$$+ \frac{m_{\mathrm{a}}w_{\mathrm{L}}^2}{\hbar^2}\left(-\frac{2\hbar^2|F|^2}{3m_{\mathrm{a}}k_{\mathrm{L}}^2 w_{\mathrm{L}}^4}|\psi|^2 + \frac{16\pi\hbar^4\epsilon_0|\delta|a_{\mathrm{gg}}}{k_{\mathrm{L}}^2 w_{\mathrm{L}}^4 m_{\mathrm{a}}^2\mu^2}|\psi|^2\right)\psi,$$

$$\Rightarrow \qquad = s|F|^2\psi - \frac{2s^2|F|^2}{3k_{\mathrm{L}}^2 w_{\mathrm{L}}^2}|\psi|^2\psi - s\frac{|F|^4}{|\delta|}\psi - \frac{2|F|^2}{3k_{\mathrm{L}}^2 w_{\mathrm{L}}^2}|\psi|^2\psi$$
$$+ \frac{16\pi\hbar^2\epsilon_0|\delta|a_{\mathrm{gg}}}{k_{\mathrm{L}}^2 w_{\mathrm{L}}^2 m_{\mathrm{a}}\mu^2}|\psi|^2\psi, \tag{A.32}$$

where Eqn. (A.32) is equivalent to Eqn. (5.50) of Chapter 5.2.

A.6.2 Optical Field

We also perform a similar operation to Eqn. (5.44), the optical field. Using the relationship for the excited state as outlined in Eqn. (5.45), this becomes

$$(i\partial_\zeta + \nabla_\perp^2)F = -\frac{k_{\mathrm{L}}^2 w_{\mathrm{L}}^4 m_{\mathrm{a}}\mu^2}{4\epsilon_0\hbar^2\sqrt{|\delta|}}\Phi_{\mathrm{g}}^*\left[-\frac{sF\Phi_{\mathrm{g}}}{\sqrt{|\delta|}}\left[1 - \frac{1}{|\delta|}\left(\frac{sm_{\mathrm{a}}w_{\mathrm{L}}^2}{\hbar^2}\frac{\mu^2}{6\epsilon_0}|\Phi_{\mathrm{g}}|^2 + |F|^2\right)\right]\right],$$
$$= \frac{sk_{\mathrm{L}}^2 w_{\mathrm{L}}^4 m_{\mathrm{a}}\mu^2}{4\epsilon_0\hbar^2|\delta|}|\Phi_{\mathrm{g}}|^2 F\left[1 - \frac{1}{|\delta|}\left(\frac{sm_{\mathrm{a}}w_{\mathrm{L}}^2}{\hbar^2}\frac{\mu^2}{6\epsilon_0}|\Phi_{\mathrm{g}}|^2 + |F|^2\right)\right],$$
$$\Rightarrow \qquad = \frac{sk_{\mathrm{L}}^2 w_{\mathrm{L}}^4 m_{\mathrm{a}}\mu^2}{4\epsilon_0\hbar^2|\delta|}|\Phi_{\mathrm{g}}|^2 F\left[1 - \frac{sm_{\mathrm{a}}w_{\mathrm{L}}^2\mu^2}{6\epsilon_0\hbar^2|\delta|}|\Phi_{\mathrm{g}}|^2 - \frac{|F|^2}{|\delta|}\right]. \tag{A.33}$$

Applying the atomic transfer of Eqn. (5.49), Eqn. (A.33) becomes

$$(i\partial_\zeta + \nabla_\perp^2)F = \frac{sk_{\mathrm{L}}^2 w_{\mathrm{L}}^4 m_{\mathrm{a}}\mu^2}{4\epsilon_0\hbar^2|\delta|}\frac{4\hbar^2}{k_{\mathrm{L}}^2 w_{\mathrm{L}}^4\mu^2}\frac{\epsilon_0|\delta|}{m_{\mathrm{a}}}|\psi|^2 F\Big[1$$
$$- \frac{sm_{\mathrm{a}}w_{\mathrm{L}}^2\mu^2}{6\epsilon_0\hbar^2|\delta|}\frac{4\hbar^2}{k_{\mathrm{L}}^2 w_{\mathrm{L}}^4\mu^2}\frac{\epsilon_0|\delta|}{m_{\mathrm{a}}}|\psi|^2 - \frac{|F|^2}{|\delta|}\Big],$$
$$= s|\psi|^2 F\left[1 - \frac{2s}{3k_{\mathrm{L}}^2 w_{\mathrm{L}}^2}|\psi|^2 - \frac{|F|^2}{|\delta|}\right],$$
$$= s|\psi|^2 F\left[1 - \frac{|F|^2}{|\delta|} - s\beta_{\mathrm{dd}}|\psi|^2\right],$$
$$\Rightarrow \qquad (i\partial_\zeta + \nabla_\perp^2)F = s\left(1 - \frac{|F|^2}{|\delta|}\right)|\psi|^2 F - \beta_{\mathrm{dd}}|\psi|^4 F. \tag{A.34}$$

Eqn. (A.34) is equivalent to Eqn. (5.54) of Chapter 5.2 and Eqn. (8b) of Ref. [33].

Appendix B

Additional Cavity Model Derivation Details

This section contains the full details of certain mathematical procedures contained within the derivation of the cavity model outlined in Chapter 9.2.

B.1   Adiabatic Elimination of Excited Atomic State

In this section, we adiabatically eliminate the excited atomic state from the dynamics. We neglect the term in Eqn. (9.11), $(i\hbar\gamma)/2$, as for significantly large detuning, of approximately ten times the line-width and larger, spontaneous emission is negligible [33]. With these alterations and under an adiabatic assumption, Eqns. (9.9)-(9.11) become

$$(9.9): \qquad \frac{2i\omega_{\mathrm{L}}n^2}{c^2}\frac{\partial A}{\partial t} = -\frac{\omega_{\mathrm{L}}^2\mu}{c^2\epsilon_0}\Phi_{\mathrm{g}}^*\Phi_{\mathrm{e}}e^{-ik_{\mathrm{L}}z}, \tag{B.1}$$

$$(9.10): \qquad i\hbar\frac{\partial\Phi_{\mathrm{g}}}{\partial t} = -\frac{\mu}{2}A\Phi_{\mathrm{e}}e^{-ik_{\mathrm{L}}z} - \frac{\mu^2}{6\epsilon_0}|\Phi_{\mathrm{e}}|^2\Phi_{\mathrm{g}} + \frac{4\pi\hbar^2 a_{\mathrm{gg}}}{m_{\mathrm{a}}}|\Phi_{\mathrm{g}}|^2\Phi_{\mathrm{g}}, \tag{B.2}$$

$$(9.11): \qquad i\hbar\frac{\partial\Phi_{\mathrm{e}}}{\partial t} = -\frac{\mu}{2}A\Phi_{\mathrm{g}}e^{ik_{\mathrm{L}}z} - \frac{\mu^2}{6\epsilon_0}|\Phi_{\mathrm{g}}|^2\Phi_{\mathrm{e}} - \hbar\Delta\Phi_{\mathrm{e}}. \tag{B.3}$$

By grouping like terms in Eqn. (B.3), we may write that

$$\left(\frac{\mu^2}{6\epsilon_0} |\Phi_g|^2 + \hbar\Delta \right) \Phi_e = -\frac{\mu}{2} A \Phi_g e^{ik_L z} - i\hbar\partial_t \Phi_e,$$

$$\Rightarrow \qquad \Phi_e = \frac{1}{\left(\frac{\mu^2}{6\epsilon_0} |\Phi_g|^2 + \hbar\Delta \right)} \left[-\frac{\mu}{2} A \Phi_g e^{ik_L z} - i\hbar\partial_t \Phi_e \right]. \qquad (B.4)$$

As $\frac{\mu^2}{6\epsilon_0} |\Phi_g|^2 << \hbar\Delta$, it can be neglected and we can write

$$\Phi_e \approx \frac{1}{\hbar\Delta} \left[-\frac{\mu}{2} A \Phi_g e^{ik_L z} - i\hbar\partial_t \Phi_e \right]. \qquad (B.5)$$

Similarly to Eqn. (A.19), Eqn. (B.5) has a zero order term, given by

$$\Phi_e = -\frac{\mu}{2\hbar\Delta} A \Phi_g e^{ik_L z}, \qquad (B.6)$$

and its temporal derivative will therefore be given by

$$\partial_t \Phi_e = \partial_t \left(-\frac{\mu}{2\hbar\Delta} A \Phi_g e^{ik_L z} \right) = -\frac{\mu}{2\hbar\Delta} e^{ik_L z} \left[\Phi_g \partial_t A + A \partial_t \Phi_g \right]. \qquad (B.7)$$

We may calculate both of the derivatives in Eqn. (B.7) from Eqns. (B.2) and (B.1). In the case of the optical field, this is given by

$$\partial_t A = i\frac{\omega_L \mu}{2n^2\epsilon_0} \Phi_g^* \Phi_e e^{-ik_L z}, \qquad (B.8)$$

and, for the ground atomic state, is given by

$$\partial_t \Phi_g = i\frac{\mu}{2\hbar} A \Phi_e e^{-ik_L z} + i\frac{\mu^2}{6\hbar\epsilon_0} |\Phi_e|^2 \Phi_g - i\frac{4\pi\hbar^2 a_{gg}}{m_a} |\Phi_g|^2 \Phi_g. \qquad (B.9)$$

Combining these, we obtain that the temporal derivative of the atomic excited state, Eqn. (B.7), may be written as

$$
\begin{aligned}
\partial_t \Phi_{\mathrm{e}} &= -\frac{\mu}{2\hbar\Delta} e^{ik_{\mathrm{L}}z} \left[\Phi_{\mathrm{g}} \left(i\frac{\omega_{\mathrm{L}}\mu}{2n^2\epsilon_0} \Phi_{\mathrm{g}}^* \Phi_{\mathrm{e}} e^{-ik_{\mathrm{L}}z} \right) \right. \\
&\quad \left. + A \left(i\frac{\mu}{2\hbar} A\Phi_{\mathrm{e}} e^{-ik_{\mathrm{L}}z} + i\frac{\mu^2}{6\hbar\epsilon_0}|\Phi_{\mathrm{e}}|^2\Phi_{\mathrm{g}} - i\frac{4\pi\hbar^2 a_{\mathrm{gg}}}{m_{\mathrm{a}}}|\Phi_{\mathrm{g}}|^2\Phi_{\mathrm{g}} \right) \right], \\
&= -i\frac{\mu}{2\hbar\Delta} \left[\frac{\omega_{\mathrm{L}}\mu}{2n^2\epsilon_0}|\Phi_{\mathrm{g}}|^2\Phi_{\mathrm{e}} + \frac{\mu}{2\hbar}|A|^2\Phi_{\mathrm{e}} + \frac{\mu^2}{6\hbar\epsilon_0}|\Phi_{\mathrm{e}}|^2\Phi_{\mathrm{g}}Ae^{ik_{\mathrm{L}}z} - \frac{4\pi\hbar^2 a_{\mathrm{gg}}}{m_{\mathrm{a}}}|\Phi_{\mathrm{g}}|^2\Phi_{\mathrm{g}}A \right], \\
&\approx -i\frac{\mu^2}{4\hbar^2\Delta}|A|^2\Phi_{\mathrm{e}}, \tag{B.10}
\end{aligned}
$$

where we neglected smaller terms to reach Eqn. (B.10).

Finally, we substitute Eqn. (B.10) back into Eqn. (B.3), which gives

$$
\begin{aligned}
-\frac{\mu}{2}A\Phi_{\mathrm{g}}e^{ik_{\mathrm{L}}z} - \frac{\mu^2}{6\epsilon_0}|\Phi_{\mathrm{g}}|^2\Phi_{\mathrm{e}} - \hbar\Delta\Phi_{\mathrm{e}} &= \frac{\mu^2}{4\hbar\Delta}|A|^2\Phi_{\mathrm{e}}, \\
\Rightarrow \quad \hbar\Delta \left(1 + \frac{\mu^2}{4\hbar^2\Delta^2}|A|^2 + \frac{\mu^2}{6\epsilon_0\hbar\Delta}|\Phi_{\mathrm{g}}|^2 \right) \Phi_{\mathrm{e}} &= -\frac{\mu}{2}A\Phi_{\mathrm{g}}e^{ik_{\mathrm{L}}z}, \\
\Rightarrow \qquad\qquad\qquad\qquad\qquad\qquad \Phi_{\mathrm{e}} &= -\frac{\mu A\Phi_{\mathrm{g}}e^{ik_{\mathrm{L}}z}}{2\hbar\Delta \left(1 + \frac{\mu^2}{4\hbar^2\Delta^2}|A|^2 + \frac{\mu^2}{6\epsilon_0\hbar\Delta}|\Phi_{\mathrm{g}}|^2 \right)}.
\end{aligned}
$$

As the terms in μ^2 will be much smaller than 1, we approximate the denominator as $(1 + \epsilon)$, such that $(1 + \epsilon)^{-1} \approx (1 - \epsilon)$. Applying this, we obtain

$$
\Phi_{\mathrm{e}} \approx -\frac{\mu A\Phi_{\mathrm{g}}}{2\hbar\Delta} e^{ik_{\mathrm{L}}z} \left(1 - \frac{\mu^2}{4\hbar^2\Delta^2}|A|^2 - \frac{\mu^2}{6\epsilon_0\hbar\Delta}|\Phi_{\mathrm{g}}|^2 \right). \tag{B.11}
$$

Eqn. (B.11) is identical to Eqn. (9.12) in Chapter 9.2, and is the equivalent of Eqn. (7) of Ref. [33] for the case of a stationary atomic medium.

B.2 Ground Atomic and Optical Fields After Adiabatic Elimination

In this section, we use the adiabatically eliminated optical state, given by Eqn. (9.12), to transform the remaining optical and ground atomic fields, given by Eqns. (9.9) and (9.10), respectively. These three relationships are

$$\Phi_{\mathrm{e}} = -\frac{\mu A \Phi_{\mathrm{g}}}{2\hbar\Delta} e^{ik_{\mathrm{L}}z} \left(1 - \frac{\mu^2}{4\hbar^2\Delta^2}|A|^2 - \frac{\mu^2}{6\epsilon_0}|\Phi_{\mathrm{g}}|^2 \right), \tag{B.12}$$

$$\frac{2i\omega_{\mathrm{L}}n^2}{c^2}\frac{\partial A}{\partial t} = -\nabla_{\perp}^2 A - 2ik_{\mathrm{L}}\frac{\partial A}{\partial z} - \frac{\omega_{\mathrm{L}}^2\mu}{c^2\epsilon_0}\Phi_{\mathrm{g}}^*\Phi_{\mathrm{e}}e^{-ik_{\mathrm{L}}z}, \tag{B.13}$$

$$i\hbar\frac{\partial \Phi_{\mathrm{g}}}{\partial t} = -\frac{\hbar^2}{2m_{\mathrm{a}}}\nabla^2\Phi_{\mathrm{g}} - \frac{\mu}{2}A\Phi_{\mathrm{e}}e^{-ik_{\mathrm{L}}z} - \frac{\mu^2}{6\epsilon_0}|\Phi_{\mathrm{e}}|^2\Phi_{\mathrm{g}} + \frac{4\pi\hbar^2 a_{\mathrm{gg}}}{m_{\mathrm{a}}}|\Phi_{\mathrm{g}}|^2\Phi_{\mathrm{g}}. \tag{B.14}$$

The coupled optical field, Eqn. (B.13), on substitution of Eqn. (B.12), becomes

$$\begin{aligned}
\frac{2i\omega_{\mathrm{L}}n^2}{c^2}\frac{\partial A}{\partial t} &= -\nabla_{\perp}^2 A - 2ik_{\mathrm{L}}\frac{\partial A}{\partial z} \\
&\quad - \frac{\omega_{\mathrm{L}}^2\mu}{c^2\epsilon_0}\Phi_{\mathrm{g}}^* e^{-ik_{\mathrm{L}}z}\left[-\frac{\mu A \Phi_{\mathrm{g}}}{2\hbar\Delta} e^{ik_{\mathrm{L}}z} \left(1 - \frac{\mu^2}{4\hbar^2\Delta^2}|A|^2 - \frac{\mu^2}{6\epsilon_0}|\Phi_{\mathrm{g}}|^2 \right) \right], \\
&= -\nabla_{\perp}^2 A - 2ik_{\mathrm{L}}\frac{\partial A}{\partial z} \\
&\quad + \frac{\omega_{\mathrm{L}}^2\mu^2}{2\hbar\Delta c^2\epsilon_0} \left(1 - \left(\frac{\mu}{2\hbar\Delta}\right)^2|A|^2 - \frac{\mu^2}{6\epsilon_0}|\Phi_{\mathrm{g}}|^2 \right)|\Phi_{\mathrm{g}}|^2 A, \\
\Rightarrow \quad \frac{2ik_{\mathrm{L}}n}{c}\frac{\partial A}{\partial t} &= -\nabla_{\perp}^2 A - 2ik_{\mathrm{L}}\frac{\partial A}{\partial z} \\
&\quad + \frac{k_{\mathrm{L}}^2\mu^2}{2\hbar\Delta n^2\epsilon_0} \left(1 - \left(\frac{\mu}{2\hbar\Delta}\right)^2|A|^2 - \frac{\mu^2}{6\epsilon_0}|\Phi_{\mathrm{g}}|^2 \right)|\Phi_{\mathrm{g}}|^2 A, \\
\Rightarrow \quad i\frac{n}{c}\frac{\partial A}{\partial t} &= -\frac{1}{2k_{\mathrm{L}}}\nabla_{\perp}^2 A - i\frac{\partial A}{\partial z} \\
&\quad + \frac{k_{\mathrm{L}}\mu^2}{4\hbar\Delta n^2\epsilon_0} \left(1 - \left(\frac{\mu}{2\hbar\Delta}\right)^2|A|^2 - \frac{\mu^2}{6\epsilon_0}|\Phi_{\mathrm{g}}|^2 \right)|\Phi_{\mathrm{g}}|^2 A,
\end{aligned}$$

with $k_{\mathrm{L}} = \omega_{\mathrm{L}}n/c$. Using $\Delta = s|\Delta|$, with s representing the sign of Δ, we arrive at

$$i\frac{n}{c}\frac{\partial A}{\partial t} + i\frac{\partial A}{\partial z} + \frac{1}{2k_{\mathrm{L}}}\nabla_{\perp}^2 A = \frac{sk_{\mathrm{L}}\mu^2}{4n^2\epsilon_0\hbar|\Delta|} \left(1 - \left(\frac{\mu}{2\hbar|\Delta|}\right)^2|A|^2 - \frac{\mu^2}{6s\epsilon_0}|\Phi_{\mathrm{g}}|^2 \right)|\Phi_{\mathrm{g}}|^2 A. \tag{B.15}$$

The atomic ground state, Eqn. (B.14), on substitution of Eqn. (B.12), becomes

$$i\hbar\frac{\partial\Phi_{\rm g}}{\partial t} = -\frac{\hbar^2}{2m_{\rm a}}\nabla^2\Phi_{\rm g} - \frac{\mu}{2}Ae^{-ik_{\rm L}z}\left[-\frac{\mu A\Phi_{\rm g}}{2\hbar\Delta}e^{ik_{\rm L}z}\left(1 - \frac{\mu^2}{4\hbar^2\Delta^2}|A|^2 - \frac{\mu^2}{6\epsilon_0}|\Phi_{\rm g}|^2\right)\right]$$
$$- \frac{\mu^2}{6\epsilon_0}\left|-\frac{\mu A\Phi_{\rm g}}{2\hbar\Delta}e^{ik_{\rm L}z}\left(1 - \frac{\mu^2}{4\hbar^2\Delta^2}|A|^2 - \frac{\mu^2}{6\epsilon_0}|\Phi_{\rm g}|^2\right)\right|^2\Phi_{\rm g}$$
$$+ \frac{4\pi\hbar^2 a_{\rm gg}}{m_{\rm a}}|\Phi_{\rm g}|^2\Phi_{\rm g},$$

$$\Rightarrow \quad i\hbar\frac{\partial\Phi_{\rm g}}{\partial t} + \frac{\hbar^2}{2m_{\rm a}}\nabla^2\Phi_{\rm g} = \frac{\mu^2}{4\hbar\Delta}|A|^2\left(1 - \frac{\mu^2}{4\hbar^2\Delta^2}|A|^2 - \frac{\mu^2}{6\epsilon_0}|\Phi_{\rm g}|^2\right)\Phi_{\rm g}$$
$$- \frac{\mu^4}{24\epsilon_0\hbar^2\Delta^2}|A|^2|\Phi_{\rm g}|^2\left(1 - \frac{\mu^2}{4\hbar^2\Delta^2}|A|^2 - \frac{\mu^2}{6\epsilon_0}|\Phi_{\rm g}|^2\right)^2\Phi_{\rm g}$$
$$+ \frac{4\pi\hbar^2 a_{\rm gg}}{m_{\rm a}}|\Phi_{\rm g}|^2\Phi_{\rm g},$$

$$= \hbar\Delta\left(\frac{\mu}{2\hbar\Delta}\right)^2\left(1 - \left(\frac{\mu}{2\hbar\Delta}\right)^2|A|^2 - \frac{\mu^2}{6\epsilon_0}|\Phi_{\rm g}|^2\right)|A|^2\Phi_{\rm g}$$
$$- \frac{\mu^2}{6\epsilon_0}\left(\frac{\mu}{2\hbar\Delta}\right)^2\left(1 - \left(\frac{\mu}{2\hbar\Delta}\right)^2|A|^2 - \frac{\mu^2}{6\epsilon_0}|\Phi_{\rm g}|^2\right)^2|A|^2|\Phi_{\rm g}|^2\Phi_{\rm g}$$
$$+ \frac{4\pi\hbar^2 a_{\rm gg}}{m_{\rm a}}|\Phi_{\rm g}|^2\Phi_{\rm g},$$

$$= \left[s|\Delta|\left(\frac{\mu}{2\hbar|\Delta|}\right)^2\left(1 - \left(\frac{\mu}{2\hbar|\Delta|}\right)^2|A|^2 - \frac{\mu^2}{6\epsilon_0}|\Phi_{\rm g}|^2\right)|A|^2\right.$$
$$- \frac{\mu^2}{6\hbar\epsilon_0}\left(\frac{\mu}{2\hbar|\Delta|}\right)^2\left(1 - \left(\frac{\mu}{2\hbar\Delta}\right)^2|A|^2 - \frac{\mu^2}{6\epsilon_0}|\Phi_{\rm g}|^2\right)^2|A|^2|\Phi_{\rm g}|^2$$
$$\left.+ \frac{4\pi\hbar a_{\rm gg}}{m_{\rm a}}|\Phi_{\rm g}|^2\right]\Phi_{\rm g}, \tag{B.16}$$

where we have recognised that $s^2 \equiv 1$.

Eqns. (B.15)-(B.16) are identical to Eqns. (9.13)-(9.14) of the main text, and provide a coupled description of optical and ultracold atomic fields, with the atomic field stationary in the longitudinal dimension, and the excited atomic state adiabatically eliminated from the dynamics.

Appendix C

Lookup Table

This section summarises the physical constants, models, and parameter definitions used in the thesis.

C.1 Throughout the Thesis

Parameter	Definition	Unit
Free space permittivity, ϵ_0	8.85×10^{-12}	F m^{-1}
BEC refractive index, n	1	-
Reduced Planck constant, $\hbar$	1.054×10^{-34}	J s
Bohr radius, a_0	0.529×10^{-10}	m
Optical wavelength, λ	720×10^{-9}	m
Optical wavenumber, k_{L}	$\frac{2\pi}{\lambda}$	m^{-1}
Speed of light in vacuum, c	3×10^8	m s^{-1}
Optical angular frequency, ω_{L}	$\frac{k_{\mathrm{L}}c}{n}$	rad s^{-1}
Caesium atomic mass, m_{a}	2.207×10^{-25}	kg
Transition dipole matrix element, μ	2.7×10^{-29}	C m
Transition linewidth, Γ	$2\pi \times 5.234 \times 10^6$	Hz
Field detuning magnitude, $|\Delta|$	$10^2 \times \Gamma$	Hz
Adjusted field detuning magnitude, $|\delta|$	$\frac{w_{\mathrm{L}}^2 m_a \Delta}{\hbar}$	-

C.2   Part II (Propagation)

Atoms:
$$\partial_\zeta \psi = i\nabla_\perp^2 \psi - i\left(s|F|^2 - 2\beta_{\rm dd}|F|^2|\psi|^2 + \beta_{\rm col}|\psi|^2\right)\psi. \tag{5.55}$$

Light:
$$\partial_\zeta F = i\nabla_\perp^2 F + i\left(-s|\psi|^2 + \beta_{\rm dd}|\psi|^4\right)F. \tag{5.56}$$

Parameter	Definition	Reference
Atomic beam velocity, $v_{\rm a}$	$\frac{\hbar\omega_{\rm L} n}{m_{\rm a} c}$	(5.31)
Optical field amplitude, F	$\frac{\mu}{2\hbar}\frac{k_{\rm L} w_{\rm L}^2}{v_{\rm a}}\frac{1}{\sqrt{|\delta|}}A$ $\frac{w_{\rm L}\mu}{2\hbar}\sqrt{\frac{m_{\rm a}}{\hbar|\Delta|}}A$	(5.40)
Atomic field amplitude, ψ	$\frac{k_{\rm L} w_{\rm L}^2\mu}{2\hbar}\sqrt{\frac{m_{\rm a}}{\epsilon_0|\delta|}}\Phi_{\rm g}$ $\frac{k_{\rm L} w_{\rm L}\mu}{2}\sqrt{\frac{1}{\epsilon_0\hbar|\Delta|}}\Phi_{\rm g}$	(5.48)
Dipole-dipole nonlinearity, $\beta_{\rm dd}$	$\frac{2}{3k_{\rm L}^2 w_{\rm L}^2}$	(5.51)
Interatomic scattering nonlinearity, $\beta_{\rm col}$	$\frac{16\pi\epsilon_0\hbar^2 a_{\rm gg}|\delta|}{k_{\rm L}^2 w_{\rm L}^2 m_{\rm a}\mu^2}$ $\frac{16\pi\epsilon_0\hbar a_{\rm gg}|\Delta|}{k_{\rm L}^2\mu^2}$	(5.52)

C.3   Part III (Cavity)

Atoms:
$$\partial_\tau \psi = \frac{\alpha_\psi}{\kappa}\left[i\nabla_\perp^2\psi - i\left(s|F|^2 - 2\beta_{\rm dd}|F|^2|\psi|^2 + \beta_{\rm col}|\psi|^2 - iL_3|\psi|^4\right)\psi\right]. \tag{9.66}$$

Light:
$$\partial_\tau F = -\left(1+i\theta\right)F + i\alpha_F\nabla_\perp^2 F - i\frac{2L}{Tk_{\rm L} w_{\rm L}^2}\left(s|\psi|^2 - \beta_{\rm dd}|\psi|^4\right)F + F_{\rm P}. \tag{9.65}$$

Parameter	Definition	Reference
Atomic field amplitude, ψ	$\frac{k_{\rm L} w_{\rm L}\mu}{2n}\sqrt{\frac{1}{\epsilon_0\hbar|\Delta|}}\Phi_{\rm g}$	(9.15) & (9.61)
Optical field amplitude, F	$\frac{w_{\rm L}\mu}{2\hbar}\sqrt{\frac{m_{\rm a}}{\hbar|\Delta|}}A$	(9.16) & (9.60)
Dipole-dipole nonlinearity, $\beta_{\rm dd}$	$\frac{2n^2}{3k_{\rm L}^2 w_{\rm L}^2}$	(9.19) & (9.64)
Interatomic scattering nonlinearity, $\beta_{\rm col}$	$\frac{16\pi n^2\epsilon_0\hbar a_{\rm gg}|\Delta|}{k_{\rm L}^2\mu^2}$	(9.20) & (9.64)
Optical Laplacian pre-factor, α_F	$\frac{\mathcal{L}}{T}\frac{2}{k_{\rm L} w_{\rm L}^2}$	(9.26), (9.46) & (9.64)
Cavity detuning, θ	$\frac{2(\omega_{\rm c}-\omega_{\rm P})\mathcal{L}}{cT}$	(9.30) & (9.45)
Time re-scaling parameter, κ	$\frac{cT}{2\mathcal{L}}$	(9.44) & (9.57)
Optical pump, $F_{\rm P}$	$2w_{\rm L}\sqrt{\frac{m_{\rm a}}{\hbar T}}F_{\rm P}$	(9.47) & (9.64)
Three-body atomic loss, L_3	$\frac{m_{\rm a}}{\hbar k_{\rm L}^2 w_{\rm L}^2}L_3$	(9.64)
Atomic Laplacian pre-factor, α_ψ	$\frac{\hbar}{m_{\rm a} w_{\rm L}^2}$	(9.64)

Bibliography

[1] H. G. Liddell, *A Greek-English Lexicon* (Harper, 1894).

[2] H. Fritzsch, *Elementary Particles: Building Blocks of Matter* (World Scientific, 2005).

[3] C. J. Foot, *Atomic Physics*, Vol. 7 (OUP Oxford, 2004).

[4] T. Tommila, EPL **2**, 789 (1986).

[5] N. Masuhara, J. M. Doyle, J. C. Sandberg, D. Kleppner, T. J. Greytak, H. F. Hess, and G. P. Kochanski, Phys. Rev. Lett. **61**, 935 (1988).

[6] H. F. Hess, Phys. Rev. B **34**, 3476 (1986).

[7] S. Stenholm, Rev. Mod. Phys. **58**, 699 (1986).

[8] E. L. Raab, M. Prentiss, A. Cable, S. Chu, and D. E. Pritchard, Phys. Rev. Lett. **59**, 2631 (1987).

[9] J. J. Tollett, C. C. Bradley, C. A. Sackett, and R. G. Hulet, Phys. Rev. A **51**, R22 (1995).

[10] W. Petrich, M. H. Anderson, J. R. Ensher, and E. A. Cornell, Phys. Rev. Lett. **74**, 3352 (1995).

[11] C. S. Adams, H. J. Lee, N. Davidson, M. Kasevich, and S. Chu, Phys. Rev. Lett. **74**, 3577 (1995).

[12] S. N. Bose, Z. Phys. **26**, 178 (1924).

[13] A. Einstein, Sitzungsber. Kgl. Preuss. Akad. Wiss. **261** (1925).

[14] M. H. Anderson, J. R. Ensher, M. R. Matthews, C. E. Wieman, and E. A. Cornell, Science **269**, 198 (1995).

[15] C. C. Bradley, C. A. Sackett, J. J. Tollett, and R. G. Hulet, Phys. Rev. Lett. **75**, 1687 (1995).

[16] K. B. Davis, M.-O. Mewes, M. R. Andrews, N. J. van Druten, D. S. Durfee, D. M. Kurn, and W. Ketterle, Phys. Rev. Lett. **75**, 3969 (1995).

[17] B. G. Levi, Phys. Today **54**, 14 (2001).

[18] L. Pitaevskii and S. Stringari, *Bose-Einstein Condensation and Superfluidity* (Oxford University Press, 2016).

[19] J. R. Anglin and W. Ketterle, Nature **416**, 211 (2002).

[20] C. Gross and I. Bloch, Science **357**, 995 (2017).

[21] I. Bloch, T. W. Hänsch, and T. Esslinger, Phys. Rev. Lett. **82**, 3008 (1999).

[22] N. Hinkley, J. A. Sherman, N. B. Phillips, M. Schioppo, N. D. Lemke, K. Beloy, M. Pizzocaro, C. W. Oates, and A. D. Ludlow, Science **341**, 1215 (2013).

[23] K. Bongs, M. Holynski, J. Vovrosh, P. Bouyer, G. Condon, E. Rasel, C. Schubert, W. P. Schleich, and A. Roura, Nat. Rev. Phys. **1**, 731 (2019).

[24] C. N. Cohen-Tannoudji, Rev. Mod. Phys. **70**, 707 (1998).

[25] C. E. Wieman, D. E. Pritchard, and D. J. Wineland, Rev. Mod. Phys. **71**, S253 (1999).

[26] R. A. Beth, Phys. Rev. **50**, 115 (1936).

[27] R. Frisch, Z. Phys. **86**, 42 (1933).

[28] M. Aspelmeyer, T. J. Kippenberg, and F. Marquardt, Rev. Mod. Phys. **86**, 1391 (2014).

[29] T. J. Kippenberg and K. J. Vahala, Science **321**, 1172 (2008).

[30] H. Wallis, Phys. Rev. A **56**, 2060 (1997).

[31] K. V. Krutitsky, F. Burgbacher, and J. Audretsch, Phys. Rev. A **59**, 1517 (1999).

[32] M. Saffman, Phys. Rev. Lett. **81**, 65 (1998).

[33] M. Saffman and D. V. Skryabin, "Coupled Propagation of Light and Matter Waves: Solitons and Transverse Instabilities," in *Spatial Solitons*, edited by S. Trillo and W. Torruellas (Springer, Berlin, Heidelberg, 2001) pp. 433–447.

[34] K. Bongs, S. Burger, S. Dettmer, D. Hellweg, J. Arlt, W. Ertmer, and K. Sengstock, Phys. Rev. A **63**, 031602 (2001).

[35] H. Ritsch, P. Domokos, F. Brennecke, and T. Esslinger, Rev. Mod. Phys. **85**, 553 (2013).

[36] L. Allen, M. W. Beijersbergen, R. J. C. Spreeuw, and J. P. Woerdman, Phys. Rev. A **45**, 8185 (1992).

[37] J. A. Stratton, *Electromagnetic Theory*, Vol. 33 (John Wiley & Sons, 2007).

[38] B. E. Saleh and M. C. Teich, *Fundamentals of Photonics* (John Wiley & Sons, 2019).

[39] A. M. Yao and M. J. Padgett, Adv. Opt. Photon. **3**, 161 (2011).

[40] M. J. Padgett, Opt. Express **25**, 11265 (2017).

[41] S. M. Barnett, M. Babiker, and M. J. Padgett, Philos. Trans. Royal Soc. A **375**, 20150444 (2017).

[42] H. Rubinsztein-Dunlop, A. Forbes, M. V. Berry, M. R. Dennis, D. L. Andrews, M. Mansuripur, C. Denz, C. Alpmann, P. Banzer, T. Bauer, E. Karimi, L. Marrucci, M. Padgett, M. Ritsch-Marte, N. M. Litchinitser, N. P. Bigelow, C. Rosales-Guzmán, A. Belmonte, J. P. Torres, T. W. Neely, M. Baker, R. Gordon, A. B.

Stilgoe, J. Romero, A. G. White, R. Fickler, A. E. Willner, G. Xie, B. McMorran, and A. M. Weiner, J. Opt. **19**, 013001 (2016).

[43] A. Yevick, D. J. Evans, and D. G. Grier, Philos. Trans. Royal Soc. A **375**, 20150432 (2017).

[44] M. Ritsch-Marte, Philos. Trans. Royal Soc. A **375**, 20150437 (2017).

[45] A. E. Willner, Y. Ren, G. Xie, Y. Yan, L. Li, Z. Zhao, J. Wang, M. Tur, A. F. Molisch, and S. Ashrafi, Philos. Trans. Royal Soc. A **375**, 20150439 (2017).

[46] P. S. Russell, R. Beravat, and G. K. L. Wong, Philos. Trans. Royal Soc. A **375**, 20150440 (2017).

[47] M. Krenn, M. Malik, M. Erhard, and A. Zeilinger, Philos. Trans. Royal Soc. A **375**, 20150442 (2017).

[48] R. P. Cameron, J. B. Götte, S. M. Barnett, and A. M. Yao, Philos. Trans. Royal Soc. A **375**, 20150433 (2017).

[49] B. J. McMorran, A. Agrawal, P. A. Ercius, V. Grillo, A. A. Herzing, T. R. Harvey, M. Linck, and J. S. Pierce, Philos. Trans. Royal Soc. A **375**, 20150434 (2017).

[50] G. Thirunavukkarasu, M. Mousley, M. Babiker, and J. Yuan, Philos. Trans. Royal Soc. A **375**, 20150438 (2017).

[51] S. Franke-Arnold, Philos. Trans. Royal Soc. A **375**, 20150435 (2017).

[52] H. He, M. E. J. Friese, N. R. Heckenberg, and H. Rubinsztein-Dunlop, Phys. Rev. Lett. **75**, 826 (1995).

[53] N. B. Simpson, K. Dholakia, L. Allen, and M. J. Padgett, Opt. Lett. **22**, 52 (1997).

[54] M. E. J. Friese, J. Enger, H. Rubinsztein-Dunlop, and N. R. Heckenberg, Phys. Rev. A **54**, 1593 (1996).

[55] A. T. O'Neil and M. J. Padgett, Opt. Commun. **185**, 139 (2000).

[56] V. Garcés-Chávez, D. McGloin, M. J. Padgett, W. Dultz, H. Schmitzer, and K. Dholakia, Phys. Rev. Lett. **91**, 093602 (2003).

[57] M. Dienerowitz and K. Dholakia, Topologica **2**, 008 (2009).

[58] Z. Hong, J. Zhang, and B. W. Drinkwater, Phys. Rev. Lett. **114**, 214301 (2015).

[59] V. Belyi, N. Khilo, S. Kurilkina, and N. Kazak, J. Appl. Spectrosc. **80**, 458 (2013).

[60] F. Bouchard, H. Larocque, A. M. Yao, C. Travis, I. De Leon, A. Rubano, E. Karimi, G.-L. Oppo, and R. W. Boyd, Phys. Rev. Lett. **117**, 233903 (2016).

[61] G. Baio, G. R. M. Robb, A. M. Yao, and G.-L. Oppo, Phys. Rev. Res. **2**, 023126 (2020).

[62] F. Castellucci, T. W. Clark, A. Selyem, J. Wang, and S. Franke-Arnold, Phys. Rev. Lett. **127**, 233202 (2021).

[63] S. Franke-Arnold, J. Leach, M. J. Padgett, V. E. Lembessis, D. Ellinas, A. J. Wright, J. M. Girkin, P. Öhberg, and A. S. Arnold, Opt. Express **15**, 8619 (2007).

[64] C. Ryu, M. F. Andersen, P. Cladé, V. Natarajan, K. Helmerson, and W. D. Phillips, Phys. Rev. Lett. **99**, 260401 (2007).

[65] W. Ketterle, D. S. Durfee, and D. M. Stamper-Kurn, arXiv:cond-mat/9904034 (1999).

[66] D. S. Durfee and W. Ketterle, Opt. Express **2**, 299 (1998).

[67] T. Ackemann, G. Labeyrie, G. Baio, I. Krešić, J. G. M. Walker, A. Costa Boquete, P. Griffin, W. J. Firth, R. Kaiser, G.-L. Oppo, and G. R. M. Robb, Atoms **9** (2021).

[68] L. De Broglie, Nature **112**, 540 (1923).

[69] M. Greiner, C. A. Regal, and D. S. Jin, Nature **426**, 537 (2003).

[70] C. A. Regal, M. Greiner, and D. S. Jin, Phys. Rev. Lett. **92**, 040403 (2004).

[71] M. W. Zwierlein, C. A. Stan, C. H. Schunck, S. M. F. Raupach, S. Gupta, Z. Hadzibabic, and W. Ketterle, Phys. Rev. Lett. **91**, 250401 (2003).

[72] T. Bourdel, J. Cubizolles, L. Khaykovich, K. M. F. Magalhães, S. J. J. M. F. Kokkelmans, G. V. Shlyapnikov, and C. Salomon, Phys. Rev. Lett. **91**, 020402 (2003).

[73] V. Bagnato, D. E. Pritchard, and D. Kleppner, Phys. Rev. A **35**, 4354 (1987).

[74] W. Ketterle, K. B. Davis, M. A. Joffe, A. Martin, and D. E. Pritchard, Phys. Rev. Lett. **70**, 2253 (1993).

[75] S. Chu, Rev. Mod. Phys. **70**, 685 (1998).

[76] W. Petrich, M. H. Anderson, J. R. Ensher, and E. A. Cornell, J. Opt. Soc. Am. B **11**, 1332 (1994).

[77] M. R. Andrews, C. G. Townsend, H.-J. Miesner, D. S. Durfee, D. M. Kurn, and W. Ketterle, Science **275**, 637 (1997).

[78] I. Georgescu, Nat. Rev. Phys. **2**, 396 (2020).

[79] W. Ketterle, Nat. Phys. **11**, 982 (2015).

[80] G. Modugno, G. Ferrari, G. Roati, R. J. Brecha, A. Simoni, and M. Inguscio, Science **294**, 1320 (2001).

[81] S. Inouye, M. R. Andrews, J. Stenger, H.-J. Miesner, D. M. Stamper-Kurn, and W. Ketterle, Nature **392**, 151 (1998).

[82] P. Courteille, R. S. Freeland, D. J. Heinzen, F. A. van Abeelen, and B. J. Verhaar, Phys. Rev. Lett. **81**, 69 (1998).

[83] T. Weber, J. Herbig, M. Mark, H.-C. Nägerl, and R. Grimm, Science **299**, 232 (2003).

[84] C. Chin, R. Grimm, P. Julienne, and E. Tiesinga, Rev. Mod. Phys. **82**, 1225 (2010).

[85] D. G. Fried, T. C. Killian, L. Willmann, D. Landhuis, S. C. Moss, D. Kleppner, and T. J. Greytak, Phys. Rev. Lett. **81**, 3811 (1998).

[86] F. Pereira Dos Santos, J. Léonard, J. Wang, C. J. Barrelet, F. Perales, E. Rasel, C. S. Unnikrishnan, M. Leduc, and C. Cohen-Tannoudji, Phys. Rev. Lett. **86**, 3459 (2001).

[87] D. S. Hall, M. R. Matthews, J. R. Ensher, C. E. Wieman, and E. A. Cornell, Phys. Rev. Lett. **81**, 1539 (1998).

[88] D. S. Hall, M. R. Matthews, C. E. Wieman, and E. A. Cornell, Phys. Rev. Lett. **81**, 1543 (1998).

[89] J. Stenger, S. Inouye, D. M. Stamper-Kurn, H.-J. Miesner, A. P. Chikkatur, and W. Ketterle, Nature **396**, 345 (1998).

[90] C. J. Myatt, E. A. Burt, R. W. Ghrist, E. A. Cornell, and C. E. Wieman, Phys. Rev. Lett. **78**, 586 (1997).

[91] J. P. Burke, J. L. Bohn, B. D. Esry, and C. H. Greene, Phys. Rev. Lett. **80**, 2097 (1998).

[92] G. Modugno, M. Modugno, F. Riboli, G. Roati, and M. Inguscio, Phys. Rev. Lett. **89**, 190404 (2002).

[93] G. Roati, F. Riboli, G. Modugno, and M. Inguscio, Phys. Rev. Lett. **89**, 150403 (2002).

[94] J. Goldwin, S. B. Papp, B. DeMarco, and D. S. Jin, Phys. Rev. A **65**, 021402 (2002).

[95] A. Griesmaier, J. Werner, S. Hensler, J. Stuhler, and T. Pfau, Phys. Rev. Lett. **94**, 160401 (2005).

[96] M. Lu, N. Q. Burdick, S. H. Youn, and B. L. Lev, Phys. Rev. Lett. **107**, 190401 (2011).

[97] K. Aikawa, A. Frisch, M. Mark, S. Baier, A. Rietzler, R. Grimm, and F. Ferlaino, Phys. Rev. Lett. **108**, 210401 (2012).

[98] Z. Hadzibabic, C. A. Stan, K. Dieckmann, S. Gupta, M. W. Zwierlein, A. Görlitz, and W. Ketterle, Phys. Rev. Lett. **88**, 160401 (2002).

[99] D. C. Aveline, J. R. Williams, E. R. Elliott, C. Dutenhoffer, J. R. Kellogg, J. M. Kohel, N. E. Lay, K. Oudrhiri, R. F. Shotwell, N. Yu, and R. J. Thompson, Nature **582**, 193 (2020).

[100] F. Dalfovo, S. Giorgini, L. P. Pitaevskii, and S. Stringari, Rev. Mod. Phys. **71**, 463 (1999).

[101] W. Heisenberg, Z. Phys. **33**, 879 (1925).

[102] S. Giorgini, L. P. Pitaevskii, and S. Stringari, Rev. Mod. Phys. **80**, 1215 (2008).

[103] E. P. Gross, Riv. del Nuovo Cim. **20**, 454 (1961).

[104] E. P. Gross, J. Math. Phys. **4**, 195 (1963).

[105] L. P. Pitaevskii, Sov. Phys. JETP **13**, 451 (1961).

[106] R. Y. Chiao, E. Garmire, and C. H. Townes, Phys. Rev. Lett. **13**, 479 (1964).

[107] R. W. Boyd, *Nonlinear Optics* (Academic Press, 2020).

[108] M. Edwards and K. Burnett, Phys. Rev. A **51**, 1382 (1995).

[109] G. Baym and C. J. Pethick, Phys. Rev. Lett. **76**, 6 (1996).

[110] Y. Castin and R. Dum, Phys. Rev. Lett. **77**, 5315 (1996).

[111] H. Kogelnik and T. Li, Proc. IEEE **54**, 1312 (1966).

[112] S. M. Barnett and R. Zambrini, "Orbital Angular Momentum of Light," in *Quantum Imaging*, edited by M. I. Kolobov (Springer New York, New York, NY, 2007) pp. 277–311.

[113] L. Allen, M. J. Padgett, and M. Babiker, "IV The Orbital Angular Momentum of Light," in *Progress in Optics*, Vol. 39, edited by E. Wolf (Elsevier, 1999) pp. 291–372.

[114] A. E. Siegman, *Lasers* (University Science Books, 1986).

[115] N. Sonine, Math. Ann. **16**, 1 (1880).

[116] G. Szego, in *Amer. Math. Soc. Colloquium* (1959).

[117] G. Turnbull, D. Robertson, G. Smith, L. Allen, and M. Padgett, Opt. Commun. **127**, 183 (1996).

[118] L. Marrucci, C. Manzo, and D. Paparo, Phys. Rev. Lett. **96**, 163905 (2006).

[119] T. W. Clark, R. F. Offer, S. Franke-Arnold, A. S. Arnold, and N. Radwell, Opt. Express **24**, 6249 (2016).

[120] N. R. Heckenberg, R. McDuff, C. P. Smith, and A. G. White, Opt. Lett. **17**, 221 (1992).

[121] M. Mirhosseini, O. S. M. na Loaiza, C. Chen, B. Rodenburg, M. Malik, and R. W. Boyd, Opt. Express **21**, 30196 (2013).

[122] F. Gori, G. Guattari, and C. Padovani, Opt. Commun. **64**, 491 (1987).

[123] D. McGloin and K. Dholakia, Contemp. Phys. **46**, 15 (2005).

[124] J. Durnin, J. J. Miceli, and J. H. Eberly, Phys. Rev. Lett. **58**, 1499 (1987).

[125] V. Garcés-Chávez, D. McGloin, H. Melville, W. Sibbett, and K. Dholakia, Nature **419**, 145 (2002).

[126] S. Monk, J. Arlt, D. Robertson, J. Courtial, and M. Padgett, Opt. Commun. **170**, 213 (1999).

[127] C. Paterson and R. Smith, Opt. Commun. **124**, 121 (1996).

[128] D. McGloin, Philos. Trans. Royal Soc. A **364**, 3521 (2006).

[129] J. Arlt, V. Garcés-Chávez, W. Sibbett, and K. Dholakia, Opt. Commun. **197**, 239 (2001).

[130] K. Volke-Sepulveda, V. Garcés-Chávez, S. Chávez-Cerda, J. Arlt, and K. Dholakia, J. Opt. B **4**, S82 (2002).

[131] S. Li and J. Wang, Sci. Rep. **7**, 43233 (2017).

[132] T. Dauxois, *Physics of Solitons* (Cambridge University Press, 2010).

[133] G. I. Stegeman and M. Segev, Science **286**, 1518 (1999).

[134] J. S. Russell, Edin. Roy. Soc. **XIV**, 47 (1840).

[135] Nature **376**, 373 (1995).

[136] L. F. Mollenauer, R. H. Stolen, and J. P. Gordon, Phys. Rev. Lett. **45**, 1095 (1980).

[137] J. Wu, R. Keolian, and I. Rudnick, Phys. Rev. Lett. **52**, 1421 (1984).

[138] A. Kosevich, B. Ivanov, and A. Kovalev, Phys. Rep. **194**, 117 (1990).

[139] Y. Tanaka, Phys. Rev. Lett. **88**, 017002 (2001).

[140] L. Khaykovich, F. Schreck, G. Ferrari, T. Bourdel, J. Cubizolles, L. D. Carr, Y. Castin, and C. Salomon, Science **296**, 1290 (2002).

[141] J. Denschlag, J. E. Simsarian, D. L. Feder, C. W. Clark, L. A. Collins, J. Cubizolles, L. Deng, E. W. Hagley, K. Helmerson, W. P. Reinhardt, S. L. Rolston, B. I. Schneider, and W. D. Phillips, Science **287**, 97 (2000).

[142] S. Burger, K. Bongs, S. Dettmer, W. Ertmer, K. Sengstock, A. Sanpera, G. V. Shlyapnikov, and M. Lewenstein, Phys. Rev. Lett. **83**, 5198 (1999).

[143] B. Eiermann, T. Anker, M. Albiez, M. Taglieber, P. Treutlein, K.-P. Marzlin, and M. K. Oberthaler, Phys. Rev. Lett. **92**, 230401 (2004).

[144] J. Satsuma and N. Yajima, Prog. Theor. Exp. Phys. **55**, 284 (1974).

[145] R. H. Stolen, L. F. Mollenauer, and W. J. Tomlinson, Opt. Lett. **8**, 186 (1983).

[146] A. Di Carli, C. D. Colquhoun, G. Henderson, S. Flannigan, G.-L. Oppo, A. J. Daley, S. Kuhr, and E. Haller, Phys. Rev. Lett. **123**, 123602 (2019).

[147] Z. Chen, M. Segev, and D. N. Christodoulides, Rep. Prog. Phys. **75**, 086401 (2012).

[148] W. J. Firth and D. V. Skryabin, Phys. Rev. Lett. **79**, 2450 (1997).

[149] A. S. Desyatnikov and Y. S. Kivshar, Phys. Rev. Lett. **87**, 033901 (2001).

[150] M. S. Bigelow, P. Zerom, and R. W. Boyd, Phys. Rev. Lett. **92**, 083902 (2004).

[151] W. Walasik, S. Z. Silahli, and N. M. Litchinitser, Sci. Rep. **7**, 11709 (2017).

[152] J. Sun, S. Z. Silahli, W. Walasik, Q. Li, E. Johnson, and N. M. Litchinitser, Opt. Express **26**, 5118 (2018).

[153] A. Turing, Bull. Math. Biol. **52**, 153 (1990).

[154] A. Gierer and H. Meinhardt, Kybernetik **12**, 30 (1972).

[155] A. Yochelis, Y. Tintut, L. L. Demer, and A. Garfinkel, New J. Phys. **10**, 055002 (2008).

[156] A. J. Koch and H. Meinhardt, Rev. Mod. Phys. **66**, 1481 (1994).

[157] S. Kondo, Genes Cells **7**, 535 (2002).

[158] A. Garfinkel, Y. Tintut, D. Petrasek, K. Boström, and L. L. Demer, Proc. Natl. Acad. Sci. U.S.A. **101**, 9247 (2004).

[159] J. von Hardenberg, E. Meron, M. Shachak, and Y. Zarmi, Phys. Rev. Lett. **87**, 198101 (2001).

[160] Q.-X. Liu, P. M. Herman, W. M. Mooij, J. Huisman, M. Scheffer, H. Olff, and J. Van De Koppel, Nat. Commun. **5**, 1 (2014).

[161] V. Shenoy and A. Sharma, Phys. Rev. Lett. **86**, 119 (2001).

[162] A. Sharma and R. Khanna, Phys. Rev. Lett. **81**, 3463 (1998).

[163] Q. Ouyang and H. L. Swinney, Nature **352**, 610 (1991).

[164] P. K. Maini, K. J. Painter, and H. N. P. Chau, J. Chem. Soc., Faraday Trans. **93**, 3601 (1997).

[165] J. S. Langer, Rev. Mod. Phys. **52**, 1 (1980).

[166] F. H. Busse, Rep. Prog. Phys. **41**, 1929 (1978).

[167] E. L. Koschmieder, "Bénard Convection," in *Advances in Chemical Physics* (John Wiley & Sons, Ltd, 1974) pp. 177–212.

[168] L. A. Lugiato and R. Lefever, Phys. Rev. Lett. **58**, 2209 (1987).

[169] P. Mandel and M. Tlidi, J. Opt. B **6**, R60 (2004).

[170] L. Lugiato, F. Prati, and M. Brambilla, *Nonlinear Optical Systems* (Cambridge University Press, 2015).

[171] S. Ciliberto, P. Coullet, J. Lega, E. Pampaloni, and C. Perez-Garcia, Phys. Rev. Lett. **65**, 2370 (1990).

[172] R. Gallego, M. San Miguel, and R. Toral, Phys. Rev. E **61**, 2241 (2000).

[173] F. Arecchi, S. Boccaletti, and P. Ramazza, Phys. Rep. **318**, 1 (1999).

[174] A. M. Yao, C. J. Gibson, and G.-L. Oppo, Opt. Express **27**, 31273 (2019).

[175] T. Ackemann, Y. A. Logvin, A. Heuer, and W. Lange, Phys. Rev. Lett. **75**, 3450 (1995).

[176] G. Grynberg, E. Le Bihan, P. Verkerk, P. Simoneau, J. Leite, D. Bloch, S. Le Boiteux, and M. Ducloy, Opt. Commun. **67**, 363 (1988).

[177] W. Lange, A. Aumann, T. Ackemann, and E. Büthe, J. Opt., B Quantum Semiclass. Opt. **10**, R23 (1998).

[178] G. Labeyrie, E. Tesio, P. M. Gomes, G.-L. Oppo, W. J. Firth, G. R. Robb, A. S. Arnold, R. Kaiser, and T. Ackemann, Nat. Photonics **8**, 321 (2014).

[179] G. Baio, G. R. M. Robb, A. M. Yao, G.-L. Oppo, and T. Ackemann, Phys. Rev. Lett. **126**, 203201 (2021).

[180] E. Tesio, G. R. M. Robb, T. Ackemann, W. J. Firth, and G.-L. Oppo, Phys. Rev. A **86**, 031801 (2012).

[181] J. A. Greenberg, B. L. Schmittberger, and D. J. Gauthier, Opt. Express **19**, 22535 (2011).

[182] B. L. Schmittberger and D. J. Gauthier, J. Opt. Soc. Am. B **33**, 1543 (2016).

[183] K. Kudo and Y. Kawaguchi, Phys. Rev. A **88**, 013630 (2013).

[184] F. Manni, K. G. Lagoudakis, T. C. H. Liew, R. André, and B. Deveaud-Plédran, Phys. Rev. Lett. **107**, 106401 (2011).

[185] Z. Zhang, K.-X. Yao, L. Feng, J. Hu, and C. Chin, Nat. Phys. **16**, 652 (2020).

[186] J. Sabbatini, W. H. Zurek, and M. J. Davis, Phys. Rev. Lett. **107**, 230402 (2011).

[187] Y.-C. Zhang, T. Pohl, and F. Maucher, Phys. Rev. A **104**, 013310 (2021).

[188] J. Hertkorn, J.-N. Schmidt, M. Guo, F. Böttcher, K. S. H. Ng, S. D. Graham, P. Uerlings, T. Langen, M. Zwierlein, and T. Pfau, Phys. Rev. Res. **3**, 033125 (2021).

[189] Y.-C. Zhang, F. Maucher, and T. Pohl, Phys. Rev. Lett. **123**, 015301 (2019).

[190] M. A. Norcia, C. Politi, L. Klaus, E. Poli, M. Sohmen, M. J. Mark, R. N. Bisset, L. Santos, and F. Ferlaino, Nature **596**, 357 (2021).

[191] J. P. Kernevez, G. Joly, M. C. Duban, B. Bunow, and D. Thomas, J. Math. Biol. **7**, 41 (1979).

[192] G.-L. Oppo, A. M. Yao, and D. Cuozzo, Phys. Rev. A **88**, 043813 (2013).

[193] A. Visintin, "Mathematical models of hysteresis," in *Modelling and Optimization of Distributed Parameter Systems Applications to engineering*, edited by K. Malanowski, Z. Nahorski, and M. Peszyńska (Springer US, Boston, MA, 1996) pp. 71–80.

[194] K. A. Morris, Appl. Mech. Rev. **64** (2012), 10.1115/1.4007112.

[195] S. Yang and Y. Shen, Chaos Solitons Fractals **40**, 1808 (2009).

[196] S. Eckel, J. G. Lee, F. Jendrzejewski, N. Murray, C. W. Clark, C. J. Lobb, W. D. Phillips, M. Edwards, and G. K. Campbell, Nature **506**, 200 (2014).

[197] L. Amico, D. Anderson, M. Boshier, J.-P. Brantut, L.-C. Kwek, A. Minguzzi, and W. von Klitzing, Rev. Mod. Phys. **94**, 041001 (2022).

[198] L. Amico, M. Boshier, G. Birkl, A. Minguzzi, C. Miniatura, L.-C. Kwek, D. Aghamalyan, V. Ahufinger, D. Anderson, N. Andrei, A. S. Arnold, M. Baker, T. A. Bell, T. Bland, J. P. Brantut, D. Cassettari, W. J. Chetcuti, F. Chevy, R. Citro, S. De Palo, R. Dumke, M. Edwards, R. Folman, J. Fortagh, S. A. Gardiner, B. M. Garraway, G. Gauthier, A. Günther, T. Haug, C. Hufnagel, M. Keil, P. Ireland, M. Lebrat, W. Li, L. Longchambon, J. Mompart, O. Morsch, P. Naldesi, T. W. Neely, M. Olshanii, E. Orignac, S. Pandey, A. Pérez-Obiol, H. Perrin, L. Piroli, J. Polo, A. L. Pritchard, N. P. Proukakis, C. Rylands, H. Rubinsztein-Dunlop, F. Scazza, S. Stringari, F. Tosto, A. Trombettoni, N. Victorin, W. V. Klitzing, D. Wilkowski, K. Xhani, and A. Yakimenko, AVS Quantum Sci. **3**, 039201 (2021).

[199] J. Delcourt, N. W. Bode, and M. Denoël, Q. Rev. Biol. **91**, 1 (2016).

[200] G. K. Batchelor, *An Introduction to Fluid Dynamics*, Cambridge Mathematical Library (Cambridge University Press, 2000).

[201] C. J. Gibson, A. M. Yao, and G.-L. Oppo, Phys. Rev. Lett. **116**, 043903 (2016).

[202] G. Dvali, F. Kühnel, and M. Zantedeschi, Phys. Rev. Lett. **129**, 061302 (2022).

[203] T. W. Neely, A. S. Bradley, E. C. Samson, S. J. Rooney, E. M. Wright, K. J. H. Law, R. Carretero-González, P. G. Kevrekidis, M. J. Davis, and B. P. Anderson, Phys. Rev. Lett. **111**, 235301 (2013).

[204] K. E. Wilson, E. C. Samson, Z. L. Newman, and B. P. Anderson, Phys. Rev. A **106**, 033319 (2022).

[205] M. R. Matthews, B. P. Anderson, P. C. Haljan, D. S. Hall, C. E. Wieman, and E. A. Cornell, Phys. Rev. Lett. **83**, 2498 (1999).

[206] K. C. Wright, R. B. Blakestad, C. J. Lobb, W. D. Phillips, and G. K. Campbell, Phys. Rev. Lett. **110**, 025302 (2013).

[207] K. C. Wright, R. B. Blakestad, C. J. Lobb, W. D. Phillips, and G. K. Campbell, Phys. Rev. A **88**, 063633 (2013).

[208] A. I. Yakimenko, K. O. Isaieva, S. I. Vilchinskii, and E. A. Ostrovskaya, Phys. Rev. A **91**, 023607 (2015).

[209] J. R. Abo-Shaeer, C. Raman, J. M. Vogels, and W. Ketterle, Science **292**, 476 (2001).

[210] K. W. Madison, F. Chevy, W. Wohlleben, and J. Dalibard, Phys. Rev. Lett. **84**, 806 (2000).

[211] J. Keeling and N. G. Berloff, Phys. Rev. Lett. **100**, 250401 (2008).

[212] M. O. Borgh, J. Keeling, and N. G. Berloff, Phys. Rev. B **81**, 235302 (2010).

[213] S. K. Adhikari, J. Phys. Condens. Matter **31**, 275401 (2019).

[214] H. Bouchiat, Physics **1**, 7 (2008).

[215] H. Bary-Soroker, O. Entin-Wohlman, and Y. Imry, Phys. Rev. Lett. **101**, 057001 (2008).

[216] M. Büttiker, Y. Imry, and R. Landauer, Phys. Lett. A **96**, 365 (1983).

[217] J. File and R. G. Mills, Phys. Rev. Lett. **10**, 93 (1963).

[218] W. A. Little, Phys. Rev. **156**, 396 (1967).

[219] S. Beattie, S. Moulder, R. J. Fletcher, and Z. Hadzibabic, Phys. Rev. Lett. **110**, 025301 (2013).

[220] P. L. Halkyard, M. P. A. Jones, and S. A. Gardiner, Phys. Rev. A **81**, 061602 (2010).

[221] G.-S. Paraoanu, Phys. Rev. A **67**, 023607 (2003).

[222] A. I. Yakimenko, K. O. Isaieva, S. I. Vilchinskii, and M. Weyrauch, Phys. Rev. A **88**, 051602 (2013).

[223] T. Isoshima, M. Nakahara, T. Ohmi, and K. Machida, Phys. Rev. A **61**, 063610 (2000).

[224] A. Muñoz Mateo, A. Gallemí, M. Guilleumas, and R. Mayol, Phys. Rev. A **91**, 063625 (2015).

[225] M. Modugno, C. Tozzo, and F. Dalfovo, Phys. Rev. A **74**, 061601 (2006).

[226] W. Guerin, J.-F. Riou, J. P. Gaebler, V. Josse, P. Bouyer, and A. Aspect, Phys. Rev. Lett. **97**, 200402 (2006).

[227] J. Javanainen, Phys. Rev. Lett. **75**, 1927 (1995).

[228] G. Lenz, P. Meystre, and E. M. Wright, Phys. Rev. Lett. **71**, 3271 (1993).

[229] C. Kittel and P. McEuen, *Introduction to Solid State Physics*, Vol. 8 (Wiley New York, 1996).

[230] D. A. Steck, "Alkali D Line Data," `https://steck.us/alkalidata/` (1998), accessed: 29/08/2023.

[231] A. Gatti, H. Wiedemann, L. A. Lugiato, I. Marzoli, G.-L. Oppo, and S. M. Barnett, Phys. Rev. A **56**, 877 (1997).

[232] A. Di Carli, G. Henderson, S. Flannigan, C. D. Colquhoun, M. Mitchell, G.-L. Oppo, A. J. Daley, S. Kuhr, and E. Haller, Phys. Rev. Lett. **125**, 183602 (2020).

[233] L. Bergé, Phys. Rep. **303**, 259 (1998).

[234] P. A. Altin, G. R. Dennis, G. D. McDonald, D. Döring, J. E. Debs, J. D. Close, C. M. Savage, and N. P. Robins, Phys. Rev. A **84**, 033632 (2011).

[235] P. Köberle, D. Zajec, G. Wunner, and B. A. Malomed, Phys. Rev. A **85**, 023630 (2012).

[236] Y. Kagan, A. E. Muryshev, and G. V. Shlyapnikov, Phys. Rev. Lett. **81**, 933 (1998).

[237] P. J. Everitt, M. A. Sooriyabandara, M. Guasoni, P. B. Wigley, C. H. Wei, G. D. McDonald, K. S. Hardman, P. Manju, J. D. Close, C. C. N. Kuhn, S. S. Szigeti, Y. S. Kivshar, and N. P. Robins, Phys. Rev. A **96**, 041601 (2017).

[238] T. Kraemer, M. Mark, P. Waldburger, J. G. Danzl, C. Chin, B. Engeser, A. D. Lange, K. Pilch, A. Jaakkola, H.-C. Nägerl, and R. Grimm, Nature **440**, 315 (2006).

[239] G. W. Henderson, G. R. M. Robb, G.-L. Oppo, and A. M. Yao, Phys. Rev. Lett. **129**, 073902 (2022).

[240] G. Henderson, G. R. M. Robb, G.-L. Oppo, and A. M. Yao, in *OSA Nonlinear Optics 2021* (Optica Publishing Group, 2021) p. NM1B.6.

[241] G. Henderson, G. R. M. Robb, G.-L. Oppo, and A. M. Yao, in *Optica Advanced Photonics Congress 2022* (Optica Publishing Group, 2022) p. NpM2E.3.

[242] G. W. Henderson, G. R. M. Robb, G.-L. Oppo, and A. M. Yao, in *Complex Light and Optical Forces XVII*, Vol. 12436, edited by D. L. Andrews, E. J. Galvez, and

H. Rubinsztein-Dunlop, International Society for Optics and Photonics (SPIE, 2023) p. 1243608.

[243] C.-C. Chien, S. Peotta, and M. Di Ventra, Nat. Phys. **11**, 998 (2015).

[244] J. B. Götte, K. O'Holleran, D. Preece, F. Flossmann, S. Franke-Arnold, S. M. Barnett, and M. J. Padgett, Opt. Express **16**, 993 (2008).

[245] K. Fuse, Laser Tech. J. **12**, 19 (2015).

[246] A. D. Carli, C. D. Colquhoun, S. Kuhr, and E. Haller, New J. Phys. **21**, 053028 (2019).

[247] D. S. Petrov, G. V. Shlyapnikov, and J. T. M. Walraven, Phys. Rev. Lett. **87**, 050404 (2001).

[248] A. Fromhold, *Quantum Mechanics for Applied Physics and Engineering*, Dover Books on Physics Series (Dover Publications, 1991).

[249] A. O. Sushkov, E. Williams, V. V. Yashchuk, D. Budker, and S. K. Lamoreaux, Phys. Rev. Lett. **93**, 153003 (2004).

[250] A. Snyder, L. Poladian, and D. Mitchell, Opt. Lett. **17**, 789 (1992).

[251] D. Rozas, C. Law, and G. Swartzlander, J. Opt. Soc. Am. B **14**, 3054 (1997).

[252] A. S. Arnold, Opt. Lett. **37**, 2505 (2012).

[253] M. Saffman and Y. Wang, "Collective Focusing and Modulational Instability of Light and Cold Atoms," in *Dissipative Solitons: From Optics to Biology and Medicine* (Springer, Berlin, Heidelberg, 2008) pp. 1–20.

[254] C. Ryu, K. C. Henderson, and M. G. Boshier, New J. Phys **16**, 013046 (2014).

[255] L. Amico, A. Osterloh, and F. Cataliotti, Phys. Rev. Lett. **95**, 063201 (2005).

[256] S. Moulder, S. Beattie, R. P. Smith, N. Tammuz, and Z. Hadzibabic, Phys. Rev. A **86**, 013629 (2012).

Bibliography

[257] L. A. Lugiato, F. Prati, M. L. Gorodetsky, and T. J. Kippenberg, Philos. Trans. Royal Soc. A **376**, 20180113 (2018).

[258] A. Scroggie, W. Firth, G. McDonald, M. Tlidi, R. Lefever, and L. Lugiato, Chaos Solitons Fractals **4**, 1323 (1994).

[259] A. Petrossian, M. Pinard, A. Maître, J.-Y. Courtois, and G. Grynberg, EPL **18**, 689 (1992).

[260] P. Parra-Rivas, D. Gomila, M. A. Matías, S. Coen, and L. Gelens, Phys. Rev. A **89**, 043813 (2014).

[261] I. D. Mayergoyz, *Mathematical Models of Hysteresis and Their Applications* (Academic Press, 2003).

[262] A. H. Silver and J. E. Zimmerman, Phys. Rev. **157**, 317 (1967).

[263] J. E. Zimmerman, P. Thiene, and J. T. Harding, J. Appl. Phys. **41**, 1572 (1970).

[264] H. Wang, Y. Wu, C. Cong, J. Shang, and T. Yu, ACS Nano **4**, 7221 (2010).

[265] F. Gerbier and Y. Castin, Phys. Rev. A **82**, 013615 (2010).

[266] B. M. Garraway and H. Perrin, J. Phys. B **49**, 172001 (2016).

[267] V. Schweikhard, I. Coddington, P. Engels, S. Tung, and E. A. Cornell, Phys. Rev. Lett. **93**, 210403 (2004).

[268] A. Y. Aladyshkin, A. V. Silhanek, W. Gillijns, and V. V. Moshchalkov, Supercond. Sci. Technol. **22**, 053001 (2009).

[269] S. Eckel, A. Kumar, T. Jacobson, I. B. Spielman, and G. K. Campbell, Phys. Rev. X **8**, 021021 (2018).

[270] M. N. Tengstrand, P. Stürmer, E. O. Karabulut, and S. M. Reimann, Phys. Rev. Lett. **123**, 160405 (2019).

[271] G. W. Henderson, G. R. M. Robb, G.-L. Oppo, and A. M. Yao, in *Complex Light and Optical Forces XVII*, Vol. 12436, edited by D. L. Andrews, E. J. Galvez, and H. Rubinsztein-Dunlop, International Society for Optics and Photonics (SPIE, 2023) p. 1243607.

[272] G. W. Henderson, G. R. M. Robb, G.-L. Oppo, and A. M. Yao, in *Conference on Lasers and Electro-Optics/Europe (CLEO/Europe 2023) and European Quantum Electronics Conference (EQEC 2023)* (Optica Publishing Group, 2023) p. ea_2_5.

[273] G. Baio, T. Ackemann, G.-L. Oppo, G. R. M. Robb, and A. M. Yao, Phys. Rev. A **105**, 023318 (2022).

[274] T. Bland, Q. Marolleau, P. Comaron, B. A. Malomed, and N. P. Proukakis, J. Phys. B **53**, 115301 (2020).

[275] J. E. Mooij and C. J. P. M. Harmans, New J. Phys. **7**, 219 (2005).

[276] J. Mooij and Y. V. Nazarov, Nat. Phys. **2**, 169 (2006).

[277] J. Preskill, Quantum **2**, 79 (2018).

[278] L. Salasnich, Opt. Quantum Electron. **49**, 409 (2017).

[279] C. J. Gibson, P. Bevington, G.-L. Oppo, and A. M. Yao, Phys. Rev. A **97**, 033832 (2018).

[280] G. J. de Valcárcel, E. Roldán, and F. Prati, Opt. Commun. **216**, 203 (2003).